UNIVERSITY OF STRATHCLYDE
DEPARTMENT OF PHYSICS

On the Role of Focal Spot Size in Ultra-Intense Laser-Solid Interaction Physics

by

Robbie Wilson

in partial fulfilment of the requirements for the degree of Doctor of Philosophy in Physics

2018

Copyright Declaration

Signed:

Date:

Abstract

This thesis reports on experimental investigations examining the role of laser-pulse focal spot size on key aspects of laser-solid interactions, namely laser-driven proton acceleration and laser-energy absorption, at the current state-of-the-art peak laser intensities (10^{20}–10^{21} W/cm^2). This includes the development of new optical tools and diagnostics to achieve these intensities and explore the resultant physics. The interaction of intense laser pulses (>10^{18} W/cm^2) with solid foils has received considerable attention over the last few decades, motivated by their ability to generate high energy particles (electrons and ions), photons (x-rays, γ-rays and THz emission) and gigagauss magnetic fields. The development of these novel sources of high energy particles and radiation requires understanding of the underpinning physics on parameters such as the laser focal spot size. The work reported here is structured into three main studies.

The first study presents the development of an ellipsoidal F/1 focusing plasma mirror (FPM) capable of increasing the peak intensity achievable on a petawatt level laser system, through focal spot size reduction. A factor of 2.5 reduction in spot size (from 4.0 μm to 1.6 μm [FWHM]) is achieved when compared to F/3.1 focusing with a conventional (solid state) optic. This corresponded to a factor of 3.6 enhancement in peak intensity, taking into account changes in plasma mirror reflectivity and focal spot quality. The sensitivity of FPM operation to misalignment is also investigated, this is vital for its successful development. An example use of a FPM, in an investigation of laser-driven proton acceleration, is demonstrated. The intensity increase (3×10^{20} W/cm^2 to 10^{21} W/cm^2) results in a factor of 2 increase in the maximum energy (from 27 MeV to 53 MeV) of sheath-accelerated protons from a foil target. This study helps to move the concept of focusing plasma mirrors beyond demonstration, towards routinely used tools in laser-plasma research, and enables a window into future research through the intensity enhancement achieved.

The developed F/1 FPM is employed in the second study to investigate the influence

of using tightly focused (near-wavelength sized) focal spot geometry on the properties of beams of accelerated protons generated by the target normal sheath acceleration (TNSA) mechanism. When comparing beam measurements for tight focusing to relativity larger ($\times$2.5 larger) focal spot irradiation, significant variations are found. These include, a slower maximum proton energy scaling with laser intensity (from $I^{0.6}$ to $I^{0.2}$), a $\times$2.5 enhancement in laser-to-proton energy conversion efficiency and a significant degree of target edge emitted protons with tight focusing compared to the larger focal spot measurements. The findings are explained in terms of changes to the evolution dynamics of the rear surface electron spatial distribution, with enhanced lateral electron spreading and subsequent recirculation, under tight focusing compared to the larger spot. Through 2D particle-in-cell simulations this effect is suggested to derive from the front surface interaction dynamics, with a wider angular distribution of fast electrons throughout the target observed with tight focusing. This study is timely considering the employment of low F/# optics is a pulse focusing scheme under consideration by several existing, and future laser facilities as a route to higher intensities.

The final study reports on an investigation of laser-energy absorption into dense plasma. Using a suite of diagnostics, the total reflected laser energy as a function of intensity is measured, distinguishing between the influence of laser energy and focal spot size on energy absorption. Good agreement is found with previously published data on the scaling of absorption with intensity, by variation of pulse energy. However, when the intensity is controlled by variation of the focal spot size, higher absorption values are measured (45% with a relatively large [270 μm FWHM] focal spot, compared to 22% with a tight focus [7 μm FWHM], both at an intensity of $\sim 5\times10^{17}$ W/cm^2) and a slower absorption scaling is observed, relative to the pulse energy variation case. Through 2D particle-in-cell simulations this difference is shown to arise from additional energy gained by the population of electrons recirculating within the target due to multiple interactions with the laser pulse, a process dependent upon; the pulse duration, target thickness, focal spot size, and the energy spectrum and divergence of the fast electrons. A simple geometric electron recirculation model is presented to explore this absorption concept. This investigation has important consequences for fundamental understanding, application development and, most immediately, for experimental methodology.

Acknowledgements

I am immensely fortunate to be working in a subject I feel passionate about, a statement few ever get to say. To quote Marie Curie '*I am among those who think that science has great beauty. A scientist in his laboratory is not only a technician: he is also a child placed before natural phenomena which impress him like a fairy tale.*' The opportunity to be a part of this community has relied upon numerous people, whom deserve my utmost gratitude. I feel privileged to have worked with these people, without whose support and varying knowledge it would not have been possible to conduct the research presented in this thesis. To state this more poetically, '*if I have seen further it is by standing on the shoulders of giants.*'

Firstly, I express my sincere gratitude to my Ph.D supervisor Prof. Paul McKenna, not only for providing the opportunity to work with such an amazing research group, but for being the perfect example of a supervisor, researcher and person. Without his continual support, guidance, patience and immense knowledge, the work within this thesis, and the valuable skills I have learnt throughout, would have not been possible. I could not envision a better supervisor, and for that I am forever grateful.

Besides my supervisor, there are also a number of others key to my Ph.D journey, whom I would like to thank. First of all, Dr. Ross Gray, for passing on his vast and unique knowledge of our research field and life, not only as a colleague but as a friend. He is a continual source of inspiration and one of the best examples of an experimentalist I can name. I would also like to thank Dr. Martin King for his continuous cooperation and guidance regarding the work presented in this thesis. His patience and computational skills are to be envied. Furthermore, my thanks must be given to Prof. David Neely, whose encouragement and immense knowledge has helped throughout my entire Ph.D. He is a great example of someone who asks the 'right', yet often challenging questions, to push work forward, and for that I have a great deal of admiration. I would additionally like to thank my undergraduate project supervisor,

Dr. Mark Wiggins, for introducing me to experimental laser-plasma physics, which has acted as a strong foundation for the research presented in this thesis.

I would additionally like to acknowledge the staff at both the Central Laser Facility (CLF) and the PHELIX laser system, whose world-class expertise enabled the investigations presented in this thesis. Particular praise must be given to Dr. David Carroll, at the CLF, for helping with numerous aspects of this work and for teaching me many experimental skills and the importance of a detailed lab book.

Furthermore, I sincerely thank both Nicholas Butler and Matthew Duff for the proof-reading of this thesis and their valuable insights during this process. I hope to repay this favour through the reading of both your theses, which I know will be of the highest quality. Special mention must be given to Nicholas for being an excellent peer, flatmate and most of all friend.

I additionally thank my numerous, current and previous, colleagues and friends, namely; Bruno, Haydn, David, Rachel, Remi, Adam, John, Sam, Zoë, Chris, Graeme and Dean. Each has provided support, stimulating discussion and contributed to some exceptionally funny situations. Without these people the long days on experiments would have not been the same.

Finally is the enormous thanks I own my family. To my parents, Susan and Maurice, sisters, Lisa and Aimeé, nephews, Aaron and Seth, grandmothers, Betty, Bessie and Molly, and brother-in-law, David. Without the support and wisdom of each I would not be the person I am today. I hope this work may act as a symbol of my continual apprehension. My nephew Aaron states he wishes to be a 'scientist doctor' when he grows up (which I will hold him to!). I hope I can inspire the next generation, in much the same way as I have been by the generations before me.

Role of Author

The results presented in this thesis are the work of the author over several experimental campaigns, performed as part of a team of researchers led by Prof. P. McKenna. The author had a primary role in the planning, execution, data analysis, numerical simulations and interpretation of results.

Chapter 4: The author led the planning and execution of the experimental campaign (as Target Area Operator [TAO]) reported in this chapter. The experiment was set-up by the author and Dr. R.J. Gray. The optic design (presented in chapter 4), and all testing work prior to the experimental campaign, was performed by the author. The proton dosimetry film stacks employed were designed by the author, and assembled by Dr. R.J. Dance and Mr. C. Armstrong, with digitisation conducted Mr. A. Higginson.

Chapter 5: The author led the planning and execution of the two experimental campaigns (as TAO) reported in this chapter; the first being an extension of chapter 4. The second was set-up by the author, Dr. R.J. Gray and Mr. N.M.H. Butler. The proton dosimetry film stacks were designed by the author and Mr. A. Higginson, and assembled by Ms. Z. Davidson and Ms. K. Carnell, with digitisation conducted by the author. Analysis of the proton spectra from the dosimetry stacks was achieved employing a code developed by Dr. D.C. Carroll. PIC simulations were performed by Dr. M. King and analysed by the author.

Chapter 6: The author had a key role in the planning and execution of the experimental campaign reported in this chapter. The experiment was set-up by the author and Dr. R.J Gray. The integrating sphere was designed by Mr. J. McCreadie, Dr. R.J. Gray and the author. The backscatter diagnostic was designed by Dr. R.J. Gray

and set-up by Dr. R.J. Dance and the author. Sphere testing and data analysis was performed by the author. The electron detector was designed by Dr. R.J. Gray and analysed by Mr. S.D.R. Williamson. PIC simulations were performed by Dr. M. King and analysed by Dr. R.J. Gray and the author. The presented model was developed by Dr. R.J. Gray.

Publications

Publications directly resulting from the work presented in this thesis

1. **R. Wilson**, M. King, R. J. Gray, D. C. Carroll, C. Armstrong, S. J. Hawkes, R. J. Clarke, D. J. Robertson, D. Neely and P. McKenna, *Ellipsoidal plasma mirror focusing of high power laser pulses to ultra-high intensities*, Physics of Plasmas, **21**, 033106, 2016.

2. R. J. Gray, **R. Wilson**, S. D. R. Williamson, M. King, R. J. Dance, C. Armstrong, C. Brabetz, F. Wagner, B. Zielbauer, V. Bagnoud, D. Neely and P. McKenna, *Enhanced laser-energy coupling to dense plasmas driven by recirculating electron currents*, accepted to New Journal of Physics, 2018.

3. **R. Wilson**, M. King, R. J. Gray, D. C. Carroll, C. Armstrong, S. J. Hawkes, R. J. Clarke, D. J. Robertson, D. Neely and P. McKenna, *Development of focusing plasma mirrors for ultra-intense laser-driven particle and radiation sources*, Quantum Beam Science, **2**, 1, 2018.

Additional publications resulting from this PhD work

4. B. Gonzalez-Izquierdo, R. J. Gray, M. King, R. J. Dance, **R. Wilson**, J. McCreadie, N. M. H. Butler, R. Capdessus, S. J. Hawkes, J. S. Green, M. Borghesi, D. Neely and P. McKenna, *Optically controlled dense current structures driven by relativistic plasma aperture-induced diffraction*, Nature Physics, **12**, 505-512, 2016.

5. B. Gonzalez-Izquierdo, M. King, R. J. Gray, **R. Wilson**, R. J. Dance, H. Powell, D. A. Maclellan, J. McCreadie, N. M. H. Butler, S. Hawkes, J. S. Green, C. D. Murphy, L. C. Stockhausen, D. C. Carroll, N. Booth, G. G. Scott, M. Borghesi, D. Neely and P. McKenna, *Towards optical polarization control of laser-driven proton*

acceleration in foils undergoing relativistic transparency, Nature Communications, **7**, 12891, 2016.

6. B. Gonzalez-Izquierdo, R. J. Gray, M. King, **R. Wilson**, R. J. Dance, H. Powell, D. A. Maclellan, J. McCreadie, N. M. H. Butler, S. Hawkes, J. S. Green, C. D. Murphy, L. C. Stockhausen, D. C. Carroll, N. Booth, G. G. Scott, M. Borghesi, D. Neely and P. McKenna, *Influence of laser polarization on collective electron dynamics in ultraintense laser-foil interactions*, High Power Laser Science and Engineering, **4**, e33, 2016.

7. B. Gonzalez-Izquierdo, R. Capdessus, M. King, R. J. Gray, **R. Wilson**, R. J. Dance, J. McCreadie, N. M. H. Butler, S. Hawkes, J. S. Green, N. Booth, M. Borghesi, D. Neely and P. McKenna, *Radiation pressure-driven plasma surface dynamics in ultra-intense laser pulse interactions with ultra-thin foils*, accepted Applied Sciences, 2018.

8. H. Padda, M. King, R. J. Gray, H. W. Powell, B. Gonzalez-Izquierdo, L. C. Stockhausen, **R. Wilson**, D. C. Carroll, R. J. Dance, D. A. MacLellan, X. Y. Yuan, N. M. H. Butler, R. Capdessus, R. Torres, M. Borghesi, D. Neely and P. McKenna, *Intra-pulse transition between ion acceleration mechanisms in intense laser-foil interactions*, Physics of Plasma, **23**, 063116, 2016.

9. R. J. Gray, D. A. MacLellan, B. Gonzalez-Izquierdo, H. W. Powell, D. C. Carroll, C. D. Murphy, L. C. Stockhausen, D. R. Rusby, G.G. Scott, **R. Wilson**, N. Booth, D. R. Symes, S. J. Hawkes, R. Torres, M. Borghesi, D. Neely and P. McKenna, *Azimuthal asymmetry in collective electron dynamics in relativistically transparent laser-foil interactions*, New Journal of Physics, **16**, 093027, 2014.

10. A. Higginson, R. J. Gray, M. King, R. J. Dance, S. D. R. Williamson, N. M. H. Butler, **R. Wilson**, R. Capdessus, C. Armstrong, J. S. Green, S. J. Hawkes, P. Martin, W. Q. Wei, S. R. Mirfayzi, X. H. Yuan, S. Kar, M. Borghesi, R. J. Clarke, D. Neely and P. Mckenna, *Near-100 MeV protons via a laser-driven transparency-enhanced hybrid acceleration scheme*, Nature Communications, **9**, 724, 2018.

11. B. Hidding, O. Karger, T. Königstein, G. Pretzler, G. G. Manahan, P. McKenna, R. Gray, **R. Wilson**, S. M. Wiggins, G. H. Welsh, A. Beaton, P. Delinikolas, D.

A. Jaroszynski, J. B. Rosenzweig, A. Karmakar, V. Ferlet-Cavrois, A. Costantino, M. Muschitiello and E. Daly, *Laser-plasma-based Space Radiation Reproduction in the Laboratory*, Scientific Reports, **7**, 42354, 2017.

Contents

Abstract i

Acknowledgements iii

Role of Author v

Publications vii

List of Figures xiv

List of Tables xx

1 Introduction 1

1.1 Laser-plasma interactions: Brief historical overview 3

1.2 Envisioned applications 5

1.3 Thesis outline 10

2 Fundamentals of laser-solid interactions 12

2.1 Electromagnetic radiation and high power laser pulses 12

2.1.1 Electromagnetic nature of light 13

2.1.2 Laser pulse parameters relevant to laser-solid interactions . 15

2.2 Laser induced ionisation processes 17

2.3 The plasma state 22

2.3.1 Parameters employed to define a plasma 25

2.4 Laser induced plasma expansion 27

2.5 Electromagnetic wave interaction with plasma 29

2.5.1 Motion of a single electron in an infinite plane wave 29

2.5.2 The ponderomotive force 33

2.5.3 Laser propagation in plasma 36

2.5.4 Laser energy absorption in dense plasmas 41
2.6 Properties of the laser-generated electrons 49
2.6.1 Fast electron spectrum and temperature 49
2.6.2 Fast electron transport 51
2.7 Laser-driven ion acceleration 54
2.7.1 Target normal sheath acceleration 55
2.7.2 Radiation pressure acceleration 63
2.8 Summary 69

3 Methodology: Lasers, diagnostics and simulations 70
3.1 Overview 70
3.2 High power laser technology 72
3.2.1 Chirped pulse amplification 73
3.2.2 Pulse amplification 75
3.2.3 Optical parametric amplification 77
3.2.4 Laser pulse temporal intensity profile 79
3.2.5 Plasma mirrors 81
3.2.6 The focal spot 84
3.3 High power laser facilities 87
3.3.1 Vulcan-PW 87
3.3.2 PHELIX 91
3.4 Laser-solid experimentation: Diagnostic techniques 92
3.4.1 Energetic particle diagnostics 93
3.4.2 Optical diagnostics 101
3.5 Simulation and modelling 109
3.5.1 Particle-in-cell simulations: EPOCH 109
3.5.2 Optical ray-tracing: Zemax 112
3.6 Summary 113

4 Development of ellipsoidal plasma mirrors for focusing of high power laser pulses 115
4.1 Introduction 115
4.2 Review of relevant literature 117
4.3 Principles of operation and design 119

4.4 Optical ray-trace modelling 124
4.5 Optic manufacturing 126
4.6 Optic reflectivity testing 130
4.7 Optic Testing: Non-plasma regime 133
4.7.1 FPM optimum alignment 134
4.7.2 FPM sensitivity to misalignments 138
4.8 Optic Testing: Plasma regime 142
4.8.1 Experimental method 143
4.8.2 Experimental results 144
4.9 Conclusion 148

5 Influence of focal spot size approaching the laser wavelength on proton acceleration in the TNSA regime 150
5.1 Introduction 150
5.2 Review of relevant literature 152
5.3 Experimental method 154
5.4 Experimental results 157
5.4.1 Maximum proton energy intensity scaling 157
5.4.2 Proton beam energy spectra 159
5.4.3 Proton beam divergence 161
5.4.4 Proton beam spatial distribution 162
5.4.5 Summary of experimental results 164
5.4.6 Target transverse size alteration 167
5.5 Modelling 168
5.6 Conclusion 172

6 Influence of focal spot size on energy absorption in intense laser-solid interactions 175
6.1 Introduction 175
6.2 Review of relevant literature 177
6.3 Experimental method 178
6.4 Experimental results 188
6.4.1 Measurements of laser absorption 188
6.4.2 Measurements of escaped electron fraction 190

6.5 Modelling 192
6.5.1 PIC simulations 192
6.5.2 Geometric model of recirculation-enhanced absorption . . . 197
6.6 Conclusion 200

7 Conclusions & future work **203**
7.1 Development of ellipsoidal plasma mirrors for focusing of high power laser pulses 203
7.2 Influence of focal spot size approaching the laser wavelength on proton acceleration in the TNSA regime 205
7.3 Influence of focal spot size on energy absorption in intense laser-solid interactions 206
7.4 Concluding remarks 208

Bibliography **209**

List of Figures

1.1 Time-integrated picture of the visible light emission during a laser-solid interaction . . . 2
1.2 Progress in peak laser intensity since its first demonstration . . . 3
1.3 Plot depicting the energy deposition of ionising radiation through matter . . . 7
1.4 Schematic illustrating the fast ignition approach to inertial confinement fusion . . . 10

2.1 Illustration depicting optical polarisation states . . . 17
2.2 Depictions of the ionisation mechanisms relevant to laser-solid interactions . . . 22
2.3 Plot displaying various types of plasmas throughout the universe . 26
2.4 Schematic of the pre-plasma at the laser-target interaction surface 29
2.5 Illustration of single electron motion in a plane wave electromagnetic field . . . 31
2.6 Illustration of the evolution of the position of a test electron in a focused laser electric field . . . 35
2.7 Group and phase velocities of an EM wave propagating through plasma as a function of its frequency . . . 39
2.8 Graphical representation of the wave dispersion relation for EM wave propagation in plasma . . . 41
2.9 Illustration depicting the resonance absorption mechanism for a p-polarised laser pulse . . . 45
2.10 Schematic illustration of both vacuum and $\mathbf{J} \times \mathbf{B}$ electron heating mechanisms . . . 47

2.11 Graphical representation of the energy spectra of three distinct fast electron distributions 50
2.12 Illustration of the relevant processes involved in fast electron transport within a solid density target 54
2.13 Depiction of the principle of the target normal sheath acceleration mechanism 56
2.14 Plot of a typical TNSA proton beam energy spectrum measured experimentally 61
2.15 Schematic illustrating the energy dependent divergent nature of a TNSA ion beam 62
2.16 Graphical representation of the hole-boring radiation pressure acceleration regime 66
2.17 Illustration depicting the light-sail regime of radiation pressure acceleration 68

3.1 Map showing the location of the laser facilities employed throughout this thesis 71
3.2 Flow diagram illustrating the basic concept of a CPA based laser system 74
3.3 Schematic of the main components and arrangement of a basic regenerative amplifier 76
3.4 Schematic of the basic design of a multi-pass amplifier arrangement 77
3.5 Schematic of the three wavelength components used in optical parametric amplification 78
3.6 Illustration depicting a simple realistic high intensity laser pulse and a real Vulcan PW pulse temporal intensity profile. 80
3.7 Basic principle of operation of a planar plasma mirror 82
3.8 Photographs of the OAPs used for pulse focusing in this thesis . . 85
3.9 Gaussian distribution depicting two common parameters used to characterise its spatial extent 86
3.10 Comparison of the spatial intensity distributions of two focal spots 87
3.11 Overview of the Vulcan laser facility 88
3.12 Overview of the PHELIX laser facility 91
3.13 Composition of the two RCF types employed in this thesis 94

3.14 Typical results of RCF film exposed to a laser-driven proton beam 96
3.15 Composition of the image plate type employed in this thesis 99
3.16 Illustration of the typical set-up employed to characterise the laser light specularly reflected from the target 102
3.17 Illustration of the basic principle of an integrating sphere operating on a laser-foil interaction investigation 103
3.18 Photographs showing the collection of target debris inside an integrating sphere 105
3.19 Plot of the neutral density value for four various attenuation filters as a function of transmitted light wavelength 107
3.20 Principle of operation of a Shack-Hartmann wavefront sensor . . . 108
3.21 Illustration of the steps involved in the simulation of a plasma system employing the PIC approach 111
3.22 Screenshot of the basic interface of the Zemax OpticalStudio software 113

4.1 Schematic illustration of an ellipse, annotated with the main parameters used to describe its geometry 121
4.2 Schematic diagram showing principle of operation of an ellipsoidal focusing plasma mirror 122
4.3 Plot of the percentage of laser light specularly reflected from a plasma mirror as a function of the incident laser intensity 123
4.4 Screenshot of the optical model created using Zemax ray-trace software 124
4.5 Calculated laser focal spot spatial-intensity distributions from optical ray-trace modelling 125
4.6 Magnification of the input focal spot for FPM design as a function of θ_{In} 126
4.7 Images of the injection moulding approach for FPM manufacturing 128
4.8 Images of the diamond machining approach for FPM manufacturing 129
4.9 Plot showing the cold reflectivity of the manufactured FPM as a function of the incident photon wavelength 131
4.10 Plot of the experimenatlly measured percentage of laser light specularly reflected from the plasma mirror as a function of the laser intensity 132

4.11 Photograph of the experimental set-up developed to characterise the manufactured focusing plasma optics in non-plasma operation . . . 134
4.12 Measured laser focal spot spatial-intensity distributions using the characterisation set-up 136
4.13 Images of the beam spatial-intensity distributions as a function of distance from best focus 137
4.14 Typical measured spatial-intensity distributions of the optimised focal spot formed by FPMs of varying quality 138
4.15 Spatial-intensity distribution of the output focus as a function of ±10 μm x, y and xy OAP focal spot displacement from optimal alignment 139
4.16 Spatial-intensity distributions of FPM output focus as a function of OAP focus shift in the z-direction, from optimal alignment 140
4.17 Quantification Spatial-intensity distributions of FPM output focus as a function of OAP focus shift in the z-direction, from optimal alignment 141
4.18 Photograph of the set-up used to pre-align a FPM before transferring to the Vulcan-PW vacuum chamber 144
4.19 Photographs of the experimental set-up employed to quantify the maximum energy of laser-accelerated protons from a 6 μm thick Al target 145
4.20 Measured laser focal spot spatial-intensity distributions at f_1 and f_2, using the Vulcan-PW laser 146
4.21 Plot of the measured maximum proton energy achieved using both FPMs and PPMs, as a function of the laser intensity on-target 147

5.1 Basic experimental set-up used for both FPM and PPM investigations 155
5.2 Measured laser focal spot spatial-intensity distributions formed by the FPM, for varying degrees of input focus displacement 156
5.3 Plot of the maximum proton energy as a function of the laser intensity, recorded in Experiment A and Experiment B 158
5.4 Plot of the proton beam energy spectra obtained in Experiment A 160
5.5 Plot of the proton beam divergence as a function of proton energy in Experiment A 162
5.6 Example proton beam spatial-intensity distribution, obtained though RCF spectroscopy 163

5.7 Plots of proton beam profile lineouts in the X-axis at various Y-axis angular positions 164
5.8 Example proton beam spatial-intensity distribution for varying target transverse dimensions for both focusing cases 168
5.9 PIC simulation results of the target electron density for both focal spot cases as a function of time 169
5.10 PIC simulation results of the 2D target electron density distribution for electrons with energy >1 MeV 170
5.11 Illustration of the recirculation of fast electrons within a target irradiated by either tight focusing or a relatively larger focal spot 171

6.1 Schematic of the experimental set-up used to measure the degree of laser energy absorbed during a laser-solid interaction 180
6.2 Schematic drawings of the integrating sphere design top and bottom hemispheres and images of the manufactured spheres 181
6.3 Plot displaying the scattered spectrum measured inside both the manufactured test sphere and the reference sphere 183
6.4 Combined energy response curve for the sphere and each optical spectrometer 184
6.5 Photographs of the scatter screen set-up employed to quantify the energy content of specularly reflected and backscattered laser light 186
6.6 Schematic of the set-up employed to achieve an absolute calibration for the energy response of the screen-imager diagnostic 187
6.7 Schematic and image of the wrap-around electron detector stack used to characterise escaping electons 188
6.8 Plot of the percentage of laser energy absorbed as a function of laser irradiance 189
6.9 Plot of the total number of escaping electrons per steradian, n_e/Sr, for electron energies, above 2.3 MeV, measured using the wrap-around stack detector 191
6.10 PIC simulation results for the interaction of 6 μm Al targets with two varying spot sizes 193
6.11 PIC simulation results for the interaction of varying thicknesses of Al target for the two focal spot size cases 195

6.12 PIC simulation results for the interaction of two focal spot sizes with a reduced pulse length 196
6.13 Time-space plot of the electron density of electrons with energy ≥150 keV, travelling in the negative direction 197
6.14 Target thickness and focal spot parameter space plots, showing electron energy gain described by the recirculation model 199

List of Tables

2.1 Table summarising the main parameters frequently used to characterise laser pulses 16

3.1 Table summarising the Vulcan-PW system's laser parameters . . . 89
3.2 Table summarising the PHELIX system's laser parameters 92

5.1 Table summarising the proton spectrum temperature and laser-to-proton energy conversion efficiency for each shot in Experiment A 161

6.1 Fractional absorption values as shown in Fig. 6.8 for 6 μm aluminium targets, either varying E_L or ϕ_0. 190

Chapter 1

Introduction

The subject matter of this thesis is the experimental investigation of intense laser-plasma interactions. This branch of plasma physics has attracted significant interest in the last few decades, primarily motivated by the exotic phenomena which is exhibited. The high energy density nature of ultra-high intensity laser pulses enables the creation of non-linear and collective phenomena of great scientific interest, with exciting envisioned applications. This field encompasses several branches of physics, including lasers, condensed matter, atomic and plasma physics. This makes for a highly active research field with numerous exciting sub-fields and new findings published every day.

Experimental research in this field would not be possible without the invention of the laser, and the various technological advances it has produced. Since the theoretical principle of the optical laser by Albert Einstein, and the first physical demonstration in 1960 by Theodore Maiman [1], this tool has had remarkable impact. The unique properties of such a light source, such as its monochromaticity, coherency and high directionality, have enabled its use in numerous research areas and everyday technologies. It is easy to see the impact which it has had, becoming ubiquitous in everyday life. Maiman remarked that '*the laser is a solution looking for a problem*', it has clearly found a myriad of 'problems' over the decades.

Building upon its demonstration, researchers continued to develop and enhance laser technologies, with the next major step in terms of enhancing peak laser intensity, being the generation of pulsed systems. This was first realised in a controlled way through 'Q-switching' in 1961 [2], then through 'mode-locking' in 1964 [3]. Q-switching allowed for the generation of up to kilo-Joule energy pulses of nanosecond duration, while mode-locking has led to the realisation of ultra-short pulse durations (tens of

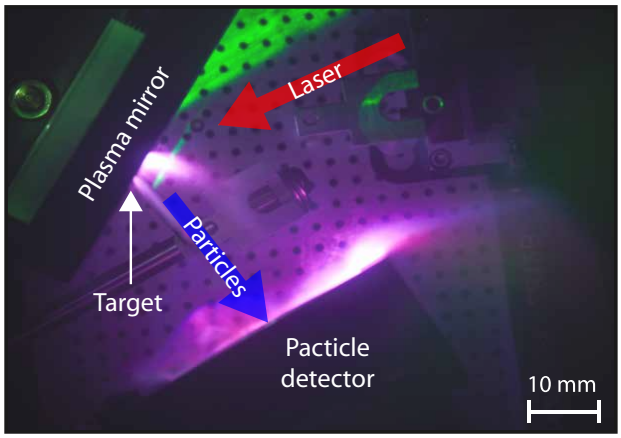

Figure 1.1: Time-integrated picture of the visible light emission during a laser-solid interaction captured during a typical ion acceleration experiment employing the Vulcan-PW laser system. The image gives an impression of the compactness of a laser-driven acceleration experiment, with the main components labelled.

femtoseconds to few picoseconds). These developments facilitated the birth of the field of laser-plasma interactions exploring the exotic phenomena which they display, in the 1970s to early 1980s, in the laser intensity regime of 10^{14}–10^{16} W/cm^2.

For a long period it seemed that this intensity range was the limit, imposed by the damage threshold of optics employed in the laser chain, which led to large beam diameters, and thus large systems restricted to national laboratory facilities. Significant progress in terms of peak intensity, however, was made possible in 1985 with the demonstration of a technique which allowed for significantly higher amplification of laser pulses than previously feasible. This process is called chirped pulsed amplification (CPA), and was developed by D. Strickland and G. Mourou [4]. Through the temporal stretching of the pulse before amplification, lasers in the terawatt, and later petawatt, classification were enabled. This advancement has led to focused intensities of 10^{20}–10^{21} W/cm^2 now being possible on numerous laser systems, which at the time of writing this thesis is the current intensity regime which is being explored. Figure 1.2 provides a visual representation of the peak laser intensity progress throughout the years, highlighting the significant advancements which have pushed the intensity frontier ever higher. With the impeding escalation of focused intensity before the end of this decade, with such upcoming laser facilities as APOLLON [5] and the Extreme Light Infrastructure (ELI) [6], aiming to deliver focal intensities in the range 10^{22}–10^{23} W/cm^2, the field is about to enter uncharted territories of experimental laser-plasma interaction physics.

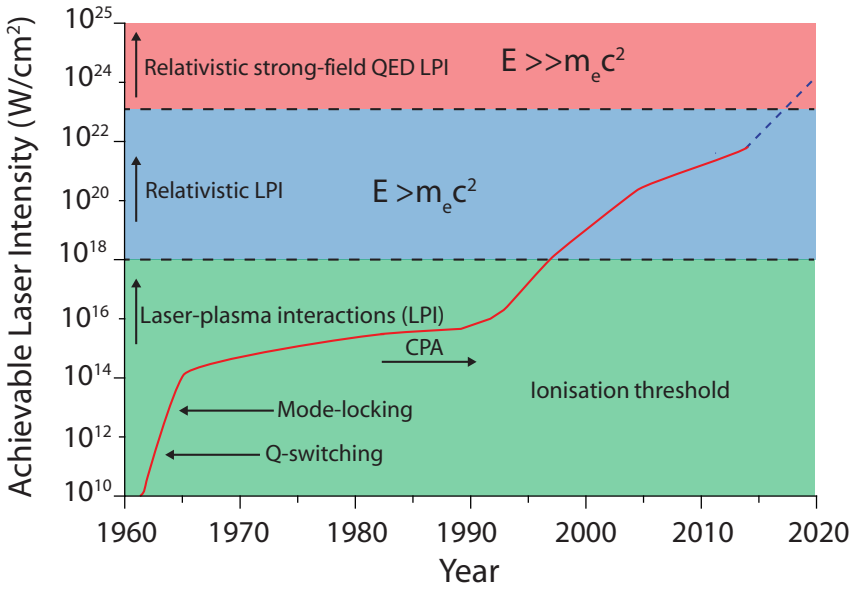

Figure 1.2: Progress in peak laser intensity since the first demonstration of the laser in 1960, highlighting the significant advancements which have increased intensity. Additionally, the three laser-plasma interaction (LPI) regimes are highlighted.

The interaction of such high intensity laser pulses with matter produces a wide range of phenomena, including the generation of extremely strong magnetic and electric fields, sources of energetic particles (electrons, ions and neutrons) and intense energetic photons (x-rays and γ-rays). A main research goal of this field is to have the ability to enhance and have controllability of these sources, with the aim of them being viable for envisioned applications (discussed later in this chapter). Significant progress has been achieved to this end in recent years, with some desired applications now becoming a reality. As such, the remainder of this chapter provides a brief historical overview of this field, and explores some envisioned applications. This serves to provide the reader with some background and motivation for the work presented in this thesis. Finally, an overview of the structure and content of the chapters forming this thesis is presented.

1.1 Laser-plasma interactions: Brief historical overview

The key to understanding intense laser-solid interaction physics is in the fact that matter will be rapidly ionised in the high intensity interaction. The resultant state of matter, known as plasma, allows for a population of free electrons to then be subject to the high intensity laser field, enabling them to acquire significant energy and leading

to numerous exciting physical processes.

A prime interest of this interaction is its potential use as a complement to conventional particle acceleration, owing to the strong acceleration fields generated. Additionally, this acceleration approach is inherently smaller in size and is capable of generating acceleration gradients thousands of times higher than present in conventional accelerators based on radio-frequency (RF) acceleration, which are limited by the breakdown voltage of the accelerating structures (limited to maximum accelerating gradients of $\sim$100 MV/m). Possibly the most well known conventional accelerator is the Large Hadron Collider (LHC), based at the CERN facility. This is a 27 km long circular accelerator capable of producing TeV protons. A promising complementary approach, to address this problem of scale, is to accelerate particles using intense laser pulses and the resulting plasma the laser generates during its interaction with matter. As plasma is in an ionised state, breakdown is not an issue in this acceleration medium. Although laser-plasma accelerators can overcome some of the limitations associated with conventional RF acceleration, such as enhancing particle energy, beam quality and controllability, numerous challenges still remain if this form of acceleration is to become a viable complement to conventional accelerators.

The concept of laser-driven particle acceleration was first proposed in 1979 by Tajima and Dawson [7]. They proposed that a plasma wave, resulting from the wake of an intense laser pulse propagating though a plasma, would accelerate electrons to relativistic energies. At the time of their proposal, unfortunately, laser pulses with the required properties to test this concept did not exist. It was not until 1994 that Nakajima *et al.* [8] experimentally demonstrated this acceleration process, now commonly known as laser wakefield acceleration. Using this scheme, quasi-monoenergetic electron bunches in a highly collimated beam with energies in the region of a few GeV have now been experimentally realised [9, 10, 11]. These high energies are achieved over an acceleration distance from a few hundred microns to a few centimetres, resulting from GV/m to TV/m acceleration gradients.

In terms of the acceleration of ions, at the point of writing this thesis, with current laser intensities ion motion is negligible due to the laser field, only achieving a very small energy gain due their relatively large mass with respect to electrons. Therefore, to date, ions are accelerated as a result of high electrostatic fields generated from charge separation, i.e. displacement, of electrons from ions during the laser-plasma interaction.

Early research into ion acceleration, in the 1980s, employed relatively long nanosecond laser pulses, from gas based CO_2 laser systems. However, these were only capable of generating protons of maximum energy of ∼5 MeV [12], with undesirable beam quality. With increased laser intensities, however, (through the aforementioned CPA technique) protons with maximum energies up to 60 MeV were enabled through the interaction of an intense pulse with thin metallic foils [13], in an acceleration scheme named target normal sheath acceleration [14]. These proton beams display high luminosity [13], energy dependent divergence [15], short duration [16] and a broad band energy spectrum [17]. A significant number of experimental investigations and theoretical studies in this field have been reported, each contributing to a better understanding of these complex interactions, including a number of review articles summarising progress in this field [18, 19, 20, 21].

1.2 Envisioned applications

The study of intense laser-solid interactions is motivated by its uniquely high energy density nature, generating phenomena of great scientific interest which promise a wide range of potentially hugely beneficial applications which have been conceived, and are being actively developed. This section conveys a brief description of two areas where laser-solid interactions may play roles. These are: (i) healthcare [22, 23] and (ii) energy [24]. Numerous other envisioned applications of laser-solid interactions exist, such as x-ray and neutron imaging [25, 26], pre-accelerators for conventional accelerators [27] and isochoric heating of matter [28, 29], to name a few. Additional applications are discussed in detail in numerous sources, including Refs. [30, 31].

Healthcare

Two possible future applications of laser-solid interactions in the medical healthcare sector are explored below. These are hadron therapy for the treatment of cancerous tumours and radioisotope production for employment in medical imaging.

Conventional treatment of cancerous tumours often involves the use of x-rays to irradiate the cancerous area, typically from numerous incident angles to minimise damage of surrounding healthy tissue. Inevitably, though, healthy tissue is damaged due to the energy deposition profile of x-rays. An alternative treatment approach is to use en-

ergetic particles, and in particular protons and heavier ions, in a treatment commonly referred to as hadron therapy. The most common form to date has been proton therapy, which is a highly attractive alternative to radiotherapy. This can be best understood with the aid of Fig. 1.3, depicting the characteristic way in which protons and x-rays deposit energy when interacting with matter. For x-rays the highest energy deposition occurs near the beginning of their interaction, with deposition decaying with propagation distance. Applying this to the treatment of a tumour deep within a patient, this would correspond to the irradiation of healthy tissue which x-rays pass through to reach the tumour. In contrast, protons propagate through matter depositing relativity little energy until they are stopped, at which point maximum energy deposition occurs. The peaked shape of this deposition profile, named the Bragg peak, has become a symbol of the main advantage of hadron therapy, as this phenomenon potentially allows more precise spatial irradiation of the tumour, whilst minimising irradiation of surrounding healthy tissue.

The concept of treating tumours with energetic protons was first proposed in 1946 by Robert Wilson, the founder of the Fermi National Accelerator Laboratory, in which he proposed the use of accelerator-produced protons to treat tumours [32]. It was not until 8 years after this, in 1954, at Lawrence Berkeley Laboratory, the first use of protons to treat a human patient was conducted [33]. Despite the clear advantages of proton therapy, widespread adoption of this treatment approach has been relatively slow compared to x-ray radiotherapy. This is mainly due to technical difficulties and the cost of implementing these systems, in addition to the lack of evidence of cost-effectiveness against other cancer treatment forms [34]. Currently there are only ∼40 hadron therapy facilities worldwide employing conventional accelerators, with only an extremely small percentage of patients with treatable tumours receiving this form of therapy. In the UK, presently there is only one proton therapy centre, based at the Clatterbridge Cancer Centre, for the treatment of eye tumours which utilises 50 MeV protons. However two new centres are being built, in Manchester and London, and several private clinics are being designed to offer proton radiotherapy.

To date the proton energies required for the treatment of deep seated tumours (up to 200 MeV) can only be generated by conventional accelerators. However, laser-driven ion sources are quickly approaching this energy and, additionally, offer unique capabilities over conventional acceleration. For example, laser-solid interactions do not solely

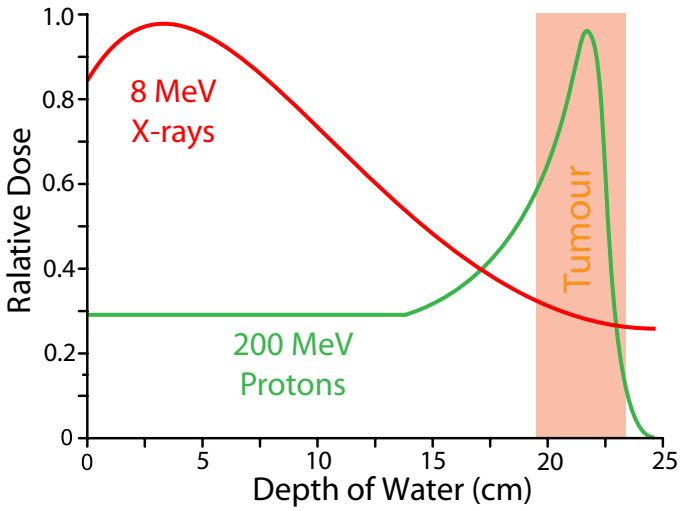

Figure 1.3: Plot depicting the energy deposition of ionising radiation, x-rays (red data) and protons (green data), as they propagate through matter (in this case water simulating a human body).

generation energetic protons, but also larger ion species such as carbon and oxygen, as well as energetic electrons and x-rays. Therefore this acceleration approach offers the possibility to combine laser-driven ions, x-rays and electrons for multi-modality treatment. Additionally, the short duration of the ion beams, coupled with their high flux make them advantageous for hadron therapy. A number of experiments have investigated the use of laser-driven ion acceleration and their biological effects on cellular media reporting on-cell dose rates of $\sim 10^9$ Gy/s [35]; 9 orders of magnitude higher than normally used in radiobiology.

A key research goal for laser-driven proton sources, which has received considerable attention, is the enhancement of the maximum proton energy, to a level feasible for hadron therapy (up to 200 MeV). In addition, tumour therapy requires a marked improvement of the beam parameters currently available; aspects such as the control over the particle energy spectrum and beam focusability still require significant research effort.

The second envisioned healthcare application of laser-solid interactions is the employment of the energetic ion beams generated in the production of radioisotopes used for medical imaging techniques [36]. One such popular technique is positron emission tomography (PET) imaging, in which radioisotopes, such as ^{11}C, ^{13}N, ^{15}O or ^{18}F [37], are injected into a patient's body. The decay of such particles results in the emission of positrons, which are subsequently annihilated through the interaction with electrons

within the patient. This in turn generates two 511 keV photons with equal and opposite momenta, which are measured by a coincidence detection system.

To stimulate the nuclear reactions required to form radioisotopes, a large number of MeV energy protons, for example, are required to irradiate a target to produce the desired quantity and species of isotope. The radioisotopes most suitable for this process are currently produced employing conventional proton accelerators, however due to their relatively short half-life (typically a few minutes to a few hours) accelerators must be relatively close to the PET device to reduce time between formation and use. As such an increase in availability of accelerators, such as laser-driven accelerator facilities, would enable more hospitals to receive the required quantities of radioisotopes, in response to the growing demand [38].

Laser-driven ion sources have demonstrated their ability to generate these desirable medical radioisotopes [39]. Research into these sources, at present, is focused on achieving this production with relativity less powerful, high repetition rate laser systems and enhancing the conversion efficiency, to produce a higher quantity of radioisotopes per interaction.

Energy production

An envisioned application of laser-plasma interactions, which has received considerable research effort, is in the quest for controlled laboratory scale nuclear fusion as an energy source. This involves the fusion of two light nuclei to form a more stable nucleon, with the difference in rest mass energies released as the kinetic energy of particles such as neutrons, protons, deuterons or alpha particles. For reactions to occur, the electrostatic repulsion between reactants must be overcome, requiring particles to have extremely high temperatures (around a hundred million degrees). Achieving such a condition in the laboratory for a sufficient plasma confinement time, however, has proved extremely difficult, with no scheme to produce a fusion reactor producing energy gain at present.

The concept of employing lasers to induce nuclear fusion reactions was first proposed in the 1960's [40], and gained traction in 1972 when theoretically explored by Nuckolls *et al.* [41]. This laser based approach to fusion energy production is called inertial confinement fusion (ICF). This, in its simplest form, involves the compression and heating of a fuel target containing a deuterium-tritium (DT) mixture, to such a

temperature and density that fusion reactions are initiated and a propagating burn wave is induced. The scheme relies on the inward inertia of the target compressing the bulk material, resulting in ignition and energy release in a quantity greater than was required to initiate the process. Compression is induced via laser irradiation of the target outer layer (in the direct drive approach), which ablates off, and due to momentum conservation, drives a corresponding inward acceleration, compressing the fuel. This scheme is often referred to as 'central hot-spot' ICF, which requires highly uniform compression. At present this is still extremely problematic, due to the nanosecond pulse duration employed to drive compression and the subsequent fuel dynamics thus occurring on hydrodynamic time-scales. This leads to the growth of instabilities [42], such as those in the Rayleigh-Taylor classification [43, 44], which can adversely affect confinement and the delivery of laser energy to the target.

To address certain limiting aspects of the basic ICF approach, and to achieve fuel ignition using relatively lower laser energy requirements (thus enhancing reaction gain), a modified scheme known as fast ignition (FI) was conceived, first proposed by Tabak *et al.* [45] in 1994. This approach, as in ICF, involves the compression of the fuel target, though to a lower density than in the central hot-spot scheme, where it is then irradiated by a secondary ultra-short high intensity laser pulse, to deliver energetic particles to the compressed fuel and induce ignition. The novelty of this approach is in decoupling of the compression and ignition phases. The main potential advantage of FI is the reduction in energy required to achieve fusion gain. Furthermore, FI is less susceptible to hydrodynamic instabilities, due to a lower dependency on symmetric compression.

Two variations of this scheme which receive considerable research effort are the 'plasma bore-through' and the 'cone-in-shell' approaches. In the former, an ultra-short igniter pulse tunnels into the compressed fuel to heat the dense core [46]. In the latter approach, the fuel target is attached to the end of a hollow cone of high atomic number material [47, 48]. The cone is used to guide the igniter pulse to the imploded fuel core and thus reduces energy losses with respect to that used to bore through plasma in the former approach. The addition of the cone, however, can affect implosion dynamics. In this approach, ignition can be induced by either energetic electrons or ions accelerated from the cone tip. The first proof-of-principle experiment demonstrating cone usage was

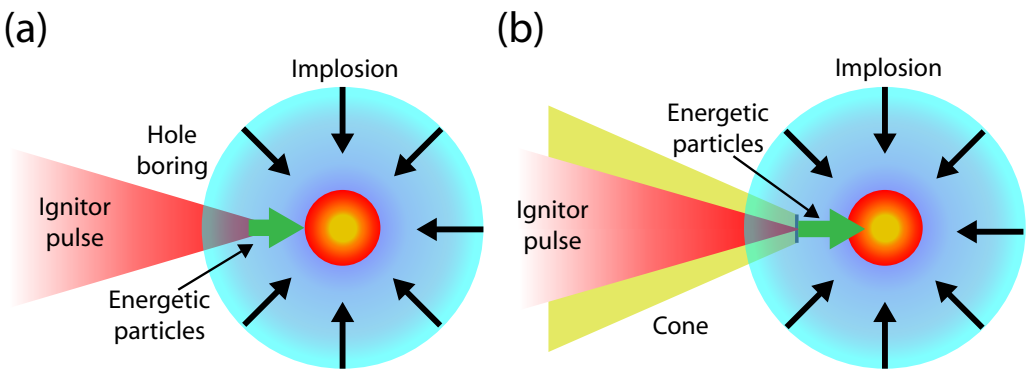

Figure 1.4: Schematic illustrating the fast ignition approaches to inertial confinement fusion, where (a) is the hole-boring scheme and (b) the cone-guided scheme.

presented in Kodama *et al.* [49], where an enhanced neutron yield from fusion reactions was measured. Additionally in this approach to FI, a target foil can be located inside the cone which acts to convert laser energy to energetic ions through the target normal sheath acceleration method. Curvature of the foil can act to focus emitted particles to the compressed fuel core. In a similar way to the aforementioned treatment of deep seated tumours, the stopping profile of ions in matter is advantageous for depositing ion energy to a localised spatial region [50, 51].

1.3 Thesis outline

This thesis reports on experimental investigations exploring the role of laser focal spot size on ultra-intense laser-solid interaction physics. This has necessitated the development of innovative optical tools and diagnostics. In particular, the dependencies of such aspects as laser-energy absorption and laser-driven proton acceleration are examined. The remainder of this thesis is comprised as follows:

- **Chapter 2:** This explores the background physical concepts of laser-solid interactions, essential for understanding the results presented in later chapters.
- **Chapter 3:** This details the experimental and numerical techniques employed to obtain and analyse the experimental findings forming the results chapters. This includes a description of the laser systems, diagnostic techniques and simulation tools utilised.

- **Chapter 4:** Here research centering around the development of a plasma optic for the tight focusing of high power laser pulses is presented. The aim of this is to enhance the achievable intensity through focal spot size reduction. The design, modelling, manufacture and, ultimately, the experimental testing of such an innovative optic is presented.

- **Chapter 5:** Utilising the focusing plasma optic presented in chapter 4, this chapter experimentally investigates the influence of low F-number ($\sim$F/1) tight focusing, forming focal spots of a size approaching the laser wavelength, on laser-driven proton acceleration in the target normal sheath acceleration regime. Experimental findings are accompanied by 2D PIC simulations.

- **Chapter 6:** This final results chapter reports on an investigation exploring the role of laser pulse focal spot size on the coupling of laser energy to plasma electrons in intense laser-solid interactions. Experimental results are presented, accompanied by 2D PIC simulations and analytical modelling.

- **Chapter 7:** Finally, a summary of the results and interpretation of the investigations presented in chapters 4, 5 and 6 is provided. This includes a discussion of potential future avenues of the research presented.

Chapter 2

Fundamentals of laser-solid interactions

The field of laser-solid interactions encompasses numerous disciplines in physics which merge to form an extremely scientifically rich field. Consequently it is relatively difficult to determine its boundaries in order to gain insight into these numerous areas. Nevertheless it is the objective of this chapter to explore the fundamental theory which, at present, underpins the field of laser-solid interactions, relevant to the concepts investigated in this body of work.

To communicate this in a coherent fashion the order in which physical processes occur in a laser-solid interaction (though many overlap) is used to form the structure of this chapter. The sequence of events begins with a laser pulse irradiating an initially cold solid density target held in vacuum. Ablation of the target occurs forming a dense plasma in a few femtoseconds, hence the remainder of the pulse can interact with this and couple energy to free electrons within the plasma. This exchange leads to the aforementioned scientifically rich physics and motivation for research in this field. Further detail on the concepts presented in the forthcoming sections can be found in numerous existing literature, including the textbooks by Kruer [52] and Gibbon [53].

2.1 Electromagnetic radiation and high power laser pulses

Light is a fundamental phenomena thats existence is often taken for granted, with most people caring little for its origins. However, in the field of laser-solid interactions an

apprehension of the nature of light is fundamental. The aim of this section is therefore to provide a brief description of the nature of light, which forms the laser pulses employed in this work, and a description of some frequently used parameters employed in its characterisation. This will aid in the understanding of the relatively more complex interaction concepts presented in the forthcoming sections. The practical methods employed in high power generation of the optical pulses will be covered in chapter 3.

2.1.1 Electromagnetic nature of light

An accidental mathematical discovery by Scottish physicist James Clerk Maxwell, led to light being described as a electromagnetic (EM) wave. This occurred while he was formulating the classical theory of electromagnetism, unifying electricity and magnetism together into a single theory [54]. The famous set of equations (Eq. 2.1-2.4) which resulted from this work can be employed in order to acquire a deeper understanding of the nature of light.

$$\nabla \cdot \mathbf{E} = \frac{\rho}{\varepsilon_0} \quad \textit{Gauss's law of electric field generation} \tag{2.1}$$

$$\nabla \cdot \mathbf{B} = 0 \quad \textit{Gauss's law of magnetic field generation} \tag{2.2}$$

$$\nabla \times \mathbf{E} = -\frac{\partial \mathbf{B}}{\partial t} \quad \textit{Faraday's law of induction} \tag{2.3}$$

$$\nabla \times \mathbf{B} = \mu_0 \mathbf{J} + \frac{1}{c^2}\frac{\partial \mathbf{E}}{\partial t} \quad \textit{Ampére's circuital law} \tag{2.4}$$

where $\mathbf{E}$ and $\mathbf{B}$ are the electric and magnetic field vectors, and $\mathbf{J}$ and ρ are the current and charge densities, respectively. Additionally, bold parameters ($\mathbf{A}$) denote a vector, and the spatial and temporal derivatives are represented with ∇ and $\frac{\partial}{\partial t}$, respectively. The additional terms are physical constants; c the speed of light, ε_0 the permittivity and μ_0 the permeability, of free space. Utilising these relations, a wave equation describing the propagation of EM radiation in vacuum can be derived, by taking the curl ($\nabla \times \mathbf{A}$) of Faraday's Law (Eq. 2.3), in conjunction with the vector identity $\nabla \times (\nabla \times \mathbf{A}) = \nabla(\nabla \cdot \mathbf{A}) - \nabla^2 \mathbf{A}$;

$$\nabla \times (\nabla \times \mathbf{E}) = \nabla \times (-\frac{\partial \mathbf{B}}{\partial t}) = \nabla(\nabla \cdot \mathbf{E}) - \nabla^2 \mathbf{E} \tag{2.5}$$

As the EM wave is propagating in vacuum it is assumed that $\rho = 0$ and $\mathbf{J} = 0$, eliminating the $\nabla(\nabla \cdot \mathbf{E})$ term, through Eq. 2.1. By substitution of Eq. 2.5 into Ampere's Law (Eq. 2.4), the wave equation is obtained;

$$\nabla^2 \mathbf{E} = \frac{1}{c^2} \frac{\partial^2 \mathbf{E}}{\partial t^2} \tag{2.6}$$

One special solution to this equation (Eq. 2.6), assuming the EM field is an undisturbed harmonic wave (referred to as a plane wave) is;

$$\mathbf{E} = E_0 \hat{\mathbf{e}}_x e^{[i(\mathbf{k}.\mathbf{z} - \omega t)]} \tag{2.7}$$

where the wavevector and angular frequency of the EM wave are $\mathbf{k}$ and ω respectively, $\mathbf{z}$ is along the light propagation direction, and t is time. The electric field amplitude of the EM field is given by E_0 and $\hat{\mathbf{e}}_x$ is a unit vector describing the direction of this field in the x-plane. This solution (Eq. 2.7) can be substituted into the wave equation (Eq. 2.6) to form a key relationship in describing the propagation of light through a vacuum, known as the dispersion relation;

$$\omega = ck \tag{2.8}$$

This is a linear relation, thus the phase and group velocity (v) of the wave are of equal value, being c, a frequency-independent constant;

$$v = \frac{\omega}{k} = \frac{d\omega}{dk} = c \tag{2.9}$$

An additional relationship, key to furthering our understanding of EM radiation, is that between the electric and magnetic fields of light, found by firstly substituting the general solution (Eq. 2.7) into Faraday's Law (Eq. 2.3);

$$\mathbf{B} = \frac{1}{c} \hat{e}_y e^{[i(\mathbf{k}.\mathbf{z} - \omega t)]} \tag{2.10}$$

A simple relation to describe the connection between the two fields of a linearly polarised electromagnetic wave (Eq. 2.11) is found comparing Eq. 2.10 and Eq. 2.7. This reveals that these fields are orthogonal, and the maximum amplitudes of each is related to c

as follows;

$$|B_0| = \frac{1}{c}|E_0| \tag{2.11}$$

2.1.2 Laser pulse parameters relevant to laser-solid interactions

In laser-solid interaction studies our interest is in the use of short, high intensity optical pulses, interacting with a solid density material. The terminology 'short' refers to the temporal duration of the pulse, typically ranging from 10 ps to 10 fs, and 'high intensity' is employed to describe pulses with peak intensities ranging from 10^{18}–10^{22} W/cm^2 (though 10^{21}–10^{22} W/cm^2 may often be referred to as 'ultra-high'). The parameters of the pulses employed are of fundamental importance to the resultant interaction physics, and as they are frequently mentioned in this thesis, the main parameters are summarised in Tab. 2.1.

High-power laser pulses are typically Gaussian in nature; this is to say they have spatial and temporal Gaussian profiles. The temporal profile is characterised by the pulse duration (sometimes referred to as pulse length), τ_L, which is essentially the full width half maximum (FWHM) of the pulse's Gaussian temporal envelope. To characterise the Gaussian spatial extent three parameters are often employed; the spot waist/size, the Rayleigh range and the Gouy phase. The former two will be explored in detail in chapter 3 (see section 3.2.6). The Gouy phase describes an additional phase shift acquired by a focusing laser as it goes through focus. This results in an increased distance between wavefronts compared to before focus and thus can impact on the pulse's spatial quality. In essence a wavefront is a surface which connects all the waves in a collection at points of equal phase, an idea used by Christiaan Huygens to aid in a description of the wave-like nature of light. The simplest form of a wavefront, the plane wave, consists of waves parallel to each another, also referred to as collimated light. The wavefront model is also useful for describing non-ideal situations in optical systems, such as aberrations.

An additional parameter to acknowledge in this description, possibly the most common parameter used to characterise a laser system, is the peak focal intensity, I_L. Intensity is defined as the rate at which radiant energy is transferred (peak power) per unit area. This is mathematically equal to the Poynting vector, being the energy flux

Laser Pulse Parameters	Symbol	Units
Energy Before Compressor	E_{L_0}	J
Energy On Target	E_L	J
Pulse Length/Duration (FWHM)	τ_L	fs
Wavelength	λ_L	μm
Frequency	ω_L	Hz
Spot Waist	ω_0	μm
Spot Size (FWHM)	ϕ_0	μm
Percentage Energy in ϕ_0	EE	%
Percentage Compressor Throughput	F_c	%
Peak Intensity	I_L	W/cm^2
Irradiance	$I_L\lambda_L^2$	W/cm$^2\mu$m^2
Temporal Intensity Contrast Ratio	–	–
Polarisation	–	–

Table 2.1: Table summarising the main parameters frequently used to characterise the laser pulses employed throughout this thesis.

density time averaged over the fast oscillations of the laser field (denoted by $\langle\,\rangle$);

$$I = \left\langle \left| \mathbf{E} \times \frac{\mathbf{B}}{\mu_0} \right| \right\rangle = \frac{\varepsilon_0 c}{2} {E_0}^2 \tag{2.12}$$

Practically, however, energy losses occur experimentally, resulting from the imperfect reflectivity of optics for example, thus some fraction, F_c, of the total energy, E_{L_0}, is lost. Consequently, the energy incident on a target is $E_L = E_{L_0} \times F_c$. Assuming the pulse is spatially Gaussian the peak intensity on target is commonly calculated using the fraction of energy, EE, contained within the focal spot (FWHM), ϕ_0;

$$I_L = \frac{EE \times E_L}{\pi(\phi_0/2)^2 \tau_L} \tag{2.13}$$

A final parameter of significance to forthcoming concepts, is the orientation of the laser electric field, relative to the target plane of incidence, i.e. the optical polarisation. The three forms this parameter may take are linear, circular, or elliptical. Linear polarised light can be split into two subsections, either 'p' or 's'. The former describes an electric field orientated in the plane of incidence, and the latter when orientated perpendicular to this plane. Circular polarisation, denoted as 'c', describes light composed of two perpendicular electromagnetic waves, of equal amplitude out of phase by 90°. If one could see the peak of the electric field vector along its propagation axis, it would appear to move in a circular path. The final form is elliptical polarisation, denoted by 'e'. Similar to circular polarised light this consists of two perpendicular waves, however in this case they are of unequal amplitude and out of phase by 90°, or a value other

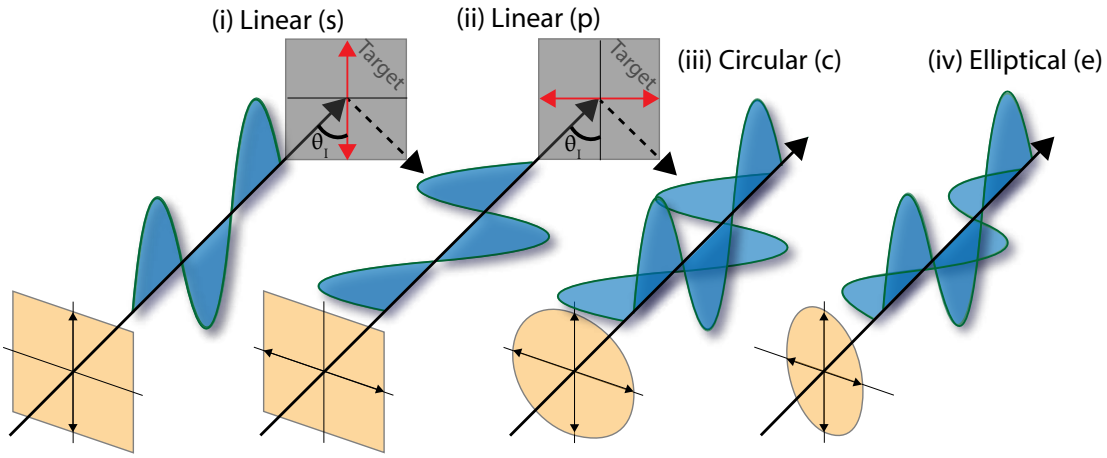

Figure 2.1: Illustration depicting the direction of the electric field of an electromagnetic wave relative to its propagation direction. Where (i) displays linear s-polarisation, (ii) linear p-polarisation (iii) circular polarisation, and (iv) elliptical polarisation. In (i) and (ii) an interaction target being irradiated by each field, at an incident angle of θ_I, is included to aid in distinguishing between s and p polarisation. Note the magnetic field has not been included so the electric field direction could be displayed clearly.

than zero. Each polarisation form is illustrated in Fig. 2.1.

2.2 Laser induced ionisation processes

Although the primary study of this thesis is examining the behaviour of an intense laser field interacting with dense plasma, it is important to have an understanding of how a solid target is transformed into plasma via laser pulse irradiation. This transformation occurs as a result of ionisation, in which ions are formed when an atom, or molecule, loses one or more of its electrons due to having gained sufficient energy. This section explores ionisation mechanisms relevant to short pulse laser-solid interactions, at the intensities considered throughout this thesis (10^{12}–10^{21} W/cm^2).

Generating plasma from a solid clearly involves a state change, which requires sufficient energy to, firstly, overcome the binding energy of the material lattice, then molecular bonds, and finally, the binding energy of electrons within atoms. For a high degree of ionisation electrons must be stripped from the outer to the inner most atomic orbitals. This requires enough energy to eject an electron to such a distance that there is no electrostatic interaction between it and the ion; known as the ionisation potential, U_I.

A natural starting point for gaining insight into ionisation, is to examine some

quantities describing a hydrogen atom. From the atomic model, introduced by Niels Bohr, the mean radius of orbit for hydrogen's ground state electron around the nucleus, i.e. the Bohr radius a_B, given by;

$$a_B = \frac{4\pi\varepsilon_0\hbar^2}{m_e e^2} \tag{2.14}$$

$$= 0.053 \text{ nm}$$

where $\hbar$ is the reduced Planck's constant, and m_e and e are the electron mass and charge, respectively. This radius can then be used to obtain the electric field magnitude holding the electron to the nucleus, E_a, by inserting the Bohr radius into Coulomb's law, assuming the nucleus and electron act as point charges;

$$E_a = \frac{e}{4\pi\varepsilon_0 a_B^2} \tag{2.15}$$

$$\simeq 5.1 \times 10^9 \text{ V/m}$$

It is possible to obtain the equivalent peak laser intensity to match the magnitude of this field binding the electron to the nucleus, with Eq. 2.12, known as the atomic intensity, I_a. This yields an intensity of $\sim 3.51 \times 10^{16}$ W/cm^2. Consequently a pulse of $I_L > I_a$ guarantees ionisation of hydrogen. Ionisation is, however, seen to occur experimentally at intensities orders of magnitude below I_a via numerous mechanisms which can circumvent this limit. A description of each of these mechanisms and the regime in which they are dominant follows.

Multiphoton ionisation

An electron will be ejected from an atom if it absorbs a photon of energy larger than its ionisation potential. Using hydrogen as an example, the ionisation potential of its ground state electron, U_H, equals 13.6 eV; equivalent to a $\sim$91 nm wavelength photon, located in the extreme ultra-violet region of the EM spectrum. This phenomenon is more commonly known as the photoelectric effect. The laser systems employed in this thesis are, however, in the infra-red (IR) region (photon energy of 1.2 eV, at $\lambda_L = 1$ μm). Hydrogen's ground state electron would therefore have to absorb $\sim$12 IR photons to overcome the ionisation potential. This is the process which occurs in the multiphoton ionisation (MPI) mechanism, where the atom absorbs a sufficient

number of photons, which collectively have enough energy to liberate an electron. This mechanism is depicted in Fig. 2.2(a). The probability of this scenario occurring is found by expanding the one photon dipole transition theory to higher orders according to perturbation theory, thus the n-photon ionisation rate, W_n, is given by;

$$W_n = \sigma_n I_L^n \tag{2.16}$$

The MPI rate (Eq. 2.16) depends on σ_n, the cross section of photon absorption, which decreases with n. However, the I_L^n dependency ensures that an ionisation event will occur provided the laser intensity is sufficiently high, initiating around $>10^{12}$ W/cm^2. This mechanism was experimentally observed in the late 1960's in Voronov *et al.* [55] and Agostini *et al.* [56].

Furthermore an electron may absorb more photons than is required to overcome its U_I, resulting in it gaining some kinetic energy, E_K, as described by Eq. 2.17;

$$E_K = (n + s)\,\hbar\omega_L - U_I \tag{2.17}$$

Where n is the number of photons with collective energy of U_I, and s the excess number of photons absorbed. This extension of MPI is termed above-threshold ionisation (ATI). It is experimentally diagnosed to have occurred by the presence of distinct peaks in the electron energy spectrum separated by the laser photon energy, as reported in Gontier *et al.* [57].

Tunnelling ionisation

An assumption made in the description of MPI is that the atomic potential of an atom is unperturbed by the irradiating laser. However, for the majority of forthcoming concepts explored in this chapter, the laser field strength dwarfs inter-atomic fields by many orders of magnitude. This acts as a retarding potential modifying the atomic potential holding electrons. Therefore perturbation theory, as used for MPI, can no longer be applied. Figure 2.2(b) illustrates the alteration of an atom's Coulomb potential, due to an external field. This modification can be shown analytically by considering an electron trapped in an atom's Coulomb potential, with an external field, E_{Ext}, applied,

to give a resulting potential, $V(x)$;

$$V(x) = \frac{-Ze^2}{x} - eE_{Ext}x \tag{2.18}$$

The negative sign preceding the second terms on the RHS of this equation, shows the external field acts to suppress the atom's Coulomb potential. Quantum mechanically, an electron may then tunnel through this suppressed barrier with some finite probability, in a mechanism termed tunnelling ionisation (TI).

The Keldysh parameter

Having presented two ionisation schemes, it is important to distinguish which is likely to dominate under various interaction conditions. This was accomplished by Keldysh *et al.* [58] and Perelomov *et al.* [59, 60], in which a key parameter, named the Keldysh parameter (Eq. 2.19), to distinguish between the dominance of each mechanism was formulated;

$$\gamma_K = \omega_L \sqrt{\frac{2U_I}{I_L}} \sim \sqrt{\frac{U_I}{\Phi_{pond}}} \tag{2.19}$$

where Φ_{pond} is the ponderomotive potential of the laser field (described in section 2.5.2). At this point Φ_{pond} is important to note that it is proportional to $I_L\lambda_L^2$. As a rule of thumb, when $\gamma_K \gg 1$ multiphoton ionisation dominates, and conversely, $\gamma_K \ll 1$, tunnelling ionisation will prevail, as the ponderomotive potential begins to dominate (assuming relatively long wavelength photons such as those employed in this thesis).

Looking again at the ground state of hydrogen (U_H= 13.6 eV), the transition between MPI and TI (i.e. γ_K= 1) occurs at an intensity of ~7.3×10^{14} W/cm^2. This suggests that the dominating mechanism in the interaction of lower intensity (<10^{14} W/cm^2) light preceding the main pulse is MPI. Though at relativity higher intensities, present in the main pulse, ionisation will be dominated by field suppression processes.

Barrier suppression ionisation

In the tunnelling ionisation description the potential barrier is lowered sufficiently to allow an electron to tunnel through the potential barrier. However if the laser field strength is relatively larger further reduction of the potential barrier occurs, leading to the point where it is lower than the electron binding energy, as depicted in Fig. 2.2(c);

this mechanism is referred to as barrier suppression (BS) ionisation, or over-the-barrier ionisation.

The intensity threshold for BS to occur is found by obtaining the electric field strength the barrier must be reduced to, to be called 'suppressed';

$$E_{BS} = \frac{U_I^2 \varepsilon_0 \pi}{e^3 Z} = 1.73 \times 10^8 \text{ V/m} \cdot \frac{U_I^2/\text{eV}}{Z} \tag{2.20}$$

Again through Eq. 2.12, the equivalent peak laser intensity required to match this electric field can be found;

$$I_{BS} = \frac{U_I^4 \varepsilon_0^3 c \pi^2}{2 Z^2 e^6} = \frac{4 \times 10^9}{Z^2} \frac{U^4}{eV} \quad [\text{W/cm}^2] \tag{2.21}$$

Going back to the useful example of hydrogen, its ground state electron will have a E_{BS} of 3.2×10^{10} V/m, equivalent to a laser intensity of 1.4×10^{14} W/cm^2.

Collisional ionisation

The final ionisation mechanism relevant to laser-solid interactions is one involving electrons already freed from their atoms. Once ionisation of the target, even partially, has begun the resultant plasma has a certain electron density, n_e, and these electrons are free to potentially collide with atoms and ions. In these collisions energy may be transferred, which can be in excess of the atomic binding energy and thus causing further ionisation. This process is depicted in Fig. 2.2(d). The ionisation rate of this collisional effect, ν_C, is calculated from the velocity of the colliding electrons, v_e, the electron density, n_e, and the mean electron temperature, T_e [16];

$$\nu_C \approx n_e v_e 4\pi a_b^2 \left(\frac{U_H^2}{U_I k_B T_e} \right) \ln \left(\frac{k_B T_e}{U_I} \right) \tag{2.22}$$

This relatively simple estimation of the collisional ionisation rate correctly predicts that the rate is higher at a lower electron temperature and higher electron density. This is the case as at these conditions the cross section of collisions is relatively high compared to a low density, high temperature plasma. As collisional ionisation does not require the laser field its occurrence is not limited to the irradiation time. If a large number of electrons, of sufficient energy to ionise, are present this process can grow exponentially in a process known as avalanche ionisation.

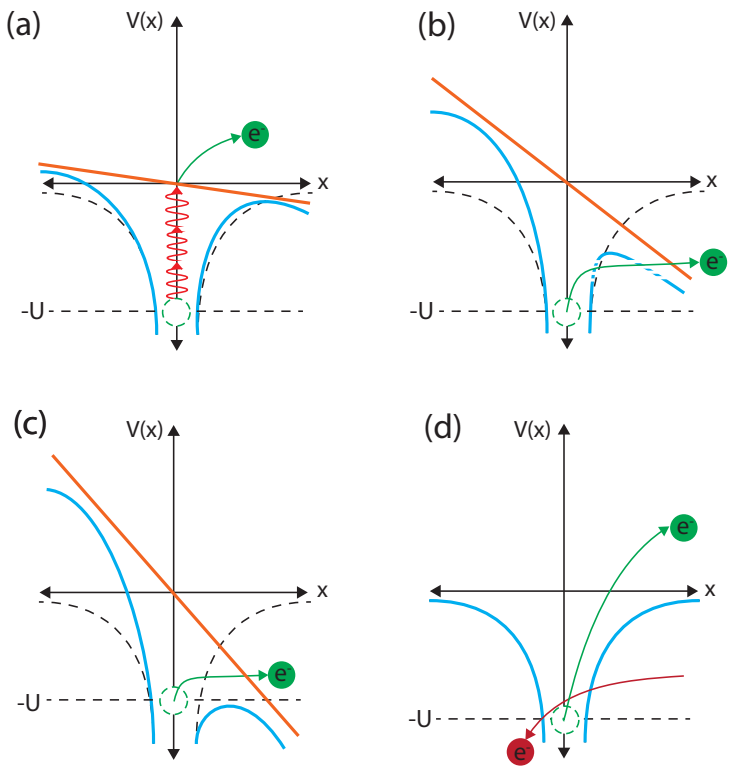

Figure 2.2: Depictions of the ionisation mechanisms relevant to laser-solid interactions: (a) multi-photon ionisation; (b) tunnelling ionisation; (c) barrier suppression ionisation; and (d) collisional ionisation. Where black dashed lines represent unperturbed Coulomb potential, blue the perturbed Coulomb potential, and orange the incident laser potential.

2.3 The plasma state

Plasma plays a key role in high power laser-solid interactions and the physical concepts presented in the forthcoming sections, thus an understanding of its nature is highly beneficial. To give a brief historical context, the plasma state was first experimentally observed in the laboratory by Crookes and Thomson in 1879, where they coined the term '*the fourth state of matter*' to describe the matter they were observing. It was not until 1928, however, the word 'plasma' was first used by Langmuir, while studying plasmas in tungsten filament bulbs. The three familiar states of matter (solid, liquid and gas) are abundant on Earth, though universally speaking plasma is believed to form 99% of all visible matter, in the known universe. A useful initial definition of plasma can be gained from its classical description;

> *"A plasma is a quasi-neutral assembly of electrically charged and neutral particles in sufficient numbers to exhibit collective behaviour."*

This description is helpful, though to gain a more in-depth insight into plasma and

what makes it unique compared to the other states, it is necessary to focus on two key parts of this description; (1) '*quasi-neutral*' and (2) '*collective behaviour*'.

Collective behaviour results due to the fact plasma consists of charged particles. In the familiar states, constituent particles interact through binary collisions. The dynamics of plasma are, however, more complex due to its ionised state. In plasma particles interact through long range Coulomb interactions, due to their charged nature. Thus a particle may influence many others nearby simultaneously, via local electric fields.

The second term highlighted in the classical description of plasma, '*quasi-neutral*', denotes that, on a macroscopic scale, plasma is neutral due to approximately equal numbers of electrons and ions. However on the microscopic scale neutrality is broken due to the aforementioned localised electromagnetic fields – thus the inclusion of '*quasi*'.

To further understand these two terms, and consequently plasma, it is convenient to introduce three criteria which matter must satisfy to be classified as being plasma;

1. $\lambda_D \ll L$ – the dimensions of the assembly of particles must be much larger than the distance localised fields can influence particles (i.e. the screening distance, λ_D).

2. $N_D \gg 1$ – there must be many particles within the screening volume for the screening effect to occur.

3. $\omega_p > \omega_c$ – the plasma frequency (ω_p) must be greater than the frequency of collisions (ω_c).

Each criteria will now be explored;

1. $\lambda_D \ll L$

   A key property of plasma is its tendency to shield externally applied electric fields. This is a result of charged particles arranging themselves to generate an oppositely-directed electric field to effectively cancel the external field on a macroscopic scale; a phenomenon termed 'Debye Shielding'. The electric field of a test charge immersed in plasma will only interact with other charged particles within a volume called the 'Debye Sphere', with radius equal to the screening

distance, referred to as the Debye length, λ_D, described by Eq. 2.23;

$$\lambda_D = \sqrt{\frac{\varepsilon_0 k_B T_e}{e^2 n_e}} \tag{2.23}$$

where k_B is Boltzmann's constant, T_e is the electron temperature, and n_e is the electron density. In this approximation ions are assumed to be static. The resultant electrostatic Coulomb potential, ϕ, on the test charge of charge, q, is thus;

$$\phi(r) = \frac{q}{4\pi\varepsilon_0 r^2} \exp\left(\frac{-r}{\lambda_D}\right) \tag{2.24}$$

The Debye length is the characteristic scale over which the potential of the test charge is exponentially attenuated by a factor of 1/e, as opposed to the inverse square decay in free space. It therefore defines the minimum distance over which charge neutrality is maintained, which is to say a charged particle will feel no electric field effects from another charge when it is at a distance greater than λ_D. Effectively, it is a characteristic distance over which quasi-neutrality may be breached. Likewise, it is also a measure of the depth an externally applied field can penetrate into plasma. As was defined by this criteria for screening effects to occur, and for the matter to be described as plasma, λ_D must be much smaller than the linear dimensions of the plasma, L.

2. $N_D \gg 1$

   This criteria sets a condition which matter must exhibit for Debye shielding to be valid, and thus for it to be plasma. It states that there must be many particles within a Debye sphere. The number of particles, N_D, contained within this volume is given by Eq. 2.25;

$$N_D = \frac{4}{3} n_e \pi \lambda_D^3 = 1.38 \times 10^6 T_e^{3/2} n_e^{-1/2} \tag{2.25}$$

   It is due to the fact that there are many particles within a Debye sphere that collective behaviour is present in plasma.

3. $\omega_p > \omega_c$

   The final plasma criteria distinguishes it from simply an ionised gas (ionised to a relatively lesser degree). In an ionised gas charged particles will collide with

neutral particles frequently enough that the dynamics of the assembly may be described through normal hydrodynamic forces, as opposed to the electromagnetic forces required to describe plasma dynamics. The condition necessary for a plasma is therefore that the plasma frequency, ω_p, (defined later in this section) is larger than the frequency of collisions ω_c, defined as the mean time between particle collisions, τ_c, i.e. the collisions which will dominate particle dynamics.

2.3.1 Parameters employed to define a plasma

It is important when describing phenomena resulting from the interaction of a laser pulse with plasma to have an appreciation of some parameters employed to quantify plasma. Typically three basic parameters are employed; plasma frequency, electron density and electron temperature. Each is described below.

Electron temperature

Electron temperature (T_e) is a statistical parameter quantifying the mean kinetic energy of the electrons in the plasma. The SI unit for this value is the Kelvin (K), though in plasma physics it is often quoted in units of energy (i.e. $k_B T_e$), that being Joules (J), or the more commonly employed electron-volts (eV); where 1 eV= 1.6×10^{-19} J, equivalent to ∼11600 K.

Plasma density

Plasma density typically refers to the free electron density (n_e) of a plasma, a quantity of significance to plasma dynamics and its interaction with electromagnetic radiation. It is defined as the number of free electrons per unit volume and is typically given in units of cm^{-3}. Not only is it an important parameter for defining the optical properties of plasma (discussed in section 2.5.3), but it is also a measure of the degree of ionisation. The free electron density created in a particular ionisation state is found through;

$$n_e = Z^* n_i = \frac{Z^* N_A \rho}{A} \tag{2.26}$$

For example, in an aluminium plasma, at a temperature of ∼200 eV and an average ionisation state of Z^*=9, the electron density is 5×10^{23} cm^{-3} (for Al density ρ= 2.3

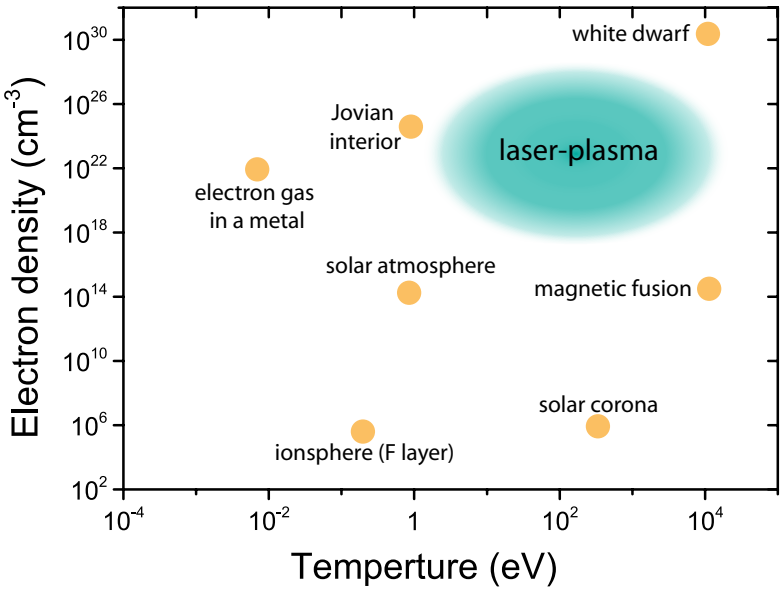

Figure 2.3: Plot displaying where various types of plasmas throughout the universe and the research laboratory exist in terms on electron density and temperature

g/cm^{-3}, mass number A= 26 and Avogadro's number N_A= 6.02×10^{23}). To compare to the sun's corona, of average temperature ∼0.5 eV, this only has a free electron density of ∼10^6–10^{10} cm^{-3}. Figure 2.3 shows graphically where various plasmas throughout the universe, and the research laboratory, exist in terms of plasma density and electron temperature.

Plasma frequency

When a plasma electron is displaced from a positively charged ion, an electric field is formed as a result of the separation. This results in the particles being pulled towards each other, restoring quasi-neutrality. However, this restoring force, coupled with the electron's inertia, will cause the electron to overshoot the ion. Consequently it will oscillate around its equilibrium position at a characteristic frequency, referred to as the plasma frequency, or Langmuir frequency. This parameter is key in defining the optical properties of a laser-plasma interaction (covered in section 2.5.3).

To derive an expression for the plasma frequency the oscillations of a hypothetical neutral homogeneous 1D plasma slab is considered. The description of the single electron above is now applied to this plasma slab, in which the electrons are displaced from the quasi-neutral position by a distance δx. The resulting charge density present on the leading face of the slab is $\rho = en_e\delta x$. Therefore from Gauss's Law (Eq. 2.1) the

electric field generated inside the slab is shown to be;

$$E = \frac{\rho}{\varepsilon_0} = -\frac{en_e\delta x}{\varepsilon_0} \tag{2.27}$$

This electric field sets up a restoring force, F_e, which can be described using Newton's second law, linking mass and acceleration, for a single electron in the slab;

$$F_e = m_e\frac{d^2\delta x}{dt^2} = -eE \tag{2.28}$$

Substituting Eq. 2.27 into the above expression, and rearranging for the acceleration term (i.e. $\frac{d^2\delta x}{dt^2}$), one obtains;

$$a = \frac{d^2\delta x}{dt^2} = \frac{-e^2n_e\delta x}{m_e\varepsilon_0} \tag{2.29}$$

This equation is in a form describing a simple harmonic oscillator, i.e $a= -\omega^2\delta x$, where ω is the oscillation frequency, i.e. the plasma frequency (in the non-relativistic regime), equal to;

$$\omega_p = \sqrt{\frac{n_e e^2}{\varepsilon_0 m_e}} \tag{2.30}$$

This frequency describes the most fundamental time-scale in plasma physics, the plasma period ($\tau_p= \frac{2\pi}{\omega_p}$). Thus oscillations are only observed if the plasma is studied for a period greater than this. Similarly there is an ion plasma frequency (ω_{pi}), defined simply by replacing the electron mass and density with ion equivalents in Eq. 2.30. This frequency is typically small enough to be neglected due to the larger mass of the ions compared to the electrons and the timescale of the laser-plasma interaction.

2.4 Laser induced plasma expansion

Now that a description of plasma, and the mechanisms which form it in the context of laser-solid interactions, has been presented, it is possible to further our picture of an intense laser pulse interacting with a solid target and describe the characteristics of the plasma formed at the target front surface. This is required for describing many of the forthcoming interaction concepts, such as laser energy coupling to electrons.

The interaction of a pulse with the target front surface is complex due to a multitude of laser parameters involved, specifically pulse energy, duration (thus peak intensity) and, importantly, the pulse temporal intensity contrast. This parameter is used to quantify the ratio between the peak intensity to the intensity of light preceding the main pulse (this is explored in detail in section 3.2.4). This plays a key role in the generation of plasma before the arrival of the main pulse, termed pre-plasma, and thus defining the interaction dynamics. The interaction of this preceding light, in the region of I_L=10^{10}-10^{15} W/cm^2, results in surface ablation and ionisation. Due to thermal pressure generated during this heating, matter will be ejected from the target resulting in an expanding plasma travelling at approximately the local sound speed, c_s, given by;

$$c_s = \sqrt{\frac{Z^* k_B (T_e + T_i)}{m_i}} \tag{2.31}$$

Expansion results in the front surface plasma possessing a characteristic density profile, due to a range of particle velocities. Its density decreases away from the surface, as shown in Fig. 2.4, and is of the approximate form of an exponential decay;

$$n_e(z) = n_0 \exp\left(-z/L_s\right) \tag{2.32}$$

where $n_e(z)$ is the electron density at position z from the target surface, n_0 the initial target electron density, and L_s is the so-called density scale-length. This parameter is used to quantify the spatial extent of pre-plasma, and is equal to the distance over which the density falls to $1/e$ of n_0 (where e is Euler's number). The scale-length is an important parameter to quantify for given interaction conditions as it can greatly affect the interaction dynamics, such as laser energy coupling to electrons, as shown in Gray *et al.* [61] and McKenna *et al.* [62]. This parameter may be estimated using the sound speed (c_s) and the laser pulse duration (τ_L);

$$L_s = c_s \tau_L \tag{2.33}$$

Typically this value is not estimated in this way, but rather by employing hydrodynamic simulations of the interaction, and fitting Eq. 2.32 to the resultant density profile.

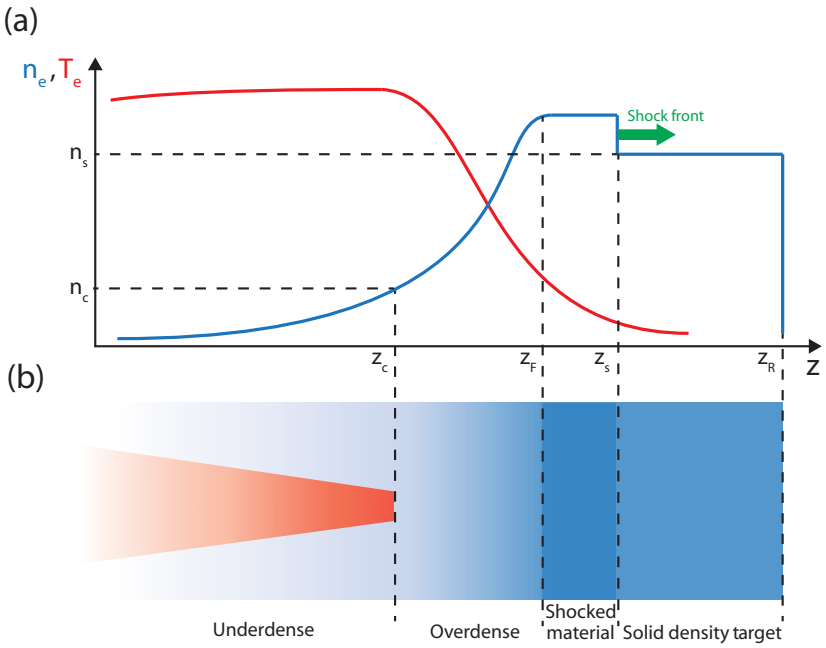

Figure 2.4: Schematics of the pre-plasma at the laser-target interaction surface, with (a) displaying the electron density and temperature profile, where n_s is the target solid density and n_c in the plasma critical density, and (b) the resultant regions of the target; where Z_F and Z_R represent the position of the initial target front and rear surfaces, respectively, Z_C the position of the plasma critical surface and Z_S the position of the shock front launched into the target. (The terminology underdense, overdense and critical density is discussed in section 2.5.3).

2.5 Electromagnetic wave interaction with plasma

In the previous sections the main components of a laser-plasma interaction were introduced, being the laser and plasma. It is the interaction of these, however, which is explored in the following section, enabling an understanding of the complex dynamics and physical concepts of these interactions to be attained.

A sensible place to begin describing the interplay between the laser and plasma is to examine the behaviour of electrons in the presence of an electromagnetic field; firstly the dynamics of a single electron in an infinite plane electromagnetic wave. This will act as a foundation to begin exploring more complex phenomena of laser-plasma interactions, such as relativistic effects and electron heating mechanisms.

2.5.1 Motion of a single electron in an infinite plane wave

To begin describing the dynamics of a group of electrons in the presence of a laser pulse it is highly advantageous to first consider the relatively more simplified interaction case

of a single electron and an infinite plane EM wave.

In comparison to protons, and heavier ions, electrons are predominately accelerated by virtue of their lower mass. Classically the dynamics of a free electron, of mass m_e and charge e, in the presence of electric and magnetic fields are described by the Lorentz force equation (Eq. 2.34);

$$\mathbf{F}_L = \frac{d\mathbf{p}}{dt} = -e(\mathbf{E} + \mathbf{v} \times \mathbf{B}) \tag{2.34}$$

where $\mathbf{p}= \gamma m_e \mathbf{v}$ and $\gamma= \sqrt{1 + \mathbf{p}^2/m_e c^2}$ is the relativistic Lorentz factor. This equation contains all the information necessary to begin describing the motion of a single electron due to a particular EM field. To begin, one can examine its motion due to the electric and magnetic fields separately. For an electric field of plane wave form, $\mathbf{E}= E_0 \sin(\omega_L t - kz)\hat{x}$ (with wave number $k= \omega_L/c$), an equation of motion for a non-relativistic free electron can be formed, employing Eq. 2.34;

$$m_e \frac{d\mathbf{v}}{dt} = -eE_0 \sin(\omega_L t - kz)\, \hat{x} \tag{2.35}$$

$$v_{os} = \frac{eE_0}{\omega_L m_e} \cos(\omega_L t - kz) \tag{2.36}$$

An electron, initially at rest, subject to a plane wave electric field will be accelerated transversely to the wave propagation direction, with motion orientated along the polarisation direction, i.e. the electric field direction, and will oscillate at the field frequency, ω_L. The oscillation velocity, v_{os}, (Eq. 2.36), also referred to as the quiver velocity, reaches a maximum velocity of $v_{max}= eE_0/\omega_L m_e$.

Now examining the electron dynamics due to the magnetic field, it can be seen studying Eq. 2.34 that the velocity induced by the electric field in turn results in a force due to the $\mathbf{v} \times \mathbf{B}$ component. Due to the cross product with velocity, orientated in the polarisation direction, this implies that the resultant force pushes the electron in the EM wave propagation direction, i.e. perpendicular to the polarisation orientation.

For non-relativistic electron velocities ($v_{os} \ll c$) the force acting on the electron is dominated by the electric field component; a consequence of the magnetic field being a factor of c smaller than the electric field, as shown in Eq. 2.11. Thus its contribution to electron motion can be ignored at non-relativistic velocities. However, for stronger laser fields this assumption is no longer valid as the electron velocity approaches c,

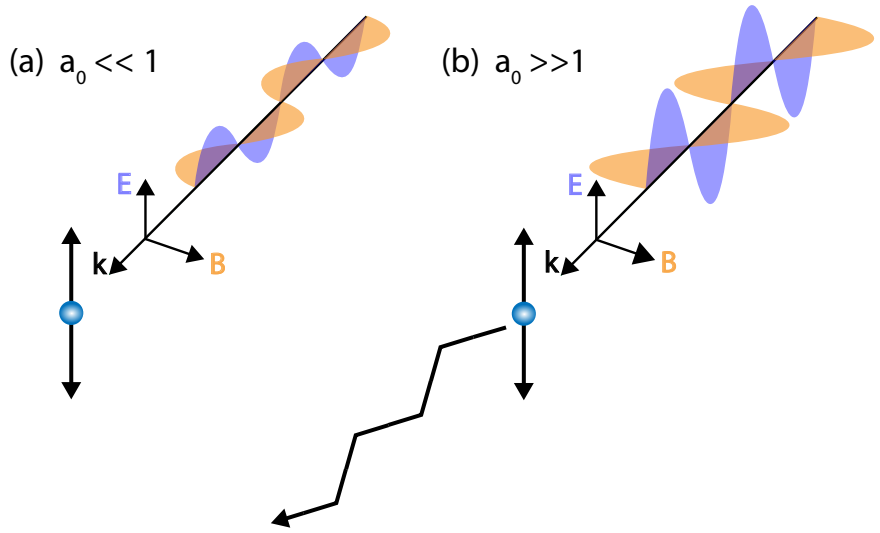

Figure 2.5: Illustration of single electron motion in a plane wave electromagnetic field, for (a) $a_0 \ll 1$- non-relativistic regime and (b) $a_0 \gg 1$- relativistic regime.

therefore the magnetic field begins to play an important role in describing the electron motion. At this point the magnitude of the $e(\mathbf{v} \times \mathbf{B})$ force component is of the same order as $e\mathbf{E}$ and consequently can no longer be ignored. In this case the motion (in the non-relativistic case) is described by the following set of equations in terms of the transverse (x) and longitudinal (z) motion;

$$x(t) = \frac{eE_0}{m_e\omega_L} sin(kz - \omega_L t) \tag{2.37}$$

$$z(t) = \frac{e^2E_0^2}{4m_e^2\omega_L}\left((kz - \omega_L t) + \frac{1}{2}\sin(2(kz - \omega_L t))\right) \tag{2.38}$$

The transverse motion (Eq. 2.37) is identical to the non-relativistic case, that being oscillations in the polarisation direction. However in terms of longitudinal motion, the first terms on the RHS of Eq. 2.38 describes the electron being pushed in the wave propagation direction. The combined effect of the two components of the oscillating EM field is thus electron motion forward longitudinally as it oscillates transversely, resulting in so-called figure-of-8 motion in the reference frame following the average motion. Moreover, this longitudinal force occurs at twice the laser frequency, as seen in the second terms of the RHS of Eq. 2.38. To aid in understanding these two regimes of electron motion, Fig. 2.5 depicts electron motion in each scenario.

To distinguish between these regimes of electron motion (relativistic and non-relativistic) it is convenient to introduce a parameter derived from the electron quiver

velocity, known as the normalised vector potential, a_0, to characterise the relative strength of the laser field;

$$a_0 = v_{max}/c \tag{2.39}$$

$$a_0 = \frac{eE_0}{m_e c\omega_L} \tag{2.40}$$

when $a_0 \ll 1$ the electron dynamics are in the non-relativistic regime as the magnetic force is a factor of v_{os}/c less than that due to the electric field. However, when $a_0 \geq 1$ relativistic effects need to be considered. As this parameter gives a measure of the electron's response to an EM field, incorporating both the electric field magnitude (related to laser intensity) and the frequency of light, it is a useful quantity for comparing laser systems. As such it is useful to relate the normalised vector potential to laser intensity through the Poynting vector, $\mathbf{S}= \frac{1}{\mu_0}\mathbf{E} \times \mathbf{B}$, which describes the energy flux along an EM wave. For a linearly polarised wave of the form $\mathbf{E}= E_0 \sin(\omega_0 t - kz)\hat{x}$ and $\mathbf{B} = B_0 \sin(\omega_0 t - kz)\hat{y}$, the Poynting vector can be expressed as;

$$|\mathbf{S}(t)| = \frac{1}{\mu_0} E_0 B_0 \sin^2(\omega_0 t - kz) \tag{2.41}$$

Employing Faraday's Law (Eq. 2.3) to relate the electric and magnetic fields the above becomes;

$$|\mathbf{S}(t)| = \frac{1}{\mu_0 c} E_0^2 \sin^2(\omega_0 t - kz) \tag{2.42}$$

$$|\mathbf{S}(t)| = \varepsilon_0 c E_0^2 \sin^2(\omega_0 t - kz) \tag{2.43}$$

The time average of the energy flow, represented by $\langle \mathbf{S} \rangle$, can be written as;

$$\left\langle \bar{\mathbf{S}} \right\rangle = \frac{\varepsilon_0 c E_0^2}{2} \hat{z} \tag{2.44}$$

As the intensity of the pulse is equal to $\langle \mathbf{S} \rangle$, it can be directly related to the peak magnitude of the electric field, for both linear and circular polarisation. The peak electric field magnitudes are equal in both, however its magnitude oscillates for linear, whilst remaining constant for circular polarisation. It is therefore crucial to look at the time averaged electric field magnitudes; $E_0/2$ for linear and E_0 for circular. The time average of the squared normalised vector potential, which varies with intensity

(proportional to $\langle a_0^2 \rangle \propto I_L$), thus differs for each of the polarisation cases as;

$$\langle a_0^2 \rangle = \frac{a_0^2}{2} \rightarrow a_0^2 = 2\langle a_0^2 \rangle \rightarrow a_0 \propto \sqrt{2I_L} \quad \text{for linear polarisation} \tag{2.45}$$

$$\langle a_0^2 \rangle = a_0^2 \rightarrow a_0 \propto \sqrt{I_L} \quad \text{for circular polarisation} \tag{2.46}$$

As stated earlier a_0 is a useful parameter for comparing laser systems. It is therefore helpful to communicate the above expressions in a more practical form;

$$a_0 \sim 0.85\sqrt{I_{10^{18}}\lambda_{\mu m}^2} \quad \text{for linear polarisation} \tag{2.47}$$

$$a_0 \sim 0.6\sqrt{I_{10^{18}}\lambda_{\mu m}^2} \quad \text{for circular polarisation} \tag{2.48}$$

where intensity is in units of 10^{18} W/cm^2 and wavelength in microns. More generally the onset of relativistic effects occurs when a_0=1, i.e. for laser irradiances;

$$I_L = \frac{a_0^2}{\lambda_L^2} \cdot 1.37 \times 10^{18} \ [\text{W/cm}^2\mu\text{m}^2] \tag{2.49}$$

$$I_L\lambda_{\mu m}^2 > 1.37 \times 10^{18} \ [\text{W/cm}^2\mu\text{m}^2] \tag{2.50}$$

The dependence of wavelength on the onset of relativistic motion should be noted. For a wavelength λ_L= 1 μm (such as a Nd:glass based system, e.g. the Vulcan laser) the point at which relativistic effects begin to occur is $\sim 10^{18}$ W/cm^2. However for a CO_2 gas based laser, with relatively longer wavelengths (λ_L= 10 μm), relativistic effects will start at much lower intensities, $\sim 10^{16}$ W/cm^2.

2.5.2 The ponderomotive force

In the previous section an infinite plane wave laser field (where fields extend to infinity and the intensity is constant) was assumed; where the free electron will receive no net gain of energy. In reality, however, this case is too simplistic to fully explain the motion of electrons subject to the laser pulses employed experimentally, which are inhomogeneous fields. A focused pulse, as discussed earlier, is typically temporally and spatially Gaussian (thus not homogeneous), having finite spatial extent and temporal duration, with a centrally peaked intensity distribution.

In the case of a homogeneous field, the electron returns to its initial position after one cycle of field oscillation. However in the case of an inhomogeneous field it is pushed towards lower field-amplitude regions as a result of gradients in the spatial intensity profile of the pulse. In effect, the force imposed on an electron oscillating at the laser frequency at the turning point of oscillation in a higher field amplitude is larger than that imposed at the turning point with a lower field amplitude. Consequently over many laser cycles this results in a net force acting to drive the particle toward weaker field regions. The electron thus receives a net energy gain over the laser cycle. This force is known as the ponderomotive force (illustrated in Fig. 2.6) and is defined by Gibbon [53] as the time averaged gradient of the electron oscillation. This form of force was known by Kelvin in 1846 as electrostriction, and was later reformulated as the ponderomotive force by Helmholtz. From the Lorentz equation, Eq. 2.34, the ponderomotive force, $\mathbf{F}_P$, on a single electron can be derived in terms of the spatial gradient of the electric field, E_s. The first form to consider is that for non-relativistic interactions, where the cycle average force is;

$$\mathbf{F}_P = -\frac{e^2}{4m_e\omega_L^2}\nabla\mathbf{E}_s^2 = -\frac{e^2}{8\pi\varepsilon_0 m_e c^3}\nabla(I_L\lambda^2) \tag{2.51}$$

and in the relativistic regime, where the electron's oscillation velocity approaches c, the cycle average ponderomotive force is;

$$\mathbf{F}_P = -m_e c^2\nabla\gamma = -m_e c^2\nabla\sqrt{1+a_0^2/2} \tag{2.52}$$

The energy transferred to the electron during one laser cycle, due to the ponderomotive force, is known as the ponderomotive potential, U_p, given by;

$$U_p = m_e c^2(\langle\gamma\rangle - 1) \tag{2.53}$$

where $\gamma = 1 + a_0^2/2$, again being the Lorentz factor for a single electron. Additional processes by which an electron may gain energy in an interaction are explored later (section 2.5.4). For linearly polarised light $\langle\gamma\rangle = \sqrt{1+a_0^2/2}$ and $\langle\gamma\rangle = \sqrt{1+a_0^2}$ for circular, therefore the ponderomotive potential for each polarisation case is;

$$U_p = m_e c^2\left(\sqrt{1+\frac{a_0^2}{2}} - 1\right) \quad \text{for linear polarisation} \tag{2.54}$$

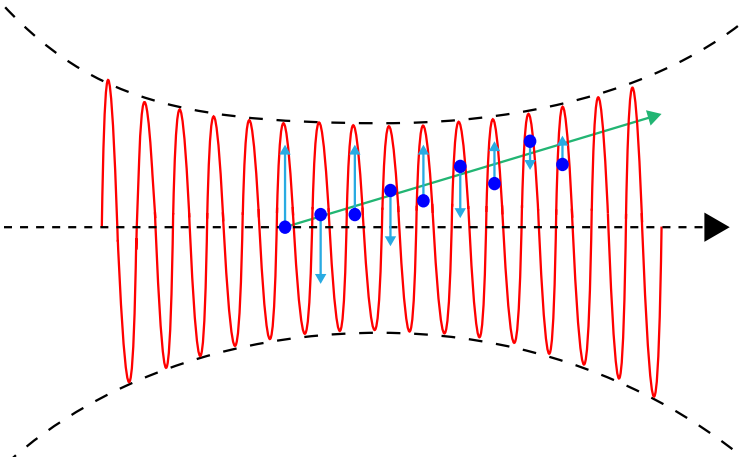

Figure 2.6: Illustration of the evolution of the position of a test electron (in blue) in a focused laser electric field (in red). The blue arrows represent the relative size of the transverse force on the electron due to the electric field and the green arrow symbolises the resultant time integrated path of the electron.

$$U_p = m_e c^2 \left(\sqrt{1 + a_0^2} - 1 \right) \quad \text{for circular polarisation} \tag{2.55}$$

One can also calculate the scattering angle of the electron, θ_s (reported in Moore *et al.* [63]), with respect to the laser propagation axis, by considering the angle between the electron's transverse momentum, $p_\perp = U_p/c$, and longitudinal momentum, $p_z = p_\perp/(2m_e c)$;

$$\tan(\theta_s) = \left(\frac{p_\perp}{p_z} \right) = \sqrt{\frac{2}{\langle \gamma \rangle - 1}} \tag{2.56}$$

The ponderomotive force is independent of particle charge, acting equally on positively and negatively charged particles (due to charged quantities being squared in Eq. 2.51), it consequently acts on positively charged particles pushing them in the same direction as electrons. However, the ponderomotive potential experienced by the heavier ions in the plasma at the intensity regime investigated in this work ($\geq 10^{21}$ W/cm^2) is far less than the rest mass energy of the ions (0.9 GeV for a proton). The ponderomotive potential of a proton interacting with a laser of intensity 10^{20} W/cm^2 and of 1 μm wavelength is equal to 5 keV. Therefore ions can be considered to be quasi-stationary compared to the electrons which experience a strong ponderomotive push.

In the relativistic regime, the light pressure due to the ponderomotive force on a solid density target is of a similar magnitude as the thermal pressure of the Sun's core (for a 1 μm laser at 10^{20} W/cm^2). This pressure thus plays an important role in the interaction, such as its ability to alter the plasma density gradient at the target front surface. It

pushes the plasma critical surface into the solid target, resulting in a curvature of the interaction region and thereby modifying the laser incidence angle across the focal spot. Additionally, as the ponderomotive force is proportional to the energy flux of the light and laser-driven particle acceleration requires tightly focused high-power pulses, i.e. a small focal spot size, the result is a large transverse intensity gradient, resulting in unstable electron motion in the radial direction. Moreover, the amplitude of electron oscillation along the polarisation direction increases with intensity, and for small focal spots ($\sim\mu$m), can exceed the spot size, causing electrons to be scattered transversely. Consequently electrons may leave the acceleration zone 'prematurely', resulting in the phase volume of the accelerated electrons becoming relatively large.

2.5.3 Laser propagation in plasma

In the previous two sections, the motion of a single electron in an infinite plane wave, and the more complex dynamics in a spatially and temporally inhomogeneous laser field were examined. This single particle description, though useful, does not fully cover the complex processes which in reality occur when the laser pulse interacts with a plasma containing a large number of charged particles, which displays collective behaviour. A key property of a plasma is its ability to optically affect interacting electromagnetic waves, and consequently change the interaction dynamics. As such, this section explores some of the optical effects a laser pulse experiences propagating in a plasma.

Plasma, in a sense, is similar to a gaseous medium, but fundamentally different in the fact that electrons are dissociated from parent atoms. Therefore, a convenient starting point to begin describing the optical properties of plasma is to define the relative permittivity of the medium, also known as the dielectric constant, ε, which for a gaseous medium is given by;

$$\varepsilon = 1 + \frac{n_a e^2}{\varepsilon_0 m_e({\omega_0}^2 - \omega_L^2)} \tag{2.57}$$

where ω_0 is the natural frequency of the atom, ω_L is the frequency of incident light and n_a is the number of atoms per unit volume. In a plasma electrons are free resulting in an ω_0 of zero and n_a equal to the electron density, n_e. Using this knowledge, one can

be obtained from Eq. 2.57;

$$\varepsilon = 1 - \frac{{\omega_p}^2}{\omega_L^2} \tag{2.58}$$

where ω_p is the plasma frequency, previously defined in Eq. 2.30. As it is the optical properties of plasma we are interested in, it is useful to define a commonly employed optical parameter; the refractive index, η. For a specific medium this is defined as the ratio of the speed of light in a vacuum, c, to the phase velocity in that medium, v_p, i.e. $\eta = c/v_p$. Moreover, it is also equal to $\sqrt{\varepsilon}$, therefore from Eq. 2.58 the refractive index for plasma can be defined as;

$$\eta = \sqrt{1 - \frac{\omega_p^2}{\omega_L^2}} \tag{2.59}$$

It would seem from this equation that if the frequency of the incident EM wave is greater then the plasma frequency then $v_p > c$, apparently in violation of the laws of relativity. Conversely, for $\omega_L < \omega_p$, the refractive index becomes imaginary according to this relation.

To interpret these optical properties it is useful to derive a wave equation describing EM wave propagation in a plasma, similar to that in Eq. 2.6 for vacuum propagation. In the vacuum case the current density, $\mathbf{J}$, was zero, however this is not necessarily the case in a plasma due to the presence of charged particles. Assuming small density variations and quasi-neutrality ($\rho = 0$) the resultant wave equation is;

$$\nabla^2 \mathbf{E} = \frac{1}{c^2}\frac{\partial^2 \mathbf{E}}{\partial t^2} + \mu_0 \frac{\partial \mathbf{J}}{\partial t} \tag{2.60}$$

where the current density is given by $\mathbf{J} = -en_e\frac{d\hat{r}}{dt}$. Given a wave solution of the form expressed in Eq. 2.7, and the electrostatic force experienced by an electron in the presence of an ion, presented in Eq. 2.28, i.e. $\mathbf{F}_e = -e\mathbf{E}$, the wave equation becomes;

$$-k^2\mathbf{E} = -\frac{1}{c^2}\omega_L^2\mathbf{E} + \mu_0\frac{e^2 n_e \mathbf{E}}{m_e} \tag{2.61}$$

Through the plasma frequency relation (Eq. 2.30) this can be reformed into a dispersion relation for light propagating through plasma (Eq. 2.62). The similarity between this and the vacuum dispersion relation (Eq. 2.8) should be noted, where the plasma version has the inclusion of the plasma frequency; effectively showing that a plasma,

unlike vacuum, will alter the velocity of the EM wave.

$$\omega_L^2 = c^2 k_0^2 + \omega_p^2 \tag{2.62}$$

A peak (or trough) of an EM wave travels at the phase-velocity, v_p, given by $v_p = \frac{\omega_L}{k}$. According to the plasma dispersion relation and Eq. 2.59, the phase velocity in a plasma can be expressed as;

$$v_p = \frac{c}{\sqrt{1 - \frac{\omega_p^2}{\omega_L^2}}} \tag{2.63}$$

This indeed reaffirms that for light of $\omega_L > \omega_p$ the phase velocity is greater than c. However this does not violate relativity, which states that information cannot travel faster than c, where the peaks of the wave, travelling at the phase velocity, do not carry information. To transmit information through the plasma by use of EM waves would require, for example, a series of short discrete pulses, to encode information in a similar fashion to Morse code. This information travels at the group velocity, equal to $v_g = \frac{d\omega_L}{dk}$, which is clearly different from the phase velocity in plasma as ω_L and k are not directly proportional. Information (composed of individual wave-pulses) travels at the group velocity, which must be less than c. Through differentiation of the plasma dispersion relation (Eq. 2.62) it is shown that the group velocity is;

$$v_g = c\sqrt{1 - \frac{\omega_p^2}{\omega_L^2}} \tag{2.64}$$

This shows that even for $\omega_L > \omega_p$ the velocity will be less than c, thus demonstrating that laser propagation in a plasma does not violate relativity. Figure 2.7 illustrates this concept for both the phase and group velocity.

Studying the dispersion relation (Eq. 2.62) it can be immediately seen that the wavevector, k, is only real for light frequencies greater than the plasma frequency, and for the opposite condition k becomes imaginary; clearly two optical regimes of laser-plasma interaction exist. The first occurs when $\omega_L > \omega_p$, in which the laser is able to propagate through the plasma i.e it is transparent. A plasma which meets this condition is referred to as 'underdense'. However when $\omega_L < \omega_p$, light cannot propagate into the plasma i.e. it is opaque. This plasma is referred to as 'overdense'. The transition point between these regimes, occurring at $\omega_L = \omega_p$, is commonly referred to as the critical

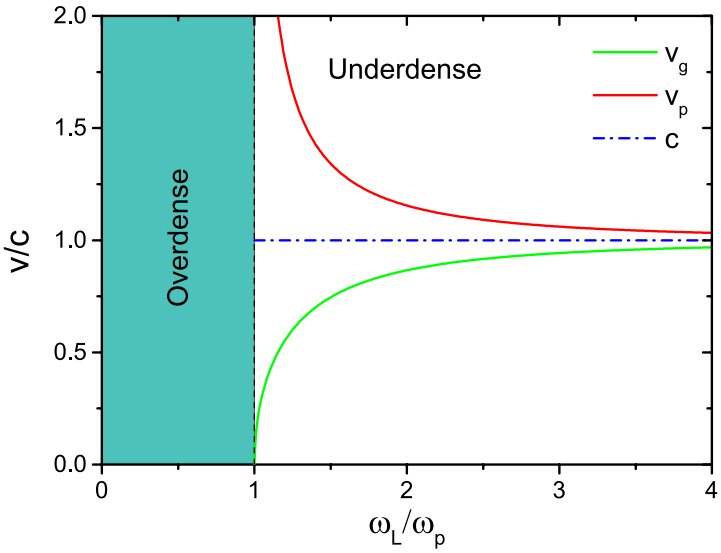

Figure 2.7: Group and phase velocities of an EM wave propagating through plasma as a function of its frequency (normalised to the plasma frequency). For $\omega_L/\omega_P > 1$ it is underdense, but if $\omega_L/\omega_P < 1$ the plasma is overdense.

density, n_{crit}, and its value is obtained by setting $\omega_p = \omega_L$ in the plasma frequency equation (Eq. 2.30) and rearranging for electron density;

$$n_{crit} = \frac{m_e \varepsilon_0 \omega_L^2}{e^2} \simeq 1.1 \times 10^{21} \left(\frac{\lambda_L}{\mu\text{m}}\right)^{-2} \text{cm}^{-3} \tag{2.65}$$

This description additionally allows one to re-write the plasma refractive index (Eq. 2.59) in terms of electron density values;

$$\eta = \sqrt{1 - \frac{n_e}{n_{crit}}} \tag{2.66}$$

It terms of a laser interacting with a target, which possesses the aforementioned characteristic pre-plasma density profile, the point at which this critical density occurs, and the laser is reflected, is named the critical surface. As our interest is primarily the interaction of a pulse with an initially solid target, the interaction is mainly dominated by overdense interaction phenomena. However underdense plasma formed at the target front surface plays a key role in defining the absorption of laser energy as will be described later (see section 2.5.4).

As discussed, light with frequency equal to, or below, the plasma frequency is reflected at the critical surface. Physically, however, some fraction of the electric field does slightly penetrate into this region, resulting in an evanescent wave form, exponen-

tially decaying over a characteristic distance known as the skin depth, δ; the distance at which the electric field amplitude falls to e^{-1} of its value at the critical surface. An equation to describe this parameter is found knowing that k is imaginary in overdense plasma, thus the spatially dependent components of the plane wave (Eq. 2.7) take the form;

$$e^{ikz} = e^{-|k|z} = e^{\frac{z}{\delta}} \tag{2.67}$$

where the skin depth, δ, can be shown to be;

$$\delta = \frac{c}{\sqrt{\omega_p^2 - \omega_L^2}} \tag{2.68}$$

This can be reduced to $\delta = c/\omega_p$ for plasmas with densities substantially higher than the critical density. This phenomenon of light being able to penetrate slightly past the critical surface plays a key role in electron heating mechanisms (explored in section 2.5.4).

An additional optical effect of importance is relativistic induced transparency (RIT). This enables the laser to propagate to higher electron densities than is classically possible. The Lorentz factor (γ) can be include to the mass terms in the critical density equation (Eq. 2.65), which scales with laser intensity, acts to increase the mass of the electrons as they acquire relativistic velocities. It thus plays an important role in defining the local plasma frequency. A consequence of a changing plasma frequency is a resultant change in the critical density value, according to Eq. 2.65, increasing n_{crit} as the electron mass increases. This effectively shifts the critical surface further up the pre-plasma density profile. This is shown graphically in Fig. 2.8. As such, the condition for underdense plasma can be met for a plasma which seems to meet the overdense condition (i.e. $n_e > n_c$) if relativistic effects were not considered. The terminology used to describe such a plasma is 'relativistically underdense'. The relativistically corrected critical density, n'_{crit}, is accordingly;

$$n'_{crit} = \frac{\gamma m_e \varepsilon_0 \omega_L^2}{e^2} = \gamma n_{crit} \tag{2.69}$$

For a 800 nm wavelength laser, a peak laser intensity of $\sim 8 \times 10^{23}$ W/cm^2 would be required for solid density Al to become relativistically transparent; an intensity $\sim$2 orders of magnitude higher than currently achievable. The RIT conditions are

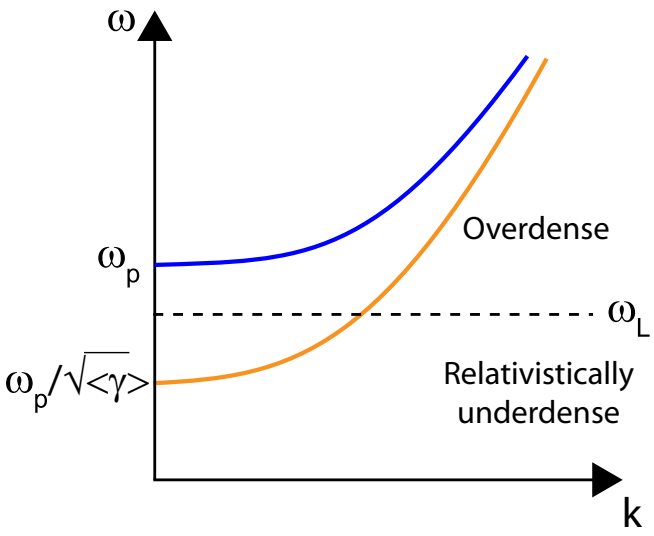

Figure 2.8: Graphical representation of the wave dispersion relation for EM wave propagation in plasma, for both the non-relativistic case (blue) and the relativistic corrected case (orange).

therefore only experimentally seen, at present, due to a combination of relativistic effects and target expansion, reducing the electron density (classically becoming closer to underdense) during the interaction. This proces is often referred to as relativistic self induced transparency (RSIT).

2.5.4 Laser energy absorption in dense plasmas

A fundamental topic which must be considered to further our picture of laser-solid interactions is that of energy transfer from the laser to the plasma. This occurs as the laser can lose energy to plasma electrons, i.e. heating them. The interaction scenario presented in section 2.5.1 (i.e. a single electron interacting with a plane EM wave) showed an electron gained no net energy gain as it oscillated in the EM field; a principle known as Lawson-Woodward theorem [64, 65]. Thus, for electrons to gain energy this theorem must be broken. The ways in which this may occur become clear when exploring the assumptions which bound this theory; (i) the interaction region is infinite, (ii) it occurs in vacuum, with no boundaries present, (iii) the electron is highly relativistic, (iv) there are no static magnetic and electric fields present, and (v) nonlinear effects are neglected. For the electron to take energy from the laser one or more of these assumptions must be violated so the laser is unable to recover energy temporally transferred to the electron in the second half cycle of the field.

For interactions involving non-plane waves, such as those employed experimentally, and in regimes with finite plasma, many electron heating mechanisms exist, relying on the plasma itself to achieve Lawson-Woodward violation. In fact, in a laser-solid interaction several of the mechanisms described in this section may occur simultaneously, due to the large span of interaction intensities (i.e. pulse temporal intensity profile). The dominance of an absorption process depends sensitively on almost every interaction parameter, such as laser intensity, incident angle and pre-plasma condition (and thus pulse contrast), making it highly difficult to control, measure and model the absorption. Each absorption mechanism described in this section is presented in its simplified case, where assumptions restrict discussion to certain aspects of the interaction and suggestions of the conditions where the particular mechanism is optimal are outlined. A natural point to begin exploring the relevant absorption mechanisms for the work presented in this thesis, is to describe the two groups which they can be divided into, described below;

1. **Collisional transfer mechanisms**

   Lawson-Woodward theorem is violated in this form of mechanism when an electron collides with an ion during the stage when it has temporally gained energy from the laser. It therefore loses coherence with the field, and a net loss in laser energy occurs, as the energy cannot be transferred back. This is reliant upon the mean free path of electrons being less than the spatial extent of plasma for collisional effects to be significant.

2. **Collisionless transfer mechanisms**

   The mechanisms in this grouping rely on the fact there is a pre-plasma, with a characteristic density profile, present at the target front prior to the main pulse arrival. Thus a region of underdense, followed by overdense plasma exists, separated by the critical density surface. Electrons can be pushed past this surface (by the mechanisms described below) into the overdense region and thus escape the presence of the laser in the second half-cycle, taking laser energy with them. At the laser intensities discussed in this thesis, up to 10^{21} W/cm^2, electrons are essentially collisionless and thus these mechanisms are highly relevant to this work.

Collisional heating- Inverse bremsstrahlung

As described above, this absorption mechanism occurs when a free electron, oscillating due to the presence of the laser electric field component of the laser, collides with a more massive ion, when the electron has temporarily 'borrowed' energy from the laser in the first half cycle of the wave. The collision results in the damping of the electron motion, and therefore the borrowed energy is unable to be retrieved by the laser, due to its transfer to the ion. Laser energy is thus converted into a thermal distribution in the plasma. This mechanism is commonly referred to as inverse bremsstrahlung, due to it being the opposite of the bremsstrahlung radiation phenomenon; a collisional process in which an electron-ion collision results in electron deceleration and the emission of a photon equal to the electron's energy loss. These collisions occur at the electron-ion collisional frequency, ν_{ei}, which is dependent on [52];

$$\nu_{ei} \propto \frac{n_e Z_i}{T_e^{\frac{3}{2}}} \tag{2.70}$$

An absorption coefficient may be found for this collisional process, κ_{IB}, by using the imaginary part of the plasma refractive index (Eq. 2.66);

$$\kappa_{IB} = \frac{v_{ei}}{2c}\left(\frac{n_e}{n_{crit}}\right)\left(1-\frac{n_e}{n_{crit}}\right)^{-1/2} \tag{2.71}$$

$$\kappa_{IB} \propto \frac{Z_i n_e^2}{T_e^{3/2}}\left(1-\frac{n_e}{n_{crit}}\right)^{-1/2} \tag{2.72}$$

Studying the absorption coefficient dependency shows this mechanism is dominant for lower electron temperatures, higher electron densities, and for a plasma of high atomic number elements (i.e. more electrons and larger ions), each of which increase the likelihood of electron-ion collisions. This mechanism consequently occurs primarily close to the plasma critical surface due to the presence of relatively more particles. The inverse temperature dependence arises as a result of higher temperature electrons having a smaller collision cross-section. This is to say as the temperature increases the mean free path of the electron increases, thus the plasma becomes less collisional. This means that this mechanism is most efficient at lower laser intensities, where the electrons remain relatively collisional. For example, during the interaction of plasma with lower intensity light preceding the main pulse [53]. Furthermore, where lower

laser intensities are present, for example at the spatial edges of the pulse, significant collisional absorption may still take place, as shown in Schlessinger *et al.* [66].

It is found that the collisional absorption regime is important up to intensities of $\sim 10^{15}$ W/cm^2, and hence is most significant in the early stage of the laser temporal pulse profile. As high absorption levels are experimentally measured at higher intensities [67] than inverse bremsstralung theory can account for, other mechanisms must also be present in the interaction; these collisionless heating mechanisms are explored below.

Collisionless heating

The coupling of laser energy to plasma through collisionless effects can occur in several forms, the most common of which are summarised here. Davies [68] provides a comprehensive review of these absorption mechanisms. A common feature of each collisionless mechanism is the reliance upon the laser driving electrons across a density gradient, with regions of underdense and overdense plasma separated by the critical density surface.

Resonance absorption

The first relevant collisionless absorption mechanism to consider is resonance absorption. In its simplest description this mechanism involves the coupling of laser energy to electrons at the critical surface in the form of resonant plasma waves. This occurs when the laser electric field resonantly excites electron oscillations at, or near, the point of reflection. As such, an essential condition of this mechanism is that oscillations are only driven when a component of the electric field is parallel to the density gradient of the pre-plasma (i.e. parallel to the normal vector of the target surface), i.e. linearly polarised. This is illustrated in Fig. 2.9. In this figure the laser is incident on the target at an oblique angle, θ_I, necessary for electrons to be driven in the direction of the electric field parallel to the density gradient. The electric field acts to drive electrons beyond the critical surface in the direction of target normal, beyond which the laser evanescently decays, resulting in the electrons escaping the field due to a reduced restoring force. The resulting electron density perturbations may either grow over many laser cycles until wave breaking occurs, and electrons are injected into the target, or over one laser

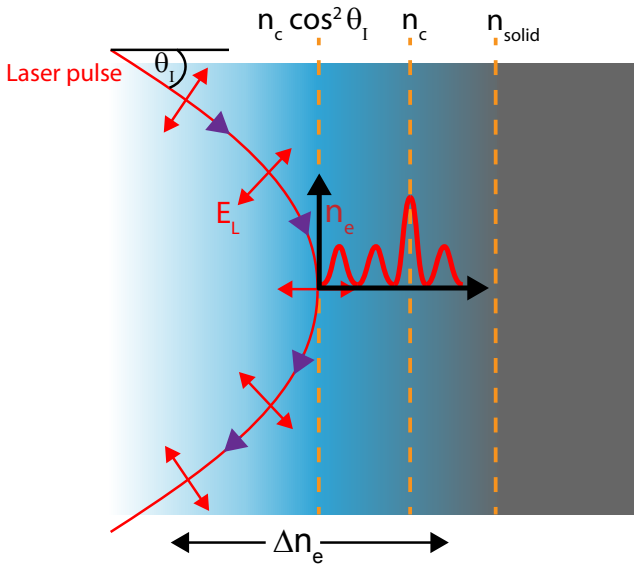

Figure 2.9: Illustration depicting the resonance absorption mechanism for a p-polarised laser pulse (where the electric field is oriented parallel to the pre-plasma density gradient) incident on a target with a relatively long plasma density scale length, at incidence angle of θ_I.

cycle, if the laser is sufficiently intense. Importantly, the generation of plasma waves is most efficient at resonance, occurring when the laser frequency is equal to the plasma frequency (i.e. at the critical surface). The resultant electron temperature generated by this mechanism has been empirically found to scale as $T_e \propto (I_L \lambda_L^2)^{1/3}$ [69].

Due to the presence of non-uniform pre-plasma (decreasing exponentially from the target surface) the laser's propagation may be significantly affected, when propagating at this oblique incident angle. This occurs as opposite sides of the pulse travel through different plasma densities, and thus refractive indices. This results in the laser being effectively turned before it can reach the critical surface, thus modifying the reflection point. The plasma density at which reflection occurs is found using the plasma dispersion relation (Eq. 2.62) in which the k-vector transverse to the density gradient is modified to include the laser incidence angle, $k_y = (\omega_L/c)\sin\theta_I$. The modified dispersion relation is;

$$\omega_L^2 = \omega_p^2 + k_x^2 c^2 + \omega_L^2 \sin^2\theta_I \tag{2.73}$$

This shows that k_x is continually changing in the presence of the density gradient and that reflection, occurring when $k_x \leq 0$, takes place when $n_e \geq n_{crit}\cos^2\theta_I$.

The fraction of laser energy which may be absorbed as a result of this mechanism, f_{RA}, for a given angle of incidence is described by the Denisov function, ξ [70], which

is dependent upon;

$$f_{RA} \propto \xi \exp\left(-\frac{2}{3}\xi^3\right) \tag{2.74}$$

$$\text{where} \quad \xi = (kL_s)^{1/3} \sin\theta_I \tag{2.75}$$

Resonant absorption is most efficient for incident angles between oblique and glancing (i.e. close to parallel with surface) [53]), as a relatively long density scale length plasma ($\sim L_s \gg \lambda_L$) must be present, thus the fraction of the laser field which propagates to the critical density would be reduced with increasing angle. The relationship between laser incident angle and absorption was reported in Friedberg *et al.* [71], finding that $\theta_I \approx 23°$ gave maximised absorption (at $L_s = 10\lambda_L/2\pi$). Good agreement is displayed between this model and experimental findings for intensities between 10^{12}–10^{17} W/cm^2. Above this intensity range relativistic effects become significant, resulting in other mechanisms dominating.

Vacuum heating

This heating mechanism, also commonly referred to as 'Brunel heating', or 'not-so-resonant absorption' [72], is similar to resonance absorption, with the exception being the plasma oscillations are driven in a pre-plasma with a very sharp density gradient ($\sim Ls \ll L$). Under this condition the electron oscillation amplitude, in the field of a p-polarised laser pulse incident at an oblique angle, will be larger than the plasma scale length.

Effectively the interaction with the sharply bounded pre-plasma results in electrons being pulled out of the plasma into vacuum during the first half of a wave cycle, and then pushed back in when the field changes orientation in the second half. Due to the sudden density change, electrons rapidly oscillate beyond the critical surface, and escape the influence of the laser field, taking some of its energy in the process [72]. This mechanism is illustrated in Fig. 2.10. Electrons are effectively accelerated through the plasma at approximately the quiver velocity (Eq. 2.36). Thus the electron's energy gain is on the scale of the ponderomotive potential, with an additional dependence on incidence angle. It was observed in simulations, by Gibbon and Bell [73], that electrons may make multiple oscillations between the vacuum and (underdense) plasma interface, before being injected past the critical surface. Unlike resonance absorption the steep plasma

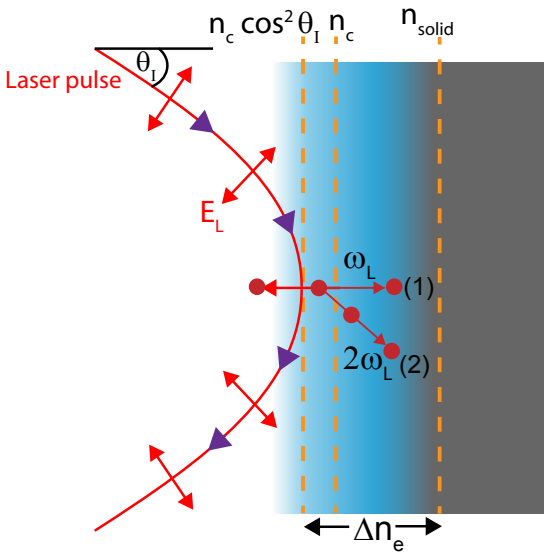

Figure 2.10: Schematic illustration of both vacuum (1) and (2) $\boldsymbol{J}\times\boldsymbol{B}$ electron heating mechanisms. For vacuum absorption a p-polarised laser is incident on a relatively steep density gradient and accelerates electrons beyond the critical surface along the target normal direction. For $\boldsymbol{J}\times\boldsymbol{B}$ mechanisms the incident laser pulse drives electron bunches at twice the laser frequency ($2\omega_L$) into the target along the laser propagation direction.

density gradient cannot support plasma oscillations which can grow over multiple laser cycles, thus in vacuum heating electrons are accelerated into the target bulk once per laser cycle. Moreover, this particular heating mechanism is prevalent at relativistic laser irradiances (i.e. $a_0 > 1; I_L\lambda_L^2 > 10^{18}$ W/cm^2 μm^2).

Relativistic J x B heating

The final absorption mechanism relevant to the research presented within this thesis, is known as relativistic $\mathbf{J}\times\mathbf{B}$ heating; introduced by Kruer and Estabrook [74]. For laser intensities of $a_0 \ll 1$ electron motion is dominated by the electric field of the laser pulse, mainly the regime in which the previously discussed heating mechanisms are dominant. However, for sufficiently high intensities ($a_0 \geq 1$), $\geq$1.38$\times$10^{18} W/cm^2 (for a 1 μm laser), the electron quiver velocity becomes relativistic, and its motion becomes dominated by the magnetic field component of the laser field (as explored in section 2.5). Here the $\mathbf{v}\times\mathbf{B}$ component of the Lorentz force equation (Eq. 2.34) starts to dominate the electron dynamics. This process is therefore similar to the ponderomotive force, in that electrons are ejected from regions of high laser intensity, but are additionally heated by the fast oscillating component of the laser field. This force is directed in the

laser propagation direction and is described by;

$$\mathbf{F} = \frac{-m_e}{4}\frac{\partial v_{os}^2(x)}{\partial x}(1 - \cos 2\omega_L t)\hat{z} \tag{2.76}$$

Studying this relationship it is seen that the first set of terms acts to drive electrons from regions of higher to lower laser intensity, pushing them in the laser propagation direction (as described in section 2.5.2). The latter set of terms is the $\mathbf{J} \times \mathbf{B}$ force component, which rapidly oscillates the electrons at twice the laser frequency, responsible for heating. Consequently, electrons are directly accelerated by the laser pulse and once pushed past the critical density surface will no longer be subject to the laser restoring force, taking laser energy with them into the target. This mechanism is illustrated in Fig. 2.10, with a comparison to the vacuum heating mechanism. The mean energy of the electrons generated is approximately equal to the ponderomotive potential (Eq. 2.53). Moreover, as the electron motion due to the magnetic field scales as ${a_0}^2$ (but only as a_0 for the electric field motion), as laser pulse intensity increases the amplitude of oscillations due to the magnetic field grows more rapidly leading to higher energy electrons than those accelerated purely by electric field mechanisms.

The $2\omega_L$ oscillatory term in Eq. 2.76, shows that electrons are injected past the critical surface in bunches at twice the laser frequency, a key difference compared to the resonance and vacuum mechanisms, which inject at ω_L. Whilst the other collisionless mechanisms, which require oblique laser incidence angles, are dependent on different pre-plasma regimes and inject electrons along the target normal, this mechanism is optimal for normal incidence and is efficient over a wide range of scale lengths. The variation in injection direction can be employed to distinguish between populations of electrons produced by $\mathbf{J} \times \mathbf{B}$ heating and vacuum/resonance heating, when the target is irradiated at an oblique angle [75, 76]. Additionally $\mathbf{J} \times \mathbf{B}$ occurs as effectively for both p- and s- polarised pulses, however not for circular polarisation. In circular polarisation the oscillatory component in the longitudinal electron motion is zero, leaving only the forward pushing force. This results in relativistic $\mathbf{J} \times \mathbf{B}$ heating being suppressed, which has dramatic effects on the interaction dynamics, often being employed when maximum electron heating is undesirable, such as for radiation pressure based laser-ion acceleration schemes (see section 2.7.2).

2.6 Properties of the laser-generated electrons

In the previous section, the discussion centred around the mechanisms by which energy can be transferred from the laser to electrons, relevant to laser-solid interactions. All of these processes give rise to the generation of a population of energetic electrons, often referred to as 'hot' or 'fast'. These propagate through the target from their source in the focal spot region, relatively unperturbed, owing to their small cross section for collisional and radiative stopping.

As these fast electrons are the source of many of the laser-solid interaction concepts of interest, such as laser-driven ion acceleration (see section 2.7), an appreciation of their characteristic properties is key. As such this section presents a description of the properties of laser-generated fast electrons and their transport dynamics through a solid target.

2.6.1 Fast electron spectrum and temperature

As presented in section 2.5.4, the laser-plasma absorption mechanisms act to transfer laser energy to the plasma electrons, heating them to temperatures much higher than the average plasma temperature. The energy which electrons may extract from the laser field is rather stochastic, resulting in fluctuating trajectories and hence a large range of injected electron energies. Bezzerides *et al.* [77] showed that averaging these single particle energies (in the non-relativistic regime) over time leads to a Maxwellian energy distribution, of the form;

$$f(E_f) = N_f \sqrt{\frac{4E_f}{\pi (k_B T_f)^3}} \exp\left(-\frac{E_f}{k_B T_f}\right) \tag{2.77}$$

where E_f is the fast electron energy and N_f the total number of fast electrons. In reality, effects which influence absorption may result in the departure from a single-temperature Maxwellian distribution. Moreover, at relativistic interaction intensities the spectrum can be modified such that a fitting of a Maxwellian will not suffice, calling

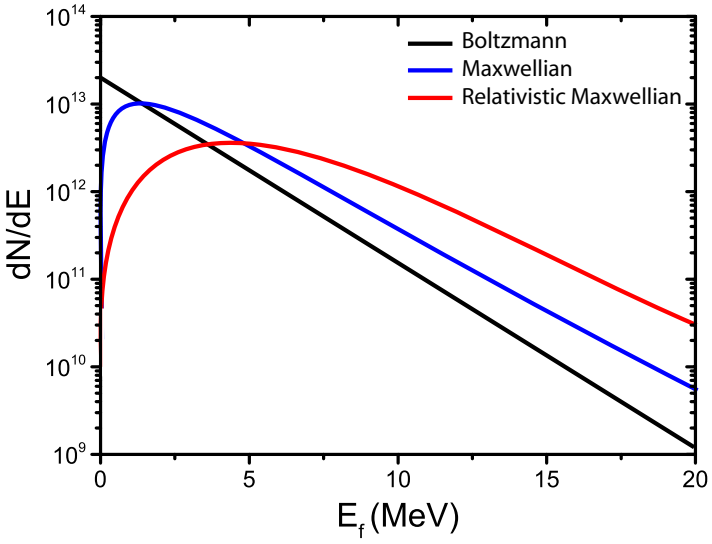

Figure 2.11: Graphical representation of the energy spectra of three distinct fast electron distributions; as identified. The Boltzmann distribution (black data) is included for comparison to the two fast electron energy distributions, defined as $dN/dE = N_f e^{E_i/K_s T_i}$.

for a Maxwell-Juttner distribution [78] to describe the spectrum;

$$f(\gamma) = N_f \frac{\gamma^2 \beta}{\frac{k_B T_f}{m_e c^2} K_n(m_e c^2/k_B T_f)} \exp\left(-\frac{\gamma}{\frac{k_B T_f}{m_e c^2}}\right) \tag{2.78}$$

where $\beta = v/c$, $\gamma = \frac{1}{\sqrt{1-\beta^2}}$ and K_n is the modified Bessel function of the second kind of order n. The typical energy spectrum distribution of the injected electrons, for various forms, is displayed in Fig. 2.11.

The mean energy of the fast electron energy distribution is often quantified by a temperature, $k_B T_f$, the scaling of which has been found to increase with laser intensity, or more accurately with irradiance, $I_L \lambda_L^2$. Several forms of fast electron temperature scaling with the irradiance exist, each describing a specific interaction regime, and thus have been the subject of much research. For the experimental conditions presented in this thesis, namely, being in the relativistic regime and of electrons accelerated by a normally incident pulse, the most relevant electron temperature scaling is the $\mathbf{J} \times \mathbf{B}$ scaling [79], often referred to as 'Wilks scaling', defined as;

$$k_B T_f = m_e c^2 \left(\sqrt{1 + \frac{I_L \lambda_L^2}{1.37 \times 10^{18}}} - 1\right) \tag{2.79}$$

This relation was analytically derived and is employed to predict the electron temper-

ature for relativistic electrons in the interaction of a target with a normally incident pulse. This can be simplified to $k_B T_f = 511[(1 + 0.73 I_{L_{18}} \lambda^2_{L_{\mu m}})^{1/2} - 1]$; where the laser intensity, $I_{L_{18}}$, is in units of 10^{18} W/cm^2 and wavelength, $\lambda_{L_{\mu m}}$ in microns.

Another highly cited electron temperature relation is that developed by Beg *et al.* [80], formulated using experimental data of γ-ray emission from irradiated targets. In this relation the electron temperature scales as $215[I_{L_{18}} \lambda^2_{L_{\mu m}}]^{1/3}$. Similarly to Wilks, this also scales with some function of $I_{L_{18}} \lambda^2_{L_{\mu m}}$, however it differs in that it is relevant for interactions where the laser is incident at some oblique angle (30° in the case of this scaling [80]).

Both discussed temperature scalings are formed using the peak laser intensity. However, as reported in Chen *et al.* [81], this approach is overly simplified, as it does not consider the focal spot intensity profile. As the ponderomotive potential is a local effect the electron spectrum should therefore be calculated with the focal spot distribution in mind.

The fact that numerous scaling laws exist, each of which fit experimental data within a limited range, indicates that this is a somewhat difficult parameter to quantify. Characterisation of the fast electrons inside the target has thus far proved extremely difficult due to strong electrostatic fields trapping the majority of fast electrons inside the target, with only a small fraction escaping into vacuum. Thus, most measurements of the spectrum of electrons propagating through the target are based on indirect methods centred on detecting secondary emission, such as x-ray or optical emission from the target, which can be used to infer information on the fast electrons. Additionally, the small escaping population of fast electrons emitted at the target rear, before strong charge separation fields are generated, can be characterised to provide information on the initial fast electron temperature inside the target [82]. Characterisation of this escaping population, to elude to the interaction dynamics, is employed in chapter 6.

2.6.2 Fast electron transport

The fast electrons generated at the target-front, which are then accelerated into the target, are of such high numbers that the peak current of the 'electron beam' within the target is of the order of mega-Amperes (MA). As a consequence of such a high current, as shown in Alfvén [83], a self induced magnetic field will act to inhibit propagation.

The current above which propagation is stopped, commonly referred to as the 'Alfvén limit' (I_a), can be estimated using [84];

$$I_A \simeq \frac{\beta\gamma m_e c^3}{e} = 17000\beta\gamma\ A \tag{2.80}$$

where β and γ have the usual meaning (defined in section 2.6.1). The limit is found to be 47.5 kA for a 1 MeV electron beam (assuming an infinitely wide beam). Clearly this value is orders of magnitude below the predicted MA fast electron beams, which have been experimentally confirmed to propagate. Therefore, there must be some additional process occurring in the interaction allowing violation of this fundamental current limit.

If one considers the net current inside the target as not only the current flowing in one direction, i.e. source to rear, then the manner in which the Alfvén limit is circumvented becomes clear. As the fast electrons, of current $\mathbf{j}_{fast}$, enter the target, a space charge field is set-up by this charge displacement, which in turn acts to draw a spatially localised current from the target bulk [85], of approximate magnitude $\mathbf{j}_{fast}$. This secondary current, called the 'return current' ($\mathbf{j}_{return}$), is of significantly lower temperature compared to the fast current, though importantly, contains a greater number of electrons (such that the currents balance). The effect of the counter propagating currents is a net current of lower magnitude than the Alfvén limit; with the current balance expressed in Eq. 2.81. Thus, it is this return current spatially overlapped with the forward going fast current which mitigates the formation of otherwise large magnetic fields, often referred to as current neutrality.

$$\mathbf{j}_{fast} + \mathbf{j}_{return} \approx 0 \tag{2.81}$$

The formation of somewhat smaller magnitude magnetic fields within the target does occur even with this near 'charge neutrality' condition. These are important to consider as they can have a major effect on the transport dynamics of fast electrons as they propagate. These magnetic fields are generated as the fast and return currents do not match exactly (symbolised by $\approx$ in Eq. 2.81). According to Faraday's law (Eq. 2.3) these fields are sourced by the spatial variation in the electric field required to draw the return current and hence are a function of the plasma resistivity, η_e;

$$\mathbf{E} = \eta_e \mathbf{j}_{return} \tag{2.82}$$

$$\frac{\partial \mathbf{B}}{\partial t} = \nabla \times \mathbf{E} = \nabla \times (\eta_e \mathbf{j}_{return}) \tag{2.83}$$

$$\nabla \times \mathbf{B} = \mu_0(\mathbf{j}_{fast} + \mathbf{j}_{return}) \tag{2.84}$$

Clearly if the currents completely neutralised each other there would be no magnetic field generation, therefore the net current is;

$$\mathbf{j}_{fast} + \mathbf{j}_{return} = \frac{\nabla \times \mathbf{B}}{\mu_0} \tag{2.85}$$

$$\mathbf{j}_{return} = -\frac{\nabla \times \mathbf{B}}{\mu_0} - \mathbf{j}_{fast} \tag{2.86}$$

$$\frac{\partial \mathbf{B}}{\partial t} = -\nabla \times \left(\frac{\eta_e}{\mu_0} \nabla \times \mathbf{B} - \eta_e \mathbf{j}_{fast} \right) \tag{2.87}$$

$$\frac{\partial \mathbf{B}}{\partial t} = -\nabla \times \left(\frac{\eta_e}{\mu_0} \nabla \times \mathbf{B} \right) + \nabla \times (\eta_e \mathbf{j}_{fast}) \tag{2.88}$$

For the plasma conditions present inside a typical target, the term η_e/μ_0 in Eq. 2.88 (the magnetic diffusion term) is $\approx$1, and therefore Eq. 2.88 can be expressed as;

$$\frac{\partial \mathbf{B}}{\partial t} = \nabla \times (\eta_e \mathbf{j}_{fast}) \tag{2.89}$$

$$\frac{\partial \mathbf{B}}{\partial t} = \eta_e (\nabla \times \mathbf{j}_{fast}) + \nabla \eta_e \times \mathbf{j}_{fast} \tag{2.90}$$

The first set of terms on the RHS of this relation ($\eta_e(\nabla \times \mathbf{j}_{fast})$ [Eq. 2.90]), describes magnetic field generation resulting from current density variations throughout the fast electron beam. Due to higher on-axis current density compared to the wings, a self-generated magnetic field exerts a radial force, directed inwards toward the propagation axis, essentially pinching the beam. Moreover, local electron density modulations in the beam will lead to local field generation and possible beam break up. The second set of terms on the RHS of Eq. 2.90 accounts for field generation resulting from resistivity gradients through the target, arising due to temperature gradients, for example. Temperature gradients occur due to the fast electron current density being highest on-axis and the return current being collisional. Therefore heating is maximised on-axis and falls off towards the beam extremities. This temperature gradient results in subsequent magnetic field generation which acts to either push, or pull, fast electrons away, or to, the propagation axis. Thus either beam expansion or pinching occurs, depending on the gradient of the resistivity profile. These two terms (of Eq. 2.90) acting together

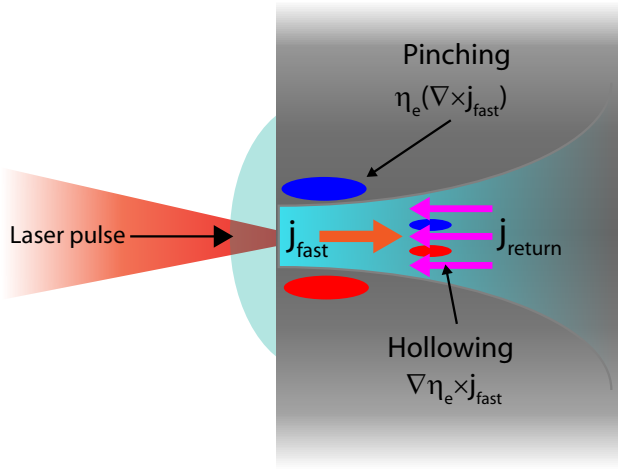

Figure 2.12: Illustration of the relevant processes involved in fast electron transport within a solid density target; including the main fast electron current, the spatially-overlapped return current, and resistive magnetic field generation (both pinching and hollowing components of Eq. 2.90).

make the evolution of the fast electron beam through the target highly complex, as induced transport effects in turn act upon the beam, producing a dynamic feed-back process. Accordingly, this topic has been the subject of numerous investigations, to further understand these processes and additionally to even employ field generation to control electron propagation, through choice of initial target temperature [86], material [87] and structure [88].

Additionally the generation of magnetic fields plays an important role in defining the fast electron divergence through the target [89]. For example the formation of a competing azimuthal pinching magnetic force and a diffusive resistively generated magnetic force will alter the beam divergence. This parameter is typically quoted as a half-angle, and experimental measurements quantify it to be ∼40–50°, at an interaction intensity of 10^{20} W/cm^2 [90], showing an increase in value with increasing intensity. This dependency on intensity was postulated to originate from increased curvature of the interaction region through the hole boring process [91] (see section 2.7.2).

2.7 Laser-driven ion acceleration

The interaction of an intense laser pulse with a solid target can be employed to accelerate ions to multi-MeV energies. This form of particle acceleration is often referred to as the 'next generation' of particle accelerators, and is becoming a promising compliment

to conventional accelerator technology.

This chapter has, thus far, largely ignored ion motion, which is justified on the sub-ps time-scale, due to their significantly higher mass relative to electrons. Ions will, however, begin to move on longer time-scales (tens of ps) or when accelerating fields are strong enough to overcome their inertia. In the case of laser-plasma interactions, direct acceleration of ions to relativistic energies, in a similar manner to the aforementioned electron acceleration, is not feasible until laser irradiances $>10^{24}$ W/cm$^2\mu$m^2 are a reality.

Over the last decade laser-driven ion acceleration has received much attention, due to the development, and increasing availability, of laser systems able to deliver pulses in the pico/femto-second regime and maximum intensities $\sim10^{21}$ W/cm^2. This has led to numerous acceleration mechanisms being theoretically proposed, some of which have been experimentally demonstrated. These mechanisms occur, first through the coupling of laser energy to plasma electrons, and subsequently the acceleration of ions due to charge separation electrostatic fields, with acceleration gradients of several TV/m; two orders of magnitude higher than achievable with conventional accelerators. This results in weakly relativistic ion energies, up to values of $\sim$94 MeV reported experimentally [92]. Since the earliest observations of laser-driven ion acceleration [13, 93] there has been a great deal of research effort devoted to characterising and developing this field.

The specific nature and dominance of the laser-driven ion acceleration mechanism occurring in an interaction depends on a number of parameters, primarily the laser pulse peak intensity and the areal density of the target. In fact, an interaction may display a combination of acceleration mechanisms as there is no sharp transition between acceleration schemes [92, 94].

The following sections are intended to give insight into the laser-driven ion acceleration mechanisms relevant to this thesis, building upon the concepts explored in the previous sections.

2.7.1 Target normal sheath acceleration

Over 15 years ago (2000) the laser-driven ion acceleration mechanism known as target normal sheath acceleration (TNSA) was first observed by Snavely *et al.* [13], Hatchett *et al.* [93] and Clark *et al.* [95]. This mechanism was later explained by Wilks *et al.*

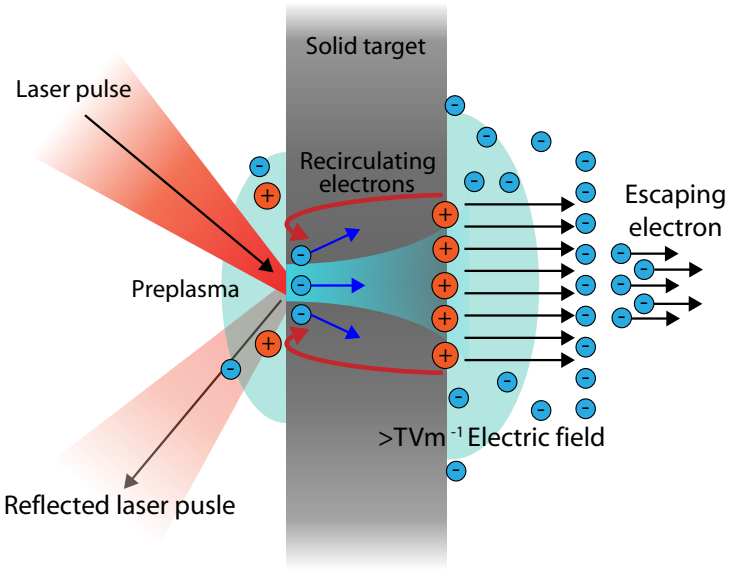

Figure 2.13: Depiction of the principle of the target normal sheath acceleration (TNSA) mechanism, showing the laser pulse irradiating the target front, generating a plasma, the subsequent injection of hot electrons into the target and the resultant acceleration of ions from the target rear surface.

[14]. Since then it has become a well established acceleration method, displaying some reliability, with a vast quantity of experimental and theoretical research reported, over a wide range of interaction conditions.

In the TNSA mechanism an intense laser pulse ($\gtrsim 10^{18}$ W/cm^2) irradiates a solid density target, of several μm in thickness, which remains opaque to the laser pulse over the interaction. The process begins with the rapid ionisation of the target front due to the pulse's preceding light, resulting in the formation of an expanding plasma (see section 2.4). The main pulse then interacts with this plasma and is partially absorbed, by the aforementioned electron heating mechanisms (see section 2.5.4). The population of energetic electrons generated (the properties of which were discussed in section 2.6) then propagates through the target from their source at the focal spot region, relatively unperturbed owing to small cross sections for collisional and radiative stopping. The electron beam has half-angle divergence of $\sim$20°–50° [90, 91], resulting in a progressive motion of electrons towards the target edges, in a process referred to as 'lateral' spreading. This can have significant effects on the transport of electrons, and consequently the TNSA dynamics [96, 97]. Additionally, as presented previously (in section 2.6.2), fast electrons are subject to numerous transport phenomena affecting their spatial distribution [86].

The fast electrons eventually reach the target rear vacuum boundary, and as a

consequence of no return current being able to be drawn at this position, further propagation is inhibited. Electron accumulation thus occurs on the target rear, though some of the most energetic electrons escape the interaction, consequently leaving the target charge unbalanced and thus positively charged. As a result the remaining population of electrons (even on the MeV level [98]) are confined at the rear by Coulomb forces, giving rise to the generation of a strong electrostatic sheath field. This sheath acts to reflect electrons still being generated by the laser back into the target. These reflected, or recirculated, electrons act to form a similar sheath field at the target front, which additionally acts to reflect electrons back to the rear [99]. Recirculation plays an important role in the TNSA process, acting to increase the duration of the accelerating sheath field [100]. The principle of the TNSA scheme is depicted in Fig. 2.13.

The longitudinal spatial extent of the rear surface sheath field is given by the Debye length of the population of sheath electrons, with density $n_{e(hot)}$ and temperature $k_B T_e$;

$$\lambda_d = \sqrt{\frac{\varepsilon_0 k_B T_e}{e^2 n_{e(hot)}}} \tag{2.91}$$

The typical extent is found to be a few microns ($k_B T_e$ ~MeV and λ_D ~μm) [101] for the interaction conditions reported. The transverse spatial extent of the sheath (the sheath area S_{sheath}), is dependent on the fast electron beam dynamics throughout the target, that is beam divergence, and its temporal evolution on the target rear. Its size can be estimated using;

$$S_{sheath} = \pi(r_0 + d\tan\theta)^2 \tag{2.92}$$

where r_0 denotes the radius of irradiating laser focal spot, d the target thickness and θ the opening angle of the fast electrons. The consequence of the sheath is to give rise to an extremely strong electric field, E_s, estimated using [14];

$$E_s \approx \frac{k_B T_e}{e\lambda_D} \tag{2.93}$$

For an electron temperature of 1 MeV and sheath electron density of 10^{21} cm^{-3}, the field strength is ~3 TV/m. The field can be considered quasi-static as electrons which are continuously pulled back into the target are replaced by more electrons generated at the target front over the interaction duration. Such a field is sufficient to ionise atoms at the target rear, through the barrier suppression mechanism (see section 2.2).

This primary occurs in the thin layer hydrocarbon contaminants present on the target surfaces [16]. Subsequent acceleration of the ions occurs, over a few μm, to several tens of MeV energies, within the rapidly expanding plasma, with the electrons transferring energy to the ions through the charge separation fields [13, 93, 95].

The TNSA mechanism is a complex, multi-dimensional process, dependent on numerous factors, including the front surface interaction dynamics, fast electron transport and the temporal/spatial dynamics of the accelerating rear surface sheath. Only a limited number of these phenomena are accessible to direct experimental measurements, therefore to enable a quantitative understanding of the acceleration process a number of analytical and numerical models describing TNSA have been formulated [102, 103, 104]. These range from simple fluid models to fully relativistic, collisional, three-dimensional computational simulations. A plasma fluid model developed by P. Mora is one of the most widely employed, a full description of which is found in Ref. [102] . The Mora model is a one dimensional plasma expansion model describing its propagation into vacuum, building upon previous models [105, 106] with the addition of charge separation into its description. The model enables the temporal evolution of the peak strength of the accelerating electric field to be calculated, and thus the energy ions gain may be modelled. The Mora formulation of TNSA successfully analytically predicts crucial features of the mechanism, such as the maximum ion energy and spectrum, over a wide range of experimental conditions [107]. This model predicts a maximum TNSA proton energy, $E_{p_{max}}$, of;

$$E_{p_{max}} \backsimeq \frac{1}{2} m_p v_{front}^2 \backsimeq 2 Z k_B T_e \left[\ln(t_p + \sqrt{t_p^2 + 1})\right]^2 \tag{2.94}$$

where v_{front} is the ion front velocity and $t_p = \omega_{pp} t / \sqrt{2\exp(1)}$ (where ω_{pp} is the plasma proton frequency). A key limiting feature of the Mora model is seen in this expression, in that there is no temporal limit to proton energy gain and it breaks down due to the assumption of a Maxwellian electron temperature distribution. In reality, expansion can only be considered isothermal as long as the laser pulse is generating fast electrons. Thus as the pulse has a finite duration, an upper limit, or maximum cutoff ion energy E_{pmax} is obtained using an acceleration time, t_{acc}, approximately equal to the laser pulse length. Simulations have shown this to be $t_{acc} \approx 1.3\tau_L$, at laser intensities $>3\times10^{19}$ W/cm^2 [107].

TNSA ion beam characteristics

Motivation for the study of TNSA is primarily based on the unique characteristics of the generated ion beams, namely relating to composition, energy spectrum, divergence, source size, laminarity and emittance. In general TNSA ion beams are very energetic and intense bursts ($\sim 10^{13}$ protons for a Vulcan-PW type laser system) of particles which are emitted in a high quality beam-like structure, exhibiting key characteristics making them suitable for a wide range of applications. The intense nature of the proton beam is attributed to a relatively high laser-to-proton energy conversion efficiency, experimentally measured to be as high as 15% [108]). This section explores the main properties of a TNSA ion beam and the underlying physics behind each.

Ion source and composition

Early in the study of ion emission from laser-solid interactions it was ambiguous as to where the ions were being emitted from, i.e. the front or rear surface of the target. Some experimental observations indicated that accelerated ions were sourced from the front surface [95, 109], while others concluded it was the rear [13, 93]. This confusion was solved in a study reported in Allen *et al.* [110] through a demonstration that ions were in fact emitted from both surfaces of the target. They concluded this by removing contaminants from each separately and then characterising ion emission. Rear surface emission was shown to dominate over the front emission in Fuchs *et al.* [111].

Compositionally the ion beam consists of a number of species, in various degrees of ionisation. Interestingly the majority of ions are not sourced from the target material but from the aforementioned contamination layer. This population consists mainly of water vapour and hydrocarbon molecules present in the atmosphere, which accumulate on the target surface [16] and remain due to the limit of achievable vacuum conditions. Ion species generated from this layer are preferentially accelerated according to their charge-to-mass ratio (q/m); which is to say ions with the highest q/m ratio (i.e. protons) will reach the highest velocities more rapidly, experiencing acceleration for the longest duration relative to ion species of lower q/m ratio (such as carbon and oxygen ions). Furthermore, once protons have been generated they act to screen heavier ions from the sheath field, thereby reducing acceleration efficiency. Consequently, protons will contain the majority of laser energy converted into particle kinetic energy.

Although, as carbon and oxygen have relatively low ionisation states, they are still somewhat efficiently accelerated and are thus observed alongside protons. Target element ions, typically heavier compared to the contaminants, can be accelerated more efficiently by partial removal of the contaminant layer. This can be achieved through various methods such as ohmic heating [17], irradiation by an ion gun [110] or laser ablation using a relatively long (nanosecond) duration pulse, of the target [112].

Energy distribution

Experimentally, and through analytical modelling, a TNSA ion beam is found to possess a broad ion energy distribution. The spread is typically Maxwellian in nature, exhibiting a sharp maximum energy cut-off, dependent on the driving electron temperature (and thus peak laser irradiance). It is possible to give the ion beam spectrum an average temperature through fitting of the following distribution;

$$N_i(\varepsilon) = N_{i0} \exp\left(- \frac{\varepsilon}{k_B T_i} \right) \tag{2.95}$$

where ε is the ion energy and N_{i0} is a fitting parameter. It is often the case that the best fit to a spectrum is found using multiple average temperature fits at various ion energy ranges. The broad energy distribution exists as a result of acceleration of ions from the spatially and temporally evolving inhomogeneous fast electron distribution at the target rear and thus ions experience varying sheath field strengths. Figure 2.14 shows a typical proton energy spectrum obtained experimentally using radiochromic film spectroscopy (see section 3.4.1).

The maximum proton energy achievable via this mechanism is strongly correlated to the peak laser intensity (being experimentally observed in numerous investigations [107, 113]), via the temperature and density of the fast electrons produced in the interaction. As discussed previously (see section 2.6.1) the fast electron temperature is dependent on the laser irradiance [79]. Borghesi *et al.* [30] published a review of ion maximum energy as a function of laser intensity obtained employing experimental data collected from numerous laser systems, of varying parameters. They showed that for pulse durations between 0.3–1 ps the maximum ion energy scales as $\sqrt{I_L \lambda^2}$, and as $I_L \lambda^2$ for pulse durations under <150 fs. Knowledge of these scalings is extremely useful, as measurement of the maximum energy of TNSA accelerated protons can be

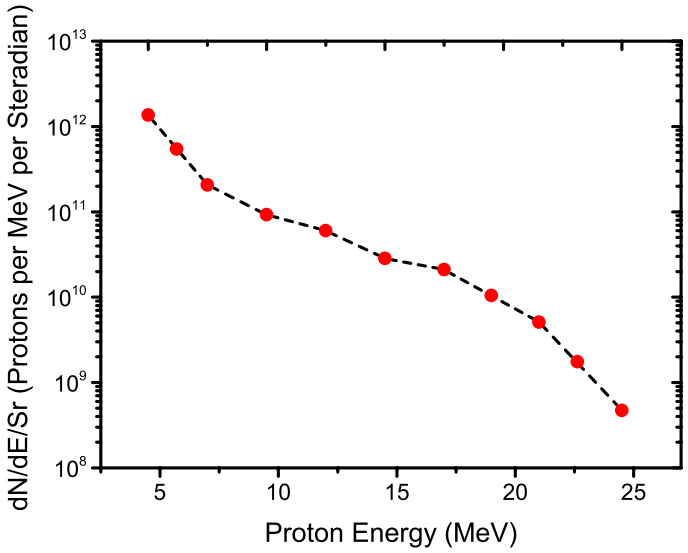

Figure 2.14: Plot of a typical TNSA proton beam energy spectrum measured experimentally using radiochromic film spectroscopy. This data is taken from chapter 4 and was obtained employing the Vulcan-PW laser, irradiating a 6 μm thick aluminium foil.

an indirect diagnostic of the interaction intensity, which will be employed in chapter 4.

Beam divergence and ion source size

The trajectories of accelerated ions from the target rear are directed normal to the local orientation of the time-dependent spatial profile of the evolving sheath field. Consequently, the spatial characteristics of the sheath, driven by changes in the density distribution of fast electrons, is not only responsible for the ion beam energy distribution but additionally its spatial characteristics. The spatial profile of the sheath also results in another important TNSA beam characteristic; its energy dependent beam divergence. TNSA beams exhibit the largest divergence at the lowest particle energies, reducing in magnitude as the energy increases. This feature arises as the spatial profile of the electron density distribution forming the accelerating sheath is typically Gaussian (or parabolic in some cases) in nature [114, 115], peaked on-axis and decaying transversely. This profile arises as a result of a combination of effects, including the intensity distribution of the irradiating focal spot altering the generation of fast electrons at the interaction region [116]. This was investigated in Roth *et al.* [117] using various focal spot intensity distributions to modify the spatial distribution of accelerated protons. As a consequence of the sheath field being centrally peaked, in a comparatively small area, the highest energy ions are generated primarily in this region, whereas lower

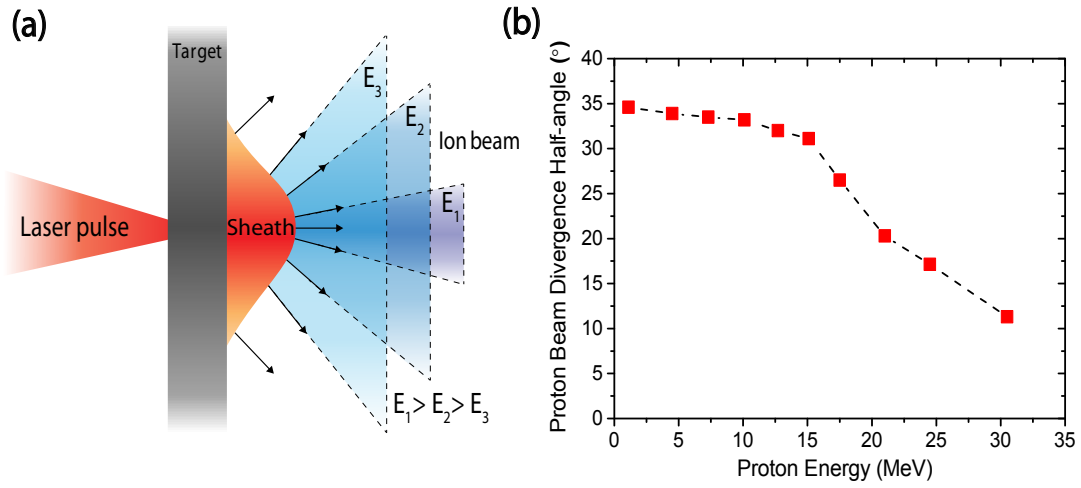

Figure 2.15: (a) Schematic illustrating the energy dependent divergent nature of a TNSA ion beam as a result of the sheath profile. (b) Plot of the typical TNSA proton beam energy resolved half-angle divergence measured experimentally. This data is taken from chapter 4 and was obtained employing the Vulcan-PW laser, irradiating a 6 μm thick aluminium foil.

energy ions are accelerated at relatively weaker field regions, which comprises a larger area of the sheath. Furthermore, due to the ion trajectories being normal to the local orientation of the sheath the resultant divergence varies across the changing gradient of the sheath's transverse profile, thus an energy dependent beam divergence is formed. This is illustrated in Fig. 2.15.

This source-size energy dependence was experimentally demonstrated in Cowan *et al.* [118], through employment of structured targets with linear micro grooves on their rear surface to project modulations into the accelerated proton beams spatial intensity distribution. The grooves were identical and equally spaced, thus by counting the number of grooves reproduced in the proton beam, the size of the emission region, at a given energy, could be measured. An alternative method for characterising this parameter, reported in Borghesi *et al.* [119], utilised micro-structured meshes situated in the path of the accelerated protons, again to add modulations to the spatial-intensity distribution of the beam. These investigations found that for laser intensities between 10^{18} and 10^{20} W/cm^2 (and 1 ps pulse lengths) the ion source size is a few hundred microns for the lowest energy protons, and tens of microns for the highest energy protons, for tens of micron thick targets. Borghesi *et al.* [119] also highlighted that the source size is derived from the early stages of the TNSA process.

Beam laminarity and emittance

The fact that the aforementioned imprinting of groove structures from the target rear into the spatial-intensity distribution of accelerated ions [118] occurs is due to the fact that a TNSA ion beam possesses a high degree of laminarity. This is to say, individual ion trajectories do not cross significantly, as opposed to a turbulent beam where trajectories cross many times. This feature is key for the efficient mapping of the rear surface sheath spatial intensity profile to that of the protons.

The transverse emittance of a beam of charged particles is a measure given to quantify the average spread of particle coordinates in position and momentum phase space, and is a key parameter in accelerator physics for providing a figure of merit in describing a charged particle beam. In the case of a TNSA beam this is defined using the emission source size and the angle of emission, and further can be used to estimate the beam laminarity [119]. An emittance value of $<4\times10^{-4}$ mm.mrad [118] is typically measured for TNSA proton beams; approximately $\times100$ smaller than achievable in conventional RF accelerators.

These TNSA beam characteristics are a consequence of the beam's low divergence and the fact that ions are rapidly accelerated (from an initially cold state), thus limiting thermal spreading. Additionally, accelerated ions co-propagate with the accelerated electrons preventing space charge spreading.

2.7.2 Radiation pressure acceleration

Another promising laser-driven ion acceleration mechanism, distinct from TNSA, which has received a great deal of attention in recent years is radiation pressure acceleration (RPA). The concept behind this mechanism is that the radiation pressure of the laser pulse, resulting from the fact photons carry momentum [120] ($\hbar k$) and energy ($\hbar\omega_L$), can be transferred to a target upon reflection from the target surface. It was postulated shortly after the first experimental demonstration of the laser [1] that the radiation pressure of such a light source could be utilised to propel a space craft using a terrestrial based laser system [121]. From Maxwell's equations we know an electromagnetic wave can exert a pressure upon reflection from a surface, and the magnitude of this pressure

can be approximated by conservation of momentum [122];

$$P_{rad} = (2R + A)\frac{I_L}{c} \tag{2.96}$$

where R is the reflectivity coefficient of the target and A the absorption coefficient. For current peak laser intensities ($\sim 10^{21}$ W/cm^2) this pressure can be in excess of 100 Gbar, which can be significantly higher than the thermal pressure of the plasma. In terms of the interaction of an intense laser pulse with an overdense target, if the radiation pressure exceeds the plasma thermal pressure, RPA will occur, resulting in direct acceleration of the plasma electrons. Consequently, this sets up strong electrostatic fields due to charge separation, acting to accelerate ions and theoretically, resulting in a mono-energetic ion energy distribution. The fundamental difference from TNSA is that RPA relies on the fact the interaction is not mediated by heating of electrons, but their direct acceleration by photon pressure. Furthermore in comparison to TNSA, the scaling of maximum ion energy is predicted to be relatively more favourable in RPA. Esirkepov *et al.* [123, 124] proposed theoretically that at laser intensities $>10^{23}$ W/cm^2 RPA would become the dominant acceleration process and could result in GeV proton energies.

The above description of RPA is for linearly polarised pulses with ultra-high (which at the time of writing this thesis, is not yet achievable) intensities of 1.2×10^{23} W/cm^2. However, it was theoretically and computationally proposed in Robinson *et al.* [125], and in Macchi *et al.* [126], that significant RPA may be accessible at current peak laser intensities through the use of normally incident circularly polarised pulses. In this polarisation case, as described earlier (see section 2.5.4), $\mathbf{J}\times\mathbf{B}$ heating of electrons is suppressed due to there being no oscillating component in the ponderomotive force. As such, sheath acceleration is inhibited, as this requires energetic fast electrons.

Looking at an example of a perfect reflector moving at a velocity equal to $v = \beta c$, interacting with a circularly polarised pulse (thus assuming suppressed electron heating) then further insight into RPA may be gained. This case is often referred to as a 'moving mirror', with the surface reflectivity a function of the laser frequency, $R(\omega')$, as measured in the rest frame. Since the radiation pressure is an invariant quantity,

the pressure in the laboratory frame and rest frame (denoted by $'$) can be expressed as;

$$P_{rad} = P'_{rad} = \frac{2I_L}{c} R(\omega)' \frac{1-\beta}{1+\beta} \tag{2.97}$$

with the relationship between the incoming (ω') and reflected (ω) pulse frequencies due to the Doppler effect in the rest frame being;

$$\omega' = \omega \sqrt{\frac{1-\beta}{1+\beta}} \tag{2.98}$$

RPA can be broadly split into two interaction regimes; namely (i) Hole-Boring (HB) and (ii) Light-Sail (LS). The former, HB, is significant for relatively thick (μm scale) overdense targets, where the laser pressure can push into the plasma, boring a hole, and effectively causing plasma density profile steepening. The displacement of electrons from ions then results in the aforementioned electrostatic field which in turn accelerates the ions. The latter regime, LS, is applied to interactions with ultra-thin (nm scale) targets, where the pulse can accelerate the region contained in the focal spot volume of an overdense target. Each regime is explored in more detail below.

Hole-Boring regime

From early PIC simulations of intense pulses interacting with overdense plasmas (with steep front surface density profiles), radiation pressure was found to push the critical surface into the target [79, 127]. This effectively bores a hole, hence the name of this mechanism, Hole-Boring, sometimes referred to as the laser-piston regime [128]. In this RPA regime electrons are driven in the laser propagation direction forming a compressed high density layer, resulting in a charge depleted region containing only ions. The charge separation and the generation of an electrostatic field between the two oppositely charged populations, acts to accelerate the ions. This process is illustrated graphically in Fig. 2.16(a). The recession velocity of the critical surface due to radiation pressure, called the Hole-Boring velocity, v_{HB}, was first derived in Wilks *et al.* [79], using momentum conservation between the laser and accelerated ion species;

$$\frac{v_{HB}}{c} = \sqrt{\frac{n_c}{n_e} \frac{I_L \lambda^2}{2.74 \times 10^{18}} \frac{Z}{A} \frac{m_e}{m_p}} \tag{2.99}$$

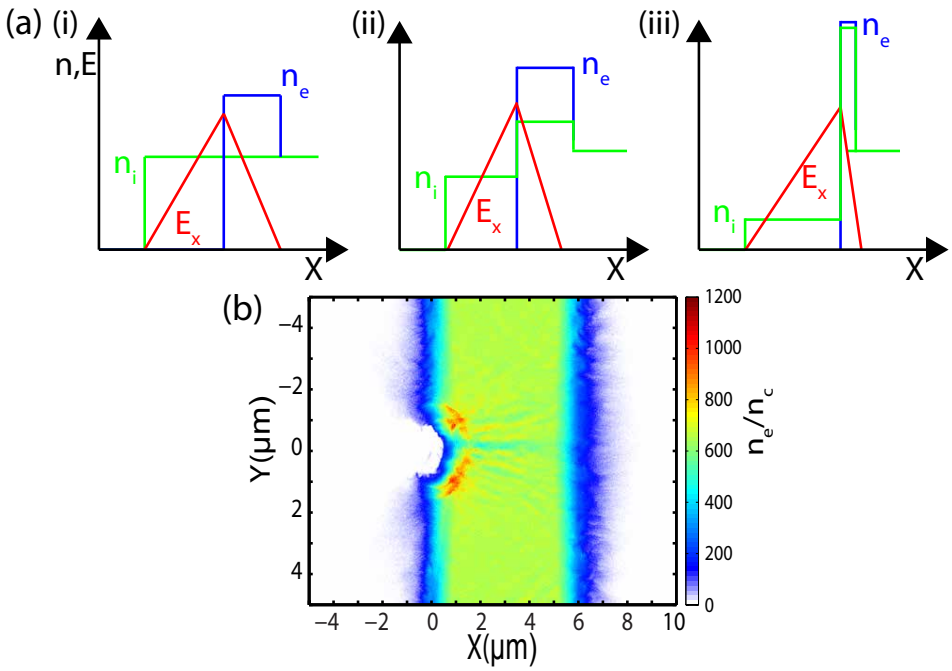

Figure 2.16: (a) Graphical representation of the Hole-Boring radiation pressure acceleration regime, showing the temporal evolution of the hole-boring front, increasing in time through (i)-(iii). These demonstrate the compression in electron density (n_e), the depleted region behind this layer, the corresponding longitudinal electric field (E_x) and the resultant ion acceleration (n_i). (b) 2D PIC simulation of a 4×10^{20} W/cm^2 pulse interaction with a 6 μm aluminium target, showing the curvature of the target electron density profile as a result of radiation pressure.

where Z is the ionisation state and A the ion mass number. This equation only describes the HB velocity for non-relativistic interactions, therefore it is necessary to modify this for relativistic cases, as Eq. 2.99 can predict unphysical hole-boring velocities $>c$. Robinson *et al.* [129, 130] achieved this correction leading to the following expression;

$$\frac{v_{HB}}{c} = \frac{\sqrt{B}}{1+\sqrt{B}} \tag{2.100}$$

where;

$$B = a_0\sqrt{\frac{Z}{A}\frac{m_e}{m_p \cdot n_e/n_c}} = \frac{I_L}{n_i m_i c^3} \tag{2.101}$$

This description shows that the HB velocity depends on the laser intensity, the target density and the ion mass. As such target material is an important selection if one either wishes to enhance or suppress HB, for a given laser. Additionally, this model can predict the maximum ion energy feasible using this acceleration model, described by;

$$E_i = m_i c^2\left(\frac{2B}{1+2\sqrt{B}}\right) \tag{2.102}$$

HB will continue until the moving front reaches the target rear surface, or the interaction with the pulse has ended. Additionally, the target may become transparent during the interaction effectively ending the 'moving mirror'. This transparency occurs either classically through target decompression (i.e. a reduction in electron density), relativistically (as discussed in section 2.5.3), or a combination of both. The energetic ions generated through HB are predicted to have an energy scaling proportional to the laser irradiance, $E_i \propto I_L\lambda^2$, thus more favourable than that displayed in TNSA ($E_i \propto \sqrt{I_L\lambda^2}$) [19]. Furthermore, the ion energy distribution is predicted to take a quasi-monoenergetic form.

For a typical experimental pulse (i.e. Gaussian intensity profile focus) radiation pressure will bend the plasma critical surface inward following the shape of the focal spot, enabling deeper penetration into the target, as displayed in Fig. 2.16(b). This can have numerous effects on the interaction due to this dramatic change in the interaction region. For example, for a normal incident laser pulse, target curvature results in the laser electric field no longer being normal to the surface, thus altering absorption and electron dynamics [131]; this effect is explored in more detail in chapters 5 and 6.

Light-Sail regime

In the HB regime, acceleration lasts until the pulse ends, or the ion front leaves the target rear. However if the target is relatively thin (tens of nm-scale), this occurs very quickly. Under these conditions this regime of RPA is referred to as Light-Sail (LS). In this regime the whole target volume within the focal spot region may be accelerated as a high density plasma bunch, reflecting the pulse. Esirkepov *et al.* [124] proposed theoretically this ion acceleration mechanism, in which electrons are expelled from a target when they are accelerated by $\mathbf{J}\times\mathbf{B}$ heating in a single cycle of a relativistic pulse. As radiation pressure continuously pushes the electrons at the critical surface over the duration of the pulse, the accelerating potential is maintained, and sheath acceleration is suppressed. As the ions reach relativistic velocities rapidly they can stay close to the electron layer. In such a description the target can be considered as a relativistic plasma mirror co-propagating with the pulse, where the reflected light is Doppler red shifted and energy is transferred to the plasma slab [20]. This acceleration mechanism is depicted in Fig. 2.17. The velocity at which the target moves when accelerated by

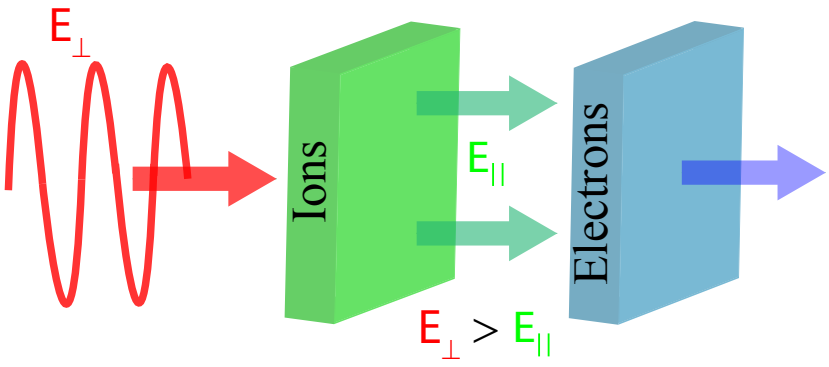

Figure 2.17: Illustration depicting the light-sail regime of radiation pressure acceleration. The linear polarised laser electric field ($E_\perp$) (in red) sweeps away all electrons (in blue) forming an electrostatic field ($E_\parallel$) which subsequently accelerates ions (in green).

radiation pressure can be found through the conservation of momentum between the target and pulse, assuming a 'top-hat' pulse spatial intensity profile, given in [132];

$$v_{LS} = \frac{(2R + A)\tau_{acc}}{n_{i0} m_i d} \frac{I_L}{c} \tag{2.103}$$

where d is the target thickness. From this it is seen that ion energies scale as $E_i \propto I_L^2$, with the acceleration time on the time-scale of the pulse length ($\tau_{acc} \approx \tau_L$) [19]. Additionally, according to this model, all ion species should gain the same final velocity. However studies have shown that the different inertias of various species will affect RPA dynamics, such as protons with the highest charge to mass ratio may move ahead of other ion species in the ion front, thus gaining higher velocities [133].

A hallmark of this mechanism, making it distinct from TNSA, is the formation of a quasi-monoenergetic ion spectrum, as opposed to the continuous energy distribution generated in TNSA. Due to the advantages quasi-monoenergetic ions would bring to envisioned applications of laser-driven ion sources, this mechanism has received considerable interest over the past few years. An additional feature which makes LS highly attractive is its maximum ion energy scaling with peak laser irradiance. As seen previously the maximum ion energy in TNSA scales as $\propto \sqrt{I_L \lambda^2}$, however this mechanism displays a much faster scaling of $\propto I_L \lambda^2$. As such when higher peak laser intensities are available in the future, this mechanism may be a route to achieving the desirable hundreds of MeV monoenergetic proton beams required for laser-driven hadron therapy (explored in chapter 1).

As with HB, LS acceleration can be enhanced through the employment of circularly

polarised laser pulses to suppress target heating and expansion. Through this technique, signatures of LS have been observed in numerous experimental investigations employing current laser systems. For example, an investigation reported in Kar *et al.* [134] found evidence of narrow energy features in the ion energy spectra from the interaction of ultra-thin (nanometer scale) foils with pico-second duration pulses.

2.8 Summary

The purpose of this chapter was to provide a summary of the laser-solid interaction concepts relevant to the forthcoming results chapters (chapters 4, 5 and 6). This discussion has demonstrated that this research field encompasses a broad range of physics, including plasma physics and electromagnetism, the combination of which determines key aspects of the interaction, such as the coupling of laser energy to electrons and to quantum effects present in laser-induced ionisation processes. The interplay of these numerous disciplines makes unravelling the physics of laser-solid interactions a complex process. As such, the study of laser-solid interactions requires the use of both experimental investigations, applying a vast range of diagnostic techniques, and the use of numerical and theoretical modelling to interpolate findings. The range of diagnostic techniques employed in this thesis are discussed in the next chapter (chapter 3).

Chapter 3

Methodology: Lasers, diagnostics and simulations

In the previous chapter the fundamental physics underpinning the interaction of intense laser pulses with solid density matter was discussed. As this thesis reports on experimental investigations involving these interactions it is necessary to have an understanding of how these experiments are conducted, in terms of the laser systems employed, the diagnostics used to characterise the interactions and the simulation codes employed to probe the underlying physics and help in the understanding of experimental findings. As such, it is the purpose of this chapter to provide a brief description of the laser systems, the key diagnostic techniques and numerical methods employed throughout the result chapters 4, 5 and 6.

3.1 Overview

The investigations presented in this thesis employ a combination of state-of-the-art experimental facilities, diagnostic technologies and data analysis, utilising sophisticated numerical simulation models. A key component to laser-solid interaction studies is the laser system employed, as this defines crucial parameters of the interaction (i.e. pulse wavelength, duration and energy), and thus the peak intensity achievable. The work conducted in this thesis required high power lasers which can deliver pulses of focused intensity up to $\sim 10^{21}$ W/cm^2, the current highest possible intensity (at the time of writing this thesis). Such systems are expensive to construct and to operate, therefore,

Figure 3.1: Map showing the location of the laser facilities employed throughout this thesis, in relation to the University of Strathclyde (1); with (2) identifying the Central Laser facility and (3) the PHELIX laser system.

typically the most intense laser systems are situated in large national facilities; for example the Central Laser Facility (CLF) at the Rutherford Appleton Laboratory (RAL) in the UK, or the PHELIX laser system based at the GSI Helmholtz Centre for Heavy Ion Research in Germany, as presented in Fig. 3.1. Both these facilities were employed to make the measurements reported in this thesis and are described in further detail later in this chapter.

The allocation of experimental time at these facilities is highly competitive, thus access is granted through proposals for beam-time, which typically last from 3-6 weeks in duration. Once an experiment has been accepted, planning for the experiment begins, which goes through several stages over many months, leading up to the beam-time, involving facility personnel, researchers and collaborating groups. Effective planning should ensure the aims of the proposal are realistic and mitigate the majority of issues which may arise throughout the experiment.

The running and set-up of an experiment typically consists of around 6-8 people, each taking on various roles within the team. These roles include, for example at the CLF, a Target Area Operator (TAO) and Deputy Target Area Operator (DTAO), whose roles are to manage activities within the target area. These roles are typically

taken on by an experienced student or post-doctoral researcher. The research team also has a 'Principle investigator' (PI), whose role is to provide guidance and overall vision of the experiment. Typically this is the senior academic of the research team. Additionally there is also a dedicated team of facility operators responsible for the performance and delivery of the laser pulses to the target area.

In terms of the physical experimental set-up, the interaction point between the laser focus and target is typically referred to as the 'target-chamber centre' or TCC, although it is often not at the physical chamber centre (but is so-called as historically it was the interaction point in spherical chambers). It is first defined within a few microns using the tip of a thin wire ($\sim\mu$m diameter) and referenced by multiple diode lasers allowing a fixed point to be established to align diagnostics to. An array of diagnostics are usually employed to characterise the interaction on each laser shot, capturing the measurements required for the objectives of the experiment. These include, for example, particle and optical diagnostics which can record spatial, spectral and temporal interaction aspects.

Once the set-up is complete, the experiment moves onto firing 'laser shots', initially with simple targets (typically micron-scale metal foils) to test, optimise and calibrate diagnostics. Once this is achieved, and the diagnostics are providing meaningful measurements, the experiment can begin to focus on conducting measurements, forming high quality data sets which aim to address the physics presented in the experimental proposal and possibly (as is often the case) reveal new concepts.

3.2 High power laser technology

In order to investigate the interaction physics of intense pulses of light with matter one must use a high power laser system. It is extremely useful, if not crucial, in the field of laser-solid interactions to have at least a basic knowledge of how these systems operate to generate the intense pulses and their limitations, especially concerning key interaction parameters, such as pulse duration, energy and thus intensity.

In this section, some of the relevant technologies utilised in the generation of high power laser pulses used throughout the results chapters of this thesis will be explored, before a brief description of the laser facilities employed in this work is conveyed.

3.2.1 Chirped pulse amplification

Since the first demonstration of the laser, by Theodore Maiman [1], there has been constant advancements and innovations pushing the laser intensity frontier. One such advancement, which revolutionised laser-plasma research, is the chirped pulse amplification (CPA) technique. Developed by D. Strickland and G. Mourou [4] in 1985, this technique allowed, for the first time, peak laser intensities $>10^{18}$ W/cm^2 (and hence enabled the relativistic interaction regime to be investigated), which were previously inaccessible due to the energy fluence of pulses surpassing the damage threshold of optics in the laser chain. Intensities $>10^{10}$ W/cm^2 will begin to induce damage to solid state optics in the laser amplifiers, as well as those further in the chain, such as focusing optics. Additionally, as intensities increase further, non-linear optical effects such as self-focusing or self-phase modulation, resulting from the optical Kerr effect, begin to become appreciable. This may lead to intensities surpassing the damage threshold even for relatively low pulse energies. These effects become clear when defining the intensity dependent refractive index;

$$\eta = \eta_0 + \eta_2(I_L) \tag{3.1}$$

where $\eta_2(I_L)$ denotes the intensity dependent component of the refractive index. As stated previously, laser pulses typically have a spatially Gaussian transverse intensity profile, which for sufficiently high intensities leads to a variation in refractive index across the pulse when propagating through a medium. In effect the pulse edges (of lower intensity) move faster compared to the pulse centre (of higher intensity), thus leading to a focusing effect resulting in increased intensity. To quantify the degree of non-linear optical effects a parameter known as the 'B-integral' is often employed. This describes the accumulated phase (ϕ) after propagating a distance of L through an optical medium, expressed as;

$$\phi = \frac{2\pi}{\lambda_L} \int_0^L \eta(z) dz \tag{3.2}$$

$$= \frac{2\pi}{\lambda_L} \int_0^L \eta_0(z) dz + \frac{2\pi}{\lambda_L} \int_0^L \eta_2 I_L(z) dz \tag{3.3}$$

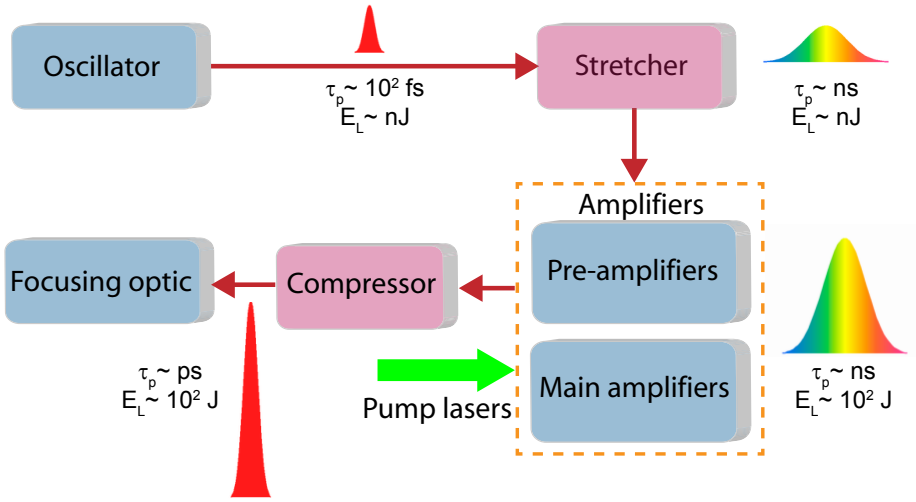

Figure 3.2: Flow diagram illustrating the basic concept of a CPA based laser system. A single pulse from the oscillator is first temporally stretched to reduced its intensity so its energy content can be safely increased by the systems amplifiers. Finally, the pulse, now of higher energy, is temporally compressed back to near its original duration, before being focused to high intensity. The evolution of the pulse throughout these sections, in terms of duration and energy, is also included.

The intensity dependent term in Eq. 3.3, is the so-called 'B-integral' (B) expression.

$$B = \frac{2\pi}{\lambda_L} \int_0^L \eta_2 I_L(z) dz \tag{3.4}$$

Rather than increasing the laser beam diameter in order to reduce the intensity on optics, CPA bypasses this issue by keeping the intensity of the pulse low (below the damage threshold and low B-integral), through utilising a relatively long pulse length, as it propagates through the amplification stages. After amplification the pulse is then compressed before being focused to the interaction point. The basic stages of this process thus involve the stretching, amplification and recompression of an initially short seed pulse. This process is depicted in Fig. 3.2.

Stretching spectrally, i.e. chirping, acts to decrease the pulse's peak power and hence intensity, typically taking the pulse from femto/picoseconds to a few nanoseconds in duration. Pulse chirping is achieved using optical diffraction gratings which create different optical path lengths for the range of wavelengths present in the pulse bandwidth (positive group velocity dispersion). This optical element can therefore temporally stretch, or compress, a pulse by a factor of 10^3–10^5, depending on the wavelength range forming the pulse. In doing so the power density is significantly reduced, below where non-linear effects and optic damage may occur. This allows the pulse to

be safely amplified (the techniques of which are presented in section 3.2.2), often over multiple stages. Finally, pulse stretching is reversed by the compressor stage, to, in the ideal case, recover the original pulse shape and duration, however now of higher energy content. The duration of the final pulse is typically slightly longer than that before the stretching stage due to a combination of non-linear dispersion and gain-narrowing in the amplifiers [135]. Gain-narrowing is an effect which results in a reduction of the pulse bandwidth due to preferential amplification of photons closer to the central laser wavelength.

3.2.2 Pulse amplification

In order to increase the energy content of the seed pulses, CPA based systems commonly employ two forms of pulse amplification; (i) regenerative amplification, and (ii) multi-pass amplification. Both techniques involve propagating the seed pulse through an optically pumped gain medium. The former, regenerative amplification, involves the pulse being injected into an optical cavity containing the gain medium, which it passes through multiple times, extracting energy on each pass. These are often employed in the pre-amplification stages of a laser system. Figure 3.3 illustrates the basic concept of a regenerative amplifier.

This form of amplifier is distinct from other forms in that its input and output gating is controlled through active optical polarisation. Pulse entry into the amplifier is controlled first by a half-wave plate and subsequently a Faraday rotator. The wave plate, set at 45° to the input polarisation plane, rotates the pulse polarisation by 90° i.e. initially s-polarised becomes p-polarised and visa versa. Upon passing through the Faraday rotator the polarisation is again altered, by an amount dependent on the parameters of the rotator, such as the strength of the applied magnetic field and its length. The pulse then passes through a second polariser which acts to transmit the original polarisation state before entering the amplifier set-up and reflect the polarisation state formed by the initial waveplate/Faraday rotator. After reflection from this, the pulse propagates through a Pockels cell. When no voltage is applied after a single round trip the pulse will be ejected from the cavity, due to its polarisation state. However, when a voltage at the so-called ‘quarter-wave’ voltage is applied, named so as this acts like a quarter-wave plate, then the aforementioned polariser will transmit and trap

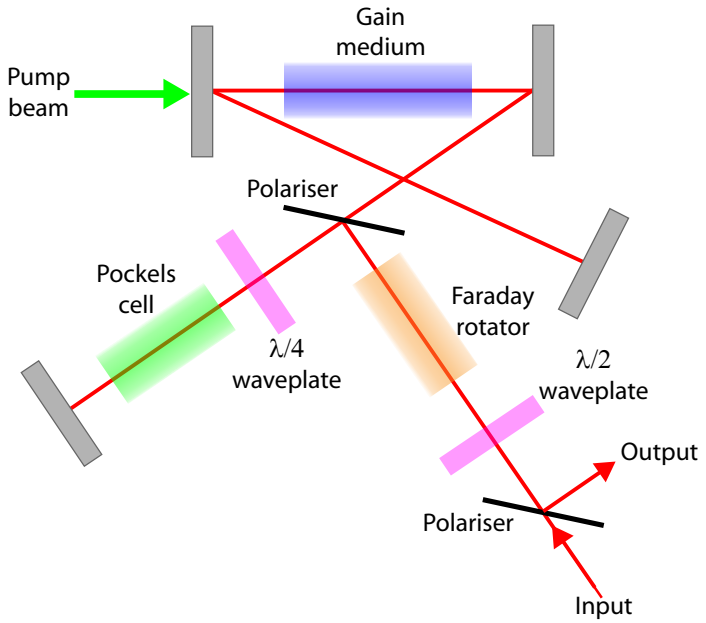

Figure 3.3: Schematic of the main components and arrangement of a basic regenerative amplifier, often employed in CPA based laser systems.

the pulse to the gain medium cavity for amplification. This process will continue until the desired number of passes through the gain medium has been achieved, at which point the Pockels cell again applies the $\lambda/4$ rotation to the pulse returning it to its original polarisation. The Faraday rotator then acts to change the polarisation to the condition of reflection from the first polariser allowing the pulse to leave in a direction separate from the input direction. As such, this system allows one to control the level of amplification in the system through a polarisation gating system.

The second commonly used amplification technique employed in a CPA based system is the multi-pass amplifier. A gain medium can achieve only a finite degree of amplification, therefore to get the most from it one can use a geometry based system to enable multiple passes though a gain medium. In this amplifier form the pulse is reflected by a series of mirrors, with each pass between mirrors resulting in propagation through an optically pumped gain medium. Instead of the polarisation based gating system used in a regenerative amplifier this system's pulse exiting mechanism is purely geometric. Figure 3.4 shows an illustration of this amplifier form, which is typically used in the final stages of energy enhancement in a CPA system. This is due to the fact the single pass gain can be set relatively high with respect to a regenerative amplifier as the beam passes through a minimal number of optics where B-integral could be an issue.

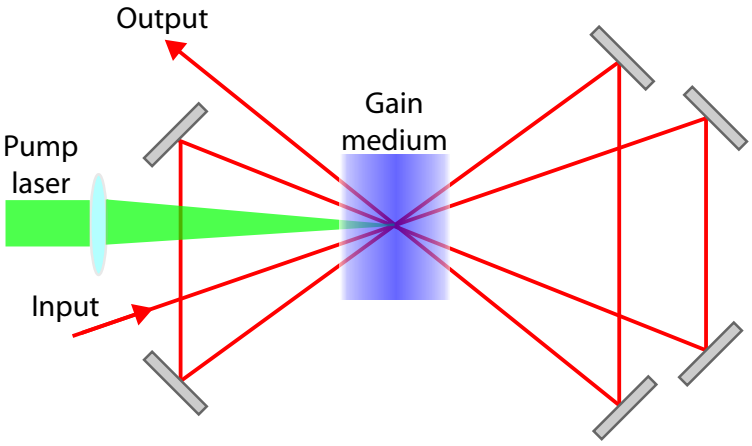

Figure 3.4: Schematic of the basic design of a multi-pass amplifier arrangement typically employed in a CPA based laser system.

3.2.3 Optical parametric amplification

The two commonly employed CPA pulse amplification techniques, presented in the previous section, result in the highest total gains in the system, however the nature of these amplification techniques (optical pumping of a gain medium) often results in less than ideal pulse temporal intensity profile (explored in detail in section 3.2.4). Thus other amplification forms must be considered to minimise this issue. One such technique is optical parametric amplification, typically used in the pre-amplification stages of CPA systems to amplify pules directly from the oscillator, from nJ to mJ level.

This amplification form utilises a crystal material with lack of inversion symmetry which exhibits a so-called 'χ^2 non-linearity', such as β-barium borate. The seed pulse, or signal pulse, propagates through the medium coincident with a higher energy pump pulse of shorter wavelength. Under correct phase matching conditions (achieved using the birefringence of the crystal), photons from the pump pulse, at frequency ω_p, are converted to the same frequency as the signal pulse, ω_s, and to a third component of 'idler photons' (ω_i), with the photon energy of the idler wave being the difference between the photon energies of the pump and signal waves. This is to say $\omega_p = \omega_s + \omega_i$ and is illustrated in Fig. 3.5.

The main reasons for using this complex configuration for amplification over more simplistic techniques are as follows. Firstly, the transfer of energy from pump to signal is highly efficient, with minimal losses to crystal heating. Consequently, the effect of

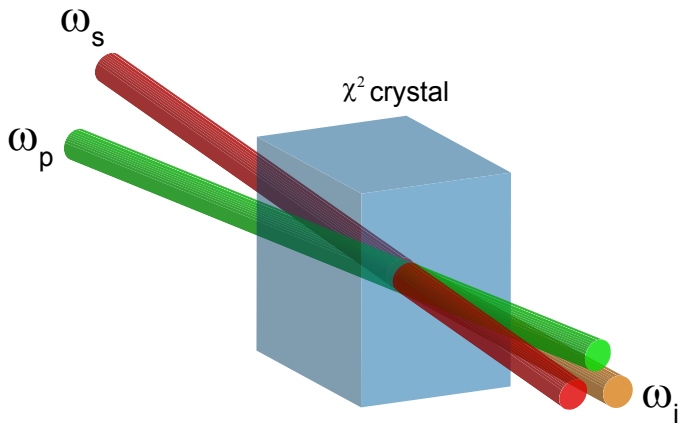

Figure 3.5: Schematic of the three wavelength components used in optical parametric amplification in a non-linear crystal.

thermal lensing caused by temperature gradients (and thus refractive index) across the amplifier medium is significantly reduced. Thermal lensing can cause considerable alterations to the pulse divergence when propagating through the laser chain, leading to possible damage to optics or off-sets in the final focal spot position. The second advantage OPA brings is pulses with a very large frequency/wavelength bandwidth can be amplified [136]. Consequently, the effect of gain narrowing is reduced [137], leading to more effective recompression after amplification. Moreover, and possibly the main advantage of OPA in this system being employed for laser-solid interaction studies, is its ability to produce pulses of relatively high intensity contrast, compared to solely CPA. This occurs as a result of the non-linear interaction within the crystal, leading to no generation of ASE (see section 3.2.4), as parametric conversion does not occur without the presence of the seed pulse, thus no spontaneous emission is present in the medium. However, there is an equivalent to ASE in OPA, known as amplified optical parametric fluorescence (AOPF), in which an OPA may emit light when there is no signal and idler photons present. In a semiclassical model, this may be attributed to vacuum fluctuations of the optical field which enters the input of the amplifier. Essentially a pump photon may spontaneously split into two lower frequency photons (equal to ω_s and ω_i) in the non-linear material. Unlike ASE, however it is limited in time to the duration of the pump pulse, not the excitation duration of the the gain material.

3.2.4 Laser pulse temporal intensity profile

To further aid in describing laser-solid interaction experimentation, it is highly beneficial to consider a realistic laser pulse, produced through the processes described previously. As mentioned throughout this thesis, peak intensity is a key factor in a laser-solid interaction due to the role it plays in defining the interaction properties. However, this is not the only intensity parameter to consider. One must also consider the pulse's temporal intensity profile, which in reality is more complex than the previously mentioned ideal Gaussian profile.

In addition to the 'main pulse', the slowly-varying Gaussian envelope (i.e. short duration, peak intensity), there is additionally a degree of lower intensity light which exists out-with this envelope, forming light preceding, and following, the main pulse, of longer duration (up to several nanoseconds). This is referred to as the pulse 'pedestal' and in terms of interacting with matter it can significantly alter the interaction dynamics. The pedestal is thus an extremely important aspect to have knowledge of. A useful parameter employed to quantify preceding light is the temporal intensity contrast. This is defined as the ratio of the pulse's peak intensity to the intensity of the pedestal, and varies depending where the pedestal is sampled temporally. As such, the contrast ratio of a pulse is typically quoted at two time-scales; (i) tens of picoseconds before the main pulse, and (ii) at nanoseconds before the main pulse. For example, one of the laser systems employed in this thesis, the PHELIX laser (see section 3.3.2), has a temporal intensity contrast on the nanosecond time-scale of 10^{10} and 10^{4} at 10 ps from the main pulse [138]. Note that for ultra-high intensity pulses ($\sim 10^{20}$ W/cm^2), explored in this thesis, the intensity of the pedestal is of a significant level. Improving contrast is consequently a major challenge in this intensity regime due to undesirable target heating prior to the main pulse. One approach employed to enhance contrast in this regime is explored in the next section (section 3.2.5).

The origins of pedestal light comes from numerous inherent imperfections in the laser chain, the most significant of which are now explored. Pedestal light can be split into three main categories, which aid in describing their origin. Figure 3.6 depicts a schematic of a pulse with each of these defects. The first category, amplified spontaneous emission (ASE) [139], results from atoms in the laser's numerous amplifier crystals being excited by the flash lamps (of hundreds of microsecond duration)

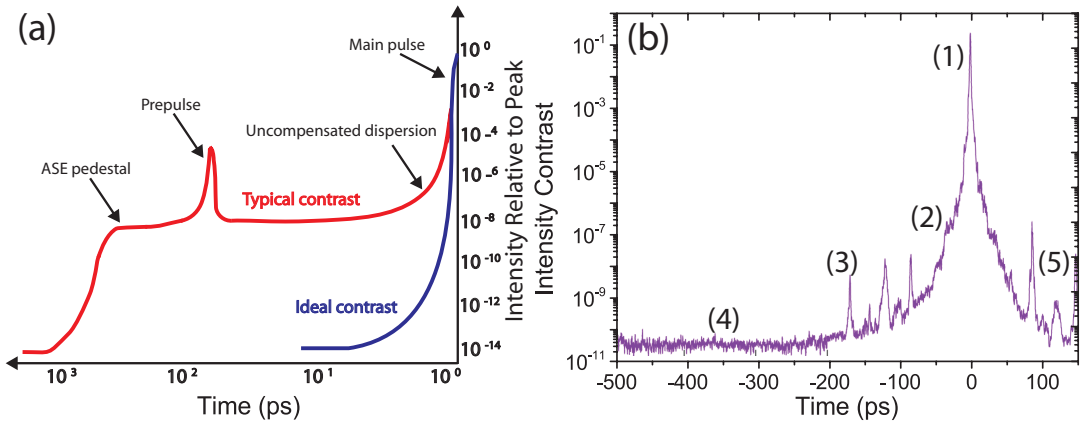

Figure 3.6: (a) Illustration depicting a simple realistic high intensity laser pulse created through CPA (propagating from right to left). The three main components which form preceding light are labelled. (b) Plot of the temporal intensity contrast (on the picoseconds timescale) for a real Vulcan PW pulse, with the main components labelled; (1) main pulse, (2) 'triangular' component due to light scattering from CPA gratings, (3) pre-pulses, (4) picosecond OPA amplifier contributions and (5) post-pulses.

or nanosecond pump lasers, then spontaneously decaying to a lower energy state after a certain lifetime, and emitting photons with a spectrum related to the line width of the decay transition, rather than emitting when stimulated by a coherent laser photon. As this is a random process in the amplification crystals, photons are emitted in all directions, though a significant percentage of this radiation is emitted at a small angle to the central propagation direction, thus can remain in the system and in turn be amplified by further amplification stages. The typical contrast level of ASE is between $\sim 10^6$–10^{10} and with a duration of a few nanoseconds, determined by the exit gating systems employed in the amplification stages, for example Pockels cells which, at best, gate on the nanosecond time-scale. After compression this leaves ASE able to act upon a target for a relatively long nanosecond duration before the arrival of the comparatively short main pulse. For example, a focused pulse of peak intensity 10^{20} W/cm^2 even with an ASE level 8 orders of magnitude lower than this (10^{12} W/cm^2) would still result in significant target ionisation and plasma expansion.

The second form that preceding light may take is that of uncompensated dispersion. This is situated on the rising edge of the main pulse (approximately tens of picoseconds in duration) and exists as a result of regions of the pulse which have not been optimally compressed by the final stage of the CPA process. This occurs due to imperfections and misalignments of the compressor gratings, or by other sources of dispersion or scattering [140].

Finally 'leakage' pulses may also be present, commonly referred to as pre-pulses.

These arise from internal reflections in the laser chain from any of the numerous optics and may be tens to hundreds of picoseconds before the main pulse, having a duration similar to the main pulse or longer, due to various material dispersion, and exhibit a wide range of contrast ratios. These can often be eliminated through the employment of wedged optics which send reflections along a different direction to the main pulse path. Like all forms of preceding light these can have a severe impact on a laser-solid interaction, such as destroying the target before the main pulse has arrived.

Often the inherent contrast level of a pulse cannot be enhanced easily through alterations to the laser system and thus *in situ* measures must be employed before the interaction. One technique employed is frequency doubling of the pulse. As the efficiency of this process is intensity dependent ($\propto I^2$) then only the highest intensity regions of the pulse are efficiently converted to second harmonic photons, while the lower intensity regions are not. As such, this acts as an intensity filtering technique. Another commonly employed contrast enhancement technique, which also acts as an intensity filter, is the 'plasma mirror' which is explored in the next section.

3.2.5 Plasma mirrors

To address concerns of employing pulses with low temporal intensity contrast (as explored in section 3.2.4), one can employ an optical tool known as a 'plasma mirror' (PM) [141, 142] to enhance this parameter by more than two orders of magnitude. This can completely change the nature of a laser-foil interaction. Focal intensities in excess of 10^{21} W/cm^2 are now becoming a reality at numerous laser facilities and thus a contrast level of $\geq 10^8$ is required to prevent significant pre-plasma formation during the interaction of the target with light preceding the main pulse, based on the fact intensities of $\sim 10^{13}$ W/cm^2 will ionise most materials. It is, however, demanding for a laser system based on the CPA process to achieve pulse contrasts higher than 10^6–10^7 and thus PMs can be employed, which can achieve a $\times 100$ contrast enhancement, and therefore move the interaction into the desired contrast regime.

Typically a PM is a planar dielectric glass slab, transparent to the laser wavelength, often including an anti-reflective (AR) coating, which reflects around 0.25% [143] of incident light. Moreover, the optic surface is also of 'optical quality'; this terms describes deviations in the surface away from a perfectly smooth figure, and is often quoted in

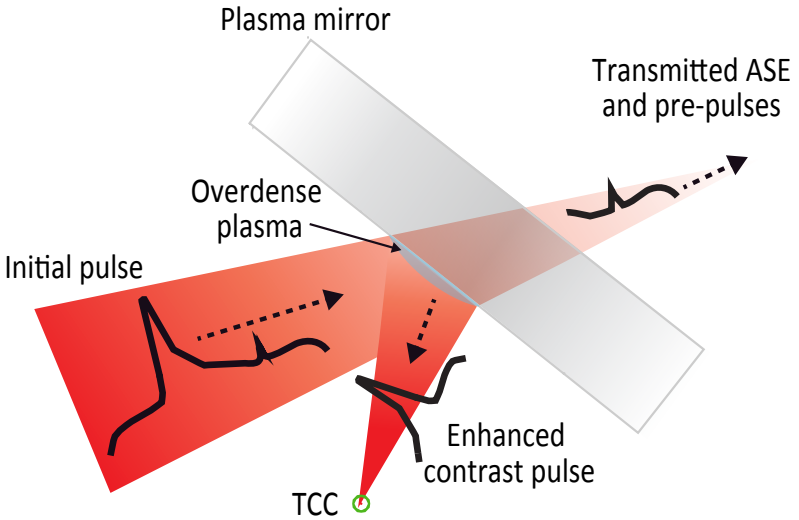

Figure 3.7: Basic principle of operation of a planar plasma mirror used to enhance the temporal intensity contrast of a high intensity laser pulse.

terms of the size of these irregularities as a function of the laser wavelength. When preservation of the input wavefront geometry is crucial $>\lambda_L/8$ irregularity is desired to prevent aberrations and degradation of the system's optical performance. Figure 3.7 depicts the principle of operation of the PM concept, where a focusing laser pulse is intercepted by the PM, positioned in the beam path such that light which is below the ionisation threshold of the PM substrate, $\sim 10^{12}$ W/cm^2, is transmitted through the optic due to its transparent nature in the non-plasma regime, with minimal reflection. Transmission may be maximised by setting the angle of incidence between the optic and pulse equal to the Brewster's angle for the optic material. As the intensity profile of the pulse increases, however, ionisation will occur temporally at some point on the steep rising edge of the main pulse (situated in the region a few picoseconds prior to the peak), rapidly forming a layer of overdense plasma which acts to reflect the remainder of the pulse (as presented in section 2.5.3). Through this intensity filtering the pulse is 'cleaned' by splitting it into two components as the optic switches from highly transparent to highly reflective on the sub-picosecond timescale. This fast switch-on time reduces the possibility of instability growth which could otherwise affect the reflected beam quality. The result is that only the reflected part, now separated from the lower intensity preceding light (and thus with enhanced contrast) interacts with a target.

The contrast enhancement achieved with a PM does, however, come at a cost, this being a reduction in laser energy delivered to the target. This consequently lead to a

reduction in interaction intensity, typically in the region of 15–30% per plasma mirror. This arises as the reflection from a PM is less than unity, which can be attributed to numerous reasons. For example, some laser energy will transferred to the plasma electrons, (as described in section 2.5.4). As explored, laser absorption in dense plasma is dependent on such parameters as laser polarisation and the angle of incidence to the target. Consequently the percentage of energy reflected from a PM is dependent on these. Additionally, the reflectivity of a PM exhibits an intensity dependency, with high specular reflectivity occurring in the intensity range of 10^{15}–10^{16} W/cm^2, as shown experimentally in [144] and [145].

For optimal PM operation, in terms of maintaining a high quality focal spot after reflection, it should ideally show no degradation after reflection from the plasma. For this to occur it is highly important that ionisation, and reflection, occurs only a few ps before the main pulse, key in reducing wavefront degradations during reflection, arising from propagation through expanding plasma. In Dromey *et al.* [144] it was found that minimal wavefront distortion of a reflected pulse, that is when the pulse will experience high specular reflectivity, is achieved when the overdense plasma surface has almost the identical waveform as the original optical quality dielectric slab, essential remaining optically 'flat'. A condition for this to occur is estimated by the inequality $c_s \Delta t < \lambda_L$; where c_s is the ion sound speed, and Δt is the time from plasma formation to the peak of the main pulse. Conversely, if this condition is violated, diffuse reflectivity will occur, reducing the quality of the reflected beam. The upper limit of Δt can be estimated using the inequality, with a typical value of $c_s = 3 \times 10^7$ cm/s and $\lambda_L = 1$ μm, to give a value of $\sim$3.5 ps. Thus, several picoseconds after plasma formation significant distortion of the reflected wavefronts would be expected. Moreover, wavefront distortions may also arise due to inherent modulations present in the spatial-intensity profile of the laser. These seed inhomogeneous plasma expansion, leading to ionisation occurring at different times across the optic, and thus the formation of a diffusely reflective surface.

PMs have proven to be valuable tools for suppressing pre-pulses and ASE [146, 147], and as such have validated several characterisation studies [145, 148, 149]. These investigations have not only verified the contrast enhancing ability of this optic type, but have quantified the quality of the focal spot formed after reflection and the ability for the optic to also act as a spatial filter, vital for a clean, and high intensity laser-foil interaction.

3.2.6 The focal spot

Another key aspect of a laser-plasma experiment to have knowledge of is the focus of the laser pulse, often referred to as the 'focal spot'. This is typically imaged and optimised before every target shot (at low power), during the target alignment process, highlighting its importance in the interaction. Importantly, knowledge of the focal spot size and quality are key to calculating the peak intensity achieved in the interaction, and thus understanding the underpinning physics.

The term 'best focus' is employed to refer to the smallest and highest quality focal spot achievable, and thus maximum intensity, with a particular beam configuration. The quality of the laser focal spot is not only dependent on the pulse wavefront profile but additionally on the particular focusing optic employed, and whether it is suitably optimised. Focusing is typically achieved through the use of an off-axis parabolic (OAP) mirror; Fig. 3.8 displays photographs of the OAPs employed on the two laser systems used in this thesis. Parabolic geometry is advantageous as it reflects rays parallel to the optical axis to a single point, i.e. the focus. Off-axis operation is beneficial as on-axis results in the focus being located inside the incoming collimated beam and thus target and diagnostics placement would block a significant percentage of the input beam. The process of aligning an OAP involves fine adjustments of the optic's roll and tilt axes to form the best achievable focal spot distribution, ideally free of any astigmatism.

To characterise the focal spot formed by the focusing optic two parameters are often used; first its size (ϕ_0) and second its encircled energy (EE). The definition of the spot size arises from the distribution the focal spot forms. Typical laser systems contain circular apertures throughout the system, which in passing through the beam will experience Fraunhofer diffraction (in the nearfield i.e. far from focus) resulting in the well known 'airy disk' spatial profile at the laser focus. Using the central Gaussian part of this distribution it is possible to define the size of the focus by the spot waist (ω_0) parameter, defined as the radius at which the intensity falls to $1/e^2$ (13.5%) of its peak value. A spot of this form is often referred to as diffraction limited, having an encircled energy of 86% (in the waist area), estimated using;

$$2\omega_0 = 1.03\lambda_L f/D \tag{3.5}$$

where $2\omega_0$ is the spot diameter, f is the focal length of the optic, and D is the limiting

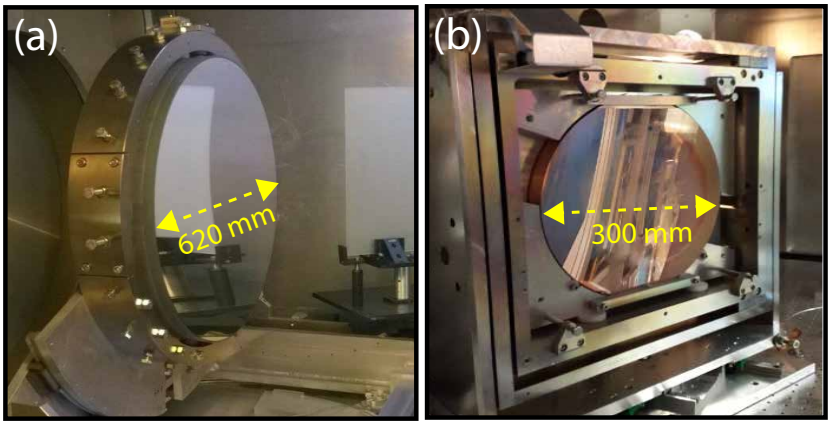

Figure 3.8: Photographs of the OAPs used for pulse focusing on (a) the Vulcan-PW and (b) PHELIX laser systems employed in this thesis.

aperture size, i.e. the diameter of the beam incident on the focusing optic. More often, however, the spot waist is not employed to characterise the size, and instead the diameter of the Gaussian profile at the FWHM (ϕ_0) is employed. This will be used to define the size of laser focus throughout this thesis. Each of these quantities is depicted in Fig. 3.9.

A dimensionless quantity often used to characterise a focusing optic in terms of the minimum spot size it can achieve, is the F-number (F/#) (sometimes called f-stop, a common term employed in photography). This is defined as the ratio of the optic's focal length to the diameter of the entrance pupil, which in the case of an OAP is the collimated beam diameter incident on the optic. This is seen in Eq. 3.5 to be one of the factors (along with the λ_L) that spot size is dependent upon.

The second commonly employed focal spot characterisation parameter, used through this thesis, is encircled energy. This is used to give a measure of the spot's spatial energy content, and thus quality. In its simplest form this is the measurement of the amount of light inside a small area (often that contained within an area with diameter equal to ϕ_0 centred on the peak intensity point) compared to the entire focal spot area. It can be easily calculated using an image of the focal spot, from the ratio of the integrated pixel counts contained within the FWHM area to the integrated counts of the entire spot. For a realistic experimental focal spot, which is optimised in terms of OAP movements, this value is typically around 10–35%. Practically speaking, the higher the encircled energy, then the higher the quality of focal spot. Figure 3.10 shows comparison of two focal spots obtained from the same high-power system, but having significantly different encircled energy values due to varying spot qualities. In the case

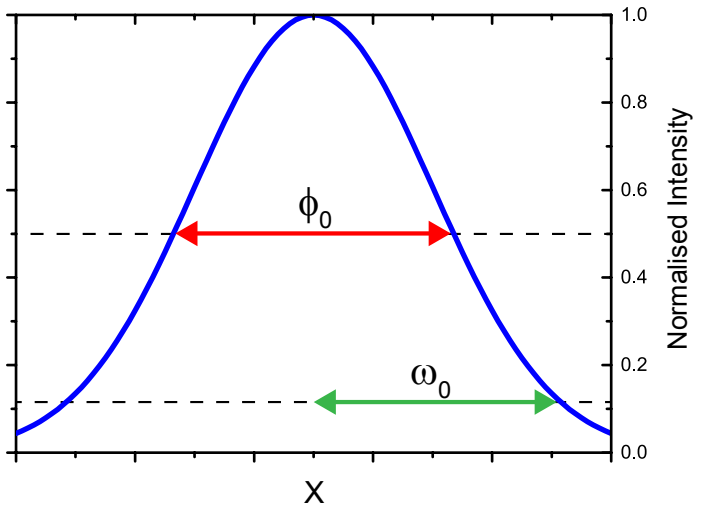

Figure 3.9: Gaussian distribution depicting two common parameters used to characterise its spatial extent (in x); where the red line is the Gaussian FWHM size, ϕ_0, and the green is the Gaussian mode waist size, ω_0.

of Fig. 3.10(b), degradation of the focal spot occurred due to thermally induced aberrations in the pulse wavefront after a period of multiple full power laser shots. This highlights the importance of characterising the focal spot before every laser shot.

Characterisation of the focal spot on full energy shots is difficult due to its high intensity nature, thus it is typically achieved before the shot through direct imaging of a lower energy equivalent (often in continuous wave or high repetition rate operation). This measurement typically involves an infinity-corrected microscope objective (×20–×50 magnification) used to image the spot on to a 16-bit CCD camera. This enables one to quantify the size and quality of the spot, and hence calculate the peak interaction intensity.

Another important focusing parameter to consider is the Rayleigh length, z_r; where $z_r = 2\pi\omega_0/\lambda_L$. This describes the distance along the propagation axis from the spot waist position to the where the size has increased by a factor of $\sqrt{2}$ for a focusing Gaussian beam, i.e. where the intensity drops to half its magnitude at the spot waist (the peak intensity location). This parameter is important as it gives an upper limit on the accuracy required for target placement at the focus of the laser. If target placement is off longitudinally by more than a Rayleigh length, then the intensity on target will be reduced by more than a factor of two.

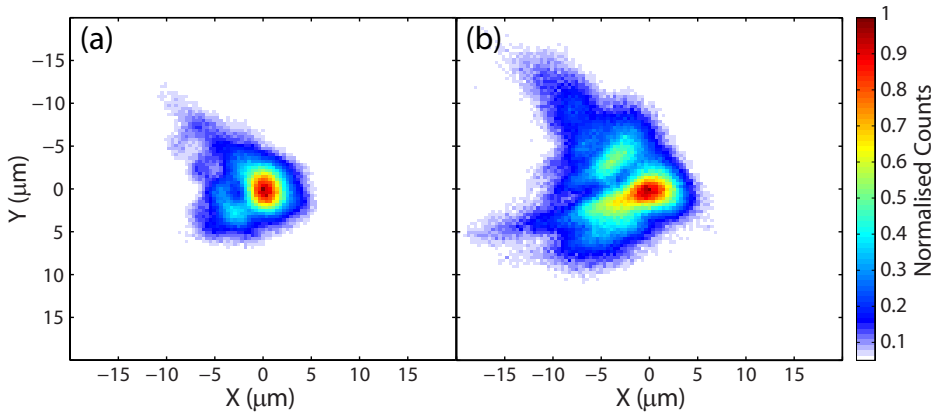

Figure 3.10: Comparison of the spatial intensity distributions of two focal spots obtained from the same laser system with (a) of relatively higher encircled energy, 19%, in comparison to (b) 11%.

3.3 High power laser facilities

As seen throughout this thesis the laser pulse characteristics are as important to the interaction outcomes as the resultant plasma dynamics. It is therefore beneficial to have an understanding of the operation of the high power laser facilities which provide these pulses, employed in the investigations of this thesis. Many high power laser systems exist around the world, based in large scale research facilities and universities, capable of generating short, high intensity pulses exceeding 10^{18} W/cm^2. Each have varying parameters and unique capabilities, thus selection of an appropriate system comes down to the physics one wishes to explore.

Two laser systems were employed in the investigations presented in chapters 4–6. These are the Vulcan-PW and PHELIX laser systems, both of which are classified as Petawatt level. The focus of this section is to give a brief description of these lasers.

3.3.1 Vulcan-PW

The Vulcan laser system is a Nd:glass based system consisting of 8 primary beam lines which provides pulses to two target areas; Target Area West (TAW) and Target Area Petawatt (TAP). Results presented in chapters 4 and 5 were obtained from experimental campaigns conducted using the Petawatt arm of the Vulcan laser. This section provides a basic description of this system and its working parameters. An overview illustration of this facility is presented in Fig. 3.11.

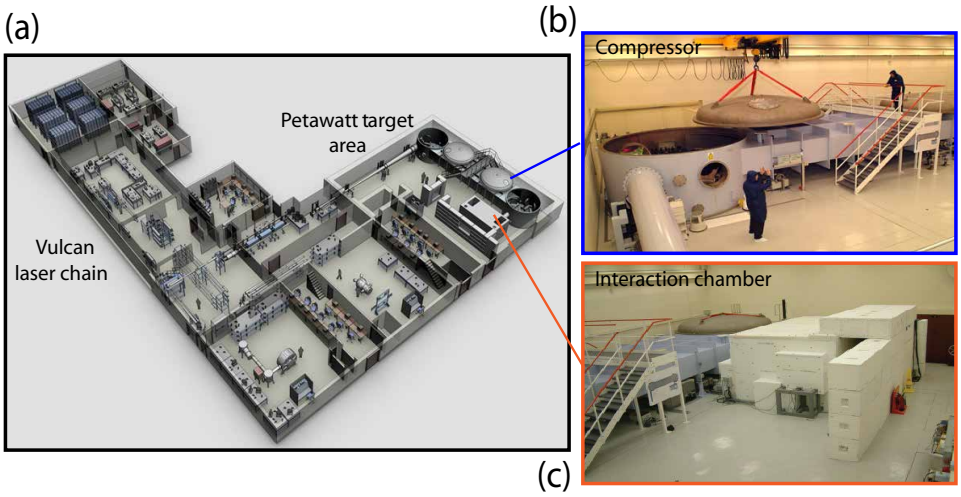

Figure 3.11: Overview of the Vulcan laser facility (a), highlighting the Petawatt target area. (b) Photograph of one end of the compressor chamber of TAP and (c) photograph of TAP interaction chamber and its radiation shielding.

This laser, located at the Central Laser Facility (CLF) in the Rutherford Appleton Laboratories, was one of the first of a generation nominally capable of generating pulsed optical power up to the Petawatt (10^{15} W) level, based on the CPA process. The pulse parameters this laser delivers are summarised in Tab. 3.1. TAP employs two of the 8 primary Vulcan beams, one of relatively long pulse length (∼6 ns), and the other a short duration primary beam line, capable of delivering pulses of 500 J in a duration of 500 fs; this is the only Vulcan beam line considered in this thesis.

Pulses originate from a mode locked oscillator based on a commercially available Ti:Sapphire gain medium oscillator pumped by a CW frequency double Nd:YAG laser. Ti:Sapphire is a common oscillator material due to the broad range of lasing frequencies it supports (600-1100 nm) . The output from this passively mode locked oscillator is a train of pulses of duration 120 fs (FWHM), at a central wavelength of 1053 nm (with a 15 nm bandwidth) and an energy of 5 nJ at a repetition rate of 80 MHz. The pulse length is limited to 120 fs, due to the central wavelength being shifted to ∼1050 nm to match later amplification stages.

The next stage in the process is the gating out of one of these pulses to seed the system's amplification sections. The first stage is pre-amplification, based on OPA [150] (see section 3.2.3). This amplification technique involves the seed pulse being propagated through a non-linear medium being pumped by a higher frequency, and energy, pulse from a commercially available Q-switched Nd:YAG laser frequency doubled to

Laser Parameters	Typical Value
Energy before compressor E_{L_0}	300
Energy on target E_L	150
Focal spot size (F/3.1 Focusing) ϕ_0	4 μm (FWHM)
Pulse duration τ_p	1 ps (FWHM)
Central wavelength λ_L	1.053 μm
Optical polarisation	p
Peak intensity I_L	$\sim 7 \times 10^{20}$ W/cm^2

Table 3.1: Table summarising the Vulcan-PW system's laser parameters, used in the investigations presented in this thesis.

543 nm, providing 1 J, 15 ns pulses. A Pockel cell is used to select the central 3 ns from the 15 ns temporally Gaussian profile pump pulse, thus providing an approximately flat-top intensity profile for the OPA process. The combination of the input and pump pulses in the non-linear medium, based on a β-Barium Borate crystal, results in the generation of a third frequency pulse, commonly referred to as the idler, and a net energy exchange from the pump to both signal and idler.

Before the next stages of amplification the pulse is first stretched. The Vulcan-PW stretcher is of the so-called 'Offner triplet' configuration [151], consisting of two highly reflective diffraction holographic gratings and concentric concave and convex mirrors to chirp the pulse. This configuration was selected to obtain a linear chirp over the maximum bandwidth to optimise stretching and, additionally to reduce spectral aberrations, as much as possible, which would otherwise affect stages further along in the system; for example pulse recompression. The effect of the stretcher on the oscillator pulse is to increase its temporal length from 120 fs to 4.8 ns, making it sufficiently less powerful and far enough below the damage threshold such that it can move onto the systems amplifiers. The main Vulcan-PW amplification stages consist of a series of rod, then disk amplifiers. The rod amplifiers consist of neodymium doped phosphate glan rods (forming the gain medium), optically pumped by white light flash lamps. As the pulse propagates to successive amplifiers its diameter is gradually increased (from 9 mm to 208 mm at the end of amplification stage), to avoid damaging amplifier optics. The resulting pulse energy at the end of the rod amplifiers is ∼85 J. The final stage of amplification in the system consists of large 208 mm diameter disk amplifiers, which increase the pulse energy to ∼650 J. The pulse is then propagated through a 19 m long vacuum spatial filter to remove high frequency spatial noise from the pulse wings,

enhancing its spatial profile, and enlarging the beam diameter to its final 600 mm size.

Finally, the pulse is re-compressed from 4.8 ns to ∼500–700 fs, using the compressor (shown in Fig. 3.11(b)), which consists of two 940 mm diameter diffraction gratings, with 1480 lines/mm separated by 13 m, with the opposite sign dispersion to those used in pulse stretching.

To further improve compression and the spatial quality of a pulse (and subsequently the focal spot quality) an adaptive optic (AO) module is employed, in conjunction with a Shack-Hartmann wavefront sensor (see section 3.4.2) to monitor wavefront distortions present in the beam introduced from propagation through the laser chain. Measurements from the wavefront sensor are sent to the AO so wavefront distortions away from an ideal flat wavefront can be corrected. It achieves this through 64 piezoelectrically controlled actuators in a 2D array manipulating a 120 mm diameter deformable mirror. Employment of this system can improve pulse focusability by more than a factor of 2, accordingly increasing intensity by ×4; thus an AO system is a vital part of a high-power laser system.

Once inside the target chamber a turning mirror directs the pulse onto a conventional OAP F/3.1 (f= 1860 mm) focusing mirror (Fig. 3.8(a)), of diameter of 620 mm. The typical best focus spot formed by this optic is of size $\phi_0 \approx 4$ μm (FWHM) and encircled energy of ∼28%. This, in conjunction with a compressor throughput of between ∼50–60% (monitored on each experiment), yields an on-target peak intensity in the region of 10^{19}–10^{20} W/cm^2.

Pulse characterisation is achieved on this system through a sample of the pulse formed by a leakage taken from a turning mirror located inside the compressor, which seeds numerous diagnostics. These include pulse length characterisation employing a second order autocorrelator [152], and an additional wavefront sensor to record the wavefront quality of the pulse prior to focusing (covered in more detail in section 3.4.2). A calorimeter situated in this diagnostic area enables an accurate measurement of the pulse energy pre-compressor.

In terms of temporal intensity contrast (discussed in section 3.2.4), of the Vulcan-PW system, it has been measured to be $\sim 10^8$ on the ns-scale prior to the main pulse. This still results in the pre-ionisation/deformation of the target prior to the arrival of the main pulse. Therefore, it is typical to operate with the addition of a plasma mirror (see section 3.2.5) on this system, to enhance the pulse contrast, up to $\sim 10^{10}$.

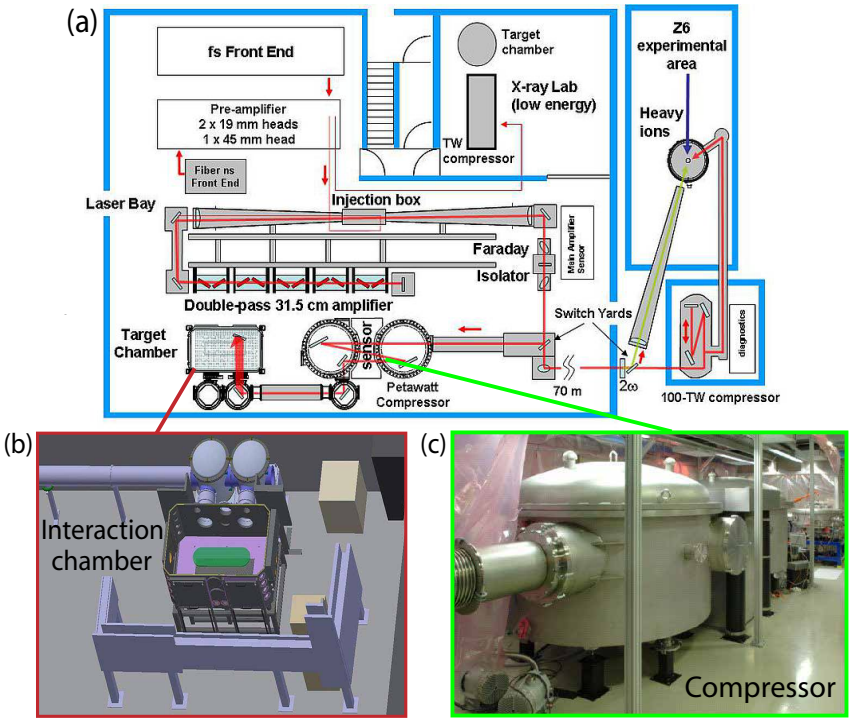

Figure 3.12: Overview of the PHELIX laser facility, with (a) a schematic diagram of the laser system and target area, indicating the position of (b) the interaction chamber, and (c) the pulse compressor.

3.3.2 PHELIX

The second laser system employed to obtain results presented in this thesis (in particular chapter 6) is the Petawatt High Energy Laser for heavy Ion eXperiments, or PHELIX, system based at the Gesellschaft für Schwerionenforschung, GSI, facility near Darmstadt, Germany. A simple schematic layout of this system and its interaction chamber is found in Fig. 3.12. The general parameters this system delivers, of interest to an experimentalist, are summarised in Tab. 3.2.

Similar to the Vulcan-PW laser, this is also a Nd:Glass based system, operating at a central wavelength of 1053 nm, based on the CPA technique. The formation of an intense pulse at PHELIX begins with an oscillator (a commercially available *Coherent Mira* device) generating 100 fs, 4 nJ pulses. A selected pulse is then either stretched to a duration of 2.4 ns, or first passed through the optional ultra-fast optical parametric amplifier (uOPA) [153] module before nanosecond time-scale stretching. Employment of the uOPA allows for enhanced and tunable temporal intensity contrast, from 10^7–10^{10} at 100 ps.

After stretching the pulse is then amplified through the combination of a pair of

Laser Parameters	Typical Value
Energy before compressor E_{L_0}	180 J
Energy on target E_L	140 J
Focal spot size (F/1.5 Focusing) ϕ_0	4 μm (FWHM)
Pulse duration τ_p	700 fs (FWHM)
Central wavelength λ_L	1.053 μm
Optical polarisation	s
Peak intensity I_L	$\sim 3 \times 10^{20}$ W/cm^2

Table 3.2: Table summarising the PHELIX system's laser parameters, relevant to the investigations presented in this thesis.

titanium doped regenerative amplifiers. This increases pulse energy to 30 mJ. The pulse is then further amplified by a series of pre-amplifiers, leading to a pulse energy near 5 J. At this stage any major wavefront aberrations present, resulting from the previous stages, in the pulse are corrected through the use of a deformable mirror coupled with a Shack-Hartmann wavefront sensor (see section 3.4.2).

To avoid the damage threshold of preceding optics the pulses are spatially expanded to 70 mm in diameter after the pre-amplification stage. After this it then passes to the main amplification stage consisting of five double pass flash lamp pumped Nd:glass cassettes which can amplify the pulse up to a maximum energy of 250 J; though this is typically limited to around ∼180 J. After amplification the pulse then moves to the compressor (pictured in Fig. 3.12(c)) where its duration is reduced to its gain narrowed bandwidth limit of ∼600 fs.

An F/1.5 copper coated OAP with a 300 mm diameter (Fig. 3.8(b)) is employed to focus pulses. This results in a minimal best focal spot size of ∼4 μm (FWHM) with an encircled energy up to ∼20%; achieving a peak intensity of the order 10^{20} W/cm^2.

3.4 Laser-solid experimentation: Diagnostic techniques

This section will discuss the diagnostic techniques employed in this thesis to characterise laser-solid interactions. Techniques can be broadly categorised into one of three groups, these being; (i) particle (such as electrons and ions) imaging and spectroscopy, (ii) photon (such as x-rays) imaging and spectroscopy and, finally, (iii) optical diagnostics. The diagnostic techniques employed in this thesis fall into the particle imag-

ing/spectroscopy and optical diagnostics categories. Each of these enable insight into the interaction dynamics, and will be presented in detail in this section.

3.4.1 Energetic particle diagnostics

The characterisation of the energetic particles generated in a laser-plasma interaction is fundamental to this research area, with numerous techniques being developed in recent years to measure the spatial and spectral information contained within this emission.

The first two results chapters (chapters 4 and 5), in some aspect, deal with the characterisation of the energetic proton beams generated in these interactions. To extract spatial and spectral information from these beams the method of radiochromic film spectroscopy is used; which is described in the coming section. The final results chapter (chapter 6) involves the detection of fast electrons escaping the interaction target. To make such a measurement, a widely used detector known as image plate is employed; covered in detail later in this section.

Radiochromic film spectroscopy

Two key parameters fundamental to characterising a beam of protons generated during a laser-foil interaction are its spatial and spectral properties, such as those described in section 2.7.1 for ion beams resulting from the TNSA mechanism. A number of techniques can be employed to measure the spatial-intensity profile and energy spectrum of emitted proton beams, such as copper activation [154], contact radiography [155], or the use of a Thomson parabola spectrometer [156]. The main proton energy and spatial-intensity profile technique employed in this thesis (in chapters 4 and 5) is Radiochromic film (RCF) spectroscopy. Details on other commonly used ion beam characterisation diagnostics are summarised in a review article by Roth [157].

When an ion interacts with a material it deposits energy, with a stopping power proportional to the square of its charge and inversely proportional to its energy. Generally as the ion's velocity is reduced when traversing the material its stopping power increases. The result of this is increased energy deposition the further the ion propagates in the material, leading to the characteristic Bragg peak in which the ion deposits the majority of its energy, shortly before the energy sharply falls to zero.

Taking advantage of this energy deposition behaviour, to characterise features of laser-driven proton beams, is the commonly employed proton imaging and spectral

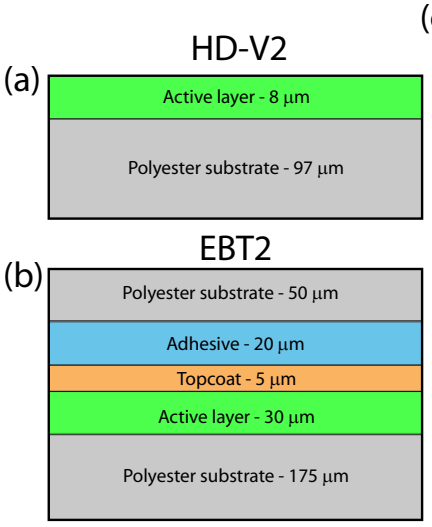

(c)

Material	Purpose	Thickness (μm)	Stopping Energy (MeV)
PTFE	Filter	115	–
Al Foil	Filter	13	–
HD-V2	Detector	105	2.7
HD-V2	Detector	105	4.1
Mylar	Filter	100	–
HD-V2	Detector	105	6.2
Mylar	Filter	200	–
HD-V2	Detector	105	9.2
Mylar	Filter	300	–
HD-V2	Detector	105	12.1
Copper	Filter	250	–
EBT2	Detector	285	17.9
Copper	Filter	500	–
EBT2	Detector	285	24.4

Figure 3.13: Composition of the two RCF types employed in this thesis; (a) HD-V2 and (b) EBT2. (c) Design of a typical RCF stack employed on laser-foil interaction experiments.

characterisation technique known as Radiochromic film (RCF) spectroscopy. This technique involves the use of layers of proton sensitive film in a stack configuration, often separated by filters; a configuration commonly referred to as an 'RCF stack'. This diagnostic has become a standard for proton beam characterisation in laser-driven research due to preferential sensitivity to protons, and its ease of use and reliable nature. Additionally, the fact that information can be retrieved relatively quickly (as no chemical based development is required) makes it a desirable diagnostic.

RCF itself is a dosimetry film, composed of layers of plastics and an organic, self-developing dye which alters in optical density (OD) with deposited dose, defined by Eq. 3.6, when irradiated by ionising radiation, such as protons, electrons or x-rays.

$$OD = -\log_{10}\left(\frac{I}{I_{BD}}\right) \tag{3.6}$$

Here, I is the intensity of a given pixel and I_{BD} is the maximum possible pixel value for an image of certain bit depth (i.e. 65535 for a 16-bit image). This value, I, is key as it is directly correlated to the incident radiation flux, where a higher OD of the dye colour (darker areas on the film) represents a higher deposited dose. This aspect of the film therefore enables the number of protons in the beam to be estimated. Various types of RCF are commercially available, each differing in composition, displaying varying sensitivities to different radiation flux ranges. For the measurements presented

in this thesis, the two forms of RCF employed are HD-V2 and EBT2 (manufactured by Vertec); the composition of each is displayed in Fig. 3.13(a)-(b). Both contain the same imaging layer, i.e. the organic dye, however the composition of filtering and thickness of the imaging layer is different. The RCF form EBT2 has a relatively thicker active layer with respect to HD-V2, resulting in it being comparatively more sensitive to protons, due to a higher deposited dose as protons traverse this region. Accordingly EBT2 is usually situated relatively 'deep' in a stack configuration for the detection of the higher energy and lower flux end of the proton spectrum. Both types of RCF have been implemented and characterised on numerous laser-solid interaction experiments. Figure 3.14(a) displays example data for a typical proton beam produced by a laser-foil interaction imaged at various energy levels employing RCF spectroscopy.

The stacked nature of the diagnostic is required to measure the spatial-intensity profile of accelerated protons as a function of proton energy, accomplished by the way protons deposit their energy in matter. A typical RCF stack design is presented in Fig. 3.13(c). As previously described, they deposit almost all of their energy at the end of their propagation depth, commonly referred to as the Bragg peak. The depth of the Bragg peak is dependent on the proton's energy; with lower energy protons being stopped earlier in the stack, whereas more energetic protons propagate deeper. Thus with careful stack design, taking into account the stopping of various proton energies, one can effectively image the proton beam at various RCF levels, each corresponding to a narrow range of proton energies contributing the majority of dose on that layer. The energy of a certain layer is taken as the energy associated with the central Bragg peak for that layer. This allows for the effective reconstructing of the emitted proton spectrum, described later in this section.

In terms of the stack filtering design, the front most layer is typically a thin layer of aluminium (Al) foil ($\sim$10 μm), required to prevent heavier ions depositing energy in the RCF layers. As such the RCF stack is preferentially sensitive to protons; confirmed experimentally in Borghesi *et al.* [158] by placing a layer of CR39 (a detector of single ions which can distinguish between species) within a stack. Furthermore, this foil layer helps to prevent optical damage of the front most RCF layers from laser light which may be transmitted through the interaction target. The energy resolution which can be achieved with such a device depends on the filtering selected between RCF layers. Depending on the desired energy steps, filters such as Mylar ($C_{10}H_8O_4$)

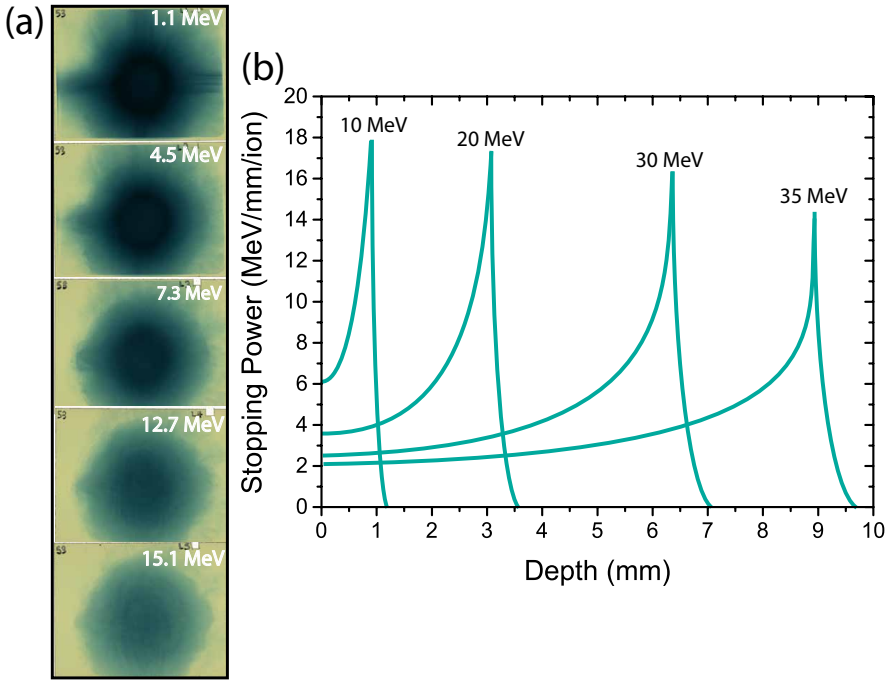

Figure 3.14: (a) Typical results of RCF film exposed to a laser-driven proton beam, imaging at various proton energies (as indicated). (b) Stopping range for various energy protons (as indicated) in a Mylar filter; calculated using SRIM software.

(which has a similar stopping power to RCF), copper (Cu) (high stopping power and can be activated by protons), and iron (Fe) (high stopping power, but less prone to activation) are commonly employed to enable a range of energies to be resolved, due to the modification of the stopping profile throughout the stack. That being said, the highest energy resolution possible with a stack is one composed entirely of RCF, as every layer is a detector, with resolution typically around 1 MeV due to the inherent thickness of a piece of film acting as a filter. To design an RCF stack, proton stopping curves are calculated using the *Stopping and Range of Ions in Matter* (SRIM) software [159], to calculate stopping range tables for the stack composition. Example stopping curves for various energy protons in Mylar are shown in Fig. 3.14(b). When copper filters are employed in the stack an additional measure of the proton energy spectrum can be obtained by exploiting the nuclear activation of copper due to irradiating protons. In ^{63}Cu a (p,n) reaction forms ^{63}Zn, which is unstable, and consequently emits positrons with a 38.47 minute half-life. Measuring the degree of activation of various layers of Cu throughout a stack allows a spatially integrated proton spectrum to be obtained, as demonstrated in McKenna *et al.* [160], using purely Cu stacks. Furthermore, it is possible through Cu activation to measure the spatial intensity profile of the proton

beam, similarly to RCF, through contact radiography with image plate (see section 3.4.1), demonstrated in Clarke *et al.* [155].

In terms of stack implementation in an experimental set-up, it is typically mounted approximately 30–70 mm behind the interaction, to capture the entire proton beam emitted from the target rear. Transversely, the RCF stack can be positioned either in-line with the target normal axis, or along the laser axis to decconvolve the direction of the proton beam. In most cases, however, the stack is close enough to the interaction that both components can be detected on the same film layer.

To extract the deposited proton dose, the exposed film is first digitised using a high-resolution optical flat-bed scanner (Nikon CoolScan3000), in transmission, with a spatial resolution of >600 pixels/inch. This ensures the high resolution nature of the film is reproduced in the output image. The scanner consists of an array of light emitting diodes, at three wavelengths of 643 nm, 532 nm and 474 nm, and a 16-bit colour CCD to measure the transmission intensity of each wavelength through the RCF. Three colour channels are required as each has a different response at various proton dose ranges. For example the 643 nm channel responds with a large change in optical density at low protons doses, but exhibits a near flat response at doses exceeding a few hundred Gray. Thus this channel is used for extracting RCF information with relatively low doses present. Conversely the 474 nm channel shows little optical density change until the dose exceeds a few hundreds of Gray, but displays a monotonic response to tens of thousands of Gray, thus making this wavelength channel ideal for extracting relatively high doses.

In order to convert the optical density of each pixel in the image to proton dose, a calibration of the number of protons to OD for each RCF type is required. This was achieved by employing a conventional proton accelerator at the University of Birmingham (MC40 cyclotron) to deposit a well-characterised current of energetic protons onto sample pieces of RCF.

Once the RCF data is digitised and the conversion from optical density to proton dose has been performed, the energy spectrum of the proton beam can be reconstructed by determining the number of protons, N_p, detected on each RCF layer, each with a central Bragg peak energy of E_{Bp}. As such, the magnitude of N_p is proportional to the total energy deposited within each layer, E_T, of thickness d_l and density ρ_l. This can be calculated by summing up the measured dose, D, and area, A, for each pixel, i, of

the image;

$$E_T = d_l \rho_l \sum_{i=1}^{N} (D_i A_i) \tag{3.7}$$

$$N_p = \frac{E_T}{E_{Bp} dE} \tag{3.8}$$

where, dE, is the difference in energy between protons stopped at either side of the RCF layer.

RCF spectroscopy not only allows for characterisation of the proton beam energy spectrum and spatial-intensity profile, but additionally the determination of two important parameters linked to these; (i) the beam divergence, and (ii) the laser-to-proton conversion efficiency (as discussed in section 2.7.1). The proton beam divergence is commonly quoted as the beam cone half-angle, θ_D, which is calculated using the trigonometric function $\theta_D = \tan^{-1}(r_D/z)$; where r_D is the radius of the proton beam circle (or an approximated quantity) produced on the RCF layer, and z the distance from target to RCF layer being analysed. The laser-to-proton conversion efficiency is calculated using the obtained proton spectrum. From this the total energy contained within the spectrum can be calculated (knowing the number of protons at each energy level), and taking this value as a percentage of the laser energy incident on-target, thus giving a measure of the laser energy converted into energetic protons.

Image plate

Image plate (IP) was employed to detect and record the emission of energetic electrons (employed in chapter 6). IP is most commonly used for the detection of x-rays in medical and biological imaging applications [161]. However, this detector type is also used as a particle detector, due to it displaying sensitivity to all forms of ionising radiation, including protons, x-rays and, importantly for this work, electrons. Additionally it displays extremely high sensitivity, a linear response over a large dynamic range and high spatial resolution. It has become a standard detector in numerous diagnostics and has been employed in many laser-plasma experimental investigations and characterisation studies [162, 163, 164].

IP is a proprietary ionising radiation detector film produced by FujiFilm, which consists of a luminescent phosphor layer (formed from $BaF(Br_{0.85}I_{0.15}):Eu^{2+}$) supported by a steel layer. Some forms of IP also include a protective Mylar layer, such as the

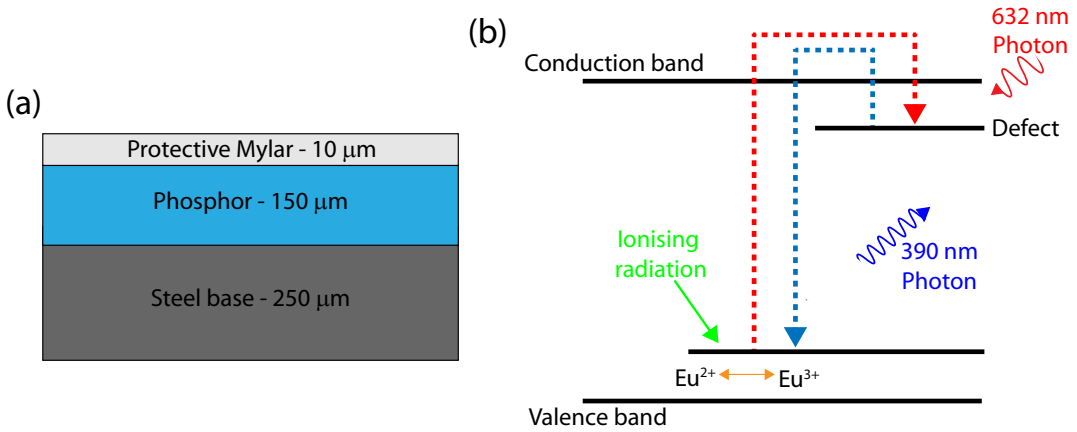

Figure 3.15: (a) Composition of the image plate type employed in this thesis. (b) Illustration of the atomic level transitions which occur during the exposure to ionising radiation and subsequent scanning of the image plate, in the image plate's active phosphor layer.

one employed in this thesis (shown schematically in Fig. 3.15(a)).

The principle of operation of IP involves the ejection of a photoelectron when Eu^{2+} ions are ionised to Eu^{3+} due to exposure to ionising radiation. This excited photoelectron moves to the phosphor's conduction band where it is subsequently trapped by the presence of lattice defects. This trapping is metastable, with a lifetime of many hours. In effect these trapped electrons hold information regarding the ionising radiation which put them in that state.

In order to record the information stored in the plates a scanner based on photostimulating emission is employed. The exposed IP is placed in the scanner where a tightly focused 632 nm laser scans across the plate exciting the trapped electrons. This results in their decay from the metastable state and subsequent recombination with the Eu^{3+} ions. This transition results in the emission of a 390 nm photon, which is detected through the use of a photomultiplier tube and amplifiers. This transition behaviour is illustrated in Fig. 3.15(b). The readout process removes 60–90% of the stored data, depending on scanner performance [165]. This photostimulated luminescence (PSL) signal is then converted into a digital image representing the signal on the exposed plate. A major advantage of this form of particle imaging compared to other forms (such as RCF or film based techniques) is after all the trapped electrons have been de-excited (through the scanning process and subsequently exposure to white light cleaning) the piece of IP can be reused for subsequent measurements.

The phosphor crystalline structure is of the order 5 μm, as such this sets the lower limit of spatial resolution this imaging technique can accomplish. However, the resolu-

tion is limited by the size of the probing laser's focal spot, typically around 25–50 μm. Due to the nature of spontaneous decays from the metastable state, IP can lose between 10–15% of its signal within the first hour after exposure to radiation. Therefore, the digitisation of data is ideally conducted within 15 minutes of exposure, with steps taken to prevent the IP being exposed to ambient light which will de-excite trapped electrons.

The image recorded by the scanner's CCD are 16-bit grey scale images, and thus do not represent the photo-stimulated luminescence of the exposed IP. One must first convert to a physical PSL unit, achieved using the formula below (Eq. 3.9) [166]. This value relates the energy stored in the promoted electron in the IP to the light detected by the scanner.

$$PSL = \left(\frac{R}{100}\right)^2 \left(\frac{4000}{S}\right) 10^{L[G/(2^B-1)-1/2]} \tag{3.9}$$

where R is the scanner resolution, S is its sensitivity setting (possible values of 1000, 4000, 10000), L is the latitude, B is the image dynamic range (typically 16 bits), and G is the raw image grayscale value. The latitude and sensitivity values of the scanner determine the range of signal intensities that can be determined from the IP by a single scan. The latitude (L) parameter is represented by a number which is the log to the base of the range of intensities measured, with possible values 4 and 5, corresponding to the dynamic ranges of 10^4 and 10^5, respectively. The sensitivity (S) parameter represents the intensity level at which the signal is measured, set by the scanner. Typically the number of photoelectrons promoted to the conduction band is significantly high such that saturation of the CCD image occurs during a single run of the scanner. Therefore IP typically requires numerous scans in order to decrease the signal before sensible data (i.e. within the image dynamic range) can be obtained. As such the number of scans gives a measure of the IP's level of exposure and thus must be accounted for in order to compare the signal level between various pieces of exposed IP. This is done by producing a response function (of exponential decay form) for the degree of IP signal drop-off as a function of number of scans, then employing this to scale the unsaturated signal back to its effective value at 'zero' scans, i.e. signal before scanning.

Specific to this thesis (in particular the investigation presented in chapter 6) is the use of IP as a detector of the number of escaping electrons during a laser-foil interaction. It is therefore necessary to have a calibration to convert the measured PSL signal to physical electron numbers deposited on the IP. Electron calibrations of IP are

typically conducted by irradiating a plate with a known electron current at a given energy, such as employing commercially available electron guns, with energies up to 30 keV. However, in laser-solid interactions, higher energy elections are typically produced (tens of MeV range). To this end, a calibration of IP response for electron energies in the range of 100 keV to 4 MeV was conducted, reported in Chen *et al.* [167]. This was achieved using the electrons generated from a short pulse laser irradiating a solid density target, then using an electron spectrometer to disperse the broadband energy spectrum produced. Using the calibration produced in this work [167] the number of electrons incident on exposed IP can be determined.

3.4.2 Optical diagnostics

Another key set of measurements are those made using optical techniques. This section covers the optical diagnostics employed throughout the results chapters, from measurement of the laser energy not absorbed by the plasma, to the characterisation of the wavefront quality of the intense pulses used.

Plasma reflectivity

Measurement of laser absorption in a laser-plasma interaction is key to understanding energy coupling to energetic particles and photons, and consequently, the development of applications of the resulting beams. This is the main topic under consideration in chapter 6.

To quantify the degree of laser energy absorbed by the plasma it is common to measure the laser energy which has not been absorbed, i.e. light reflected from the target. This unabsorbed (reflected) light can be split into two components; specularly reflected light and scattered light (the characterisation of which will be covered in the next section). One approach to characterising the specular reflected component is through imaging. This is typically achieved by employing a diffusely reflecting scatter screen to collect the reflected beam and a CCD camera in conjunction with a telephoto lens to image the spatial distribution and photon density. The screen acts similarly to a Lambertian surface, in that it scatters incident light by the same amount in all directions making its apparent brightness independent of observation angle. To

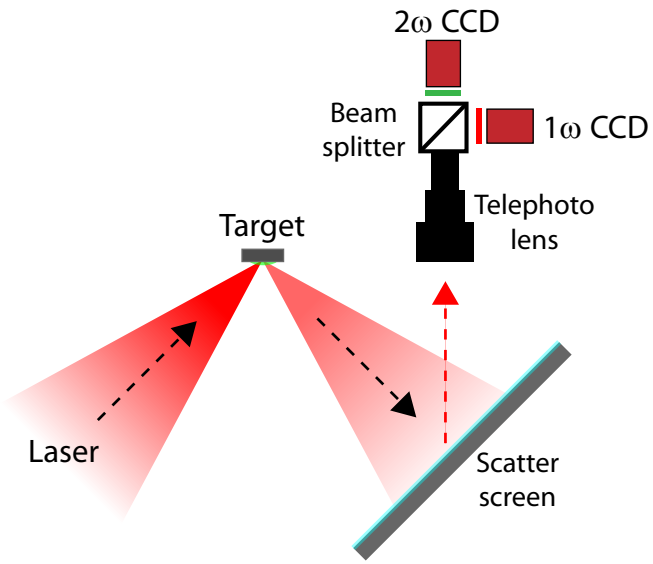

Figure 3.16: Illustration of the typical set-up employed to characterise the laser light specularly reflected from the target plasma, in terms of energy content, spatial-intensity profile and conversion to harmonics.

ensure that only reflected laser light is imaged, an interference filter at the laser central wavelength is included before the CCD camera. Furthermore, additional cameras which are optically filtered at harmonics of the laser wavelength may be included to image the screen at these frequencies, to enable characterisation of the conversion to harmonics of the fundamental laser wavelength. The basic configuration of such a device, imaging at the laser's central frequency (1ω) and its second harmonic (2ω) is illustrated in Fig. 3.16.

To convert the photon signal measured by the CCD camera to the actual laser energy reflected by the target one must conduct a calibration procedure. This typically involves the direct irradiation of the scatter screen with known laser pulse energies, enabling images to be recorded and a calibration to be performed. A similar process will be employed in chapter 6, where more detail can be found. Alternatively, an energy calorimeter may be employed to collect the reflected light, giving a direct measure of its energy content. However, using this approach no spatial information contained within the reflected light can be recorded as the calorimeter spatially integrates.

Integrating Sphere

Measurement of laser absorption in a laser-solid interaction is achieved through the characterisation of laser light which has not been absorbed by the interaction, either specularly reflected or scattered by the target plasma, as discussed in the previous

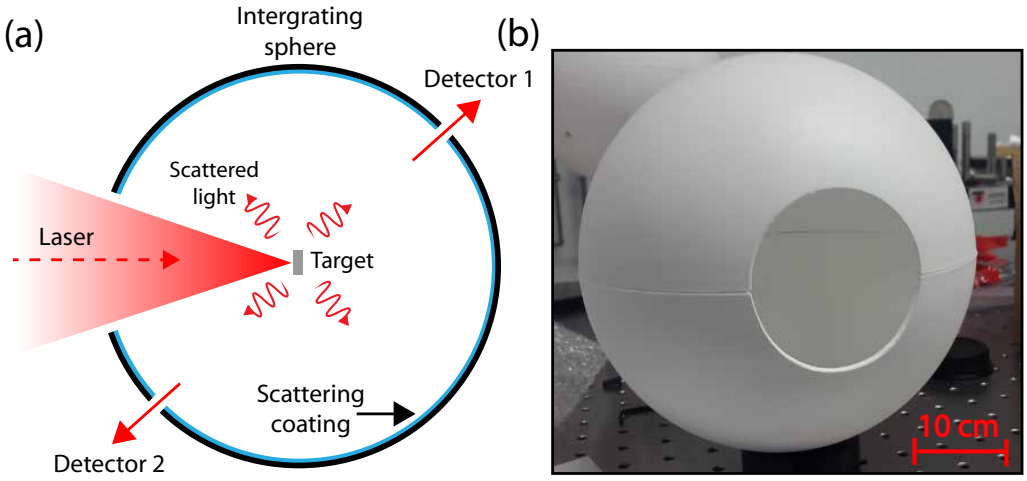

Figure 3.17: (a) Illustration of the basic principle of an integrating sphere operating on a laser-foil interaction investigation (b) Photograph of the integrating sphere developed for use in this thesis (more details in chapter 6).

section. Again this is the main topic under consideration in chapter 6, where the device presented in this section, the integrating sphere, is employed to quantify the scattered laser light component.

An integrating sphere (also commonly called an Ulbricht sphere) consists of a hollow spherical cavity with an interior surface coated with a diffuse reflective medium, with a high reflectance. Its primary function is to spatially integrate radiant flux (light). Such a device is illustrated in Fig. 3.17(a), including an image of the sphere manufactured for employment in this thesis (Fig. 3.17(b)). Before one can optimise the design of a sphere for experimental employment it is beneficial to understand the working principle of the integrating sphere. The first practical demonstration of an integrating sphere was in 1900 [168], and since then it has become a standard instrument used in the characterisation of light sources in terms of optical power and spectral content. Additionally, they are commonly employed in the measurement of reflectance or transmission of a sample material [169]. Integrating spheres have been employed on numerous laser-solid interaction experiments investigating the absorption of laser energy into target plasma [75, 170, 171, 172].

In terms of the sphere operation, when light is incident at any point within the sphere, in principle, it is distributed evenly to all points, through numerous scattering events. Thus the radiation exchange between two points is independent of the 'viewing angle' and the distance between points. The fraction of flux received at any particular area of the sphere is therefore the same for any other area of the same size within the

sphere. An integrating sphere can hence be thought as a diffuser which preserves the amplitude of incident light but destroys any spatial information. The light signal inside the sphere is best described by its radiance, L, i.e. the flux density per unit of solid angle. The radiance inside a sphere is dependent upon the light entering the sphere, the wall coating reflectivity, the sphere surface area, the multiple reflections made and losses due to openings in the sphere (such as entry and diagnostic openings, commonly called ports), as shown in Eq. 3.10 below;

$$L = \frac{\Phi}{\pi A_S} \frac{p}{1 - p(1 - f)} \tag{3.10}$$

where Φ is the amplitude of the light introduced to the sphere, A_s is the sphere wall surface area, p is the wall coating reflectivity and f the port fractional area. The first set of terms is approximately the radiance of a diffuse surface, and the second set a dimensionless quantity known as the sphere multiplier. This term accounts for the increase in radiance due to the multiple reflections and reductions due to ports in the sphere. It is essentially related to the average number of times a photon is scattered inside the sphere before it is either absorbed or escapes through a port. One may think that a simple approach to obtaining the radiant flux density inside an integrating sphere is simply the input flux divided by the sphere surface area. However, the effect of the sphere multiplier, i.e. numerous reflections, is that the sphere signal is at least an order of magnitude higher than this simple approach would predict. For a real optimum integrating sphere a rule of thumb for the main parameters used to calculate the radiant flux are; $0.94 < p < 0.99$, $0.02 < f < 0.05$ and a sphere multiplier in the range of 10 to 30; based on the total area of ports being less than about 5% of the surface area of the sphere [173].

Numerous factors must be considered in designing an integrating sphere. These include optimising performance by maximising both the sphere diameter with respect to any ports, and the coating reflectivity. Additionally an appropriate choice of inner coating is critical, where two factors must be considered; (i) coating reflectivity and (ii) durability. As shown in Eq. 3.10, the sphere operation is highly sensitive to the coating reflectivity. A small change in reflectivity will significantly alter the sphere radiance measured, due to the importance of reflectivity to the sphere multiplier value and thus coating selection is key to optimal operation. Common coatings include magnesium ox-

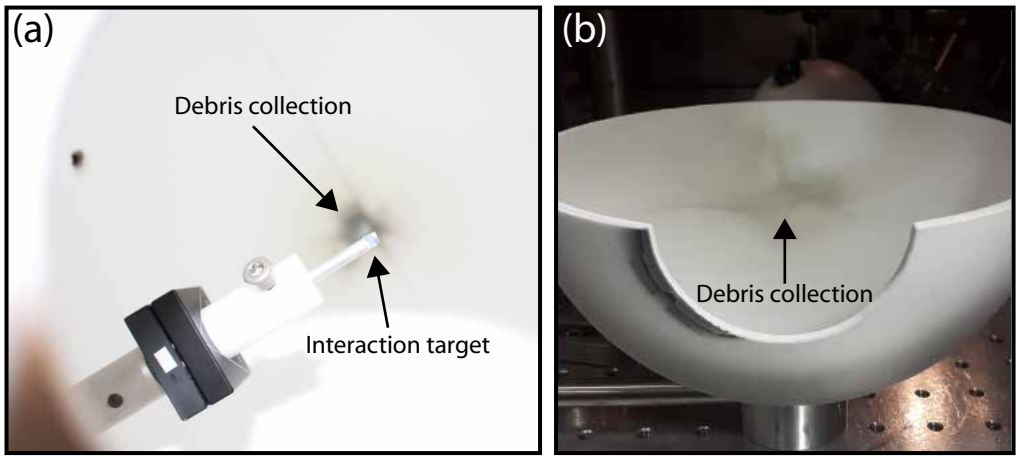

Figure 3.18: (a) and (b) Photographs showing the collection of target debris inside an integrating sphere, resulting after several laser-solid interaction shots.

ide and barium sulphate [172], for visible to near-infra-red light characterising spheres. Additionally, PTFE plastics are often employed to manufacture any items used within an integrating sphere (as will be used in chapter 6) to reduce adverse effects, such as absorption and scattering, which decreases the sphere's spatial uniformity. Furthermore, an important coating requirement is that it should not fluoresce. A coating possessing this property would absorb short wavelength photons and re-emit at relatively longer wavelengths and thus over the many reflections photons make within a sphere this effect can become significant to output results. Specific to the use of an integrating sphere in this thesis, for the characterisation of a laser-solid interaction, is the effect of target debris on the sphere operation. Figure 3.18 shows an image of target debris collected inside a sphere after several laser shots. This will alter the sphere reflectance and durability, and consequently integrating ability and thus it is highly important to minimise, or at least quantify, the effect of debris on results.

To measure the radiant flux in a sphere, a detector must be included, which ideally only collects light which has been diffusely scattered in the sphere, i.e. no direct illumination from the light source. This is often some form of energy meter (such as an energy calorimeter), or an optical device, such as a CCD camera or an optical spectrometer (as will be employed in chapter 6). Due to small alterations of the coating reflectivity or integrating ability resulting in significant difference in the sphere signal, careful calibration of the detection system response is vital before measurements can be preformed [174]. This is achieved by using the sphere to measure a well characterised (in terms of energy) light source, i.e. by supplying pulses of known energy into the

device.

Specific to the use of an integrating sphere in this thesis, is the use of two optical spectrometers as the detection system (more details in chapter 6). Optical spectrometers have become popular devices in laser-plasma interaction studies, used to measure the intensity (number of photons) of a sample of light as a function of its wavelength. An optical spectrometer, in its simplest form, comprises of a dispersive component to spatially separate individual wavelengths, such as prisms or diffraction gratings, and an optical detector, often a CCD camera. In this thesis two optical spectrometers were employed, an Ocean Optics (Maya2000Pro) and an Andor Shamrock (303i). For each, a Hg-Ar light source, with a well characterised emission spectrum, was used to calibrate the spectral response of the spectrometer.

Neutral density filter characterisation

In all the optical diagnostics presented in the previous sections, the use of neutral density filters is typically required to avoid the saturation of optical sensors, or the possible damage of optical components. A neutral density (ND) filter is an optic used to attenuate the intensity of light propagating through it, at all wavelengths equally. Whereas this may be true in photography involving visible light, the response of a ND filter can be significantly different at the infra-red wavelengths employed here.

The 'ND Number' of a given filter (essentially the filter's optical density (OD) [Eq. 3.11]) describes the amount of energy it can block, with higher values indicating lower filter transmission.

$$OD = -\log_{10}\left(\frac{T}{100}\right) \tag{3.11}$$

where T is the transmission of the filter. This value is often quoted on a ND filter, but has typically been characterised for the attenuation of 555 nm green light. As the laser systems employed in this thesis are in the near IR ($\sim$1054 nm) it is highly important to characterise the response of ND filters at this wavelength. This was achieved by employing a spectrophotometer; a device used to measure the reflectivity or transmission properties of a material as a function of optical wavelength. This enables one to calculate the actual ND value of a given filter as a function of photon wavelength (Fig. 3.19(a)) and therefore a calibration between the quoted ND value (at 555 nm) and the required value for 1054 nm light (Fig. 3.19(b)) to be produced.

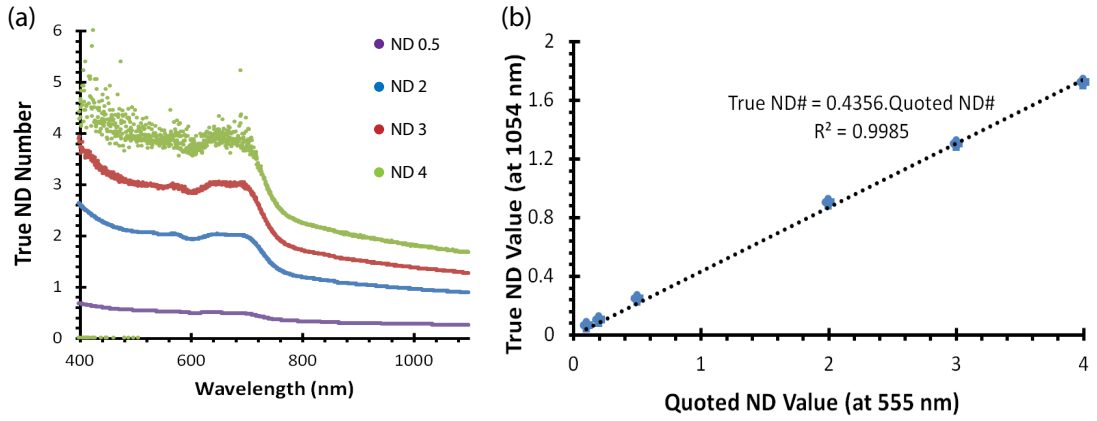

Figure 3.19: (a) Plot of the neutral density value for four various attenuation filters (quoted values in legend) as a function of transmitted light wavelength, measured using a spectrophotometer. (b) Plot of ND value at 1054 nm light as a function of the quoted ND value, including the equation used to convert between values.

This value changes significantly across the sampled wavelength range, highlighting the importance of this characterisation.

Shack-Hartmann wavefront sensor

A key laser parameter, important to the understanding of the results presented in chapters 4 and 5, is the laser wavefront profile. Numerous optics and thermal gradients throughout the laser chain can introduce aberrations and significantly alter the pulse wavefront from an idealised planar profile. This can consequently affect the focusing of pulses.

A Shack-Hartmann wavefront sensor is employed to measure the wavefront profile of a light source. In laser systems they are often used in conjunction with an adaptive optic (AO), to first measure wavefront aberrations and then relay this information to the AO to correct the wavefront in real time. A Shack-Hartmann essentially consists of a CCD (or CMOS) camera coupled with an array of micro-lenses, each of equal focal length, in front of the sensor chip, acting to divide an incoming beam into an array of smaller beams. Each of these sub-beams is additionally focused by the lens array to the CCD chip placed at the focal plane of the array; as illustrated in Fig. 3.20. When a uniform planar wavefront is incident on the array then the focal spots formed by each lens will be located on the optical axis of the lens, that is to say the image formed is a grid of equally spaced dots. However, when a distorted wavefront propagates through

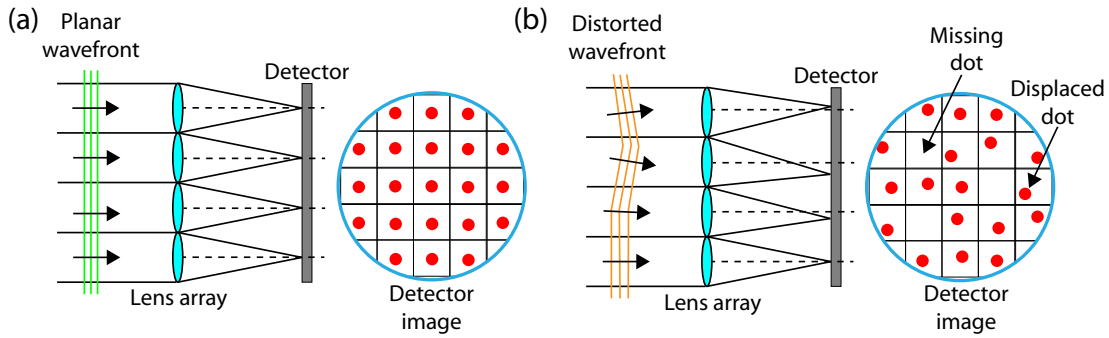

Figure 3.20: Principle of operation of a Shack-Hartmann wavefront sensor for (a) an incident planar wavefront and (b) a distorted wavefront.

the array this results in the focal point of each lens shifting from the optical axis and thus the spots on the resultant image will be displaced, or missing, according to the degree of distortion in the input wavefront profile. The image formed can then be used to reconstruct the shape of the incoming wavefront, i.e. the local tilt of the wavefront, incident on the lens array.

The output data from a Shack-Hartmann diagnostic essentially provides a measure of each type of wavefront aberration present in the incoming wavefront, i.e. deviation from a desired perfect planar wavefront. The most well known aberrations are astigmatism, coma and defocus, however higher order more complex aberrations do exist. The deviation is typically characterised by the so-called Zernike polynomials. First introduced by Fritz Zernike in 1934, these are used to mathematically describe 3D wavefront deviations from a flat profile. Each polynomial describes a specific form of deviation (i.e. coma, defocus, etc.), with their combined sum able to produce a large number of complex surface shapes, which can be fitted to specific forms of wavefront aberrations.

The sensor produces a Zernike coefficient number for each aberration type, which is the deviation (in wavelength) from a flat profile. For the work presented in this thesis (chapters 4 and 5) it is the defocus aberration which is of interest. An aberration of this form is essentially a curvature of the wavefront, which acts to change the divergence of a collimated beam. When focusing the laser pulses, this aberration will result in a displacement of the focal point along the laser propagation axis, due to the pulse having some degree of either focusing or divergence before arriving at the focusing optic. The physical distance the focus will shift from the nominal focal position, $\Delta\delta$ (i.e. for a flat wavefront), for a given focusing optic, can be related to the Zernike coefficient value,

Z_F, for this aberration type, through the following equation [175];

$$\Delta\delta = \frac{Z_F \cdot 4\lambda_L}{NA^2} \tag{3.12}$$

where NA is the numerical aperture of the focusing optic employed; related to the F/# through NA= 1/2F/#. This measurement enables the degree the focus position has effectively shifted to be quantified and consequently the calculation of the true peak intensity on-target to be obtained (as the target is aligned to the nominal focus position). This is key to the results presented in chapters 4 and 5.

3.5 Simulation and modelling

Various simulation tools are employed to aid in the understanding of the experimental results presented in chapters 4, 5 and 6. These take two main forms; (i) laser-plasma particle-in-cell (PIC) simulations, and (ii) optical ray-trace modelling.

The latter of these is employed to aid in the design and performance testing of a novel optic– the main subject of chapter 4. The other simulation tool employed, laser-plasma PIC simulations, is used to aid in understanding the underlying physics of the results presented in chapters 5 and 6. Each of these modelling techniques will be explored in detail in the coming sections.

The scale of computing resources required to perform these simulations varies greatly depending on the computational power required for each. For example, optical ray-trace programs can run on a PC, whereas laser-plasma PIC simulations require computational systems anywhere between small computational clusters to large-scale national super-computer systems. Simulations may take from seconds to weeks to run, depending on the simulation parameters and the degree of accuracy/resolution required.

3.5.1 Particle-in-cell simulations: EPOCH

Simulations can give an in-depth, though simplified, view of the evolution of a laser-plasma interaction, allowing numerous key dynamics to be quantified, which may not be directly measured experimentally, such as temporal resolution of the complex inter-

action dynamics. Analytical models can provide quantification of important interaction parameters, such as fast electron temperature or absorption scaling, but do not enable the complex dynamics of the interaction to be explored. As such, the use of more complex numerical modelling techniques provides data which complements experimental findings.

As seen in section 2.3.1 (Fig. 2.3), as a state of matter, plasma spans a large temperature and density range and thus necessitates the use of a wide verity of simulation approaches. In the case of laser-solid interactions these can be rather complex due to state transitions which must occur, i.e. solid to plasma. Generally, the plasma models used to simulate a laser-solid interaction can be split into three distinct categories; static, fluid and kinetic. A static model treats plasma as a passive medium which, for example, can alter the propagation dynamics of an EM wave passing through it. A fluid model, often referred to as a hydrodynamic model, is more complex, assuming that the plasma is locally in thermal equilibrium, with particles distributions described by well defined Maxwellian functions. In this description, the plasma can be represented by macroscopic variables such as density, pressure, etc. The main use of this modelling approach is to probe the large scale dynamics of a plasma system. Finally, kinetic models are the most complex and inclusive. They are used to describe plasmas self-consistently using particle distribution functions (not assuming Maxwellian forms), often involving huge numbers of electrons and ions. This is the main form of plasma modelling utilised in this thesis, taking the form of simulations based around the particle-in cell (PIC) approach [176].

The fully kinetic treatment of the evolution of each particle species in this modelling approach can be found by solving the Fokker-Planck equation;

$$\frac{\partial f}{\partial t} + \mathbf{v} \cdot \frac{\partial f}{\partial x} + q\left(\mathbf{E} + \frac{\mathbf{v}}{c} \times \mathbf{B}\right) \cdot \frac{\partial f}{\partial \mathbf{p}} = C(f) \tag{3.13}$$

Each species is described by a distribution function, $f(\mathbf{r}, \mathbf{p}, t)$, and collisions between the species are accounted for by the $C(f)$ term. In the case of PIC simulations, a fixed ionisation state and a collisionless plasma is assumed and therefore the collisional term is zero. In this special case, Eq. 3.13 is referred to as the Vlasov equation. The distribution function, contains 6 dimensions; three spatial and three momentum. This is highly complex to solve due to the large number of particles involved in a laser-solid

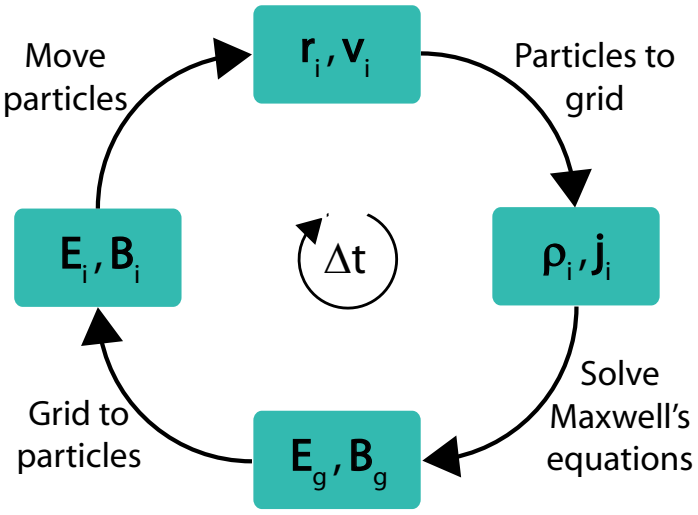

Figure 3.21: Illustration of the steps involved in the simulation of a plasma system employing the PIC approach.

interaction, and hence computationally intensive. To address such concerns, the PIC method represents the real large number of particles in the plasma by discrete, statistically weighted 'macroparticles' of a much lower number. These macroparticles occupy a finite volume and shape, as they represent a large number of real particles, assumed to have no internal degrees of freedom. Importantly, the macroparticle distributions evolve in the same way as the particles they represent. To calculate parameters of the macroparticles, such as position ($\mathbf{r}_i$), velocity ($\mathbf{v}_i$), current ($\mathbf{j}_i$) and density (ρ_g), they are mapped onto a grid. Once these parameters have been calculated for a given grid cell, Maxwell's equations are employed to calculate the resultant electric and magnetic fields, ($\mathbf{E}_g$ and $\mathbf{B}_g$). These are then used to calculate the resultant motion, and thus new position, of the macroparticles through the Lorentz force description. This motion changes the current and particle density, and thus the calculation loop begins again and is iterated for the simulation duration. Figure 3.21 illustrates this PIC cycle approach. A more detailed description can be found in Ref. [176].

Key insights into the physics occurring in a laser-solid interaction can be ascertained using PIC simulations, though there are certain limitations and potential issues to consider. The number of macroparticles per cell, for example, is key to the reproduction of realistic physical processes. This parameter determines both the resolution of the distribution function (i.e. how smooth it is) in phase space and the degree of statistical noise in output data, which may hide the desired physics under investigation. Furthermore, there are spatio-temporal requirements which are set temporally by the plasma

frequency (i.e. the highest frequency in the system) and spatially by the Debye length. If these are not satisfied then numerical instabilities can dominate the simulation. For example, if the spatial resolution of the simulation grid is not larger than the Debye length then the system will self-heat until this condition is met, leading to non-physical results. In terms of limitations to PIC simulations, some physical aspects are typically left out due to the highly complex nature of the simulations. These often including particle ionisation and collisions. This again can lead to some non-physical dynamics.

For the work presented in this thesis the EPOCH PIC code was employed (developed by the Extendable PIC Open Collaboration (EPOCH) project [177]). This is an open source code, which enables users to edit the code for their desired needs. The computational memory required to perform EPOCH modelling can be relatively large, depending on the number of dimensions simulated (i.e. 1D, 2D or 3D), the spatial extent of the simulation window, and the interaction time which is modelled. This can lead to memory requirements in excess of hundreds of gigabytes of RAM. Additionally, this PIC code operates through a message passing interface (MPI) protocol, which enables calculations involved in its operation to be divided over numerous CPUs and be calculated in parallel, enabling simulation time to be significantly reduced. Furthermore, another computational requirement to consider when using this modelling technique is the storage of simulation data. This can be relativity large, up to tens of gigabyte, depending on how often data is transferred from the simulation. Appropriate choice of storage is thus important. One must also consider the computation requirements involved with efficient visualisation of the large quantity of data which PIC codes output. This again can involve computational clusters, though relatively smaller in comparison to those required to perform the PIC simulations.

3.5.2 Optical ray-tracing: Zemax

Ray-trace modelling is the primary method by which optical engineers determine the performance, and optimisation, of an optical system design, such as lens and mirror combinations. This enables aspects of the operation and limitations to be tested before the optical system is manufactured. The technique is essentially the tracing of rays of light as they propagate through an optical system by calculating the angle of reflection, or refraction, from the optical surfaces, enabling the image forming properties of the

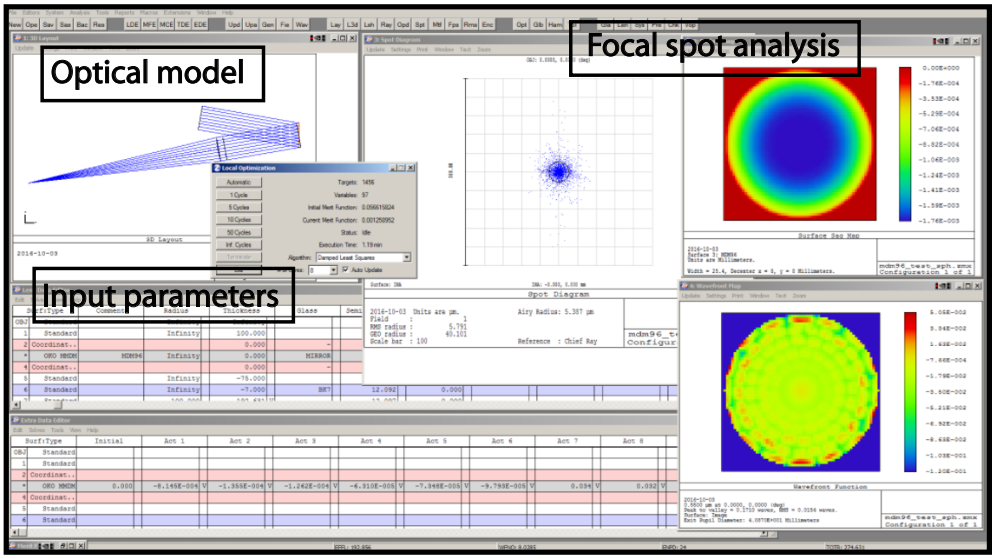

Figure 3.22: Screenshot of the basic interface of the Zemax OpticalStudio software, used to simulate and characterise an optical set-up.

system to be modelled.

For the optical modelling purposes of the work presented in this thesis, the Zemax OpticStudio software was employed. This commercially available optical design software is industry-leading, combining complex physics and interactive visuals to analyse, simulate and optimize optical systems. It is highly comprehensive and can simulate complex optical systems, allowing numerous standard physical parameters to be generated, such as the focal spot spatial-intensity distribution, the main ray-trace analysis tool utilised in chapter 4. Figure 3.22 shows a sample screen shot of the Zemax OpticalStudio operation.

3.6 Summary

To conclude, the laser systems and diagnostics employed to make measurements of laser-solid interactions, forming the results presented in this thesis have been explored. It has been shown that to characterise a laser-solid interaction in such a way as to achieve real insight into the underlying physics requires the combination of a number of technologies, including optimised laser systems and the correct deployment of diagnostic techniques. Each of these areas requires significant expertise and planning in order to come together to ensure a successful experimental campaign. Due to the

limitations of current diagnostics, especially with respect to time resolving aspects of the interactions, and the sheer complexity of the physics involved, it is typical to complement experimental evidence with modelling and simulations which help to resolve the underpinning physics. This involves anything between simple analytical modelling, to the use of large computing systems to 'recreate' the interaction.

In the following chapters the experimental methods and modelling techniques discussed in this chapter will be employed to investigate several aspects of intense laser-solid interactions.

Chapter 4

Development of ellipsoidal plasma mirrors for focusing of high power laser pulses

4.1 Introduction

Since the inception of the laser, there has been a constant push in the development of new laser technologies which has led to an increase in the achievable intensity; of between 4 and 5 orders of magnitude per decade. This drive towards higher intensities has opened up new avenues of research in laser-matter interactions and enhanced the capabilities of well known laser-plasma phenomena, such as laser-driven particle acceleration, radiation sources and relativistic optics, to name a few. The parameters of the laser employed are a major factor in the nature of these interactions. There is particularly sensitivity to the peak pulse intensity. Overall, the ability to tailor the drive pulse properties, have made many of the recent breakthroughs in laser-plasma research possible.

To exploit the transformative potential of laser-driven sources, and to open up exploration of new ultra-intense ($>10^{22}$ W/cm^2) laser-plasma phenomena, such as experimental investigation of strong-field physics studies [178, 179], characteristic parameters of the drive laser must be improved beyond present state-of-art; specifically the peak intensity and pulse intensity contrast.

A typical approach employed to boost the peak intensity is to increase the pulse

energy, or decreasing its duration; both resulting in an increase of peak pulse power. This is, however, problematic for numerous reasons, including the fact the diameter of the beam through the laser chain would have to be increased to avoid the damage threshold of conventional (solid state) optical components. This approach would hence lead to relatively expensive and larger laser systems. This is the enhancement path that upcoming laser facilities coming online in the next few years are taking, such as APOLLON [5] and the Extreme Light Infrastructure (ELI) [6], which are aiming to deliver peak focal intensities in the range 10^{22}–10^{23} W/cm^2.

Another common route for accomplishing higher peak intensities, not requiring drastic alteration of the laser system, involves focusing the laser pulse to a smaller focal spot via the use of a small F-number (F/#) optic. This is somewhat more effective than increasing the peak power as intensity scales inversely to the square of the focal spot size. This approach is however not without its drawbacks. Such optics are expensive, difficult to optimally align, and are more susceptible to damage from solid target debris. The latter arises due to the fact that as the F/# of a focusing optic is reduced, the focal length also reduces (for a fixed input beam diameter), increasing the probability of damage from debris induced by target irradiation. Clearly this approach comes at risk, with measures having to be taken to protect the optic from the close proximity to the interaction. There is thus a need for new types of optical components that can bypass this issue.

One such promising approach is the switch from conventional solid-state to plasma-based optics. A commonly used plasma optic is the 'plasma mirror' (PM) (as described in section 3.2.5), a versatile and easy-to-use tool, which has become a major component, routinely utilised in laser-foil interactions [142, 146]. A PM is a single use device replaced after being irradiated and consequently the issue of debris damage is eliminated as the optic has already served its purpose before debris reaches it. This enables the distance from the mirror surface to target (i.e. the focal length) to be dramatically shortened, enabling the use of small F/# focusing optics. Plasma optics also have the ability to sustain extremely large amplitude electromagnetic fields, and can therefore be made more than a factor of $\times 10$ smaller than conventional optics. They are likely to become an essential tool in the future of laser-plasma interaction research.

To take advantage of the PMs attributes, and the approach of producing higher peak intensities by focusing to a smaller area, a small F/# focusing plasma mirror

(FPM) has been developed. This is the topic of this chapter. The main aim of this development is to extend the peak intensity achievable with high power laser pulses by more than an order of magnitude, and secondly, simultaneously enhance the temporal intensity contrast of the pulses, as in the case of conventional planar PMs. Both of these developments make the FPM a desirable multifunctional optical device. This will enable the exploration of laser-plasma phenomena at peak intensities of $\sim 10^{21}$–10^{22} W/cm^2 with facilities available today, providing a window into the new physics achievable with future multi-PW scale projects.

The use of a such an optic for achieving higher intensities through decreasing focal spot size was first demonstrated in a proof-of-principle experiment on a terawatt (TW) level laser system (at Laboratoire pour l'Utilisation des Lasers Intenses (LULI)) reported in Kon *et al.* [180] and Nakatsutsumi *et al.* [181]. This work will be explored further in the next section (section 4.2). Due to the limited prior research in this area, the development and investigation of a focusing plasma mirror presents an opportunity for significant progress in this field.

In this chapter, the design, development and testing of our FPM, produced for use on the Vulcan petawatt laser system at Rutherford Appleton Laboratories, is presented. The results of an experimental campaign employing the FPM, to characterise its performance, are also presented. The results of this study have been published in *Physics of Plasmas* [182]. This work helps to bring plasma-based optical technology closer to maturity and specifically will help the concept of focusing plasma mirrors move beyond demonstration towards routinely used tools in laser-plasma research; much in the same way that planar plasma mirrors have been developed and are now routinely applied to enhance laser pulse contrast.

4.2 Review of relevant literature

As stated in the introduction, the employment of a FPM for laser intensity enhancement was first demonstrated on the 100 TW LULI laser system (in its 2ω [528 nm] operation mode), reported in Kon *et al.* [180] and Nakatsutsumi *et al.* [181]. In this work, a compact (<1 cm^3) F/0.4 FPM manufactured from glass (K-PBK40) was developed. The optic achieved a five-fold reduction in focal spot size (from 4.4 to 0.9 μm) compared

to the spot formed by a conventional F/2.7 off-axis parabolic mirror, resulting in a $\times 8$ intensity enhancement, due to a relatively low plasma reflectivity of (30±10)%. They postulated that such low optic reflectivity may have arisen from the low specular reflectivity in the spatial extremities of the focal spot incident on the FPM surface, where the fluence is relativity low. Spot measurements were achieved using reduced laser energy (μJ level), therefore intensity enhancement was indirectly diagnosed by the measurement of the maximum energy of protons accelerated from a thin target foil (2 μm gold) positioned at the FPM focus. An increase in the maximum proton energy was measured from 2.2 MeV, without the FPM, to 10.5 MeV, employing the optic. The energy of the laser pulse was lowered on shots not employing the FPM to achieve the same energy on target in both focusing scenarios. The observation of enhanced proton energies was reproducible from shot-to-shot, indicating a robust and reliable system for practical use. This FPM demonstration experiment produced focal spots which contained 17% of the laser energy within the FWHM spot diameter, compared to 27% in the 4.4 μm focal spot from the OAP. This parameter is key in the application of any focusing optic, and there is potential to improve this value. They additionally highlighted in this study the need for high accuracy ($\sim$1 μm) in FPM positioning relative to OAP input focus and that optic alignment time was approximately less than the repetition rate of PW level laser systems ($\sim$20 to 30 minutes).

Subsequently the same group trialled a similar FPM using the Vulcan Petawatt laser [183], once more applying the novel optic to proton acceleration. The optic developed for this testing was F/0.6, and achieved a $\times 3.3$ demagnification of the spot formed by a conventional F/3.1 off-axis parabolic mirror (from 6.3 to 1.9 μm). Although the desired FPM demagnification was observed (in the non-plasma regime), testing in plasma operation, through the optic employment in laser-driven proton acceleration, did not produce an enhancement in the measured maximum proton energy. Furthermore, the maximum proton energies were seen to be largely the same for targets ranging from 25 nm to 100 μm thickness. This finding was not expected and could not be fully explained. It was postulated that spatial intensity fluctuations in the laser beam profile may have led to imperfect plasma formation on the optic's surface, consequently affecting the quality of the produced focus. They additionally highlighted that imperfect alignment of the FPM may have led to the observed result, though this reasoning would require further investigation in future studies.

The employment of FPMs are also being considered for use on future multi-PW level laser systems. For example the 10 PW ELI-Beamlines (part of the Extreme Light Infrastructure project), is researching their use in order to achieve peak laser intensities $>10^{23}$ W/cm^2 [184]. This development is not only concerned with investigating ways to produce the optics efficiently and cheaply (due to them being replaced after every shot), but additionally the development of theoretical tools to model tight focusing in terms of laser-plasma interactions [185, 186].

4.3 Principles of operation and design

The first stage in the development of our FPM, is its design. As in the case of the FPMs in the previous work discussed above [180, 181], the design forming the work presented in this chapter is based on the confocal ellipsoidal geometry. The base design involves using this geometry to accomplish point-to-point imaging such that a focal spot formed by a main focusing optic (typically an off-axis parabola (OAP)) is reimaged and demagnified at the output focus of the ellipsoidal FPM. A natural place to start in understanding the process used to design the FPM is to review aspects of ellipsoidal geometry and its two dimensional equivalent, the ellipse.

Firstly, let us consider the properties of an ellipse. Mathematically speaking an ellipse is a curve on a plane with two perpendicular axes which define its shape; the major and minor axes. Situated on the major axis are two focal points, located such that the length of a straight line from one focus to any point on an ellipse curve, then to the second focus is constant for any point selected on the curve; equal to the length of the major axis. Consequently, the foci are of equal distance from the ellipse origin, a distance referred to as the focal distance, f, given by Eq. 4.1. The first focus will be referred to as the proximal focus, f_1, and the second the distal focus, f_2, defined by which encounters light propagation first.

$$f = \sqrt{a^2 - b^2} \tag{4.1}$$

where a is the semi-major axis length, half that of major axis, and b the semi-minor axis length the equivalent for the minor axis. This leads to another parameter frequently

used to characterise an ellipse, its eccentricity, e, representing its shape, described by Eq. 4.2, when Eq. 4.1 is used to define the focal length. This parameter can have a value ranging from 0, i.e. a circle, to arbitrarily close to, but <1.

$$e = f/a = \sqrt{(1 - b^2/a^2)} \tag{4.2}$$

In designing a FPM, it is important to consider how this geometry behaves in terms of an optical component and why it has been selected as the basis of the focusing plasma optics design. Primarily, it has been chosen as this geometry allows for point-to-point imaging, that is from focus-to-focus, which is an attribute which other typical mirror geometries, such as parabolic and hyperbolic, do not possess. Secondly, and key to the primary objective of the optic, is the ability of this geometry to enlarge or reduce the size of an image at one focus when the object is placed at the other, i.e. the optics magnification, m. Additionally, optically speaking the ellipsoidal shape also possesses no spherical aberration, giving it additional advantage over other geometries.

The magnification of an elliptical mirror is related to the object distance from mirror surface, α, and the image distance, β, thus will change as a function of the incident angle θ_{In}, with respect to the major axis, as this will vary with α and β. All the parameters used to characterise the ellipse as an optic are depicted in Fig. 4.1(a). The equations which describe the magnification are given by;

$$m = \frac{\beta}{\alpha} \tag{4.3}$$

$$m = \frac{(1 + e^2) - 2e\cos(\theta_{In})}{(1 - e^2)} \tag{4.4}$$

A full derivation of which is found in Stavroudis *et al.* [187]. It should be noted these equations, for calculating the magnification, are under paraxial approximation (i.e. optical rays make a small angle to the optical axis of the system, and remain close to the axis throughout the system), which are no longer valid when the focal spot diameter is of the order of the laser wavelength.

Finally converting to 3D ellipsoid geometry is achieved simply by adding a third axis c, thus rotating the 2D ellipse, and making the length equal to b, producing an 'oblate ellipsoid', as displayed in Fig. 4.1(b).

Now that the key equations used to describe an ellipse in terms of its geometry,

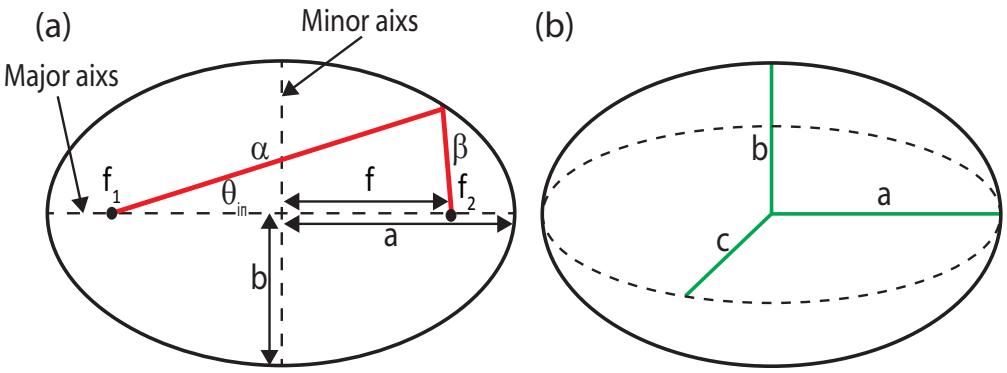

Figure 4.1: (a) Schematic illustration of an ellipse, annotated with the main parameters used to describe its geometry and characterise it's optical properties, and (b) diagram of a oblate ellipsoid with the three axes which define it's geometry.

and as an optical component have been established, the steps employed in designing a focusing plasma optic for the purpose of focusing a laser pulse can be presented. In practical terms, a conventional OAP can be aligned such that its focus coincides with position f_1 of the FPM. As the light diverges beyond this, it reflects from the plasma it forms on the curved surface and is imaged to position f_2. In doing so the focal spot at f_1, i.e. the object, is demagnified at f_2, i.e. the image, depending on the chosen geometry of the FPM and the angle θ_{In}. This concept depicted in Fig. 4.2.

The precise design of a FPM depends on the parameters of the laser system on which it is intended to be employed; chiefly the laser pulse peak power and the F/# of the conventional OAP used to bring the pulse to initial focus (at f_1). The optic developed in this work has been designed for use on the Vulcan-PW laser (as described in section 3.3.1) at Rutherford Appleton Laboratory. This laser delivers 1053 nm light pulses, with energy up to 600 J pre-compressor (typically ∼200 J on-target including losses in the compressor), and duration ∼750 fs (FWHM). Pulses are focused using an F/3.1 OAP to produce a focal spot of typical diameter of ∼4 μm (FWHM). The resulting calculated peak intensity is of the order of 6×10^{20} W/cm^2 (assuming 30% of the energy is contained within the FWHM focal spot).

As the purpose of the FPM is to increase the achievable peak intensity through focal spot size reduction, the first step in it's design is the selection of a suitable demagnification. Although the smallest F/# possible is desired, smaller values are more sensitive to optic alignment. Thus a compromise value is selected which produces significant intensity enhancement while enabling the ease of use and robustness to a non-optimum alignment. A demagnification value of 3 (m= 1/3) was selected based on

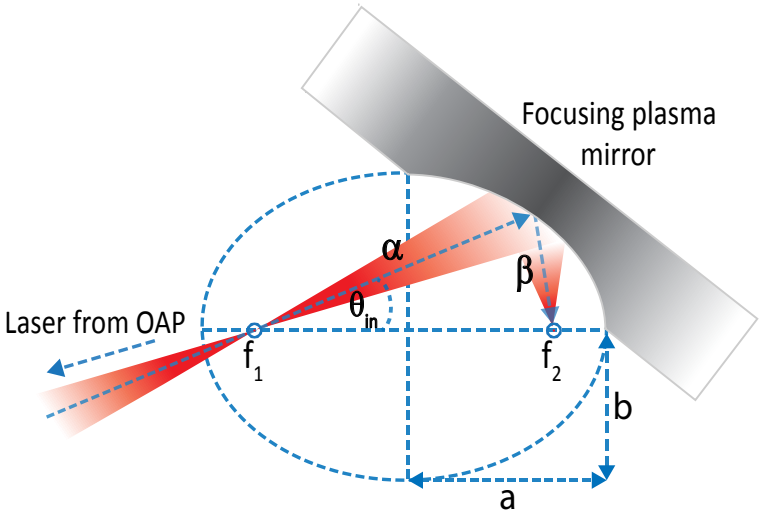

Figure 4.2: Schematic diagram showing principle of operation of an ellipsoidal focusing plasma mirror, where the incoming laser is focused by a conventional OAP to position f_1 and the FPM refocusing the beam to position f_2, with the magnification given by β/α.

the F/3.1 OAP, such that the FPM is designed to yield a focal spot size of ∼1.3 μm FWHM (close to the central wavelength of light used on the Vulcan laser).

The dimensions of the FPM depend on the desired optic energy reflectivity and thus the incident laser intensity on the optics surface (the reflectivity dependence of plasma 'switch-on' laser intensity is discussed in references [141] and [145]). This reflectivity dependence on incident laser intensity was experimentally characterised in Dromey *et al.* [144], showing the conditions under which high reflectivity from a planar plasma mirror could be achieved. It was observed that as the intensity on the surface of the PM was increased a region of high specular reflectivity was established. However, further intensity increase beyond this region results in the reflectivity rapidly fluctuating over a large range of values; postulated to occur as a result of the expansion of plasma exceeding the optimum condition for specular reflectivity ($\sim L_s > \lambda_L$). Figure 4.3(a) displays sample results obtained in this characterisation study of the plasma reflectivity of a planar anti-reflective coated silica PM as a function of 'switch-on' intensity. A region of high specular reflectivity (∼70%) is established for an incident intensity around 10^{15} W/cm^2, as shown in Fig. 4.3(a). As such this value was selected for the incident intensity of the pulses on the surface of the FPM, as this would allow for high reflectivity, and additionally avoids the large uncertainty in reflectivity occurring close to the extreme end of this intensity range (10^{16} W/cm^2).

In terms of the FPM geometry (Fig. 4.2) the laser intensity incident on the optic's

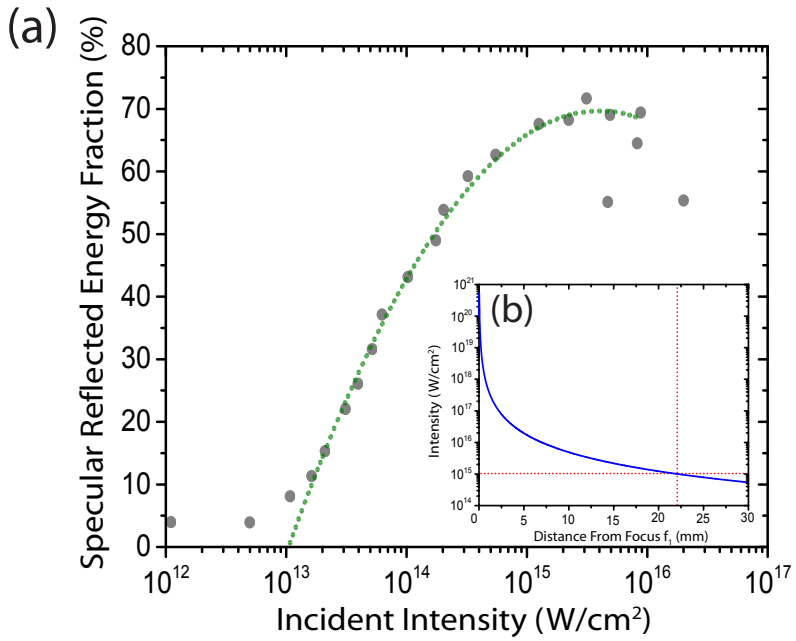

Figure 4.3: (a) Plot of the percentage of laser light specularly reflected from a plasma mirror as a function of the incident laser intensity on its surface, with grey points sample data from Dromey et al., and a quadratic fit made to this data between the incident intensities of 10^{13}–10^{16} W/cm^2, as illustrated by the dotted green curve. This data was obtained employing 500 fs pulses and a fused silica planar PM, with 6° laser incidence angle. (b) Plot displaying the intensity evolution of a diverging Vulcan-PW pulse after its focal point from an F/3.1 OAP, at f_1, where red dashed lines indicate the distance an intensity of 10^{15} W/cm^2 is located.

surface is determined by the distance the beam expands from f_1 to the surface, i.e. α. Through consideration of Gaussian beam expansion for the Vulcan-PW pulse and focusing conditions, the distance at which an intensity of 10^{15} W/cm^2 from focus occurs can be estimated, assuming a uniform expansion. Figure 4.3(b) displays the longitudinal intensity evolution of a pulse, of the Vulcan-PW parameters, as a function of it's expansion from best focus. The distance at which the beam has expanded sufficiently to achieve the desired intensity (marked in Fig. 4.3(b)) is estimated to be 22.12 mm, thus the ellipse parameter α is obtained.

Two parameters used to define FPM design geometry have now been calculated, namely magnification and the distance α. The remaining parameters required to express the optics geometry can now be calculated. The first of these, namely β (the distance from optic to f_2) is found using Eq. 4.3, knowing the magnification (m= 1/3) and the distance α; a value of 7.37 mm is obtained for β, for this particular magnification. Secondly, the aforementioned, main parameters utilised to describe the shape of a particular ellipse, the semi-major and semi-minor axis lengths, a and b, can be calculated. The semi-major axis length, a, is calculated using α and β, through $2a = \alpha + \beta$.

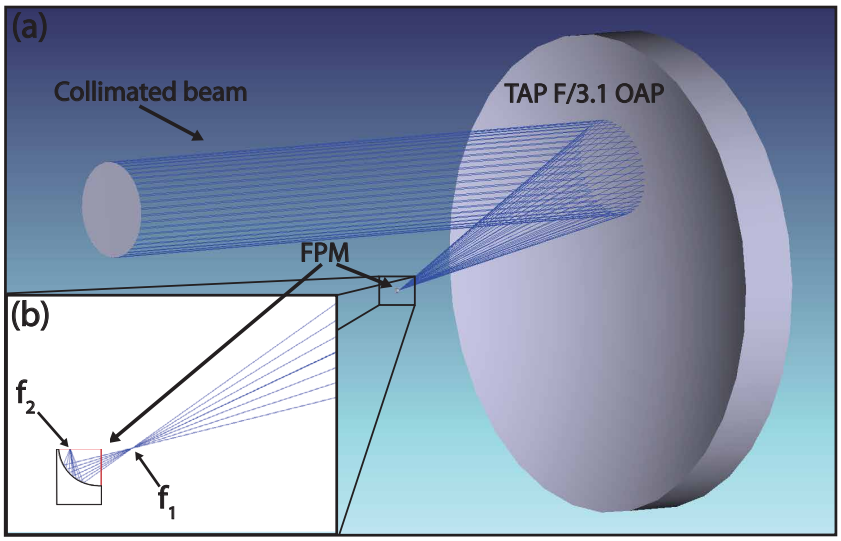

Figure 4.4: (a) Screenshot of the optical model created using Zemax ray-trace software to model the FPM design performance, and (b) a zoomed in image of the FPM in the model re-imaging light from f_1 to f_2.

The value 14.7 mm is obtained. The semi-minor axis length, b, is then calculated using Eq. 4.1, where the focal length, f, is selected to result in a distance of 4 mm from each focus to ellipse vertices, necessary for practical target placement in experimental usage. Thus the focal length is simply the semi-major axis length minus this 4 mm exclusion distance seen in Fig. 4.1(a). Therefore f is found to be 10.7 mm, and b=10.1 mm.

The final parameter required in this design stage, for optic alignment purposes, is the beam input angle relative to the major axis, θ_{In}. For the established design parameters an input angle of 19.4° is required, obtained using Eq. 4.4.

4.4 Optical ray-trace modelling

To validate the FPM design presented in the previous section, before the optics were manufactured, analytical modelling was conducted employing optical ray-tracing software (Zemax OpticStudio [discussed in section 3.5.2]). This software enables one to build an optical model of the FPM design re-imaging light from Vulcan-PW F/3.1 input focusing beam, as displayed in Fig. 4.4.

Using this FPM design ray-trace model one can first validate the design- that is to say, does the optic give the desired demagnification of an input focal spot. This is achieved by imaging the input focus (formed by the OAP) and comparing it to the

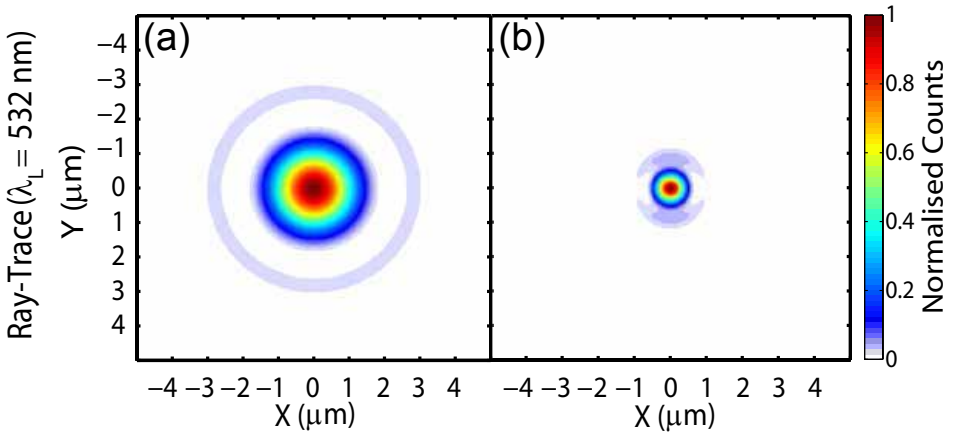

Figure 4.5: (a) and (b) Calculated laser focal spot spatial-intensity distributions at (a) f_1 and (b) f_2 from Zemax ray-trace modelling of the FPM operation.

demagnified output focus of the optic, at f_2. Figure 4.5(a)-(b) displays the results for the input focal spot and the resultant output formed by the FPM. These spots correspond to a demagnification of ×2.9 (based on the input and output focal spots of 1.71 μm and 0.5 μm (FWHM), respectively). This modelling was conducted using 532 nm light to enable direct comparison with experimental tests discussed later in the section 4.7. As established in the optic design section the desired demagnification is ×3, thus this value is in good agreement. Slight variation in values may be attributed to the optic inputs and beam configuration quantities in this ray-trace software requiring high input precision, or purely due to the nature of a small F/# optic focusing close to the diffraction limit, which may not be fully described by Eq. 4.4. This demagnification would result in an intensity enhancement factor of ×8.4, considering the optics geometry alone. In plasma operation this will be lower due to the reflection of the optic being lower than unity, and spatial filtering caused by the lower energy wings of the pulse not ionising as effectively as the central region, thus a lower reflectivity (intensity enhancement will be covered in move depth in section 4.7.1). This modelling forms a key first step in testing the FPM base-design, giving reassurance that the optic geometry and design will operate as expected in practice. As such the design could be manufactured for experimental testing, as will be explored in the next section.

The ray-trace model additionally enables the principle that FPM magnification is dependent on the beam input angle (described by Eq. 4.4) to be investigated. Figure 4.6 summarises the results of the magnification obtained as a function of the input angle. Good agreement is found between the analytical model (Eq. 4.4) and ray-tracing

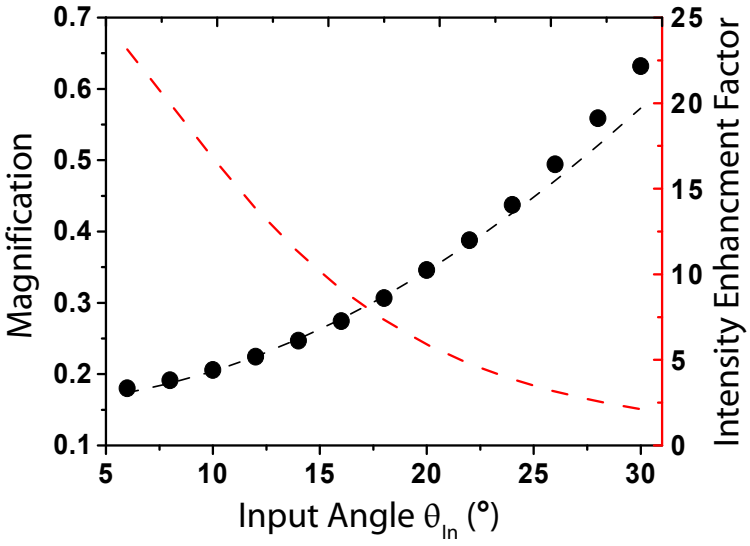

Figure 4.6: Magnification of the input focal spot for FPM design as a function of θ_{In}; where dots correspond to the ray-trace modelling, black dashed line to the analytical model (Eq. 4.4), and red data the estimated intensity enhancement factor for a optic plasma reflectivity of 70%.

model. Clearly smaller angles give rise to higher demagnification and thus higher intensities. The FPM design therefore enables for a degree of tuneability, allowing θ_{In} to be decreased to $\sim$9° (this is the lower limit, otherwise the beam will begin to miss the open aperture of the optic design), decreasing magnification to $\sim$0.2, and enhancing intensity by factor of $\times$18 compared to OAP focus (taking into consideration predicted 70% reflectivity in plasma operation). However, this demagnification is impractical, as this would in principle result in a focal spot size below the diffraction limit.

4.5 Optic manufacturing

In this section the routes employed to manufacture the ellipsoidal FPM design for experimental usage are explored. Essentially a method was required which could not only produce high quality optics (i.e. high accuracy to the design geometry and an optically smooth surface), thus forming a high quality focal spot, but also in a time and cost-effective manner, for these optics to be viable devices. The quality of the spot formed by the optic is determined mainly via the alignment of the input spot to the input focus of the FPM, i.e. f_1, but also depends on the accuracy with which the surface has been manufactured, thus selecting a suitable manufacturing technique is crucial. To this end, two techniques were employed to produce the FPM; (1) injection

moulding, and (2) diamond machining; each of which is explored in this section.

(1) Injection moulding

The first manufacturing technique considered for FPM production was that of injection moulding. This technique would in principle enable a large quantity of the single-shot optics to be produced moderately quickly, in a reasonably cost effective manner. It involves, first, the ultra-precise diamond machining of the FPM design into a metallic mould (Fig. 4.7(a)), which could then be injected with a transparent Poly(methyl methacrylate) (PMMA) plastic, by a specialist optics company (Eyejusters Ltd [in collaboration with Durham Precision Optics]). A number of test runs were conducted altering injection parameters (such as fill speed, plastic melt temperature, mould temperature, packing pressure) to achieve smooth filling and best reproducibility. The optics produced (Fig. 4.7(c)) have a near-constant thickness of 4 mm; the limit of thickness for this particular moulding process. The thicker the part the more rigid it will be, making it less prone to distortions due to stresses induced by mounting.

Metrology was performed on the manufactured moulded optics surface to determine replication accuracy and reproducibility. This was achieved employing a 3D profiling system consisting of a chromatic confocal sensor to precisely measure the surface profile across the optic face. The results of this characterisation showed that the injection moulded optics displayed significant shrinkage and warping when compared to the mould surfaces (i.e. the desired FPM design). These undesired alterations are a result of shrinkage during the plastic setting stage. As such, this method is not expected to form the accuracy required, without compensating for alterations from the mould.

Additionally, this characterisation could determine the reproducibility between multiple optics, achieved by scanning each optic to produce xyz data grid over the same region on each. For each data point a least-squares fit is performed using the 'ideal' surface data as a reference. Overall this study showed a significant non-uniform deviation from part-to-part, with an root-mean-square (RMS) variation over the optical region of up to 5.4 μm (+14/-20 μm peak-to-valley). A mean RMS variation over the optical region of 0.72 μm was measured. As these optics are for employment on the Vulcan-PW laser (operating at λ_L= 1.053 μm), this RMS variation in reflection would therefore be on the order of the λ_L. Achieving optical performance close to the diffraction limit requires wavefront variations far less than the laser wavelength, typically of

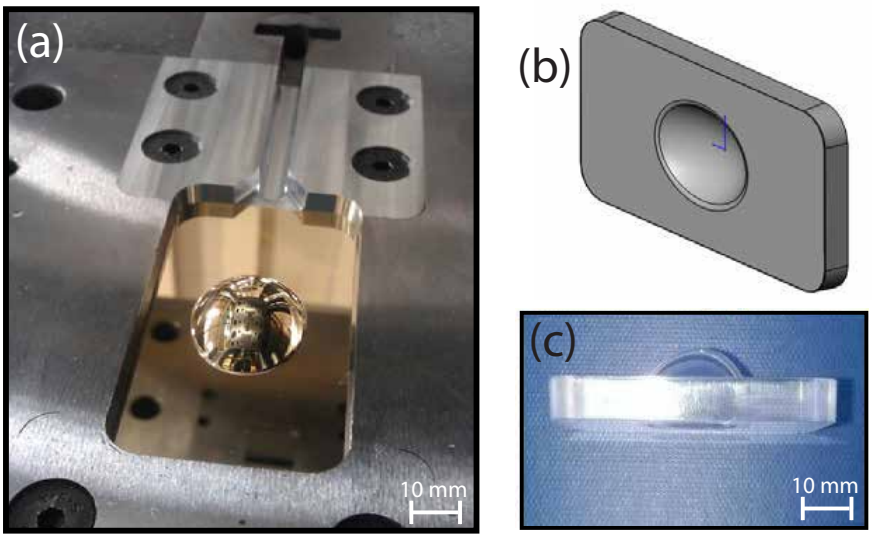

Figure 4.7: (a) Ultra-precise machined mould cast used in the injection moulding process, mounted in the injection moulding tool. (b) Schematic drawing of the injection moulded optic. (c) Photograph of the produced injection moulded FPM optic.

the order $\lambda_L/10$. Thus, the surface quality of these optics is not expected to achieve the high quality focusing required to enhance the intensity.

To summarise, the large magnitude of measured form errors of the moulded optics was deemed significant enough for this manufacturing technique to be ruled out as a viable option for production, as the required focusing performance, i.e. close to the diffraction limit of NIR wavelengths, would not be met. Moreover, even with compensation of shape errors, which is currently difficult to implement as the simulation tools required for predicting the required compensation to the mould are inadequate at the tolerances required, the weak reproducibility between optics was also a key factor in this method not being feasible.

(2) Diamond machining

Owing to the limitations of the injection moulding manufacturing route, another option was selected for FPM manufacture. As seen form the injection moulded technique, issues arose from the plastic injection stage, not from the ultra-precise machining of the mould itself. As such, ultra-precise single-point diamond machining was selected, to directly manufacture each optic, by a specialist optical machining company (Durham Precision Optics). Single-point diamond turning is a technique capable of producing sub-micron accuracy, even on steep free-form surfaces, as in the case of the FPM design. The method consists of cutting the optic material with a diamond tool which

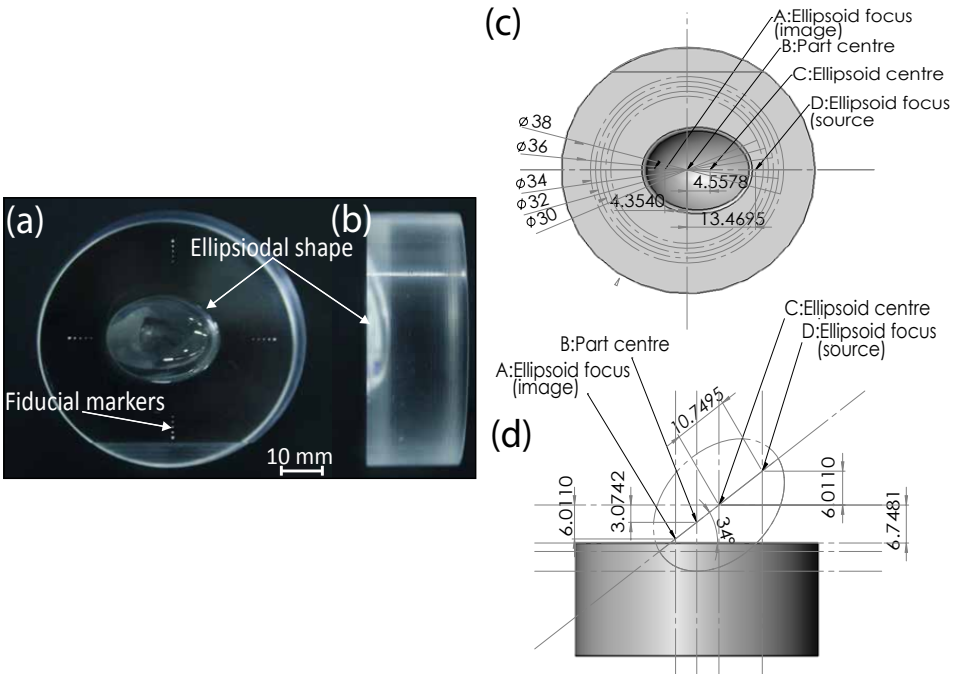

Figure 4.8: (a) and (b) Photographs of the manufactured diamond machined FPM optic showing: (a) the front surface and (b) a side view, demonstrating the ellipsoidal structure. The fiducial markers highlighted are used for alignment of the optic. (c) and (d) Schematic drawing of the FPM design, again showing (c) the front surface and (d) a side view; both annotated with the relevant geometry positions.

has xyz-translation, while the optic being machined rotates instead of the tool, to cut the desired shape. Figure 4.8(a)-(b) shows a picture of the final manufactured optic produced using the machining approach. The ellipsoidal shape was machined into the middle of a 2 inch diameter reference flat (machined flat), to ensure accurate design reproducibility. As in the injection moulding case, transparent PMMA plastic was selected as the FPM material. The optic diameter was selected for mounting in a conventional 2 inch optic mount. A thickness of 20 mm was chosen to provide sufficient rigidity, minimising surface distortions which may be induced via mounting. Additionally, the FPM mechanical aperture was over-sized to increase the surface acceptance angle, allowing the optic to work with various input angles, and thus magnifications (as described in Eq. 4.4).

The path the tool takes while machining is of key importance in minimising tool position errors. For example, the use of a circular path when forming an elliptical aperture is not optimal as cutting will be interrupted, leading to larger axial tool displacement, and the potential for increased shape error. As such the manufacturers of the FPMs used a proprietary software program to generate an optimal tool path which

minimises tool movement. The result is a tool path starting at the center of the optic with a circular spiral trajectory when cutting the reference flat surface then altering to an elliptical spiral path when cutting the optic design, with the tool never leaving the surface, minimising production time. The ellipsoid shape has been designed to have a zero gradient at the centre to avoid possible cutting artefacts induced by residual tool offset and tool height, as reported in Bourgenot *et al.* [188].

To summarise, this method is capable of accurately and precisely manufacturing the desired FPM design, with shape variation of the desired scale for achieving optical performance close to the diffraction limit (i.e. $\lambda_L/10$). The following section will present the optical testing of the FPMs manufactured employing this process, focusing on the optic's reflectivity, output focal spot characterisation, reproducibility from optic-to-optic and the sensitivity to alignment.

4.6 Optic reflectivity testing

At this point in the discussion it is useful to present the 'cold' reflectivity characterisation which was conducted on the manufactured optics. The 'cold' reflectivity is the optics reflectivity when it is not in the plasma state, behaving like a conventional partially reflecting solid-state optic. This parameter is important to quantify as the contrast enhancement factor of a plasma mirror is equal to the ratio of the plasma reflectivity to the cold reflectivity [189] (discussed in section 3.2.5), thus informing how the optic will perform in terms of temporal intensity contrast enhancement.

To achieve this measurement a spectrophotometer was employed. This device allows a measure of the intensity of light in a particular region of the EM spectrum reflected from a sample, for a given polarisation and incident angle (or range of angles), to be measured. Generally the region of the EM spectrum these devices operate in, such as the one utilised here, is that of visible light, near-UV, and near-IR. Figure 4.9 displays the spectrophotometer reflectivity results for the manufactured FPMs for p-polarised light, averaged over an incident angle range of 10°–50° (at 5° increments). This angular range ensures encompassing the full range of illumination angles of the diverging laser pulse in the optic design, 25°–45°. Additionally p-polarised light was selected as this is the polarisation configuration of Vulcan-PW pulses. At the operational central

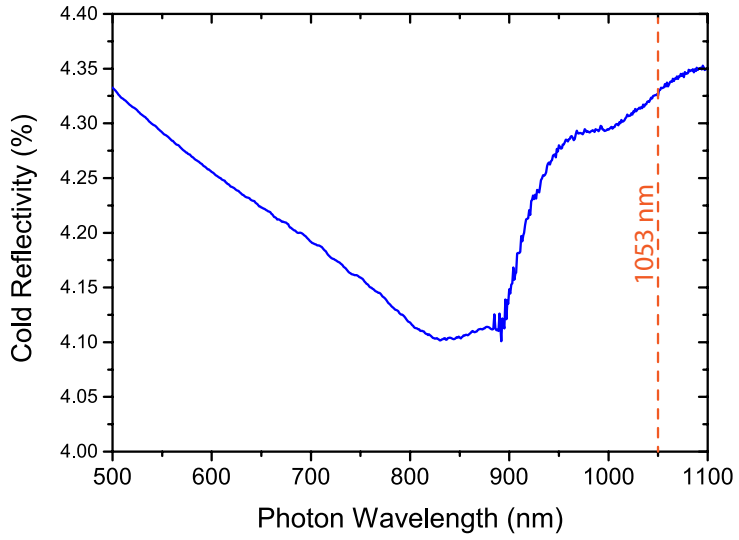

Figure 4.9: Plot showing the cold reflectivity of the manufactured FPM as a function of the incident photon wavelength, averaged over a range of photon incidence angles (10°–50°).

wavelength of Vulcan-PW laser, 1053 nm, the average reflectivity was measured to be (4.3±0.3)%. As such, for the value of plasma reflectivity predicted in the design stage, 70%, the optic would be expected to increase intensity contrast by a factor of ×16.3. The developed optics did not include an anti-reflective (AR) coating at the time of testing. Conventionally a plasma mirror includes an AR coating to minimise the magnitude of cold reflectivity, thus increasing its intensity contrast improvement ability. The cold reflectivity of an AR PM is ∼0.3% [143], giving approximately an order of magnitude higher contrast enhancement factor compared to the non-AR FPM design.

To characterise the plasma reflectivity of the selected FPM substrate material, the Vulcan-PW laser was used to measure the specular reflectivity of a planar plasma mirror (PPM), made from the same transparent PMMA material as the FPMs, as a function of incident laser intensity; thus checking that the selected switch-on intensity value from the optic design stage gives high specular reflectivity. The sample was irradiated with p-polarized pulses, at a 35° incident angle relative to the mirror surface (the same operational incident angle as the FPM). The peak laser intensity was varied by changing the distance between the optic surface and the laser focus, with a maximum intensity of approximately $\sim 10^{16}$ W/cm^2 achievable using ∼0.25 J pulses from the laser. These reduced energy shots allowed for a relativity quick succession between shots. The energy of incident and reflected light was measured using a Gentec pyroelectric energy

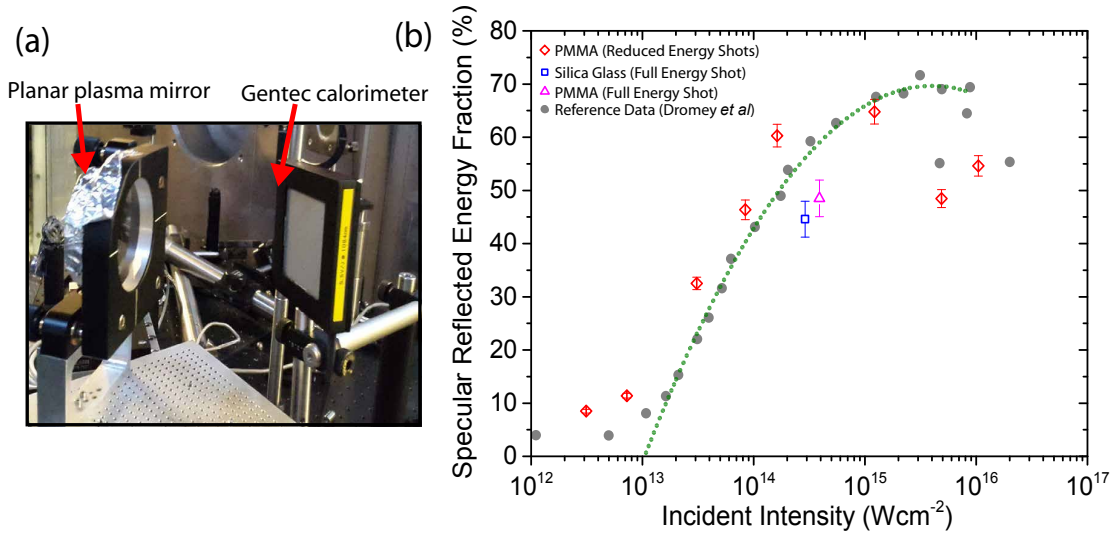

Figure 4.10: (a) Photograph of the set-up used to characterise the specular reflectivity of a planar plasma mirror, employing a calorimeter. (b) Percentage of laser light specularly reflected from the plasma mirror as a function of the laser intensity at the plasma mirror surface. Red data points are the results from reduced energy Vulcan-PW pulses on a flat PMMA sample and the grey points correspond to reference data from Dromey et al. [143] for a 500 fs pulse and a fused silica PPM, with 6° laser incidence angle. A quadratic fit is made to this data between the incident intensities of $10^{13}-10^{16}$ W/cm^2, as illustrated by the dotted green curve. The blue and pink data points represent full energy shots on flat samples of silica glass and PMMA, respectively. Each data point represents a single laser shot.

meter for absolute calorimetry, using the set-up shown in Fig. 4.10(a). The specular reflectivity as a function of incident laser intensity is shown in Fig. 4.10(b); where the data is compared to the results reported in Dromey *et al.* [144] (first displayed in Fig. 4.3). A peak specular reflectivity of (65±2)% was measured at an intensity of (1.2±0.3)×10^{15} W/cm^2. The overall trend of the reflectivity-intensity dependency is in good agreement with the data used to design the FPM [144], indicating there is little difference in terms of performance between a typically used substrate material (such as silica glass) and the plastic material chosen for the FPM design.

Additionally, two shots were taken employing the full energy capabilities of the Vulcan-PW system, one measuring the reflectivity of a silica glass PPM and the other a PMMA PPM. In contrast to the reduced laser energy data scan the reflectivity is found to be slightly lower at intensities in the range of 10^{14}–10^{16} W/cm^2 on these shots; from 46%−68% in the reference data, to 45%−55% in the experimental shots. This may be a consequence of the difference in laser incidence angle in the two data sets. The results presented in Dromey *et al.* [144] were conducted using a low incidence angle (6°) which would result in a reduced laser absorption when compared to the larger

incident angle (35°) used in the present investigation (as discussed in section 2.5.4). The reduced reflectivity for larger incidence angles has been observed in previous studies, which conclude that this arises due to increased absorption [141, 149].

4.7 Optic Testing: Non-plasma regime

An experimental set-up employing a low-power continuous wave (CW) laser was developed to characterise the manufactured diamond machined FPM design; as shown in Fig. 4.11. This enabled the focal spot reduction/quality to be quantified and the feasibility of the use of such an optic for laser-target interaction studies to be accessed. This set-up was not only used for FPM characterisation but additionally employed to pre-align the optics prior to use on the Vulcan-PW laser (discussed further in section 4.8.1). In this low-power illumination mode the substrate is not ionised and thus the optic simply functions as a conventional partially reflecting solid-state optic ('cold' reflectivity discussed in 4.6).

To emulate the Vulcan-PW F/3.1 input focusing beam, an OAP (f= 145 mm) in conjunction with a 48 mm diameter collimated input beam was selected. A 532 nm wavelength (green) laser diode was used as the light source and was propagated through a spatial filter (consisting of a ×10 microscope objective focusing through a 5 μm pinhole) prior to focusing to improve the spatial-intensity profile of the beam, thus producing a higher quality focal spot. This laser wavelength was selected for testing as it is much lower than the operational wavelength (1053 nm) of the Vulcan-PW laser system, and thus will aid in determining if there are any unwanted irregularities in the optic's focusing, which would be displayed more prominently with smaller wavelengths. To measure the focal spot formed by both the OAP and FPM, an infinity-corrected microscope objective (×50 and numerical aperture (N.A.)= 0.42) was used to image the spot to a CCD (charge-coupled device) camera (commercial available AVT Marlin) capable of 16-bit image capture. Moreover, this objective also has a 25 mm working distance (separation between initial lens and image plane), approximately double that of a typical microscope objective, necessary to allow for the imaging of the spot formed at position f_2, and importantly, not touching the face of the optic, due to the focus position being close to the FPM face. For alignment and imaging purposes the FPM, OAP and

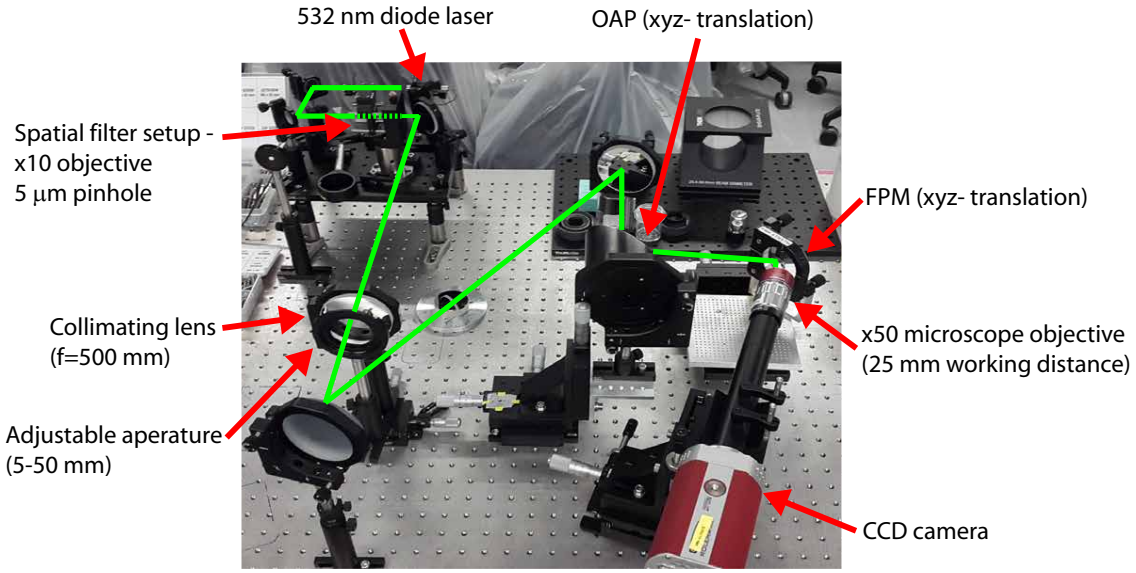

Figure 4.11: Photograph of the experimental set-up developed to characterise the manufactured focusing plasma optics in non-plasma operation, where the main components have been annotated and the beam path displayed in green.

camera set-up were mounted on micrometer controlled xyz-translation stages, where the z-axis of the FPM motion was set along the direction of the OAP input beam; an extremely useful choice of axis, as optic alignment complexity is considerably reduced. As such, the FPM is mounted at an angle relative to the input beam to ensure the correct input angle, θ_{In}, is satisfied. The FPM itself was mounted using a conventional 2-inch (front mounted) optic mount to give additional motion control (tip and tilt), and the ability to rotate the optic within the mount.

Once the OAP focal spot is optimised, the FPM set-up could be added and aligned by translating it's xyz-position, while monitoring the output focal spot (i.e. at f_2). The end goal of this process being optimum alignment, i.e. when the OAP focus spatially coincides with the first FPM focus, f_1. This will be examined below, before discussing the optics sensitivity to non-optimum alignment, i.e. misalignment. This latter case will also cover the FPM alignment process in greater depth.

4.7.1 FPM optimum alignment

Characterisation of the manufactured optics was conducted by analysing the output focal spot formed under optimum alignment, as mentioned, occurring when the OAP input focus spatially coincides with the FPM focus, f_1. Figures 4.12(a)-(b) presents the

results of the input focal spot, formed by the OAP, and an example result for one of the optics. This testing established that the typical output focal spot formed by the FPM, displayed in Fig. 4.12(b), is 0.76 μm (FWHM), with 28.3% energy encircled within the FWHM diameter. Encircled energy is a useful parameter to gauge the quality of a focal spot, and to use when calculating the peak intensity which it may produce. As the input focal spot, shown in Fig. 4.12(a), is 1.91 μm (FWHM) with 35.1% FWHM encircled energy, a demagnification of $\times$2.51 is achieved by the optic. The reduction in encircled energy at f_2 is a consequence of more energy present in the spot wings relative to that within the spot FWHM, and may be attributed to small optic misalignments, inherent deviations in the optics shape from optimal design, or purely due to the nature of a small F/# optic focusing close to the diffraction limit. It should be noted that this encircled energy is significantly larger than the 17% achieved by the FPM fielded in the first proof-of-principle experiment reported in Ref. [183]. Variation from the theoretically predicted demagnification, of $\times$3 for this FPM design, may have resulted due to a slightly higher beam input angle in this test. This would produce a smaller demagnification (according to Eq. 4.4), or may resulted from inherent alterations from the ideal optic design occurring during the manufacturing process.

Employing the above FPM characterisation results, the expected laser intensity enhancement factor, I_{Enh}, when using this optic in plasma operation mode on the Vulcan-PW system can be estimated. This parameter depends on the input (ϕ_{in}) and output (ϕ_{out}) spot sizes, the FWHM encircled energies (E_{in} and E_{out}, respectively), and the optics plasma reflectivity (Γ_p), as follows;

$$I_{Enh} = \left(\frac{\phi_{in}}{\phi_{out}}\right)^2 \cdot \Gamma_p \cdot \left(\frac{E_{out}}{E_{in}}\right) \tag{4.5}$$

For a plasma reflectivity of 70% (anticipated from the optic design), the intensity enhancement implied from testing, in Fig. 4.12(a) and (b), is $\times$3.6. The minimum plasma reflectivity at which enhancement is still achieved is 19.7%, i.e. I_{Enh}= 1, the point where the intensity of the input focal spot equals that of the output. In terms of the energy contained within the output focal spot FWHM, enhancement would begin for values exceeding 7.9% for E_{out}, in the 70% reflectivity case.

To further characterise the optic design, and test its feasibility for use in laser-foil interaction studies (its primary use), the experimental characterisation set-up was

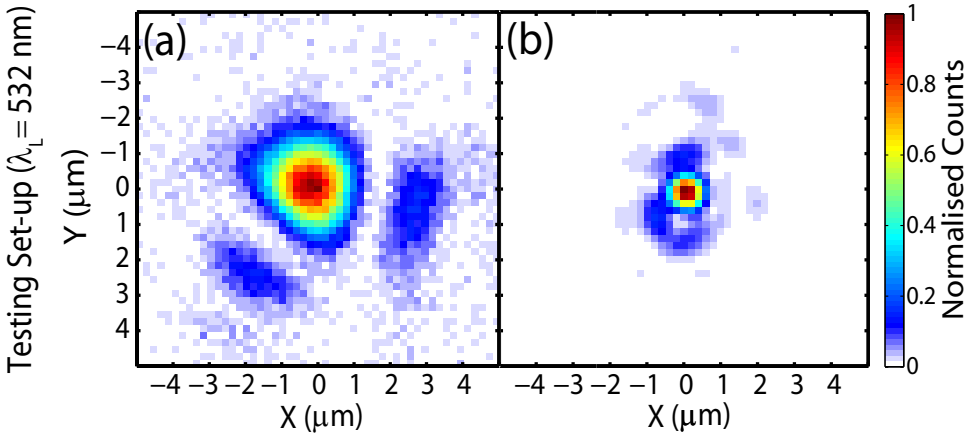

Figure 4.12: Measured laser focal spot spatial-intensity distributions at positions (a) f_1 (formed by OAP) and (b) f_2 (formed by FPM) using the characterisation set-up (with 532 nm light).

used to record the spatial-intensity distribution for both the FPM output beam and the input beam, formed by the OAP for comparison, at incremental positions 50 μm either side of the best focus along the beam propagation axis. The results are displayed in Fig. 4.13(a)-(b). It is clear from these images that the beam geometry achieved by the FPM converges (Fig. 4.13(b)), and diverges, relatively faster from best focus compared to the equivalent input beam positions (Fig. 4.13(a)). This is expected as a reduction in beam F/#, must be partnered with an increase in beam divergence. Additionally, it is evident when comparing the beams that a clear asymmetry exists in the spatial-intensity distribution in the case of the FPM (Fig. 4.13(b)), in both the experimental and ray-trace modelling results. This contrasts with the relatively symmetric distribution either side of focus obtained with the OAP beam (Fig. 4.13(a)). In typical laser-foil interaction experiments a conventional OAP is generally employed as the sole focusing optic. When the situation calls for a target to be irradiated in a defocussed position, the asymmetry present in the FPM's output beam spatial-intensity profile, may not be ideal, as the dynamics of the interaction will be altered.

While testing the initial batch of FPMs approximately only 60% of the batch displayed the high quality output focal spot displayed in Fig. 4.12(b). Figure 4.14(a) displays the typical focal spot achieved with a sub-optimal quality FPM, which will be referred to as 'Optic A', compared to the focal spot produced by the optics operating to specification (Fig. 4.14(b)), referred to as 'Optic B'. A prominent difference in the distribution of focal spot energy is seen when comparing Optic A and B cases. Optic A (Fig. 4.14(a)) exhibits a considerable drop in energy encompassed within the central

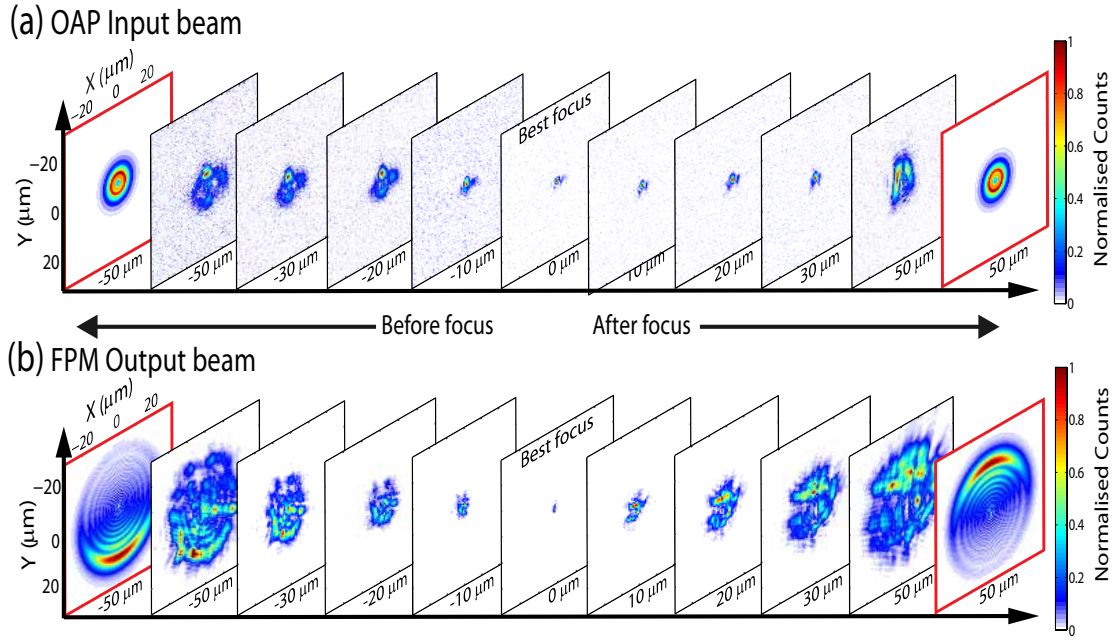

Figure 4.13: Images of the beam spatial-intensity distributions as a function of distance from best focus, for (a) OAP input beam and (b) FPM output beam, obtained employing the characterisation set-up (with 532 nm light). The relative distance from best focus is displayed below each image (0 μm indicating position of best focus). In both cases the panels highlighted in red display ray-trace modelling results of the experimental data range extremities.

spot. Significant energy is instead found to be in multiple rings surrounding the focal spot. To quantify, Optic A forms a focal spot with 5.1% energy encircled within the FWHM diameter, a ×5.5 reduction compared to Optic B case (28.3% FWHM encircled energy). Accordingly intensity enhancement would not be achieved for Optic A. The explanation for this alteration between optics becomes clear when characterising the FPM output focal spot as a function of varying input beam F/#. Modification of the F/# will alter the divergence of the input beam, and hence the area illuminated on the optic surface. This was implemented in a controlled manner through a variable aperture included in the test set-up to control the diameter of the collimated beam prior to the OAP. Figure 4.14(c) displays the results of changing the input F/# in terms of the resultant output focal spot encircled energy for each optic case. At small input F/# the optics have vastly different values, however as the F/# increases the values become broadly similar. This trend suggests a shape error in the optics geometry leading to the low quality focal spot, which is only seen when a relatively large area of the optic is illuminated (i.e. small F/#).

To correct this issue, optics displaying this low quality nature (Optic A case) were re-machined (using the diamond turning process) to the desired shape, after which they

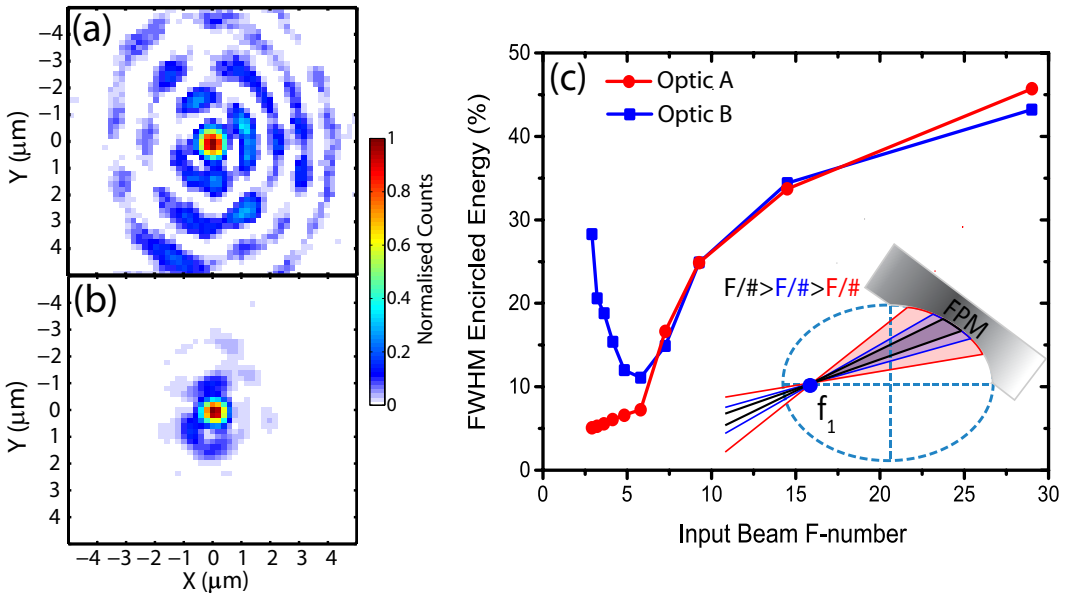

Figure 4.14: (a) and (b) typical measured spatial-intensity distributions of the optimised focal spot formed by (a) Optic A and (b) Optic B, each of varying quality, using the characterisation set-up (with 532 nm light). (c) Plot quantifying the change in output focal spot FWHM encircled energy as a function of input beam F-number, were blue represents a Optic B and red a Optic A. Insert schematic displaying the concept of input beam F/# change on illuminated area on the FPM surface, with black the largest F/#, and red the smallest.

exhibited higher quality focal spots, approximately the same as those achieved by Optic B (Fig. 4.14(b)). This highlights the sensitive nature of the manufacturing process and the need for pre-characterisation of each optic before use.

4.7.2 FPM sensitivity to misalignments

As discussed, FPM operation depends strongly on optimised alignment, as in the case presented in Fig. 4.12, reliant upon the OAP focus spatially coinciding with the ellipsoid's first focus, f_1, and thus accurate optic positioning. It is therefore crucial for successful FPM operation to explore and quantify the effect of misalignments on performance. Variations in the OAP focus position, on the μm scale, may occur on high power laser systems due to various effects, including thermal lensing in the laser chain, which can alter the divergence of the incoming pulse prior to focusing, effectively shifting the OAP focal length.

To test the effect of unoptimised FPM alignment the testing set-up was employed to implement controlled displacements in the OAP focus position, relative to f_1, for the three possible displacement directions, Δx, Δy and Δz. The effect of these dis-

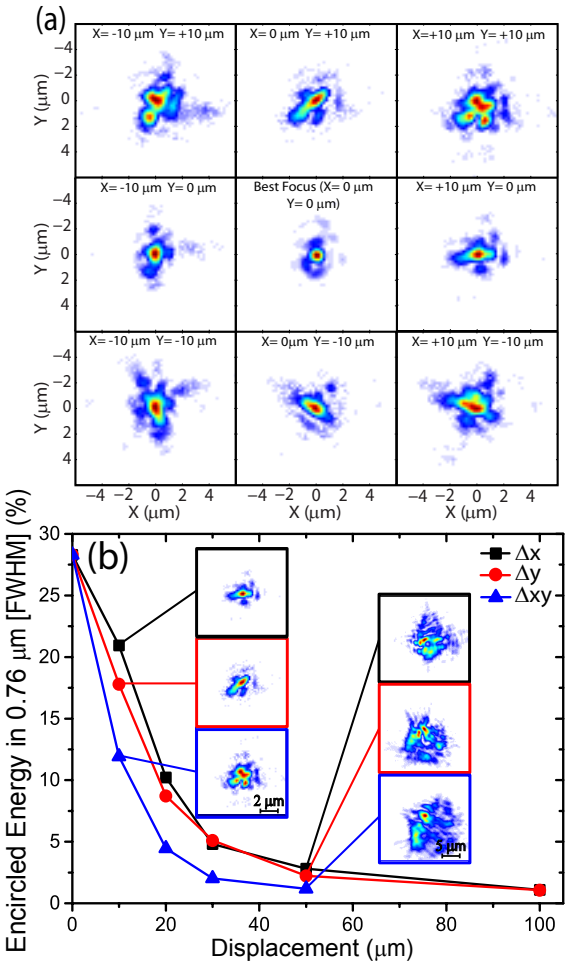

Figure 4.15: (a) Spatial-intensity distribution of the output focus as a function of ±10 µm x, y and xy OAP focal spot displacement from optimal alignment (at f_1). (b) Plot of the output focus encircled energy percentage contained within a circle of diameter equal to the FWHM optimised focal spot (i.e. 0.76 µm), as a function of these displacements from position f_1. Black symbols correspond to Δx, red symbols correspond to Δy, and blue symbols correspond to Δxy (equal magnitude in x and y) displacements.

placements was analysed by recording the resultant output focus and quantified by measuring the percentage of focal spot energy contained within a circle of diameter equal to the FWHM of the optimised focus (Fig. 4.12(b)), that being 0.76 μm FWHM. Figure 4.15(a) shows the output focal spot as a function of x, y and xy displacements from optimal alignment (also displayed, represented by 0 μm) in ±10 μm steps, and Fig. 4.15(b) quantifies the effect of misalignments in terms of encircled energy for displacements in the range of 0–100 μm from f_1. It is evident that displacements in Δx and Δy result in the quality of the output focus being rapidly degraded. Results indicate that intensity enhancement may only be achieved for displacements of <10 μm, for misalignments in only one axis (Δx or Δy). Above this value, and for misalignments

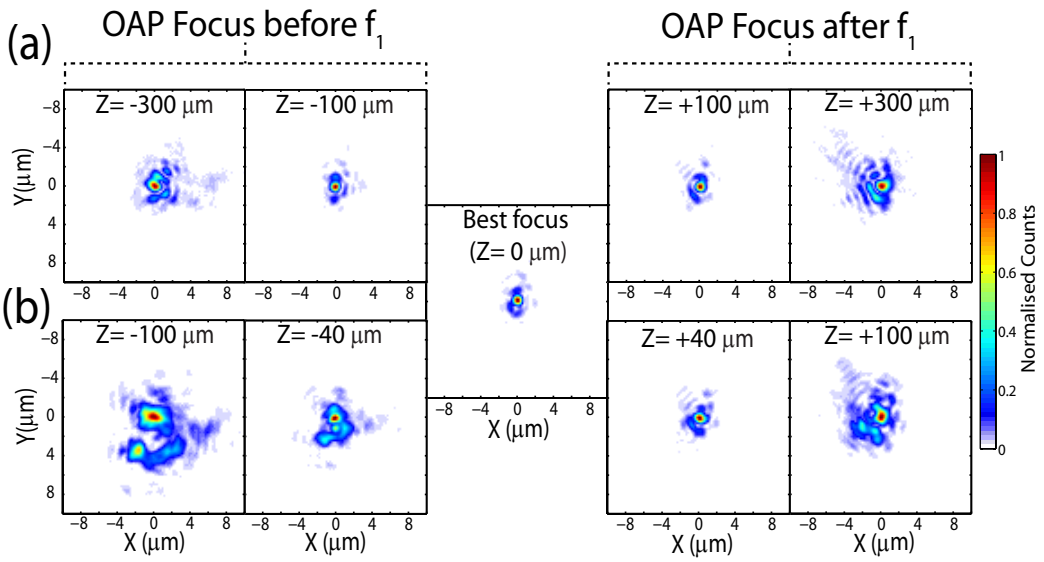

Figure 4.16: (a) and (b) Spatial-intensity distributions of FPM output focus as a function of OAP focus shift in the z-direction, from optimal position f_1, for (a) the case in which objective lens imaging the output is translated to account for displacement, and (b) when objective lens is fixed at position f_2.

in both axis simultaneously (Δxy), the focal spot quality is sufficiently degraded that no intensity enhancement will be achieved.

Figures 4.16 and 4.17 presents the effect of longitudinal OAP displacement, Δz, where, as stated earlier, FPM z-motion is along the direction of the OAP input beam. A displacement of this form results in the output image position, nominally at f_2, being displaced. Accordingly this misalignment can be characterised in two ways: (i) where the objective lens imaging the output is translated to account for the displacement, and (ii) where the objective lens is fixed at position f_2. The latter case being analogous to an interaction target placed at the nominal focus position, and is thus important to characterise for practical use of the optic.

For the case when the objective lens is translated to the effective best focus position, Fig. 4.16(a) and Fig. 4.17 (black data), the output focal spot quality remains relatively high in comparison to the other misalignment forms, i.e. Δx and Δy, over a larger range of displacement. Intensity enhancement (for a 70% reflective PM case) is achieved over a ± 300 μm range either side of the optimum alignment position. However, as the magnitude of misalignment is increased, the degree of energy being transferred to the spot extremities increases, resulting in no enhancement due to a lowering in focal spot quality. Characterisation of this misalignment form, and the Δx, Δy, and Δxy cases, are highly beneficial as the degree and direction of energy spread present relates to the direction and magnitude of the misalignment. This consequently aids in the alignment

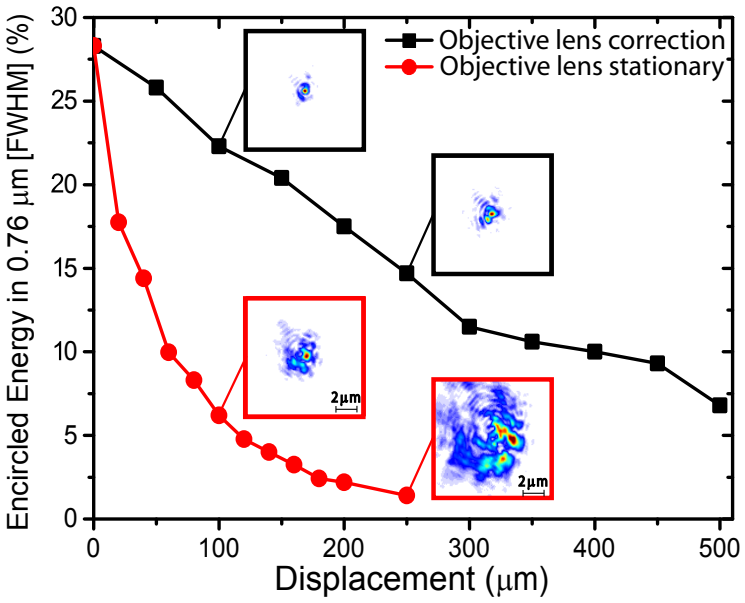

Figure 4.17: Plot of the output focus encircled energy percentage contained within a circle of diameter equal to the FWHM optimised focal spot (i.e. 0.76 µm), as a function of these displacements from position f_1. Black symbols correspond to the case where objective lens is translated to account for displacement, and red symbols correspond to the stationary objective case, imaging position f_2.

process which aims at achieving an optimised focal spot.

Results for the second case, when the objective lens remains fixed at position f_2 during the OAP displacement, are presented in Fig. 4.16(b) and Fig. 4.17 (red data). Intensity enhancement is only possible for displacements <30 μm, due to a relatively faster degradation of the focal spot quality. This is expected as the objective does not move to the new optimal image position.

As this misalignment case is analogous to an interaction target placed at the nominal focus position, this form of misalignment would have severe consequence on the peak interaction intensity. It is therefore essential to have a measure of the magnitude of longitudinal displacement in the OAP focus position from nominal (which the FPM is aligned to) which may occur on the Vulcan-PW laser to validate the use of the optic with this laser. To achieve this a Shack-Hartmann wavefront sensor was employed (see section 3.4.2) to measure the degree of phase aberrations (non-ideal focusing from the OAP) present in the laser wave-front through a beam leakage during the pulse compression stage. This measurement is critical to gauge if the use of an FPM is beneficial in terms of intensity enhancement, or if shot-to-shot fluctuations in the wavefront are too large to reliably achieve enhancement.

Fluctuations in the OAP focus position were measured over a series of full energy

shots, with average values <20 μm obtained. The resultant displacement from position f_2 to the effective best focus, Δv, as a function of this shift, Δu, is found to be equal $\Delta v = -m^2 \Delta u$ (m being the FPM magnification [m=1/3]). This is confirmed both experimentally, using the test set-up, and through the ray-trace model. A value of Δu= 20 μm would therefore yield a 2.2 μm displacement in the output focus position. The consequence of this is that a target aligned to the nominal focus would be irradiated with a pulse with a factor $\times$2.3 peak intensity reduction (from 3.4×10^{21} to 1.5×10^{21} W/cm^2). This would still result in an intensity enhancement over direct irradiation with the F/3.1 OAP. This analysis demonstrates the importance of monitoring the degree of OAP focus position displacement when using an FPM in order to assess its operation and quantify the level of intensity enhancement achieved.

4.8 Optic Testing: Plasma regime

The next stage of FPM testing, having characterised the focal spot distribution and encircled energy at low power, was to investigate its performance in terms of intensity enhancement under plasma conditions using the Vulcan-PW laser. As the focal spot formed by the optic cannot be directly measured by a CCD camera during a full power laser shot (i.e. when used in plasma operation), and there is no easy way to 'dump' or filter out energy due to the rapidly expanding beam size, the success of the FPM in enhancing the focused intensity was indirectly diagnosed via measurements of the maximum energy of protons accelerated from foil targets irradiated at f_2 (as in the previous demonstration experiments [180, 181]). The laser-plasma acceleration mechanism utilised is known as target normal sheath acceleration (TNSA) [14]; the theory of which is presented in section 2.7.1. To summarise, protons are produced and accelerated by a strong electrostatic field formed at the target rear surface by fast electrons produced at the target front side and transported through the foil. The maximum proton energy achieved via this mechanism is correlated to the peak laser intensity [107, 113], via the temperature and density of the fast electrons [102].

This section covers the experimental set-up and method used to investigate proton acceleration employing our novel focusing optic, and presents the results of the maximum proton energy achieved in this testing.

4.8.1 Experimental method

Proton acceleration measurements were made using either a FPM or a planar plasma mirror (PPM), both made from the same material (PMMA). The PPM shots were necessary to acquire reference proton beam measurements with the same reflectivity and intensity contrast enhancement, to gauge the FPM performance in terms of it's comparison to solely F/3.1 OAP focusing. P-polarised pulses incident at target normal to aluminium target foils with thickness of 6 μm and transverse dimension 1×1 mm were used throughout. Accelerated protons were detected using a stack of dosimetry radiochromic film (discussed in section 3.4.1) [190], positioned 50 mm behind the target foil and centred on the target normal axis. Each layer is filtered with increasing thicknesses of Mylar (at the low proton energy end of stack) or copper (at the higher end) to enable spectral measurements. Finally, a thin layer (13 μm) of aluminium foil is placed at the stack front in order to filter out heavy ions and laser light. This enables proton energy measurements to be made at discrete energies, ranging from 1.1 to 86 MeV.

To quantify the degree of OAP focal spot displacement from optimal position, f_1, along the z-axis, once again the Shack-Hartmann wavefront sensor (see section 3.4.2) was employed to measure the degree of phase aberrations (as discussed in 4.7.2). As seen from the non-plasma testing, this measurement is crucial for gauging FPM performance in terms of the peak intensity it achieves on target, and thus highly important for the scaling of the resultant maximum energy of laser-accelerated protons.

Before a FPM is mounted in the Vulcan-PW target chamber (Fig. 4.19) it is pre-aligned using the characterisation set-up described in section 4.7. This involved first optimising the FPM output focal spot, as for the case in Fig. 4.12, i.e. spatial overlap of the OAP focus with the ellipsoid's first focus, f_1. Once achieved it is then necessary to mark this overlapping position, as this defines the position the focus of the OAP inside the target chamber will need to be located. To achieve this, a glass fibre (7 μm diameter) mounted on an xyz-translation stage and attached to the same mounting board as the FPM was used to define position f_1 by obscuring the input focal spot. This fibre set-up relative to the optic is shown in Fig. 4.18.

Only after the pre-alignment steps were complete could the set-up board be transferred to the target chamber. This was mounted on a high resolution xyz-stage (on a

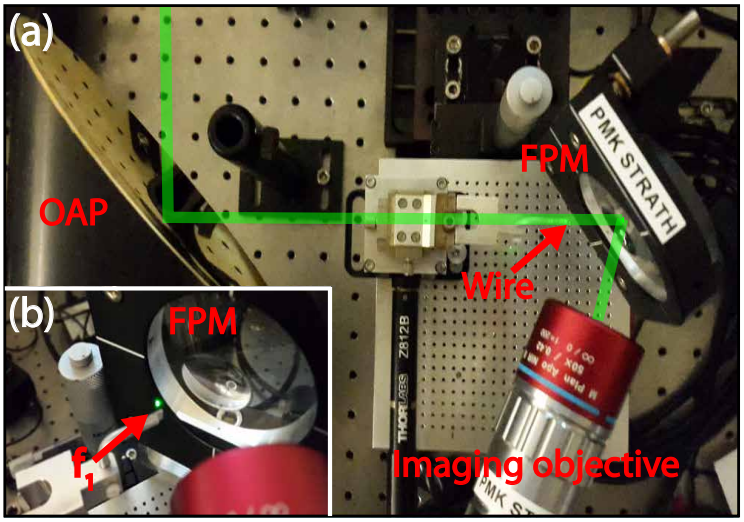

Figure 4.18: (a) Photograph of the set-up used to pre-align a FPM before transferring to the Vulcan-PW vacuum chamber, where a 7 μm diameter wire is used to define position f_1, through obscuration of the OAP focus. (b) Photograph showing the alignment wire situated at position f_1, scattering green light from the OAP focus.

kinematic base) for precise FPM positioning, giving the equivalent freedom of motion as used for optic alignment in the test set-up. Pre-alignment, and importantly defining position f_1, was necessary as it greatly reduces optic alignment time and complexity, within the target chamber, meaning that the total alignment time is less than the typical time between high power shots, or close to that of experiments not employing the complex beam geometry of a FPMs.

To align the Vulcan-PW OAP focal spot to the pre-alignment wire (defining position, f_1) the systems retro-reflection capabilities were employed to image the reflected laser light from the wire, which goes back up the laser path, brought to focus and monitored. In doing so, the FPM set-up could be translated to place the OAP focus at the tip of the wire. After this the wire was translated out of the beam path using a goniometer stage (so as not to impede optic irradiation), and final alignment of the FPM and target was performed. Figure 4.19 shows an overview of the experimental set-up for both the FPM ((a) and (c)) and PPM ((b) and (d)).

4.8.2 Experimental results

Before investigating laser-driven proton acceleration using the FPM design, the optic was first characterised in terms of optical demagnification and output focal spot quality

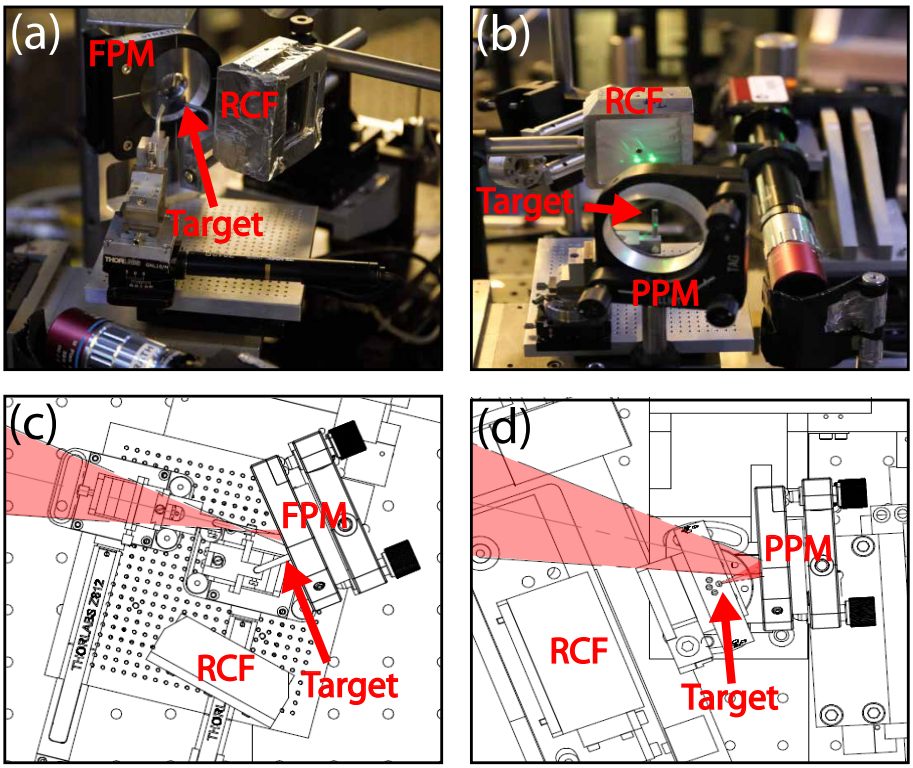

Figure 4.19: (a) and (b) Photographs of the experimental set-up employed to quantify the maximum energy of laser-accelerated protons from a 6 μm thick Al target, using a RCF stack, for (a) a focusing plasma mirror and (b) a planar plasma mirror, using the Vulcan-PW laser. (c) and (d) equivalent schematic drawings of the set-ups in (a) and (b), respectively.

(similar to the test set-up characterisation below the ionisation threshold), for operation on the Vulcan-PW laser. Figure 4.20(a)-(b) displays the typical input and output focal spots achieved under optimised CW alignment. This differs from the testing set-up in that this laser has a central wavelength of 1053 nm, thus both input and output spots are relatively larger in comparison to the 532 nm characterisation set-up. A factor of ×2.5 reduction in the spot FWHM (from 4.0 μm input to 1.6 μm output) and an increase in the FWHM encircled energy from 28.1% to 36.5% are measured. This FWHM encircled energy value for the output focus is a factor of 2.2 higher than earlier proof-of-principle experiments [181]. These measurements are in good agreement with the earlier tests using 532 nm light (Fig. 4.12). Quantifying these results in terms of intensity enhancement indicates that a calculated peak intensity equal to 3.4×10^{21} W/cm^2 could be achieved using the Vulcan-PW laser parameters, giving a factor of ×5.3 intensity enhancement over standard OAP focusing.

With confidence that the optic performs as expected in non-plasma mode, it was then used in plasma operation, with full power shots, to investigate laser-driven proton

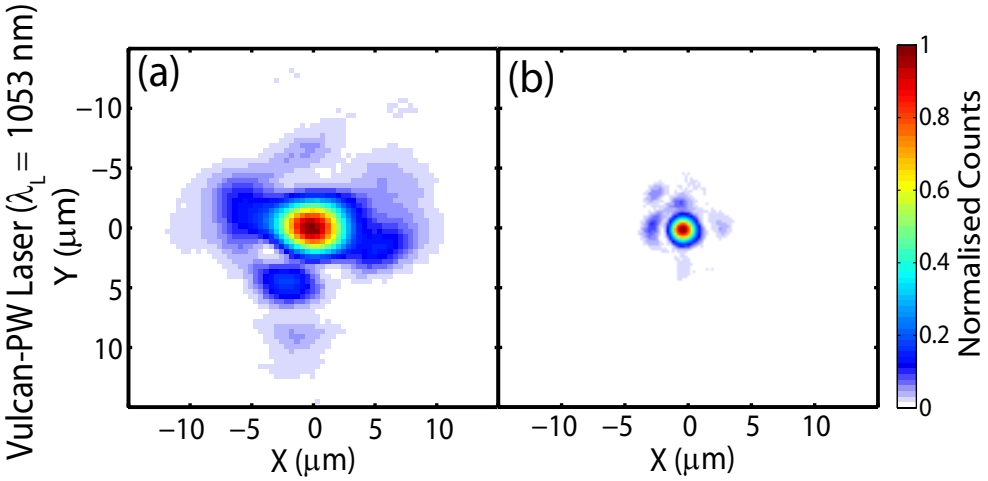

Figure 4.20: (a) and (b) Measured laser focal spot spatial-intensity distributions at (a) f_1 and (b) f_2, using the Vulcan-PW laser, with low power (CW operation) 1053 nm light.

acceleration. Figure 4.21(a) summarises the results of the maximum proton energy obtained for a series of test shots using both plasma mirror types, irradiating 6 μm Al targets. A maximum proton energy in the range 24.9−53.1 MeV was measured for all shots employing FPMs, and 19.7−29.0 MeV was measured for PPM shots. Comparing the maxima of these ranges, an enhancement of almost a factor of 2 was achieved by employing the FPM, compared to solely F/3.1 OAP focusing. This increase occurs with a calculated intensity enhancement factor of ×2.6 (from 3.9×10^{20} W/cm^2 to 1.0×10^{21} W/cm^2). It should be noted that the intensity achieved using the FPM is lower than that predicted from CW characterisation, presented in Fig. 4.20, (3.4×10^{21} W/cm^2), due to a lower on-target pulse energy on the experimental shots than that used to calculate the predicted value. This was caused by a lower than expected energy throughput from the compressor stage of Vulcan. Additionally, the optic reflectivity was measured to be ∼63%, lower than the 70% value used in the calculation of the predicted intensity.

Further, it is seen in Fig. 4.21(a) that not all of the FPM shots resulted in enhanced proton energies. This arose from a lowering of on-target intensity, caused by a thermal-lensing-induced non-optimum alignment occurring from a longitudinal shift in the input focus position, characterised in Fig. 4.21(b) for each FPM shot. On each FPM shot, the wavefront quality of the pulses was characterised using the Shack-Hartmann sensor to gauge the magnitude of misalignment which the optic is subject to. The changes in the output focal spot size and encircled energy, as characterised in section 4.7.2, are used in the calculation of the resultant intensity on-target (the values plotted in

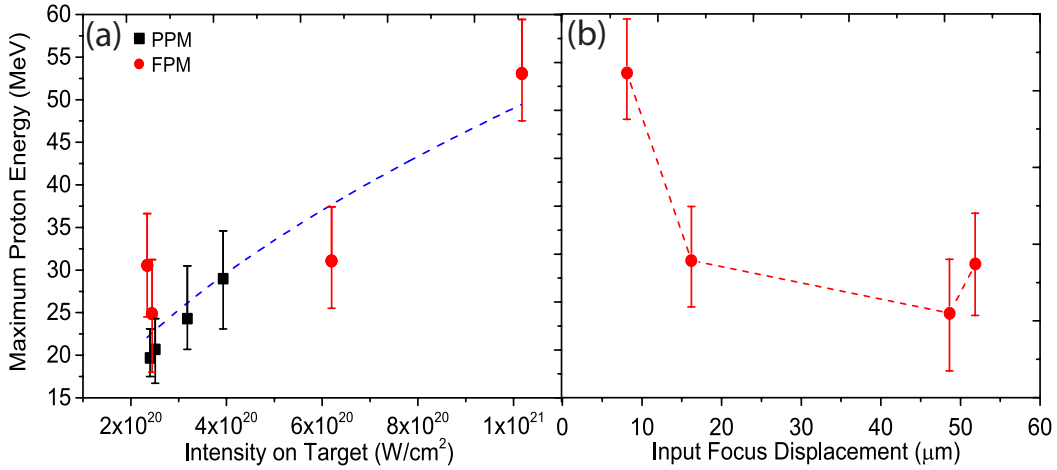

Figure 4.21: (a) Plot of the measured maximum proton energy achieved using both FPMs (red circles) and PPMs (black squares), as a function of the laser intensity (I_L) on-target, taking into account the displacement in OAP focus position. In the PPM case intensity was varied by changing the pulse energy. The blue dashed line represents a simple power fit (of the form $E_{pmax} = a.I_L^b$) to show the approximate scaling of maximum proton energy with peak laser intensity. (b) Plot of the measured maximum proton energy, achieved using FPMs, as a function of the longitudinal displacement measured in the input focal spot position from f_1.

Fig. 4.21(a)). The FPM shot which achieved the highest proton energy (53.1 MeV) was measured to have the smallest OAP focus from position f_1, thus displayed close to optimum alignment, compared to the other FPM data points which yielded lower proton energies, as shown in Fig. 4.21(b). It is clear that the reduced maximum proton energy on some FPM shots occurred due to the peak intensity being reduced to a similar level as that achieved with the PPM shots. A simple power scaling fit to the complete data set in Fig. 4.21(a), of the form $E_{pmax} = a.I_L^b$, results in $b = (0.55 \pm 0.1)$. This scaling is in good agreement with the TNSA proton energy scaling reported in Refs. [107, 113], in which the maximum proton energy is found to be proportional to the fast-electron temperature, which scales with the ponderomotive potential $\left(\propto \sqrt{I_L \lambda_L^2}\right)$ [79]. However, it should be noted that even when correcting for the reduction in intensity due to longitudinal misalignment of the OAP focus with respect to the FPM input focus, the FPM data does not follow the TNSA scaling fit as strongly as the PPM data. This may point to other sources of error affecting the peak intensity achieved, for example in the accurate positioning of the target at the output focus (f_2) of the small F/# beam due to the very small Rayleigh range of the optic ($\sim$5.5 μm). Additionally, OAP focal spot displacement from the optimised position in the x and y directions (as presented in Fig. 4.15) may also be occurring, which are not quantified.

These plasma operation test results indicate that the FPM does successfully en-

hance the intensity when optimally aligned, as indicated by the factor of 2 increase in maximum proton energy, but, additionally, that successful operation crucially depends on minimising the displacement of the input focus with respect to position f_1.

4.9 Conclusion

To conclude, the design, testing, and demonstration of a novel focusing plasma mirror, based on ellipsoidal geometry, for the tailoring of a ultra-intense laser pulse in terms of focal spot size and temporal intensity contrast was presented.

The design of such an optic was reported, involving optimisation of the incident laser intensity to maximise the plasma reflectivity. The reflected energy on full power shots employing a FPM is found to be lower than the value predicted in the design. This may have occurred due to a lower PM 'switch-on' intensity experimentally than the quantity used in the design stage. Additionally, it could be related to the pulse temporal intensity contrast incident on plasma mirror. If this parameter is lower than expected the mirror may be switching on relatively early in the pulse's temporal intensity profile, allowing more time for plasma expansion and increased likelihood of light being diffusely reflected (i.e. scattered), rather than the desired specular reflected light. Furthermore the quality of the laser wavefront reflected from the optic in plasma operation is also sensitive to the scale-length of expanding plasma. Spatial-intensity fluctuations in the laser near-field intensity distribution may lead to non-ideal ionisation dynamics, and coupled with the fact the optic is curved, there is likely a sensitivity to the delay between the plasma switch-on and the arrival of the peak of the laser pulse; a potential issue highlighted in the previous proof-of-concept experiment [183].

Two manufacturing methods used to produce the FPM, namely injection moulding and diamond machining, were presented. The latter method was selected as the most viable in the short term as it is capable of manufacturing the desired FPM design to a higher degree of accuracy and precision, thus achieving focusing performance closer to the diffraction limit.

Direct measurements of the focal spot formed by the manufactured FPM design, using the Vulcan laser in low energy CW mode, demonstrated a factor of $\times 2.5$ reduction in focal spot size, resulting in an estimated factor of $\times 3.6$ intensity enhancement,

when considering the focal spot quality (encircled energy) and the optic plasma reflectivity. Under optimum alignment and laser conditions (i.e. maximum pulse energy and shortest length), a calculated peak intensity of $\sim 4 \times 10^{21}$ W/cm^2 could be achieved whilst employing the FPM on the Vulcan-PW laser system, as determined from the focal spot characterisation. Optimisation of this laser to enhance the pulse energy and decrease it's duration could yield peak intensities close to 10^{22} W/cm^2 when employing the FPM, providing a window into a new interaction regime, some years prior to this being achieved at upcoming multi-Petawatt laser systems.

It was found that the optic's focal spot quality is extremely sensitive to misalignment in the position of input focal spot relative to the ellipsoidal's first focus. When minimised, successful FPM operation was achieved, as demonstrated through the enhancement of maximum proton energies accelerated from foil targets.

Results from an example use of the FPM in an investigation of laser-driven proton acceleration was demonstrated. The intensity enhancement achieved by the optic was utilised to increase the maximum energy of laser accelerated protons from thin foil targets, from 27 MeV to 53 MeV, almost a factor of two higher than F/3.1 OAP focusing, and consistent with TNSA laser intensity scaling. The highest proton energy is achieved when the optic is aligned within 10 μm of the optimum position. Larger misalignment results in lower proton energy, such that the benefit of the FPM over a PPM is lost.

An additional advantage, singular to the use of such an optic and further to enhanced peak intensity and temporal intensity contrast, is that it allows for the initial focusing optic, i.e. the OAP, to be of a larger F/# and thus can be at a relatively greater distance from the laser-target interaction. This is advantageous as OAPs are relatively expensive and time consuming to replace, whereas a FPM is single-use and relatively cheap to manufacture.

Due to the limited research performed to date on this novel form of focusing optic, especially in conjunction with Petawatt scale laser systems, the presented study helps to bring plasma-based optical technology closer to maturity. A push in the intensity frontier, in such a relatively affordable and reasonably reliable manner, will have wide ranging impact on many existing laser-plasma interaction phenomena, and enable for exploration of new research areas, including high field physics phenomena at the focus of ultra-intense laser pulses.

Chapter 5

Influence of focal spot size approaching the laser wavelength on proton acceleration in the TNSA regime

5.1 Introduction

The focusing plasma optic, presented in the previous chapter, was employed to investigate the influence of irradating focal spot size on laser-driven proton acceleration in the target normal sheath acceleration (TNSA) regime. Previous studies of this topic have been limited to the minimum spot size achievable by the primary focusing optic, with increased spot size being produced through target irradiation in a defocused position. The FPM, however, enables near-diffraction-limited spot formation at intensities similar to that generated by a focal spot formed using the primary focusing optic. As such, one can investigate the effects of focal spot size at the laser system's peak intensity, whereas other studies (using the defocusing approach) are limited to the intensity of the largest spot size investigated, in the case where pulse energy is altered (i.e. so all measurements are taken at the approximate same intensity, with the largest investigated focal spot containing the highest laser pulse energy possible).

One of the potential applications of FPMs is in the area of high-intensity laser-driven ion acceleration (as touched upon in the previous chapter). This acceleration form, ca-

pable of generating beams of ions with multi-MeV/nucleon energies, is an extremely active and developing research area since its inception over a decade ago [13, 95]. Applications such as proton imaging [158, 191] and proton heating for warm dense matter studies [192] have been realised using these sources and envisioned applications include medical isotope production [23] and proton oncology [193], to name a few. Each application has specific requirements on the ion beam parameters and thus has motivated numerous investigations aiming to understand the influence of various interaction parameters, such as laser focal spot size, on TNSA proton beam characteristics, such as maximum proton energy, proton energy spectrum, laser-proton conversion efficiency and beam divergence [107, 194, 195, 196, 197]. Despite the significant amount of research and progress made, the dependencies of proton beam characteristics in terms of the laser irradiation conditions are still far from fully understood, especially when employing focal spot sizes on the order of the laser wavelength (here after referred to as a 'tight focus'). Previous investigations of the effect of altering the irradiating spot size [196, 198] suggest it plays a key role in defining the properties of the beam of accelerated protons, not only in terms of the maximum proton energy, but also the number of protons accelerated (i.e. the laser-to-proton energy conversion efficiency). The laser focal spot size is thus a parameter of significant interest, rather than simply a factor in defining the interaction intensity.

The TNSA mechanism (see section 2.7.1) is the dominant ion acceleration process for the current state-of-the-art laser intensity regime, 10^{18}–10^{21} W/cm^2. A challenge remains to increase the proton energies up to ∼200 MeV, as required for proton oncology, for example. This is expected to be possible by increasing the laser intensity. As investigated in the previous chapter, one approach to achieve this is through the reduction of the laser focal spot size, though the full consequences of this approach have not been fully explored. Investigation of the effect of the focal spot size on TNSA is key to furthering our understanding of this mechanism.

An investigation of the effects of employing a tight focal spot for the acceleration of protons through the TNSA mechanism is reported in this chapter. This is achieved by comparing the use of two focal spot sizes, one of tight focus (∼F/1) and the other of typically employed focusing geometry (F/3.1), to irradiate relatively thick (micron scale) targets, for laser intensities in the range of 10^{20}–10^{21} W/cm^2. The two focal spots employed are a factor of 2.5 different in size. The characteristic proton beam

parameters under consideration are; maximum proton energy, energy spectrum, beam divergence and beam spatial-intensity profile. The combination of these enables the changes in the interaction dynamics resulting from the variation of focal spot size to be probed.

As the feasibility and availability of small F/# focusing optics capable of forming high quality focal spots on the order of the laser wavelength are becoming a reality, this investigation is highly relevant in the context of future laser systems planning to employ such focusing geometry. An understanding of the role that near-wavelength-diffraction-limited focusing plays on the dynamics of laser-driven ion acceleration is therefore highly relevant.

5.2 Review of relevant literature

Numerous experimental and analytical studies of the influence of focal spot size on proton acceleration in the TNSA regime have been conducted. However, relatively little research employing extremely tight focusing forming near-wavelength sized focal spots has been published. In this section a brief summary of the relevant findings of previous research is conveyed.

In early research investigating the intensity scaling of proton parameters, such as maximum energy and laser-to-proton conversion, through alteration of various interaction parameters (such as pulse length, pulse energy and target thickness), as reported in Fuchs *et al.* [107] and Robson *et al.* [113], it was clear that different scalings were observed based on which parameter was altered. However, both of these studies were conducted for constant focal spot size, and thus the influence of this parameter on proton beam properties was not investigated. In Robson *et al.* [113], however, it was highlighted that further experimentation to separate the geometrical effects of focal spot size from intensity would be required.

This was addressed in Brenner *et al.* [195], where the intensity scaling of proton energy and flux was investigated through separately varying focal spot size and pulse energy. Varying scaling was observed for each proton beam parameter (i.e. maximum energy and flux) depending on the laser parameter altered. Furthermore, both the maximum energy and conversion efficiency were measured to be higher for larger focal

spot irradiation, compared to a smaller spot of the same intensity. Similar findings were reported in a parametric investigation reported in Passoni *et al.* [101], for ultra-short (25 fs) pulses. Similarly, a study presented in Green *et al.* [198] observed enhanced proton flux when using defocused laser irradiation. It was postulated that this resulted from an increase in proton emission area at the target rear. These investigations all suggest that variation of the focal spot size plays an important role in defining proton beam properties.

These findings where explained in a study reported in Coury *et al.* [197], also investigating the influence of irradiating spot size on proton acceleration. In that study, the maximum energy of protons was measured to be higher under defocus irradiation (i.e. larger focal spot) compared to a relativity smaller spot. These results were interpreted in terms of geometrical changes to the injection of fast electrons, which led to alterations in the electron distribution accelerating protons at the target rear.

A common feature of these investigations is the use of relativity large focal spots (tens of microns). The primary interest of this chapter, however, is the influence of tight focusing (wavelength-scale focal spots). As the availability of small F/# (<F/1) focusing optics is still extremely limited, most laser-solid interactions experiments employ relatively larger F/# optics (>F/2). Thus there has been relatively little research effort on extremely tight focusing. As tight focusing is seen as a desirable approach for enhancing the peak intensity of a given laser system and the development/feasibility of such focusing is being actively researched (as in chapter 4 and Refs. [181, 183, 184]), researchers are beginning to investigate the use of such in laser-driven ion acceleration. A simulation study, reported in Klimo *et al.* [199] and Valenta *et al.* [200], investigated the influence tight focusing (0.5 μm (FWHM) focal spot for a laser of central wavelength of 800 nm) on laser absorption, fast electron generation and ion acceleration via the TNSA mechanism. They reported increased laser absorption compared to the use of a larger focal spot. However, this did not correspond to improved ion acceleration due to fast transverse spreading of fast electrons under tight focusing.

An experimental study, reported in Dollar *et al.* [131], employing an F/1 OAP, investigated the effects of finite spot size on ion acceleration in the RPA regime. That work shows that the use of tight focusing leads to rapid deformation of the target early in the interaction, leading to enhanced electron heating resulting from alteration in the absorption dynamics. This consequently reduces RPA efficiency as TNSA is

enhanced by the generation of sheath fields. To avoid this effect a larger focal spot geometry would be required. It is, however, impractical to simple increase spot size as a corresponding quadratic laser pulse power increase would be required to maintain high intensity.

5.3 Experimental method

The investigation presented in this chapter was conducted over two experimental campaigns. The first, hereafter referred to as 'Experiment A', is the same campaign as produced the results in chapter 4, and the second, hereafter referred to as 'Experiment B'; both performed using the same laser. The set-up employed in each is essentially the same as that used to test the operation of the FPM/PPM, in terms of measurement of laser-driven maximum proton energies, described in chapter 4 (see section 4.8.1).

To recap, the Vulcan-PW laser (see section 3.3.1) was used to provide linear polarised pulses at a wavelength of 1054 nm, focused using a conventional F/3.1 OAP (see Fig. 5.1(a)). Each pulse has an energy of between ∼100 to 200 J on-target, (including losses in the compressor and plasma mirror), and a duration of ∼750 fs (FWHM). Proton acceleration measurements were made employing either a FPM or a PPM, both of the same material (PMMA). The principle of operation of each is shown in Fig. 5.1(b) and (c), respectively. The FPM is used to form the smaller tight focal spot (ϕ_0= 1.6 μm (FWHM) with peak encircled energy of 37%) through conversion of the F/3.1 focusing geometry, and the larger focal spot (ϕ_0= 4.0 μm (FWHM) and encircled energy of 28%) is formed by the PPM, which maintains the F/3.1 focusing geometry after reflection. PPM shots are necessary to acquire measurements with the same reflectivity and intensity contrast enhancement as the FPM. The typical focal spots formed by each (in non-plasma operation) are displayed in Fig. 5.1(d) and (e). There is a factor of ×2.5 difference in spot size. In both focusing cases, pulses were incident along the target normal axis onto aluminium foils with a thickness of 6 μm and transverse dimensions 1×1 mm. As in chapter 4, rear surface accelerated protons were measured using a stack of dosimetry radiochromic film (discussed in section 3.4.1), positioned 40 mm behind the target foil and centred along the target normal axis. The stacks employed in Experiment A were of 50×50 mm transverse dimensions and 65×50 mm in Experiment B,

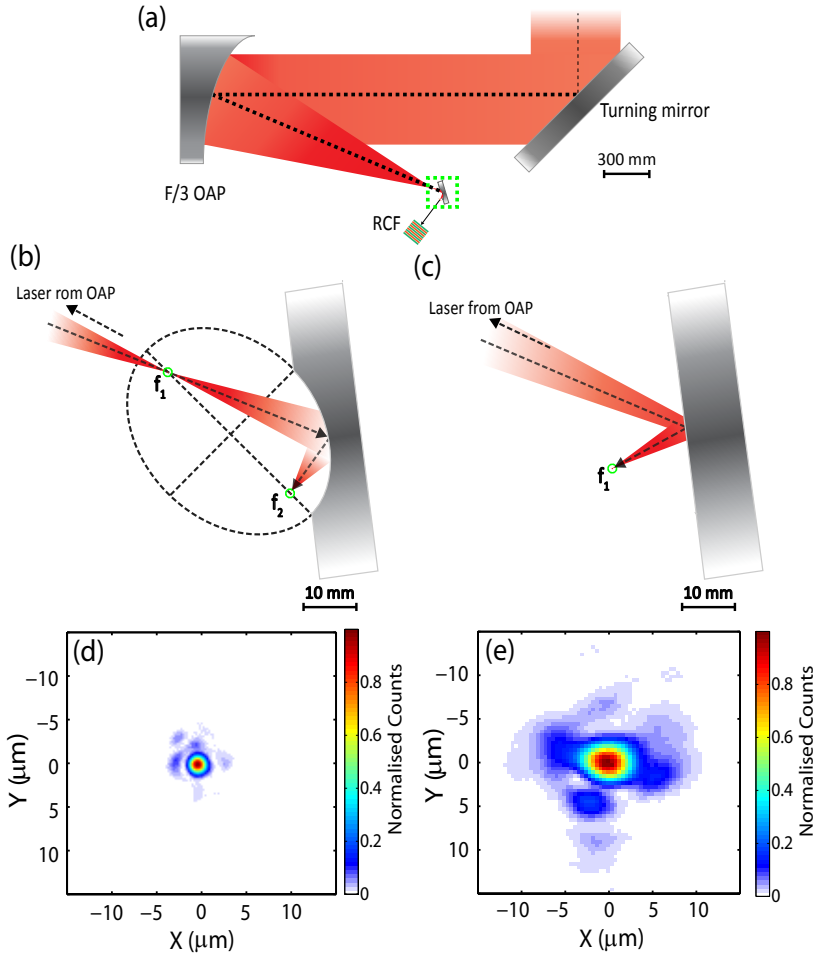

Figure 5.1: (a) Basic experimental set-up used for both FPM and PPM investigations. (b) and (c) Principle of operation of a FPM and a PPM, respectively. (d) and (e) typical focal spot obtained from the FPM and PPM focusing, respectively. Both measured employing the Vulcan laser in CW operation.

but otherwise the same. This diagnostic provides coarse energy resolution and enables the proton beam parameters under consideration to be measured.

As explored in chapter 4, successful FPM operation (i.e. high quality tight focus) depends strongly upon optimised alignment, which relies on the OAP focus spatially coinciding with the FPM input focus. However, as previously explored, misalignments in the FPM position relative to the OAP focus along the laser propagation direction, occur due to alterations in the divergence of the incoming pulse prior to focusing (e.g. due to thermal lensing). A displacement of this type results in the FPM output image position, nominally at position f_2, being displaced to a new effective best position. Thus a target placed at the nominal focus position will not be irradiated by the optimal spot. Figure 5.2 shows the effect on the output focal spot for various degrees of OAP focus position displacement relative to the FPM input focus. This data was

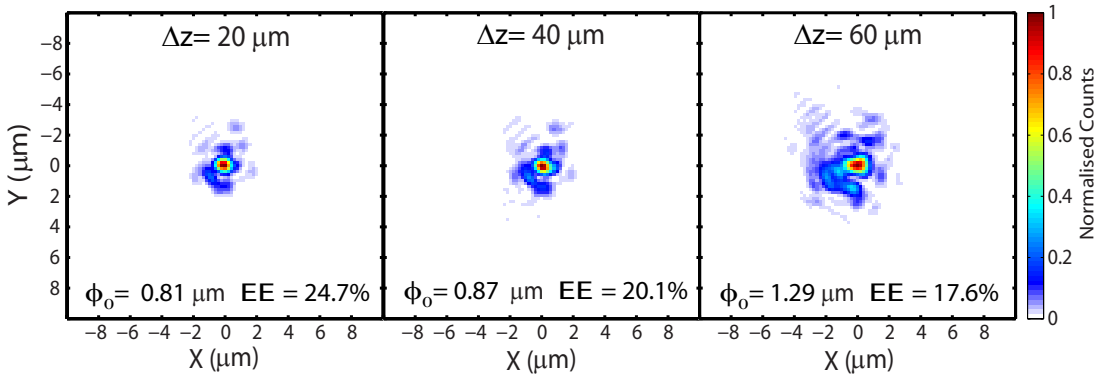

Figure 5.2: Measured laser focal spot spatial-intensity distributions formed by the FPM, for varying degrees of input focus displacement, displayed by Δz. Where the optimised spot (i.e. Δz=0) has values of ϕ_0=0.76 μm and encircled energy= 28%.

obtained using the testing set-up employed in chapter 4 (displayed in Fig. 4.11), which utilises a 532 nm diode laser as a light source, and thus smaller spots are obtained when compared to 1053 nm Vulcan laser light. It is seen that as the magnitude of misalignment is increased the focal spot size remains relatively small in comparison to focusing with the OAP only, as shown in Fig. 5.1(e). However, there is a lowering of the encircled energy with increasing misalignment, consequently producing a decrease in focused intensity. This may seem like an undesirable effect (which it is, if one aims to achieve maximum intensity), however it also presents an opportunity to investigate the effects of laser spot size at intensities equal to the PPM focusing case, $\sim 10^{20}$ W/cm^2. Typically in experimental investigations exploring the effect of spot size, the target is irradiated in a defocussed position. Therefore pulse energies must be reduced to maintain equal intensity through all investigated spot sizes (i.e. the maximum intensity is limited to that formed by the biggest spot tested and maximum pulse energy). In effect these studies cannot operate at the maximum intensity achievable by the laser system; an issue overcome by using the FPM. To quantify the magnitude of the longitudinal displacements in the OAP focus position from nominal on full power shots, enabling calculation of the on-target intensity, a Shack-Hartmann wavefront sensor (see section 3.4.2) was employed.

5.4 Experimental results

This section summarises the findings for both Experiment A and B. Measurements made employing a PPM (thus larger focal spot) will be referred to as PPM shots, and FPM findings (small focal spots) as FPM shots. Due to the range of focused intensities involved (4×10^{20}–3×10^{21} W/cm^2), care is taken to compare only comparable intensity data, and to state intensity values where necessary. Discussion will focus on notable changes in four proton beam parameters produced employing the two spot sizes (each forming a section below); these being the maximum proton energy intensity scaling, energy spectrum, beam divergence and beam spatial-intensity profile. These TNSA ion beam parameters are influenced by numerous factors, including the number and distribution of fast electrons generated at the target front, their transport through the target, and their temperature/distribution at the target rear, forming the accelerating fields.

The discussion of the possible origins of changes in the measured proton beam characteristics, produced by each focusing method, are presented in section 5.4.5, so as not to interrupt the presentation of experimental findings.

5.4.1 Maximum proton energy intensity scaling

As mentioned in the chapter introduction, one of the main challenges for laser-driven ion acceleration is to enhance the maximum achievable ion energy. Proton energy scaling relations show that the maximum energy scales with the fast electron temperature, which in turn scales with the ponderomotive potential $\left(\propto \sqrt{I_L\lambda_L^2}\right)$ [79], as has been experimentally demonstrated [107, 113]. Thus increasing pulse intensity is a route to higher maximum proton energies. As explored in the previous chapter, one approach to achieve this is through tight pulse focusing to reduce the focal spot size. However, the consequences of this approach have not been fully explored, considering previous scaling investigations [107, 113] were limited to relatively large focal spots, thus the need to revisit proton energy scaling for tightly focused pulses.

In chapter 4 the results of maximum proton energy intensity scaling for Experiment A were explored (Fig. 4.21(a)) to gauge FPM performance. Figure 5.3 summarises this data, with the addition of the findings of Experiment B, which extend the intensity

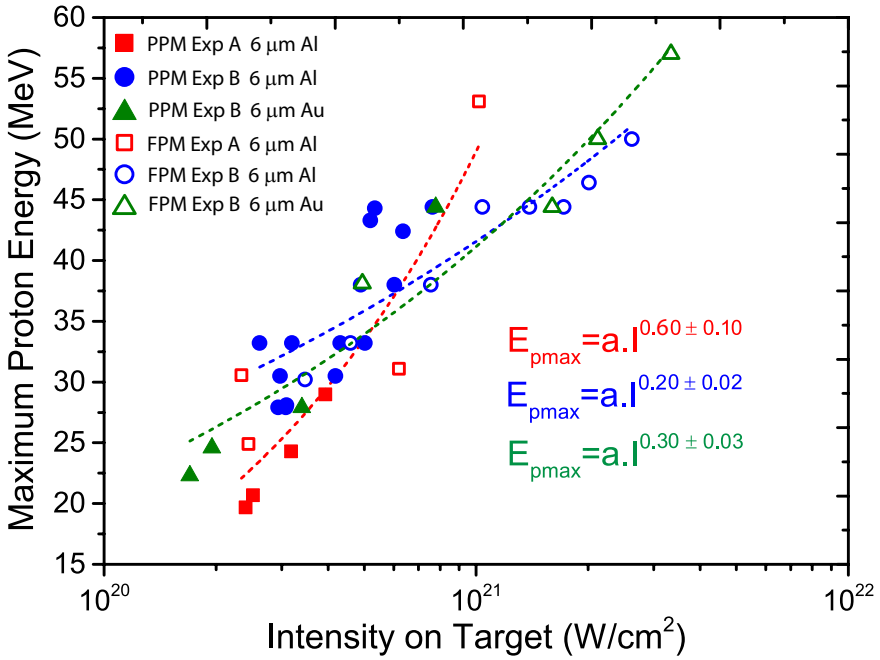

Figure 5.3: Plot of the maximum proton energy as a function of the laser intensity (I_L) on-target, recorded on Experiment A (red data) and Experiment B (blue data), both from the irradiation of 6 µm Al foil targets by either a FPM (open symbols), i.e tight focus, or PPM (closed symbols), i.e. larger focal spot. Data from Experiment B employing 6 µm gold targets (green data) is included. A simple power fit, of the form $E_{pmax} = a.I_L^b$, is made to each data set to show the approximate scaling of maximum proton energy with peak laser intensity. Each data point corresponds to a single laser shot.

range investigated up to 3.3×10^{21} W/cm^2. Additionally, results employing 6 μm thick gold targets for each pulse focusing case are included.

As discussed in chapter 4, the maximum proton energy scaling with intensity takes the form of a power law, such that $E_{pmax} = a.I_L^b$, for the results of Experiment A. These results are in good agreement with previously reported scaling findings [107, 113] in the intensity range of 10^{18}–10^{20} W/cm^2, for b= (0.6±0.1). These previous measurements were made for a single, non-tightly focused, spot size, with intensity varied through control of the pulse energy. Therefore, the findings of Experiment A would suggest that the scaling of proton energy is not dependent on spot size within this intensity range. When the intensity range is extended (up to 3.3×10^{21} W/cm^2), with the data from Experiment B, the proton energy scaling changes. The scaling, over the entire intensity range, (considering both focusing approaches) for Al target data (blue data) is far slower, deviating from the conventionally accepted scaling displayed in Experiment A, with b= (0.20±0.02). In the upper region of the intensity range (>10^{21} W/cm^2) values are tending to saturate (through difficult to see in Fig. 5.3 due to the logarithmic x-axis), which may lead to a saturation in the maximum proton energy at increased

intensities. A similar scaling is displayed in the gold target data (green data), with b= (0.30±0.03).

5.4.2 Proton beam energy spectra

In this section the influence of tight focusing on the energy spectrum of the beam accelerated protons is investigated. The beam energy spectrum is of critical importance to many envisioned applications, with the majority of experiments producing quasi-Maxwellian distributions. Control of the energy spectrum is a major challenge facing the field of laser-driven ion acceleration.

The proton energy spectra (sampled between 4.5 and 25 MeV), determined using RCF spectroscopy (see section 3.4.1), for the two focusing conditions are shown in Fig. 5.4, for the results of Experiment A. The number of protons produced in all cases is initially approximately equal ($\sim 10^{12}$ protons per MeV per steradian) at the lower end of the spectra (4.5 MeV). However, this changes with increasing proton energies. The proton beams generated through irradiation with the tight focus (FPM employment), display a slower decrease in proton numbers with increased proton energy compared to the larger focal spot data (PPM employment). Furthermore, the spectral shape, between ∼6 to 18 MeV, has different characteristics. In the large spot case, the spectrum can be fitted using a single exponential indicating that the proton population can be quantified by a single temperature, indicative of TNSA. However, in the tight focus cases the spectral shape exhibits a relatively slower decrease, tending to a plateau-like distribution, at relatively lower proton energies. To quantify, the temperature of each spectrum was determined through the fitting of Eq. 2.95, which describes the exponential decay form of the spectrum. Table 5.1 summaries the value calculated in each case, indicating the focusing method and calculated peak intensity of each shot. All proton beams generated through FPM employment display a higher temperature (of average 8.6 MeV [for shots FPM 1–3]) compared to those obtained through PPM focusing (average of 6.5 MeV [for shots PPM 1–4]). It should be noted that one shot presented in the FPM data (displayed in green) was obtained at relatively higher laser intensity (1.0×10^{21} W/cm^2) as a result of closer to optimum alignment. The inclusion of this data demonstrates that alterations to the proton beam spectral shape are a consequence of spot size, and are not strongly influenced by an intensity increase in

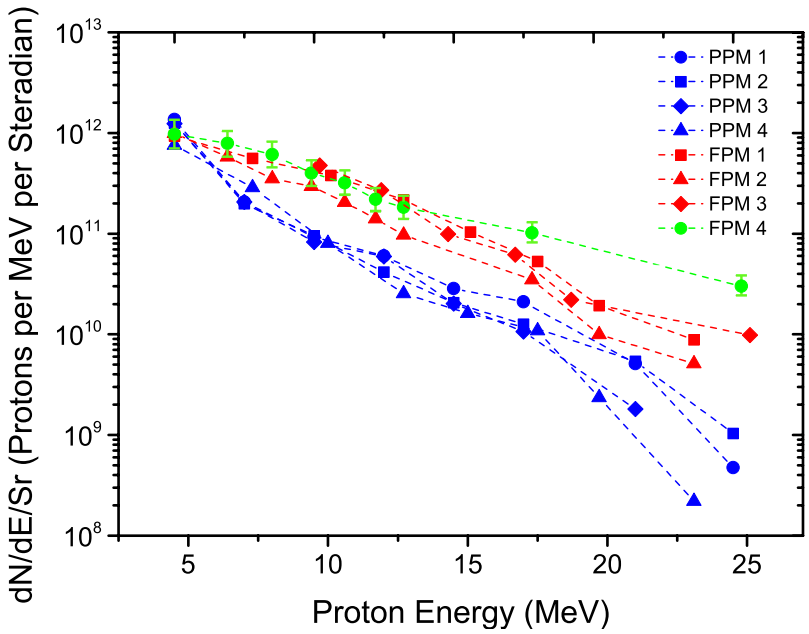

Figure 5.4: Plot of the proton beam energy spectra obtained in Experiment A from 6 μm Al targets. Data points were obtained through the employment of a FPM, producing a tight focus (red and green data), or PPM, producing a relativity larger focal spot (blue data). The spectrum displayed by green data (FPM 4) is was obtained at a relatively higher intensity with respect to the other shots, hence it being highlighted. FPM 4 data additionally includes indicative error bar.

this regime.

Variations in the proton spectral shapes will additionally correspond to changes in the laser-to-proton energy conversion efficiency. This parameter is calculated by measuring the energy contained in the proton beam, via integration of the energy spectrum between 4.5 MeV (lower energy threshold of RCF diagnostics) to 23 MeV (to compare the same region for all shots), and taking this as a percentage of the incident laser energy. Previous investigations employing the same laser system found that conversion efficiency scales with the drive laser energy, though these investigations were conducted for a single spot size [113]. Table 5.1 summaries the laser-to-proton energy conversion efficiency for the corresponding shots presented in Fig. 5.4. Conversion efficiency values are significantly higher for tight focus irradiation, on average 7.0%; a ×2.5 enhancement in conversion efficiency compared to the larger spot average, of value 2.8%. Data from shot FPM 4 was excluded from the small spot average value as this shot was at significantly higher peak intensity, as previously mentioned. The conversion efficiency is seen to show a strong dependency on spot size under these focusing conditions (i.e. tight focusing). Additionally, shot FPM 4 also exhibits the same spectral characteristics as the lower intensity FPM data, and thus enhanced conversion efficiency (value of 7.5%).

Shot	Intensity (W/cm^2)	Proton Temperature (MeV)	Laser-to-Proton Energy Conversion Efficiency (%)
PPM 1	3.9 $\times 10^{20}$	6.7 $\pm$ 0.6	2.8 $\pm$ 0.2
PPM 2	3.2 $\times 10^{20}$	7.1 $\pm$ 0.5	2.7 $\pm$ 0.3
PPM 3	2.5 $\times 10^{20}$	6.4 $\pm$ 0.4	2.9 $\pm$ 0.5
PPM 4	2.4 $\times 10^{20}$	5.7 $\pm$ 0.4	2.6 $\pm$ 0.4
FPM 1	2.4 $\times 10^{20}$	8.9 $\pm$ 0.6	7.5 $\pm$ 0.7
FPM 2	2.3 $\times 10^{20}$	8.0 $\pm$ 0.3	5.5 $\pm$ 0.6
FPM 3	6.1 $\times 10^{20}$	8.8 $\pm$ 0.9	7.9 $\pm$ 0.5
FPM 4	1.0 $\times 10^{21}$	13.1 $\pm$ 0.6	7.5 $\pm$ 0.8

Table 5.1: Table summarising the proton spectrum temperature and laser-to-proton energy conversion efficiency for each shot in Experiment A, calculated from the proton spectra displayed in Fig. 5.4, between 4.5 to 23 MeV. For each shot the focusing geometry employed and peak intensity achieved is indicated.

As such, with comparison to the lower intensity FPM results (FPM 1–3), this suggests conversion efficiency enhancement, and thus spectral variations, are due to spot size variation and not an intensity driven effect. Calculating the conversion efficiency for the entire measured spectrum in FPM 4, from 1.1 to 53.1 MeV (not displayed), a value of 10.5% is calculated, based on 110 J of laser energy on-target, thus 11.6 J converted to target rear accelerated protons. This is a relatively high conversion efficiency, comparable to results presented in Brenner *et al.* [108], which were achieved through the employment of a dual laser pulse drive approach.

5.4.3 Proton beam divergence

Another notable variation observed in the measured proton beams is the energy divergence. These results, for Experiment A, are presented in Fig. 5.5. Beam half angle divergence was calculated by measuring the radius of a circular fit to the beam image on each RCF energy level and taking into account the RCF-to-target distance.

Consistent with previous reports [118], the divergence for all shots decreases with increasing proton energy. However, the rate this occurs differs significantly when comparing the two focal spot cases, consistently over all shots. Similar to the energy spectra findings (Fig. 5.4), divergence values are initially approximately equal (at 1.1 MeV). However, for increasing sampled proton energy, in the tight focusing case (red and green data), the divergence decreases relatively slowly compared to the larger focal spot data (blue data), exhibiting a more plateau-like distribution. Essentially this results in a more collimated beam, with respect to proton energy, in the tight focus case, in contrast to a near-linear dependence measured with the larger spot, for otherwise identical

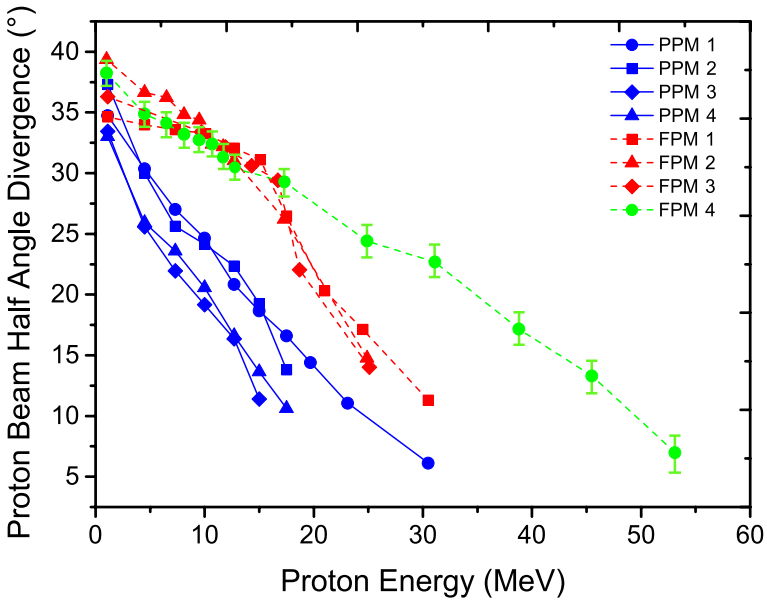

Figure 5.5: Plot of the proton beam divergence as a function of proton energy in Experiment A. In both case the red/dashed data represent FPM shots and blue/solid data PPM shots. Green/dashed data represent a shot where a near optimal focal spot was achieved employing the FPM, i.e. enhanced intensity. FPM 4 data additionally includes indicative error bar.

conditions. To quantify this result, the average reduction in beam divergence between the two sets is a factor of ×1.2 at 4.5 MeV, and ×2 at 17.5 MeV.

5.4.4 Proton beam spatial distribution

The final notable variation displayed between the proton beams generated by the two pulse focusing approaches is the spatial intensity distributions. As with the other investigated beam parameters, this was determined through beam measurements simultaneously at various energies using a RCF stack. Figure 5.6 presents example RCF proton data (from Experiment A) at various sampled energy levels for both focusing cases and Fig. 5.7 shows beam profile lineouts taken from sample images from Fig. 5.6 (at 9.5 MeV) for various beam angular positions. Note that for the tight focusing case the optimum aligned, highest intensity, FPM shot (FPM 4) is included. There are three notable changes to the beam spatial distribution; (i) structure, (ii) edge profile and (iii) evidence of target edge emission.

In terms of beam structure, there is a clear contrast between the highly smooth/diffuse beam produced by the larger focal spot (Fig. 5.6– PPM 1 and PPM 3 data, and Fig. 5.7(a) and (d)), and the significantly more structured beam displayed with

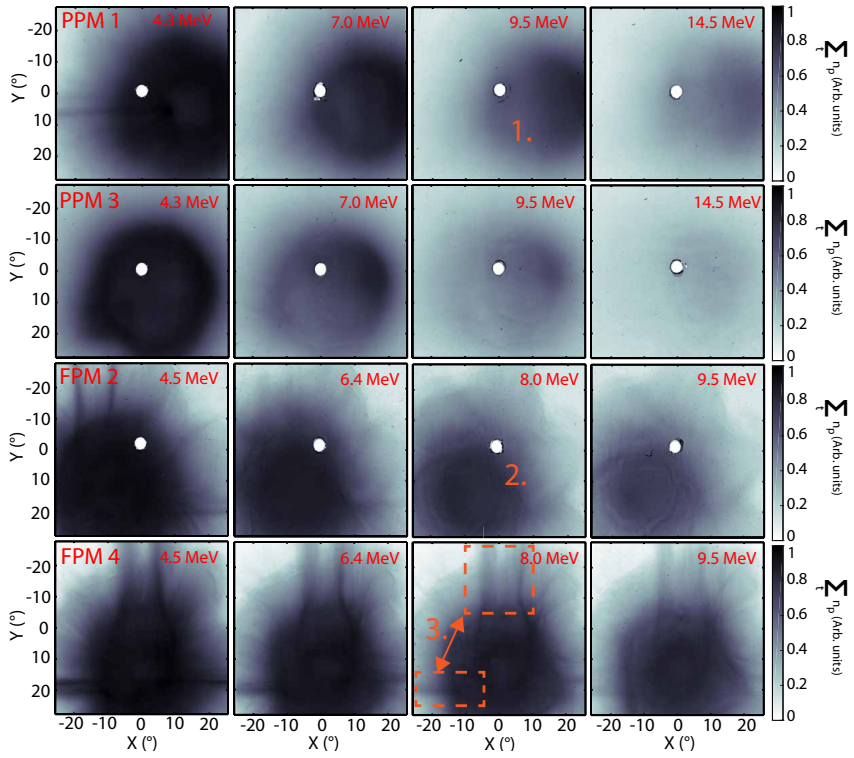

Figure 5.6: Example proton beam spatial-intensity distribution, obtained though RCF spectroscopy imaging at various proton energies (as indicated in each image), for both PPM and FPM focusing cases. Additionally, specific features discussed in the text have been highlighted; 1. highly smooth/diffuse beam, 2. structured beam and 3. linearly striped proton distributions.

tight focusing (Fig. 5.6– FPM 2 and FPM 4 data, and Fig. 5.7(b)-(f)). The structure measured employing the larger spot is that typically observed using metal foil targets in TNSA conditions, producing well defined beams. Furthermore, the large focal spot beams exhibit a more Gaussian-like transverse profile, which decreases relativity slowly with increasing beam angular position (as seen in Fig. 5.7(d)), circular-like in shape, and a diffuse edge profile. In contrast, the beams measured in the tight focus case display plateau-like, 'top-hat', transverse profiles (as seen in Fig. 5.7(b)-(f)). Additionally, they are relatively less circular with respect to the other focusing case, exhibiting sharp edge boundaries at all sampled energies. It should be noted that the distinct features displayed in the tight focusing case are also seen for shot FPM 4 (conducted at relatively higher intensity [1.0×10^{21} W/cm^2]). This highlights that beam spatial distribution changes are driven by the alteration in focusing geometry and not purely intensity driven.

A prominent feature displayed in the tight focusing data (Fig. 5.6– FPM 2 and FPM 4) at the lower proton energy range is the presence of linearly striped proton distributions crossing the main beam. These can be clearly seen in Fig. 5.7(f) as spikes

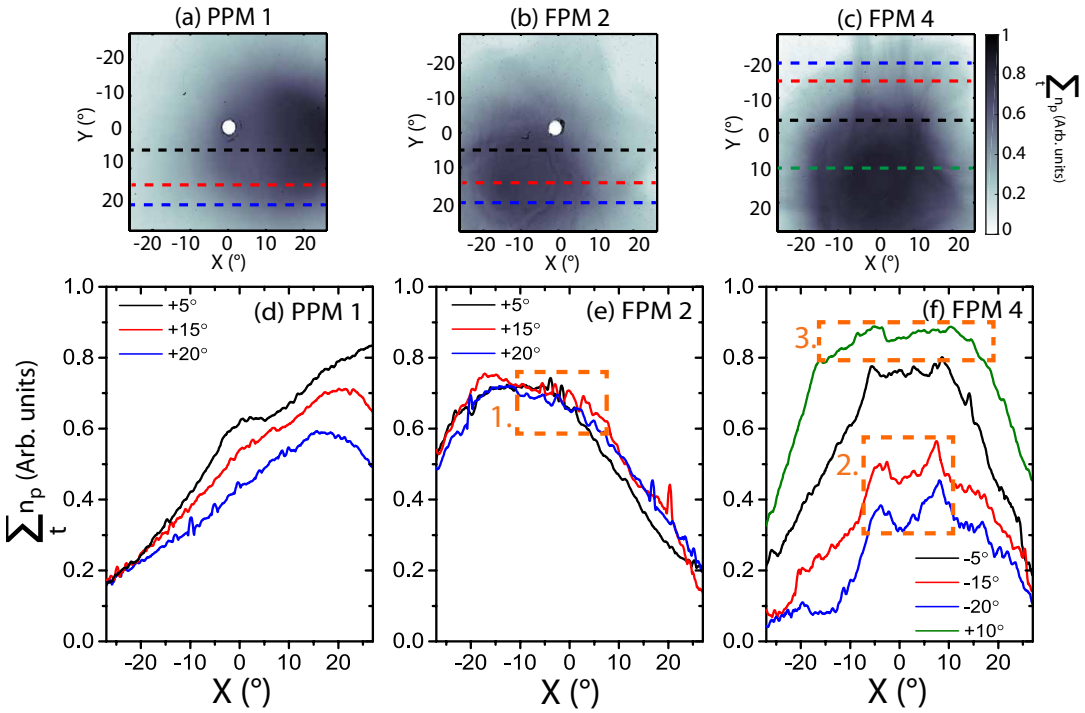

Figure 5.7: Plots of proton beam profile lineouts in the X-axis at various Y-axis angular positions, as indicated, for a sample proton energy of 9.5 MeV; for (d) PPM 1 (e) FPM 2 (f) FPM 4. Where the position of each lineout with respect to the RCF image it was calculated from are indicated in (a), (b) and (c), respectively. Additionally, specific features discussed in the text have been highlighted; 1. structured beam, 2. linearly striped proton distributions and 3. top-hat distribution.

in the RCF optical density either side of the beam center (at 0°). These distributions are produced by protons originating from the edges of the target, due to the presence of strong electrostatic sheath fields (of similar strength to the main TNSA sheath) in this region, due to confined electrons [97, 201, 202].

5.4.5 Summary of experimental results

To aid in discussing the cause of variations in the proton beam properties produced in each focusing case, it is useful to first review the notable findings observed in the experimental data, as listed below;

(i) Slower scaling of maximum proton energy with pulse intensity when employing tight pulse focusing, with respect to established scaling laws.

(ii) A slower decrease in proton numbers with increasing beam energy, thus higher average temperature, employing tight focusing, resulting in a $\times 2.5$ enhancement in laser-to-proton conversion efficiency, compared to larger spot irradiation.

(iii) The beam energy divergence exhibits a significantly slower decrease, near plateau-like in shape, with increasing proton energy in the tight focusing case when compared to the large spot findings.

(iv) A higher degree of structure, with a sharper edge and less circular proton beam was observed for tight focusing irradiation, compared to the large focal spot measurements. Additionally, the tight focusing measurements exhibited evidence of significant proton emission from the edges of the irradiated target.

As discussed earlier (section 2.7.1) the properties of the beam of TNSA protons are closely related to the dynamics of the energetic electron sheath. Accordingly variations in the proton beam properties can be correlated to the dynamics of the field distribution at the target rear. This aspect of the TNSA mechanism may explain the properties of emitted protons. However, the properties of the sheath distribution are defined by the dynamics of the front surface interaction, such as laser-energy absorption, fast electron injection, and the subsequent fast electron transport through the target. This will be explored in more detail in the coming section.

Beginning with the observed changes in the beam divergence between the focusing cases, this provides strong evidence for alteration in the distribution in the accelerating rear surface sheath shape [114]. Different sheath shapes, and thus different gradients of the sheath profile, will change the direction of emitted protons. An investigation reported in Carroll *et al.* [115], exploring the effect of sheath shape on the divergence of accelerated protons, concluded that a slowly decreasing, near plateau-like, beam divergence, as observed in the tight focusing case, is indicative of a Gaussian distribution sheath. Furthermore, that work showed that a near-linear divergence dependence with proton energy results from an inverse parabolic sheath profile, such as the dependency displayed in the larger focal spot measurements.

Combining the beam energy divergence findings, with energy spectra results suggests a strong intrinsic correlation between the spectral and divergence properties. In tight focusing irradiation the relatively slower drop in proton flux with proton energy coincides with the slow decrease in beam divergence as a function of proton energy. Similarly, in the larger focal spot case the relatively faster drop in the proton flux as a function of energy is partnered with a rapid decrease in the beam divergence. This implies that changes to the sheath distribution is not only a change in profile shape but additionally sheath area on rear surface. In the tight focusing case a larger sheath,

with relatively low electric field strengths, would result in the spectral enhancement of low energy protons, and thus higher conversion efficiency, as experimentally observed.

Further evidence for different sheath dynamics between the focusing cases is obtained from variations displayed in the proton beam spatial intensity distribution. The observation of protons emitted from the edges of the target under tight focusing, is a clear sign of significant alteration in sheath dynamics compared to larger focal spot irradiation. This result suggests that tight focusing produces a large population of fast electrons at the target edge, occurring due to the lateral spreading of expanding sheath electrons from laser axis. Once at the target edges, a return current can no longer be supported and expansion is stopped by the radial component of the electrostatic field resulting from the build-up of negative charge. This electron population is then reflected back toward laser axis, which can alter the dynamics of the spatially and temporally evolving sheath over the whole surface [96]. This electron spreading effect, and the resultant secondary ion sources from target edges, has been previously observed in Quinn *et al.* [203]. Furthermore, 2D hybrid-PIC simulations reported in McKenna *et al.* [97] demonstrated that upon reaching the edges, hot electrons are reflected back towards the centre of the target giving rise to lateral refluxing.

This indication of notable fast electron lateral transport and resultant reflection from the target edges may help explain all the significant changes to the accelerating sheath, in terms of altering its spatial-intensity distribution, which in turn results in the experimentally observed proton beam properties. For example, this effect may explain the observed deviation of proton maximum energy scaling with intensity from the well-established square-root scaling. The enhanced lateral spreading of expanding sheath electrons will result in a dilution of acceleration fields over time. Similarly, the accelerating field will decay more slowly in the larger spot case as it takes more time for electrons to spread transversally. This effect was highlighted in Zeil *et al.* [204] where a degradation in maximum proton energy was observed when the transverse size of the target was reduced to enhance the effects electron reflection from the target edges, which in turn perturbs the main accelerating region.

5.4.6 Target transverse size alteration

As postulated in the previous section, varying degrees of fast electron lateral spreading at the target rear between focusing cases may be the cause of changes in the accelerating sheath, and hence the observed proton beam properties. To further test this hypothesis and informed by the findings of Experiment A, similar to the investigation reported in Zeil *et al.* [204], the transverse dimensions of the target foil were varied. Experiment A employed targets with transverse dimensions of 1×1 mm. Square targets with side lengths of 4 mm, 3 mm, 1 mm and 0.5 mm were selected for investigation in Experiment B. This effectively modifies the time in the interaction at which reflection of electrons occurs from the target edges by moving them further from laser axis (>1 mm) or limiting its spread by moving them closer (<1 mm). This will aid in demonstrating the consequence of this on the accelerating sheath field, and the resultant proton emission, between focusing cases. Figure 5.8 displays example RCF data at two sampled energies (3.9 MeV and 8.4 MeV), over the range of investigated target foil sizes.

In the tight focusing case (FPM data) an enhancement in edge emitted protons is observed as the target transverse dimensions are reduced, as displayed by the linear features in the proton spatial distribution. Only the two smallest target sizes investigated (1 mm and 0.5 mm) display these proton features, at >8.4 MeV. The 0.5 mm target, in fact, shows evidence of edge emission up to 21.6 MeV (not displayed). Conversely, for the larger focal spot measurements (PPM data), edge emitted protons are only observed at the lowest sampled energy (3.9 MeV) for all target sizes. Furthermore, the beam spatial distribution observed in the 0.5 mm target under tight focusing irradiation displays significant departure from the circular-like beams produced by the relatively larger targets. This is not observed in the larger focal spot equivalent. This suggests the target dimensions would need to be reduced further, <0.5 mm, for a similar proton distribution to be generated.

This investigation clearly shows that the sheath dynamics are significantly different in the two focusing cases, with the tight focus producing strong accelerating fields at the target edge, capable of tens of MeV proton generation. Additionally, the reflection of electrons from the edges alters the evolution of the accelerating fields leading to the resultant measured properties in the sheath accelerated protons. A similar effect of lateral refluxing was presented in Tresca *et al.* [96], where the target shape was altered

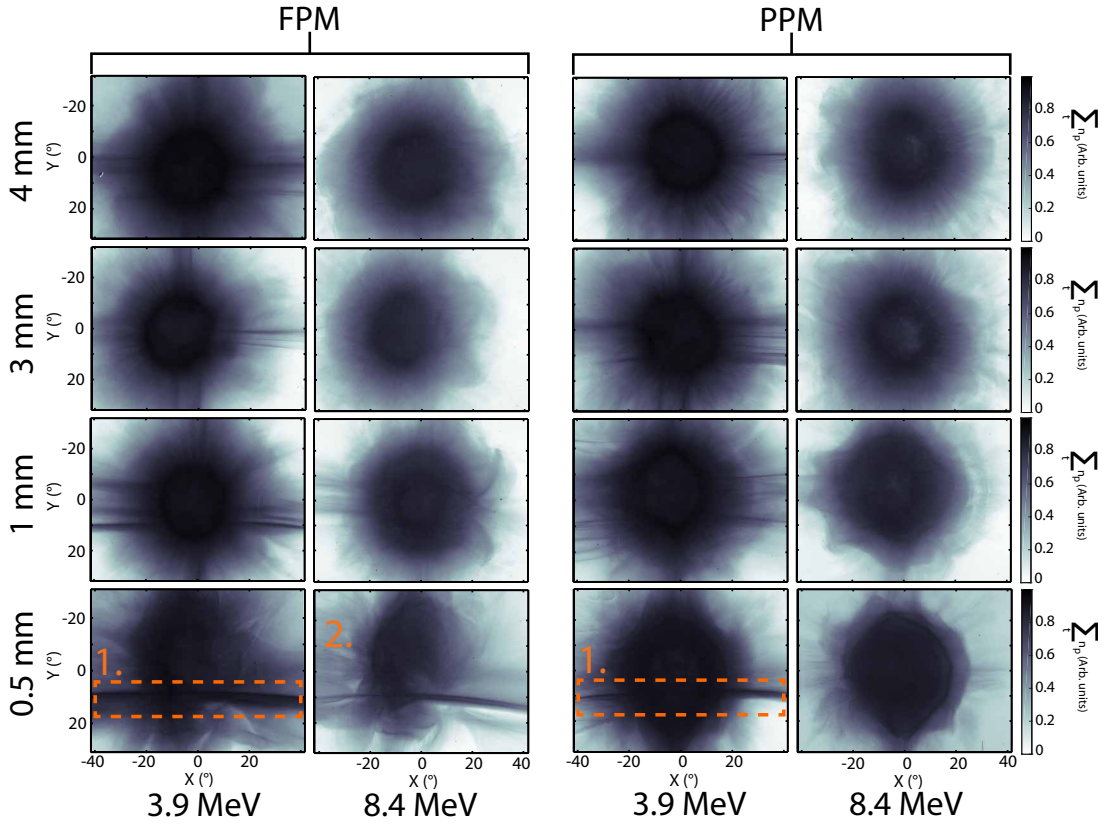

Figure 5.8: Example proton beam spatial-intensity distribution, obtained though RCF spectroscopy imaging, at two sampled proton energies (as indicated), for both focusing cases (FPM and PPM) over the range of various target sizes investigated (as indicated). Additionally, specific features discussed in the text have been highlighted; 1. linearly striped proton distributions and 2. proton beam breakup.

to control the spatial profile of the accelerated protons.

5.5 Modelling

The measured changes to the proton beam are interpreted in terms of changes to the rear surface sheath dynamics, but the source of the changes to the sheath evolution is still unclear. To this end, the front surface laser-plasma interaction dynamics must be explored, because the primary difference between the cases in the size of irradiating focal spot. This section presents the results of 2D PIC simulations (see section 3.5.1), exploring the interaction dynamics of metal foil targets irradiated under the two focusing conditions. Using the fully relativistic PIC code EPOCH the interaction of a 400 fs Gaussian laser pulse with a 6 μm thick aluminium target (at $200n_c$), assumed to be ionised to Al^{11+} and initially neutralised by a corresponding electron population. The

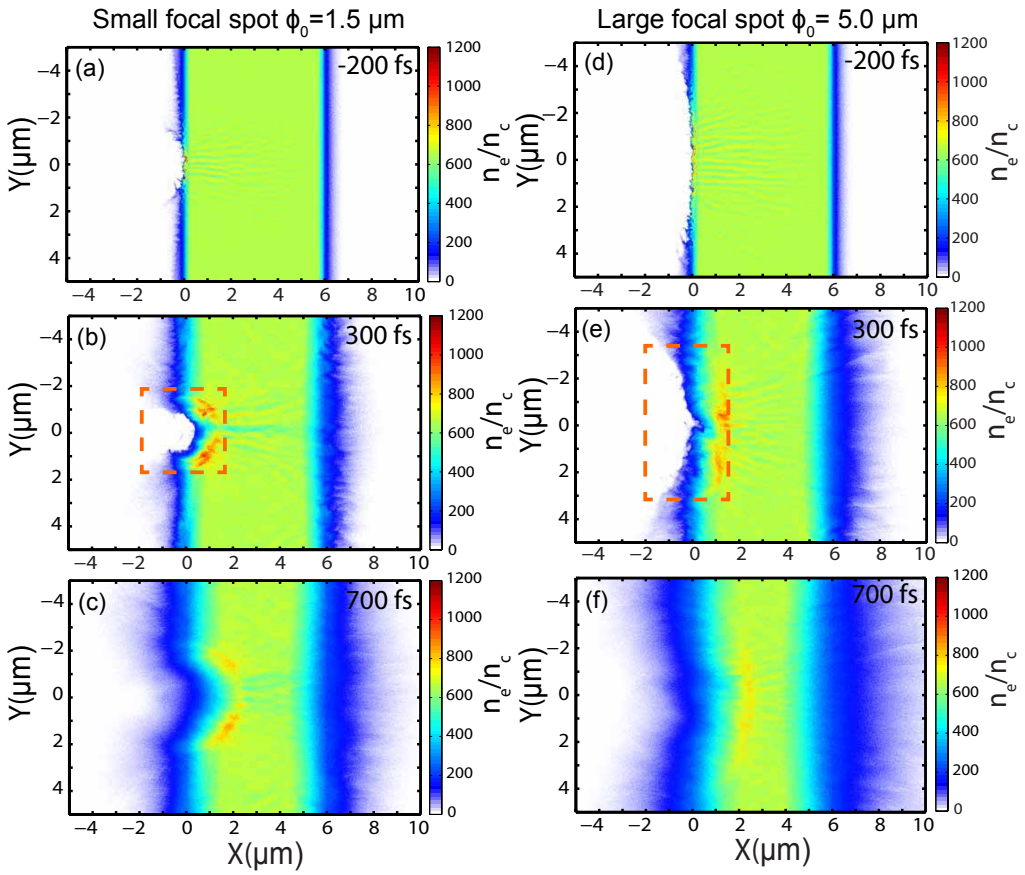

Figure 5.9: PIC simulation results of 2D target electron density, normalised to the electron critical density, for both focal spot cases ((a-(c) 1.5 μm and (d)-(f) 5 μm), at varying simulation times relative to the arrival of the pulse peak at initial target front (located X= 0 μm). The laser pulse is propagating from the left to the right, along Y= 0 μm. The highlighted areas in (b) and (e) show the main difference between spot cases discussed in the text.

initial electron temperature was set to 90 keV and initial ion temperature to 0.1 keV. A simulation box size of 150×57.6 μm is used, with 30,000×11,530 cells and 7 particles per cell. The two spot cases simulated are 1.5 μm and 5 μm (FWHM), each of equal peak intensity (6×10^{20} W/cm^2), compensated by the total energy in the pulse.

To begin examining differences between focusing cases one can first compare electron density maps from these simulation, shown in Fig. 5.9(a)-(f), for three various simulation time-steps (relative to the arrival of the peak of the pulse at the target front). It is immediately evident from these snapshots of electron density that there is a distinct difference in the critical density surface deformation during the hole boring phase. For the larger focal spot the surface radius of curvature is relatively large (Fig. 5.9(e)) in comparison to the significantly deformed condition observed in the small spot case (Fig. 5.9(b)). This variation is explained in terms of the transverse component of

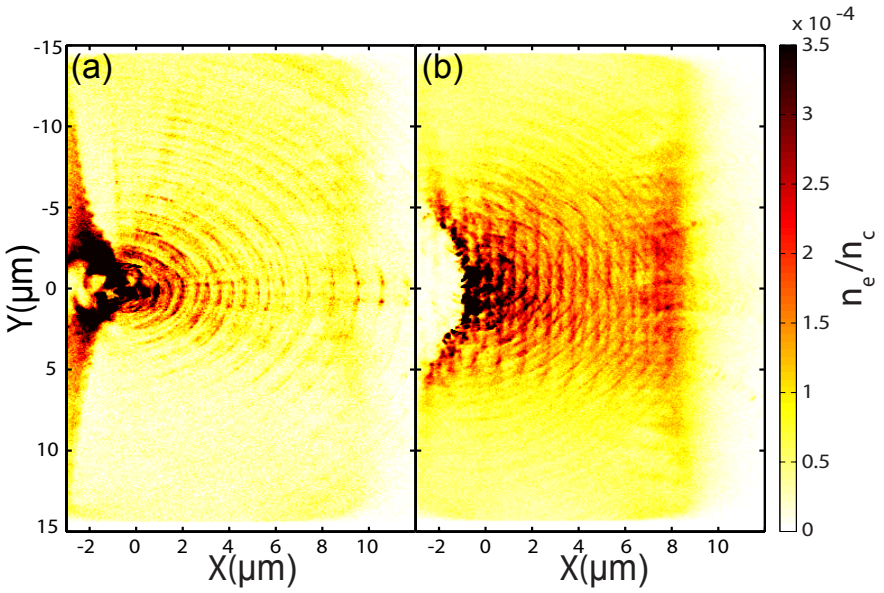

Figure 5.10: PIC simulation results of the 2D target electron density distribution for electrons with energy >1 MeV, normalised to the electron critical density, for both focal spot cases, (a) 1.5 μm and (b) 5 μm. Data was sampled approximately 100 fs before the peak of the pulse arrives at initial target front (located X= 0 μm).

the pulse's ponderomotive force (see section 2.5.2). Recalling, the collective expulsion of electrons from regions of higher to lower intensities occurs due to the ponderomotive force, arising from the inhomogeneity of the oscillating electromagnetic field. It is thus proportional to the gradient of the pulse's spatial, and temporal, intensity profile. The tighter, smaller, focal spot (of Gaussian-shaped intensity profile) has a larger ratio of transverse component of the ponderomotive force to the longitudinal component, compared to the larger focal spot. This results in greater transverse motion of electrons, moving them away from the central laser propagation axis, due to a steeper gradient in the pulse intensity profile. Thus the laser can bore further into the overdense target, with electrons being expelled from the interaction volume.

If one considers the mechanisms by which fast electrons are generated (see section 2.5.4), such a critical surface curvature, in the small spot case, will result in an enhancement in absorption processes which take place when the pulse is obliquely incident on a plasma density gradient (such as resonance and vacuum heating), in this case where the laser is incident normal to the target. This will not only effect the degree of laser energy coupled to electrons, but additionally the injection direction of the electrons. Both resonance and vacuum absorption generate fast electrons which are emitted in the direction of laser polarisation, as opposed to the $\mathbf{J} \times \mathbf{B}$ mechanism which injects along the laser propagation axis. The latter is expected to be the dominant absorp-

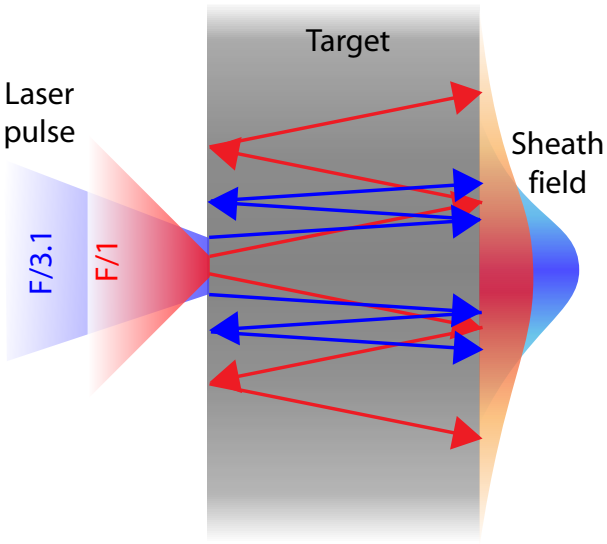

Figure 5.11: Illustration of the recirculation of fast electrons within a target irradiated by either tight focusing (F/1) or a relatively larger focal spot (F/3.1). This aids in understanding the lateral spreading of the electrons at the target rear, between focusing cases.

tion mechanism due to normal incidence. Thus, an enhanced critical surface curvature would result in a change in electron injection distribution. The effect of hole boring increasing electron divergence was highlighted experimentally in Green *et al.* [91].

To investigate changes to the spatial distribution of the fast electrons within the target, between focusing cases, one can plot the density of electrons with energy >1 MeV. This is shown, at approximately 100 fs before the peak of the pulse arrives at the target front, in Fig. 5.10. The spherical expansion of the fast electron population within the target is observed in both cases, more distinct under tight focusing (Fig. 5.10(a)). The large spot case (Fig. 5.10(b)) displays a greater density of fast electrons around the central axis (Y= 0 μm), which are more planar in distribution and highly turbulent in nature, breaking up the spherical distributions. Similar fast electron dynamics were observed in the simulation study of tight focus reported in Klimo *et al.* [199] and Valenta *et al.* [200]. The authors of that work also concluded that tight focusing leads to a wider angular distribution of fast electrons. This analysis displays the stark difference in fast electron dynamics between focusing cases, with the primary difference being in the transverse motion of fast electrons.

If one considers enhanced transverse fast electron motion, in the tight focusing case, in terms of the dynamics of electron recirculation inside the target (i.e. fast electrons reflecting from the sheath fields formed at both surfaces of the target) then this would lead to relatively faster lateral spreading of electrons as they traverse the

target numerous times, with respect to the large focal spot fast electron motion. This concept is illustrated in Fig. 5.11. This would lead to faster spreading of electrons at the target rear and, consequently, to the conclusions made in the previous section regarding the source of alterations in the proton beam properties. The simulation investigation of Klimo *et al.* [199] and Valenta *et al.* [200] also highlighted this aspect of fast transverse spreading of electrons under tight focus irradiation adversely affected ion acceleration (in the TNSA regime).

5.6 Conclusion

In this chapter the influence of employing a tightly focused laser pulse on the characteristic properties of laser accelerated protons in the TNSA regime was explored experimentally. The proton beam parameters considered were maximum proton energy, energy spectrum, beam divergence and spatial intensity distribution. A tightly focus pulse (with spot size near λ_L) was achieved employing the ∼F/1 FPM developed in chapter 4. For comparison, a planar plasma mirror was employed to maintain initial F/3.1 focusing from conventional OAP focusing. Importantly, approximately the same intensity could be achieved in each focusing case due to reduced spot encircled energy in the tight focusing scheme.

The results demonstrate significant differences in the characteristic properties of TNSA proton beams produced with both pulse focusing geometries. To summarise, the proton beams observed employing tight focusing displayed a slower maximum proton energy laser intensity scaling, a slower decreasing proton spectrum (with a $\times 2.5$ enhancement in laser-to-proton energy conversion efficiency and proton temperature increase), a significantly slower, near-plateau like, decrease in beam divergence with increasing proton energy, compared to measurements employing the larger focal spot. Furthermore, a higher degree of beam structure, with observation of significant proton emission originating from the target edges, was found for the tight focusing case.

The measured proton beam properties are explained in terms of changes in the evolution dynamics of the fast electron distribution at the target rear, which generates the accelerating fields. The observation of significantly more protons emitted from the target edges under tight focus irradiation indicates the presence of enhanced lat-

eral spreading of electrons toward the target edges. Furthermore, the reflection and recirculation of electrons from the target edges can significant alter sheath dynamics and consequently the properties of accelerated protons. This effect may also explain the observation of lower-than-expected maximum proton energies from conventionally accepted intensity scaling. The lateral spreading results in dilution of the acceleration fields, and alters the temporally evolving electron distribution shape, leading to the variations measured in both the maximum proton energy and the beam divergence.

To further test this hypothesis proton acceleration employing targets of varying transverse dimensions was investigated. This enabled a modification of the point in time in the interaction at which reflection of electrons begins to occurs from the target edges. This study clearly shows the presence of significantly varying sheath dynamics between the two focusing cases, with the tight focus producing strong accelerating fields at the target edge, capable of tens of MeV proton generation. Additionally, the reflection of electrons from the edges was seen to considerably change the evolution of the accelerating fields, leading to the breakup of proton beam structure in the smallest target size investigated (0.5×0.5 mm), where lateral spreading effects will be most dominant.

To aid in the understanding of the source of changes in the sheath dynamics between focusing scenarios, 2D PIC modelling with parameters representing the experimental conditions were employed. These highlighted two key differences using tight focusing relative to a larger spot: (i) a smaller radius of critical surface curvature, from enhanced target deformation in the hole boring phase; and, (ii) a wider angular distribution of fast electron throughout the target. The former results in an enhancement in absorption processes which take place when the pulse is obliquely incident on a plasma density gradient, in this case of a normal incident pulse. Additionally these mechanisms (resonance and vacuum absorption) inject electrons normal to the local critical surface direction, and thus an alteration of fast electron distribution within the target would be expected. This was observed when investigating the density of fast electrons in the target (of energy >1 MeV). Tight focus irradiation was seen to result in a wider angular distribution of electrons throughout the target, the second difference highlighted above. Considering this in terms of the temporal evolution of electron recirculation inside the target, the larger degree of transverse fast electron motion (in the small focus spot case) would lead to a faster lateral spreading of electrons with the target and thus the

spreading of the rear surface electron distribution. This in turn explains the measured proton beam properties.

This study highlights the importance of focal spot size in the view of laser-driven proton acceleration in the TNSA regime, far beyond a parameter which simple defines the laser intensity. More specifically, this work demonstrates the influence of an extremely small, tightly focused laser pulse on the interaction dynamics and the subsequently accelerated proton beam properties. This is particularly important when considering a main aim of laser-driven acceleration is increasing maximum proton energies. Several laboratories are actively developing FPMs, with the aim of achieving higher intensities to push the achievable ion energies higher. This study highlights that caution is required if this is to be achieved by decreasing the focal spot size towards the laser wavelength due to changes induced in the interaction physics.

Chapter 6

Influence of focal spot size on energy absorption in intense laser-solid interactions

6.1 Introduction

The coupling of laser energy into dense plasma, often referred to as absorption, and the subsequent production of fast electrons (of mega-electron Volt energies) underpins a host of intense laser-driven radiation production mechanisms. It defines not only the properties of secondary radiation, such as gamma-rays [205, 206] and ion acceleration [13, 19], but additionally the optical properties of the plasma over the course of the interaction [207, 208]. The promise of applications of laser-solid interactions (as discussed in chapter 1) has motivated considerable experimental and theoretical investigation into intense laser-solid interactions, and in turn the sub-topic of laser-plasma absorption physics.

Given that laser-electron energy coupling mechanisms are highly sensitive to numerous laser and plasma parameters (as explored in section 2.5.4), the complex and dynamic picture which emerges remains one of the most challenging areas of the field to understand. For applications which require highly efficient laser-energy coupling into fast electrons and a high degree of controllability, for example fast ignition inertial confinement fusion [45], resolving these complexities is essential. Numerous collisionless absorption mechanisms for dense plasmas have been identified in recent years, such as

those laid out earlier in section 2.5.4; including $\mathbf{J} \times \mathbf{B}$ [74], vacuum [72] and resonance absorption [209]. Each of these mechanisms are sensitive to a host of parameters, including: laser polarisation, intensity, incidence angle and plasma density scale length [210, 211, 212]. This dependency on the interaction conditions, in conjunction with the fact that several of these mechanisms may act concurrently as the interaction evolves, makes it highly non-trivial to understand the absorption dynamics. Consequently, to date it has proved exceptionally difficult to establish a theoretical framework or to conduct simulations which encompass all aspects of the complex nature of laser absorption for a given set of interaction conditions.

Experimentally, however, it is possible to at least measure the total laser absorption, though quantifying the degree of laser energy not absorbed by the target, i.e. measuring reflected and scattered light components, and comparing it to the incident pulse energy [170, 171]. Although ultimately the absorption dynamics need to be resolved and understood, we can significantly further our understanding of the absorption physics, and the key laser and plasma parameters to which this is sensitive, through such experimental measurements. These essentially empirical insights feed into the future design of experiments and applications, and are ultimately crucial in the verification of theoretical and numerical models.

Despite the inextricably vital role which laser absorption plays in laser-solid interactions, there are surprisingly few experimental studies of the total absorption in the relativistic interaction regime; these are discussed in more detail in the next section. While these findings have demonstrated that laser absorption strongly depends on intensity by variation of pulse energy, the intensity dependence by variation of other parameters, and in particular the focal spot size, has not been addressed directly by measurements of the total absorption. As discussed in chapter 5 (see section 5.2), previous investigations of the fast electron temperature scaling, inferred from the maximum energy of laser-driven protons, indicate that indeed there are more complex dynamics at play when the focal spot size is varied, which merits further investigation [113, 197].

To address this problem, this chapter reports on an investigation of the scaling of total laser absorption into overdense relativistic plasmas as a function of peak laser intensity. This is achieved by separately varying the pulse energy and the focal spot size, furthering the main theme of this thesis, i.e. investigating the effect of focal spot size on laser-solid interaction physics. This investigation is achieved by employing a

suite of diagnostics, including an integrating sphere and an angularly resolving electron detector, developed specifically for these measurements. These are essential for developing a broader understanding of laser-plasma absorption dependencies; each of which will be explored in the coming section.

6.2 Review of relevant literature

As mentioned above, there has been relatively few experimental studies of the total laser-energy absorption in the interaction with solid density targets in the relativistic regime. Moreover, most experimental studies investigating such, to date, at peak intensities up to 10^{20} W/cm^2, have involved indirectly inferring laser absorption to fast electrons through measurement of x-ray emission or ion acceleration [213, 214, 215]; though numerous processes, not linked to absorption, will effect these measurements.

One study which investigated absorption directly, through the quantification of the degree of laser energy not absorbed by the target plasma, at intensities up to 10^{20} W/cm^2, is the widely cited measurements reported in Ping *et al.* [75]. This study investigated, for the first time, direct measurements of total absorption for a short relativistic laser pulse (0.15 ps pulse length and 0.8 μm wavelength with pulse energies between 0.02 and 20 J) interacting with solid foils. These measurements demonstrated an intensity dependent scaling of laser absorption, with values up to 90% for pulses incident at 45° to the target normal axis, and 60% for near-normal incidence, at a laser intensity of $\sim 2\times10^{20}$ W/cm^2. Such high values were found to be consistent with both interaction with pre-plasma and hole boring by the laser pulse enhancing absorption, via 2D PIC simulations.

Furthermore these results were employed by Davies [68] to develop an empirical scaling law, which describes the fractional absorption, f_{abs}, as a function of laser irradiance ($I_L\lambda^2$);

$$f_{abs} = \left(\frac{I_L\lambda^2}{3.37 \times 10^{20}\ [\mathrm{Wcm^{-2}}\mu\mathrm{m}^2]} \right)^P \tag{6.1}$$

where the irradiance is units of Wcm$^{-2}\mu$m^2 and P is a fitting parameter. This is not a suitable function to describe laser absorption at any irradaince value as it is unbounded, due to it being found through simply fitting to the measurements reported in Ping *et*

al. [75]. However, it is useful for modelling absorption scaling with irradiance values between 3.0×10^{18} to 2.3×10^{20} $\mathrm{Wcm^{-2}}\mu\mathrm{m}^2$, such as the study presented in this chapter.

This review of absorption measurements reported in Davies [68] was further employed in Levy *et al.* [216] to develop a theoretical model establishing upper and lower bounds on laser-coupling for a given laser intensity with relatively thick ($>\mu$m) solid density targets. This study highlights that complex targetry (such as structured targets) or near critical density targets (such as CH foam targets) are required to circumvent these absorption bounds.

The investigation reported in Ping *et al.* [75], and thus also the work of Davies [68] and Levy *et al.* [216], was conduced by altering intensity through variation of pulse energy, with constant focal spot size. As such, the intensity dependence by variation of the focal spot size was not addressed. As was discussed in the previous chapter (see section 5.2) the scaling of such aspect as the maximum energy of laser-driven protons [195, 197] and the number of protons accelerated (i.e. the laser-to-proton conversion efficiency) [198], for example, is seen to be significantly different depending on how the intensity is varied. This indicates that there are more complex dynamics taking place when the focal spot size is varied.

6.3 Experimental method

Employing the PHELIX laser (see section 3.3.2), s-polarised pulses, of (700±100) fs (FWHM) with energy, E_L, varied between 4 J and 180 J and of central wavelength 1053 nm, were incident at 0° (i.e. along target normal) onto aluminium targets of thickness 6 μm and 20 μm. The pulse temporal intensity contrast was measured pre-experiment to be 10^{10} on the nanosecond timescale, and 10^4 at 10 picoseconds in front of the main pulse [138]. The pulse energy was controlled solely by the rotation of a calibrated waveplate between two crossed polarisers, located between the front-end and pre-amplifiers sections of the laser. Thus the investigated energy range (4 J to 180 J) can be covered without any additional changes to the laser. Consequently the temporal intensity contrast does not change significantly over this range. This was verified by test shots with extremely thin (nanometers scale) foil targets with full laser power and the employment of a 3rd order scanning autocorrelator at low energies. To

focus the pulses onto the target an F/1.5 OAP was employed, achieving a minimum focal spot size of ϕ_0= 4 μm (FWHM), varied up to a maximum spot size of ϕ_0= 270 μm by translating the OAP along the propagation axis away from best focus (towards the target). To investigate laser absorption as a function of incident laser intensity on-target, in the range of $1\times10^{17}-1\times10^{20}$ W/cm^2, this parameter was controlled by separate variation of either E_L or ϕ_0. Furthermore, this laser system was selected due to its high shot-to-shot energy stability, and was thus an excellent choice of facility for energy absorption measurements.

In order to make unambiguous measurements of the total laser energy absorption and the conversion into high energy electrons, three novel custom diagnostics have been developed which operate concurrently. These are: (1) an integrating (Ulbricht) sphere employed to quantify the degree of unabsorbed laser light diffusely scattered from the target; (2) a dual-wavelength imaging system, in conjunction with a scatter screen, to measure unabsorbed laser light backscattered and specularly reflected from the target; and (3) an angularly resolving 'wrap-around' detector to characterise the escaping fraction of fast electrons from the target rear. The first two instruments enable two components of an energy balance equation (Eq. 6.2), used to quantify the energy absorbed by the target, to be measured; the equation is as follows;

$$E_{IN} = E_{BS} + E_{SR} + E_{DS} + E_{TR} + E_{ABS} \tag{6.2}$$

where E_{IN} is the laser energy incident onto target, E_{BS} and E_{SR} are the energy of backscattered and specularly reflected light, respectively (both of which are quantified using the dual-wavelength imaging system), E_{DS} and E_{TR} are the energy of diffusely scattered light and transmitted target light respectively (both quantified employing the integrating sphere), and finally E_{ABS} is the laser energy absorbed by the target. The fraction of absorption by the plasma (K_{ABS}) can be written in terms of the fractions of each of the components as;

$$K_{ABS} = 1 - K_{BS} - K_{SR} - K_{DS} - K_{TR} \tag{6.3}$$

Therefore in order to determine the laser energy absorbed by the target, it is necessary to measure all the components of the energy balance equation.

Each of the three diagnostics involved in this measurement, including their design

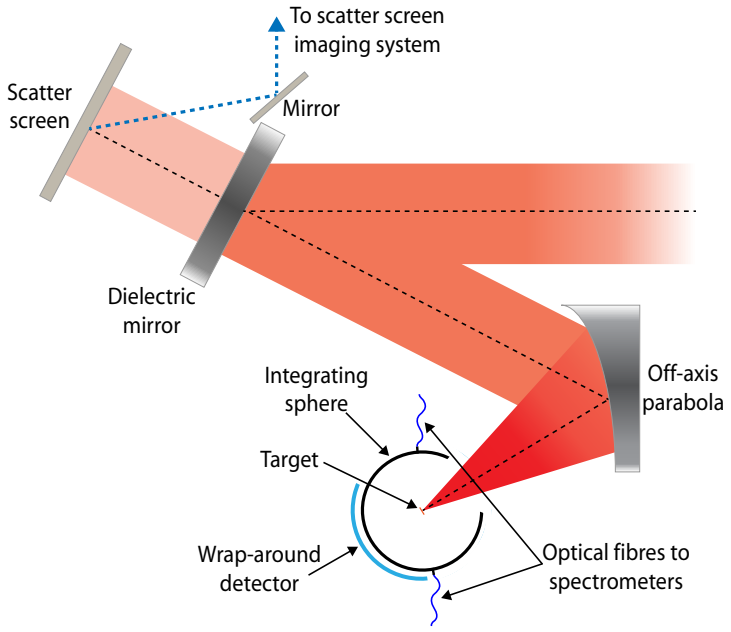

Figure 6.1: Schematic of the experimental set-up used to measure the degree of laser energy absorbed during a laser-solid interaction, indicating the position of the three main diagnostics employed in this study, these being: an integrating sphere, a scatter screen in conjunction with a dual-wavelength imaging system and an angularly resolving wrap-around electron detector.

and operation, are explored separately below. Figure 6.1 displays a schematic of the experimental set-up indicating the position of each of these diagnostics.

(1) Integrating sphere

In order to quantify the amount of light diffusely scattered from a target during irradiation (one component required in the calculation of total unabsorbed laser light) a custom integrating (Ulbricht) sphere (the principle of which is covered in section 3.4.2) was developed to make this measurement, in which a target is placed at its centre.

The design of this instrument, starting with its dimensions, was based on the maximum sphere diameter which could be employed in the PHELIX target chamber, based on knowledge of the focal length (360 mm) and off-axis angle of the focusing OAP (22.5°). This limiting maximum size is based on the fact that if the sphere was any larger it would begin to block the incoming collimated beam to the OAP. Additionally, the largest feasible diameter is desirable to minimise possible damage from laser light reflected or transmitted by the target. The maximum feasible sphere diameter was calculated to be 180 mm. Initially it was hoped that the sphere could be used to quantify not only the diffusely scattered interaction light, but also the specular re-

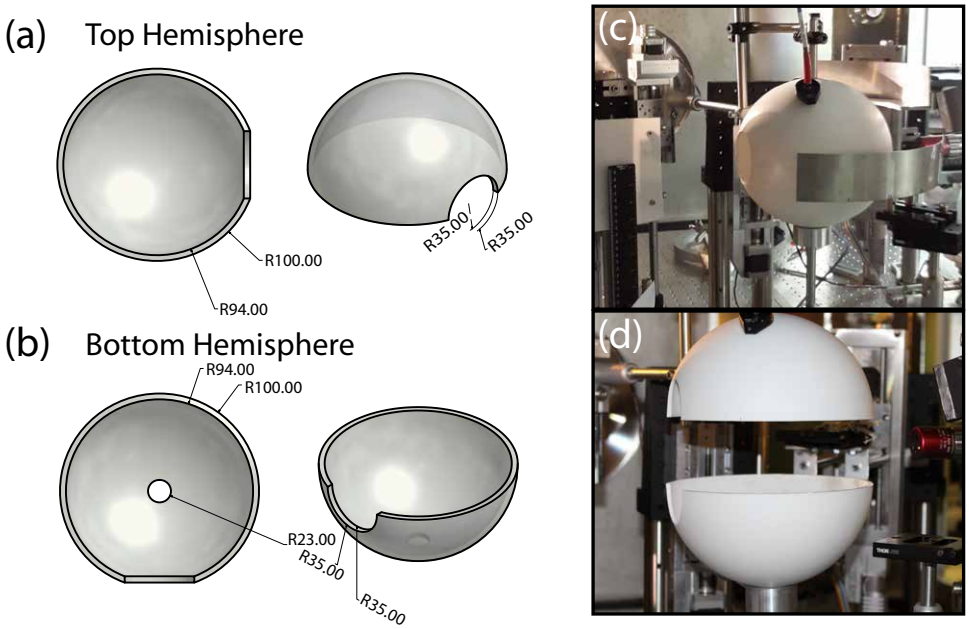

Figure 6.2: (a) and (b) Schematic drawings of the integrating sphere design top and bottom hemispheres, respectively. (c) and (d) Images of the manufactured spheres in the experimental set-up, in (c) its closed position to quantify the energy content of diffusely scattered light in the interaction and (d) its open position to allow entry of a microscope objective for focal spot optimisation and target alignment.

flected component. For this to be achieved the target would have to be irradiated at an oblique angle (∼30°), allowing the specular reflected light to be directed onto the sphere walls. However, as the specular light is 'beam-like', operating in this fashion relies on the intensity of this light being below the damage threshold of the wall (the wall coating is discussed later in this section). It was calculated, however, that for damage not to occur the sphere size would need to exceed the maximum limiting size. As such this sphere operation mode is not feasible for employment on this laser system configuration.

The next operation mode considered was to include an additional aperture in the sphere to allow specular reflected light to exit, and be quantified outside the sphere (covered in the next section). This option was also ruled out as the aperture size required to allow this rapidly expanding F/1.5 beam to exit unperturbed would overlap with the incoming beam aperture, and additionally alter the integrating ability of the sphere due to the reduction in reflective surface area.

To resolve these issues concerning the specular component of reflection, target irradiation was conducted at 0° laser incidence angle, such that specular light, and backscattered light, would propagate back up the input direction and exit through the entrance aperture, to be quantified outside the sphere (covered in the next section). In terms

of this entrance aperture, the maximum sphere size selected means the aperture size needs to be of sufficient size to enable the full F/1.5 focusing laser cone to reach the interaction target placed at the centre of the sphere. This was calculated to be 70 mm in diameter. To allow for the insertion of the target mount and positioner, an additional 23 mm diameter hole was included in the bottom pole of the sphere.

The sphere was additionally designed to be divided into two separate hemispheres. This enables access for the focal spot and target alignment camera, prior to target irradiation. Additionally, the target mounting posts were made from a highly reflective PTFE plastic as to not imped scatter measurements. Once target alignment has been achieved the two hemispheres are placed together, producing a tight seal at the interface, forming the integrating sphere.

Finally two small 5 mm diameter holes were included at 50° above the equator in the top hemisphere (60° anticlockwise along the equator from laser axis) and 45° below the equator on the bottom hemisphere (120° clockwise along the equator from laser axis) into which two multimode optical fibres could be connected for the quantification of signal inside the sphere (discussed in more detail later). The sphere itself was manufactured using a vacuum moulding technique to form each hemisphere from a 6 mm thick sheet of Polyethylene terephthalate (PETG) plastic. Figure 6.2 displays the design and manufactured sphere.

As the purpose of the integrating sphere is to spatially integrate the radiant flux of scattered laser light, it requires diffusely reflective surfaces. To this end, the inner walls were coated with a commercially available diffuse reflectance paint, known as Spectraflect. This barium sulphate based paint is a near-Lambertian scatterer and can be easily applied to many substrates (including the PETG plastic sphere). Furthermore it has a high reflectivity over a wide range of optical wavelengths (350 nm to 2400 nm), with a ∼96% reflectivity at the PHELIX laser operation wavelength (1053 nm). To apply this coating to the pre-formed plastic spheres a specialist coating company (Pro-Lite Technology) was employed, applying a coating of thickness ∼0.5 mm to ensure the sphere is opaque at the laser wavelength, i.e. minimal transmission losses. Compared to other commercially available coatings this has a relativity low damage threshold (1.7 J/cm^2, measured employing a nanosecond range Q-switched YAG laser at 532 nm). However, this low damage threshold, and the fact it is determined for a much longer pulse length, is not an issue in our sphere operation mode, i.e. for specular light

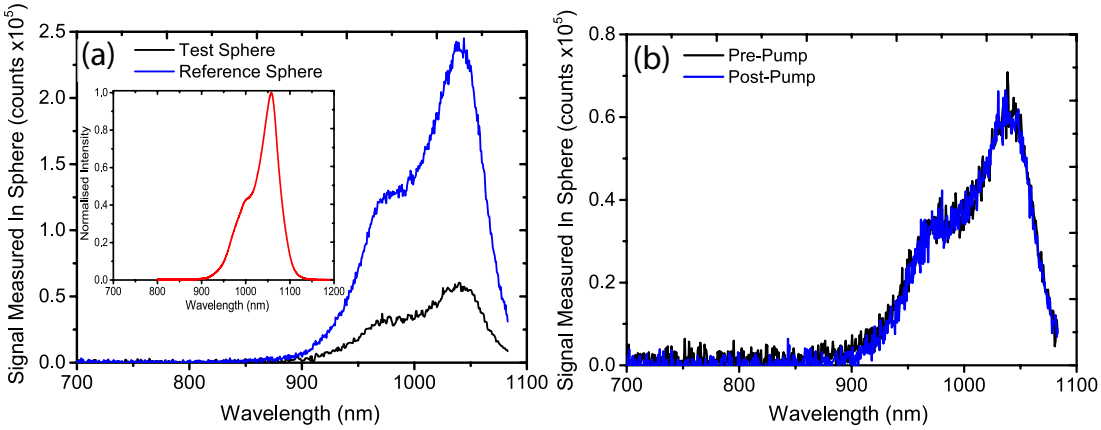

Figure 6.3: (a) Plot displaying the scattered spectrum measured inside both the manufactured test sphere (black data) and the reference sphere (blue data), for the same 1054 nm input source (spectrum displayed in inset [red data]). (b) Plot displaying the scattered spectrum measured inside the test sphere pre- (black data) and post- (blue data) vacuum testing, again for the same input signal.

being directed out of the sphere and considering the scaling of the damage threshold of materials with incident pulse length, as reported in [217]). Additionally, Spectraflect is limited by the fact that the binder used to adhere it to the sphere substrate is water soluble and therefore cannot be used in high humidity applications. This is not an issue within the interaction chamber vacuum environment, but must be considered when storing the spheres. As such, coated spheres were kept in vacuum sealed bags to avoid any undesirable degradation of the Spectraflect coating pre-employment. Other types of specular reflecting paint were considered, such as Spectralon. This possesses a higher damage threshold compared to Spectraflect (4 J/cm^2), however is relatively more complex to apply to a curved surface and comes at much higher cost. It was thus not a viable option for producing multiple spheres to be used in the experiment.

To characterise and validate the operation of the manufactured Ulbricht sphere design before employment on a laser-solid interaction experiment, its integrated signal was compared to a commercially available integrating sphere (ThorLabs 50 mm diameter integrating sphere), which will be referred to as the 'reference sphere'. This was achieved by illuminating the manufactured sphere with 1054 nm light from a light emitting diode (LED) coupled with a multi mode fibre optic connected to one of the sphere fibre ports. To measure the diffuse scattered light signal inside the sphere an optical spectrometer (Andor Shamrock 303i) was connected, also by a fibre, to the second fibre optic port. The same test was applied to the reference sphere, with a comparison of the results displayed in Fig. 6.3(a). It is clear when comparing these spectra that a

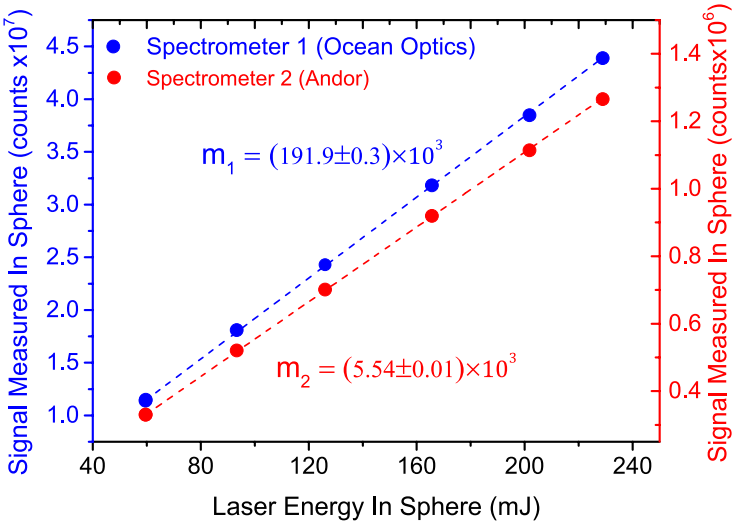

Figure 6.4: Combined energy response curve for the sphere and each optical spectrometer, with blue data representing the Ocean Optics spectrometer calibration and red data the Andor spectrometer. The two spectrometers have slightly different sensitivities which are accounted for in the calibration.

higher signal is measured inside the reference sphere compared to the manufactured sphere, with a maximum peak signal difference of approximately $\times 4$. At first this may seem like the manufactured sphere is far from an idealised integrating sphere, however as the radiant flux measured inside a sphere is inversely proportional to the illuminated surface area, i.e. the sphere surface area, (as discussed in section 3.4.2) then clearly the output signal, for the same input signal, would be expected to fall when comparing spheres of diameters 50 mm and 180 mm. This coupled with the fact the manufactured sphere also includes two open apertures (laser and target ports), which the reference sphere does not, then the integrated signal measured compares favourably to that of the reference sphere.

This characterisation of the sphere design was repeated for a sphere which had been held in vacuum (between 10^{-4}–10^{-5} Pa) for two days. This test was necessary to gauge if being held in vacuum for a period of time would have any adverse affects on the sphere's operating ability, such as degradation of the specular reflecting coating. Figure 6.3(b) shows the output spectrum measured from a sphere (again employing the 1054 nm LED input) before and after the vacuum treatment. Comparison of the spectra shows no significant difference between the operation of the sphere as a result of vacuum conditions.

In terms of sphere operation on the PHELIX experiment, the signal of diffusely scattered laser light was quantified using two optical fibres connected to the sphere;

one connected to an Ocean Optics (Maya2000Pro) spectrometer and the other to an Andor Shamrock (303i) spectrometer. The energy response of the sphere was calibrated by first measuring the energy throughput of the laser system, including all optics up to the sphere entrance, employing a calibrated large diameter calorimeter. The sphere response was then characterised by directly irradiating the sphere walls with a series of relatively low energy laser shots ranging from 60 mJ to 230 mJ. The calibration of input pulse energy to sphere signal for each spectrometer is shown in Fig. 6.4. The sphere signal was quantified from the obtained spectra by integrating around the central laser wavelength by ±40 nm (the range over which the spectrum dropped to the background level). For full power laser pulses the fibre optic cables were filtered using well characterised neutral density filters (see section 3.4.2) prior to the fibre terminal to avoid the possibility of optical damage being induced inside the fibre. The absolute energy of the scattered light in the sphere was then calculated by scaling the measured signal, obtained by integrating the 1054 nm signal measured in the spectrum, by the neutral density response.

(2) Dual-wavelength imaging system

The integrating sphere design presented in the previous section, as discussed, quantifies the energy of laser light diffusely scattered from the target, E_{DS}, during the interaction. However this is not yet enough information to calculate the total amount of laser light absorbed by the target, as explained by Eq. 6.2 and Eq. 6.3. To complete the absorption measurement, the laser energy specularly reflected, E_{SR}, and backscattered, E_{BS}, by the target plasma must be quantified. As mentioned, this component leaves the sphere through the entrance aperture. Upon exiting this light is collected and re-collimated by the OAP, which then directs it back along the laser path. To quantify a highly reflective scatter screen (seen in Fig. 6.5(a)), coated in Spectralon paint, was positioned behind the final dielectric turning mirror before the parabola, enabling its light leakage (∼1%) to be incident on the screen. The screen was then imaged by a custom dual-wavelength imaging system (as described in section 3.4.2), operating at the fundamental laser wavelength (1053 nm) and its second harmonic (527 nm). A schematic of this diagnostic is shown in Fig. 6.5(c).

An absolute calibration for the energy response of the imaging system, at the laser wavelength (1053 nm), was made by directly irradiating the scatter screen with a

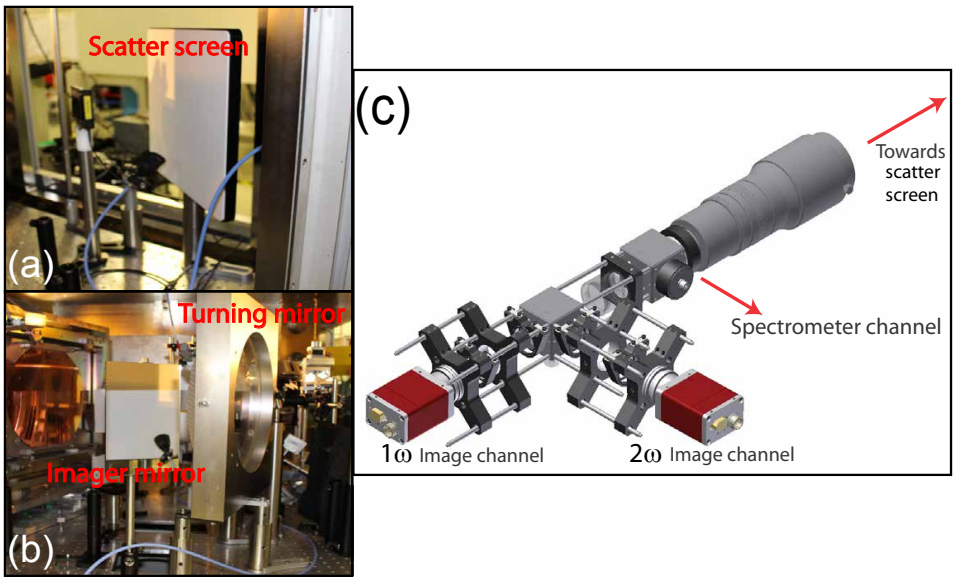

Figure 6.5: (a) Photograph of the scatter screen set-up employed to quantify the energy content of specularly reflected (E_{SR}) and backscattered (E_{BS}) laser light. (b) Photograph of the turning mirror which has a small percentage transmission (∼1%) allowing specular reflected and backscattered light to reach the scatter screen, and the mirror allowing the imaging system to observe the screen. (c) Schematic of the dual-wavelength imager employed to measure the light signal incident on the scatter screen.

∼25 mm diameter pick-off of the incoming laser pulse. This pick-off was split using a calibrated 50:50 beam-splitter, with one 50% component directed onto a calorimeter for absolute energy measurement and the other onto the scatter screen, thereby enabling a direct calibration of the imager response for laser pulse energy. The set-up of this energy calibration procedure and the resultant calibration curve is displayed in Fig. 6.6(a) and (b), respectively.

(3) Angularly resolving wrap-around electron detector

In addition to the measurement of the total laser absorption, through the optical diagnostics explored previously, the escaping fraction of fast electrons from the target during the interaction is measured using an angularly resolving 'wrap-around stack' detector (WAS), detailed previously in Refs. [218, 219]. This diagnostic surrounds part of the integrating sphere, centred on the equator. The detector consists of stacked layers of Fujifilm image plate (BAS-SR) (see section 3.4.1), filtered by iron plates (the composition of which is shown in Fig. 6.7(a)) in order to achieve some degree of spectral resolution. This detector-filter combination has a minimum energy detection threshold of ∼2.3 MeV (i.e. minimum electron energy passing through the integrating sphere wall

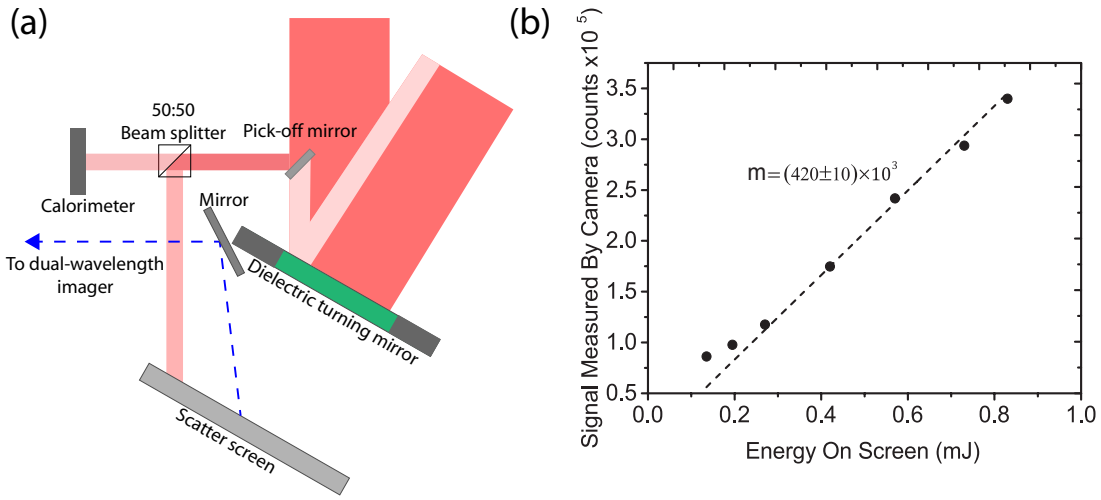

Figure 6.6: (a) Schematic of the set-up employed to achieve an absolute calibration for the energy response of the screen-imager diagnostic, used to quantify the energy content in the specularly reflected and backscattered laser light from the laser-solid interaction, with the main components annotated. (b) The resultant calibration curve for the combined response of the imaging system and camera, imaging at the laser central wavelength (1054 nm).

and first iron filter); calculated employing the electron stopping database ESTAR [220]. The image plate and filters are curved into a 180° arc in the horizontal plane, and are 50 mm wide in the vertical direction. Additionally the detector was divided into two sections, necessary to allow one section to be translated away to allow the alignment objective to be moved in; similar to the movement of the two sphere hemispheres. A picture of this diagnostic and its placement in the experimental set-up is displayed in Fig. 6.7(b).

Once the WAS has been exposed to the escaping electrons from the interaction, the image plate must first be scanned in order for the resulting data to be recorded, producing a 2D image of the angular electron distribution. An example of the raw data is shown in Fig. 6.7(c). Note that the four image plate layers are scanned simultaneously to avoid issues with inadvertent signal loss between layers due to temperature variations or exposure to ambient light. The process of converting the raw scanned image into the physical electron numbers is covered in section 3.4.1. Whilst this diagnostic is designed to provide angularly resolved spatial measurements, for the purposes of investigating the total number of escaping electrons, the signal measured in each image plate was spatially integrated for each layer. To give a measure of the total escaping electron number the signals measured on each layer were summed together. The electron number is calculated from the image plate data using the calibration presented in Chen *et al.* [167].

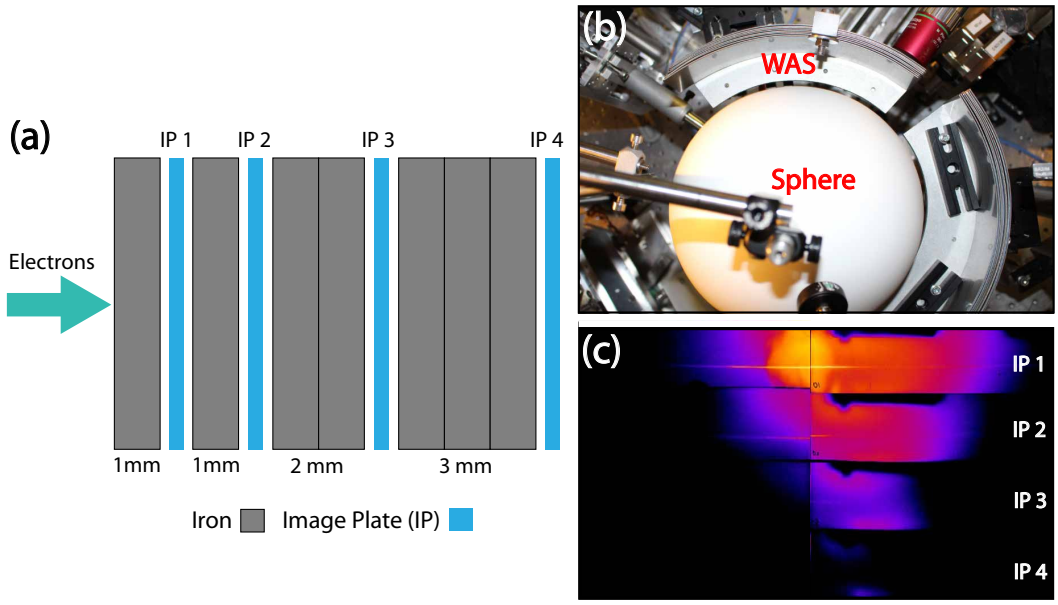

Figure 6.7: (a) Wrap-around electron detector stack composition used to achieve a degree of spectral resolution. (b) Top view of experimental set-up, showing wrap-around stack (WAS) diagnostic, covering 180° degree angular range, in relation to the integrating sphere. (c) Example image of unprocessed output from WAS detector, showing the escaping electron beam.

6.4 Experimental results

6.4.1 Measurements of laser absorption

To begin, the set-up explored in the previous section was used to investigate laser absorption scaling as a function of intensity, in the range of 10^{17}–10^{20} W/cm^2. Firstly, intensity is altered by varying E_L and keeping ϕ_0 constant (at best focus of 4 μm). This is a similar intensity range as the results reported in Ping *et al.* [75] (under somewhat different conditions). The results of this investigation are shown in Fig. 6.8, using blue triangles for 20 μm Al targets and black squares for 6 μm Al targets. To compare measurements to those reported in Ping *et al.* [75], the experimental data from this investigation is fitted with the empirical model for fractional absorption derived by Davies [68] (Eq. 6.1), found employing the Ping *et al.* findings. The most salient point demonstrated by this investigation is the good agreement found between the measurements of the fractional absorption and those of the Davies fit function, and thus with Ping *et al.* (upon which the function is based) despite being obtained under different laser pulse parameters. Additionally, the testing of two target thicknesses (6 μm and 20 μm) demonstrates the relative insensitivity of absorption in this regime to target thickness, i.e. it is dominated by a surface interaction, when

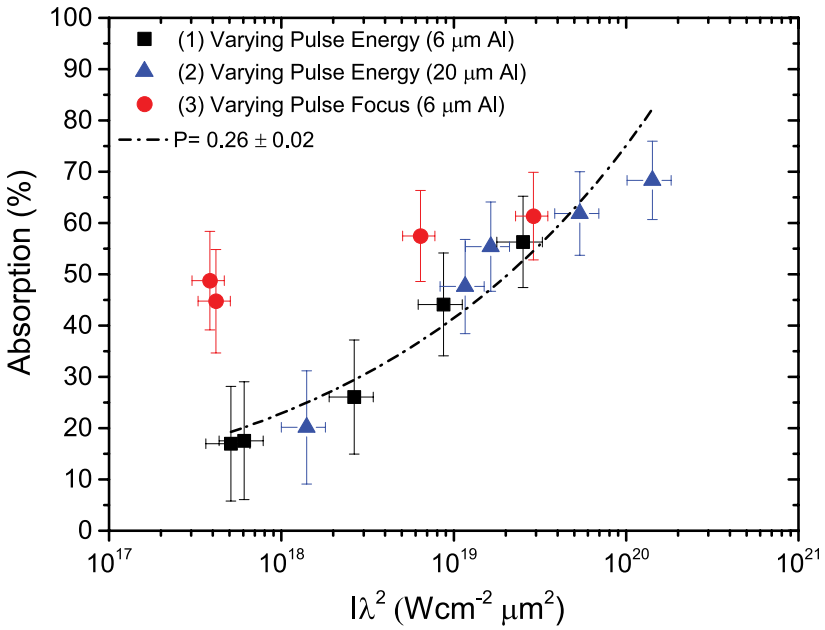

Figure 6.8: Plot of the percentage of laser energy absorbed as a function of laser irradiance. Here, the black and blue data points represent measurements made when the intensity is altered, by varying E_L at best focus for 6 μm and 20 μm thick aluminium targets, respectively. The red data points represent measurements when the intensity is varied by changing ϕ_0 while E_L is constant. The black dashed line is a fit using the empirical model derived by Davies, as shown in Eq. 6.1 with the fitting parameter P=0.26 ± 0.02.

only the pulse energy is altered. For significantly thinner targets which may become relativistically transparent during the interaction, for example, a different scaling with intensity would be expected in the transition to volumetric interaction processes, as indirectly demonstrated by a number of recent results [221, 222, 223].

Having demonstrated that the absorption measurements conducted for a range of laser intensities, through variation E_L at a constant ϕ_0, show good agreement with previously published values for similar experimental conditions, absorption scaling as a function of intensity for varying spot size and constant laser energy was investigated for 6 μm Al targets. In Fig. 6.8, red data points are the measured absorption values obtained by varying focal spot size. It is evident that this scaling is considerably slower than in the case of varying pulse energy. Two key points can be inferred from this result. Firstly, at an irradiance of $\sim 5\times10^{17}$ Wcm$^{-2}\mu$m^2 there is a factor $\sim$3 enhancement in the total absorption for directly comparable laser irradiances when using a higher energy and relatively larger focal spot. The enhanced absorption case has considerably more energy contained within the pulse (157 J compared to 4 J) and a considerably larger focal spot (270 μm compared to 4 μm). Secondly, as the irradiance increases for an otherwise constant pulse energy, the overall absorption increases only very slowly,

Irradiance ($\times 10^{19}$ Wcm$^{-2}\mu$m^2)	Laser Energy (J)	Focal Spot Size (μm)	Absorption
0.05 ± 0.01	4.2 ± 0.2	15.1 ± 2.0	0.17 ± 0.10
0.06 ± 0.02	4.9 ± 0.3	7.5 ± 0.9	0.18 ± 0.10
0.30 ± 0.08	41 ± 2.0	9.5 ± 1.0	0.26 ± 0.10
0.90 ± 0.30	93 ± 5.0	14.5 ± 2.0	0.44 ± 0.10
2.50 ± 0.70	148 ± 7.0	9.6 ± 1.0	0.56 ± 0.09
0.04 ± 0.01	172 ± 9.0	271 ± 50	0.48 ± 0.10
0.04 ± 0.02	157 ± 8.0	270 ± 50	0.45 ± 0.10
0.60 ± 0.02	151 ± 8.0	54.3 ± 10	0.58 ± 0.09
2.90 ± 0.06	154 ± 8.0	27.6 ± 5.0	0.61 ± 0.09

Table 6.1: Fractional absorption values as shown in Fig. 6.8 for 6 μm aluminium targets, either varying E_L or ϕ_0.

notably different to the case where the E_L is varied with a constant ϕ_0. Results from these respective data sets are shown in Tab. 6.1.

6.4.2 Measurements of escaped electron fraction

Employing the wrap-around electron detector stack diagnostic explored previously (section 6.3), a measure of the number of electrons which are accelerated and escape the target could be made, in addition to the measurement of the total absorbed fraction of the laser energy. Measuring this population gives knowledge of the interaction, but is not equivalent to measuring the total number of energetic electrons produced by the laser. This is a result of a significant number of electrons trapped in the target by the electrostatic sheath fields on the target surfaces, and a loss of relatively low energy electrons which are collisionally stopped when propagating through the target [224]. It can however be assumed that measuring the escaping electrons is representative of the overall change in electron production. Figure 6.9 displays the results for the number of escaping electrons scaling with laser irradiance, for the same cases presented in Fig. 6.8; red data representing the cases of varying the focal spot size (for 6 μm Al targets), black and blue data for the case of varying pulse energy, for 6 μm and 20 μm Al targets, respectively.

As in the absorption investigation, these results demonstrate a general trend of increasing escaping electron numbers with laser irradiance. For the lowest irradiances employed in this study ($\sim 0.04\times 10^{19}$ Wcm$^{-2}\mu$m^2) electron data is not available as the signal is below the detector threshold, set principally by the 2.3 MeV electron energy cut-off of the sphere wall and first filter layer combination. Thus it is difficult to see the

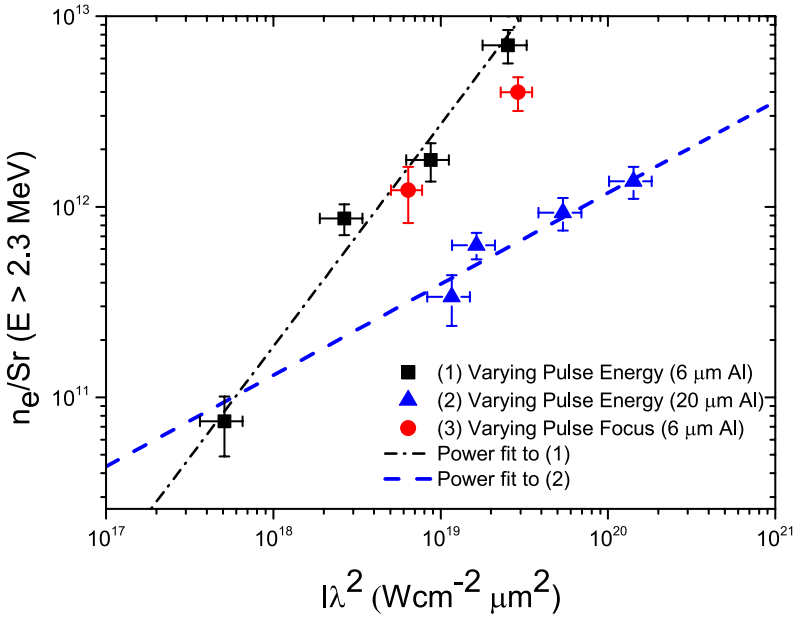

Figure 6.9: Plot of the total number of escaping electrons per steradian, n_e/Sr, for electron energies, above 2.3 MeV, measured using the wrap-around stack detector, recorded simultaneously with the laser absorption measurements in Fig. 6.8. A power law fit, of the form $n_e = (I_L\lambda^2)^n$, is made to the two data sets where irradiance is varied by changing pulse energy; with n=1.17 for data set 1 (black data) and n=0.48 for data set 2 (blue data.)

same trends as in the absorption data displayed in Fig. 6.8. This suggests that the extra fraction of laser energy absorbed at lower intensities in the case where the focal spot size is altered goes into electrons that are below the detection threshold of the detector (2.3 MeV) or are those trapped in the target. It can also be noted from these measurements that fewer total number of electrons are recorded for the 20 μm thick target compared to the 6 μm targets. Considering that similar absorption levels were measured for both target types, in the constant focal spot size case, it can be inferred that this decrease in the number of escaping electrons is a result of increased electron stopping within the thicker target. It was demonstrated in Link *et al.* [82] that as the target thickness is increased the capacitance of the target increases and, as such, the escaping fraction should be slightly higher but at the cost of a colder electron spectrum due to losses in the target from collisions and resistive fields. As stated, the detector has a low energy cut off of 2.3 MeV, as such it is likely that part of this decrease in the observed escaping fraction is as a result of part of the electron spectrum being shifted to below this cut off. From these measurements there is a clear scaling of the escaping electron fraction with intensity, but they serve to highlight, in support of the conclusions presented in Link et al. [82], that the escaping electron fraction is not an unambiguous measure of energy

coupling or the fast electron spectrum. Having measured both the total absorption and the escaping electrons simultaneously is a compelling demonstration of this effect.

6.5 Modelling

6.5.1 PIC simulations

To investigate the underlying absorption physics, when the focal spot size is changed for constant intensity, 2D PIC simulations (see section 3.5.1) are employed. Using the fully relativistic PIC code EPOCH, the interaction of a 550 fs linearly polarised Gaussian laser pulse (a 30 fs case is considered later), with a $30n_c$, aluminium target with thickness between 6 μm and 50 μm is simulated. The target is assumed to be in an ionisation state of Al^{11+}, initially neutralised by a corresponding electron population. The initial electron temperature is set to 10 keV and the initial ion temperature to 40 eV. The simulation box is of size 84×140 μm, with 12600×11520 cells and 10 particles per cell. The laser focal spot diameter and pulse energy is varied in order to fix the peak intensity.

In the first instance, two experimental data points are selected for testing and their corresponding experimental conditions (laser and target parameters) are used as the simulation input parameters to enable direct comparison. These data points have approximately the same irradiance ($\sim 1\times10^{19}$ Wcm$^{-2}\mu$m^2), though have different focal spot sizes (ϕ_0= 50 μm and ϕ_0= 4 μm), compensated by the total energy in the pulse. Using the resultant outputs of these simulations, a representative electron spectrum is obtained, approximately 334 fs after the peak laser pulse amplitude has interacted with the target front (the time prior to the fastest electrons leaving the simulation box), as displayed in Fig. 6.10(a), with electrons sampled across the entire simulation box. This shows the same tendency as found experimentally, in that the larger spot (ϕ_0= 50 μm) has a higher total energy for fast electron population than the small spot case (ϕ_0= 4 μm). To quantify, the larger spot produces a considerably higher temperature fast electron tail when compared to the smaller spot, of 2.2 MeV to 5.3 MeV. This energy gain primary comes from a non-uniform heating of electrons at the higher energy region of the spectrum, which leads to a change in the spectrum temperature (the reasons for

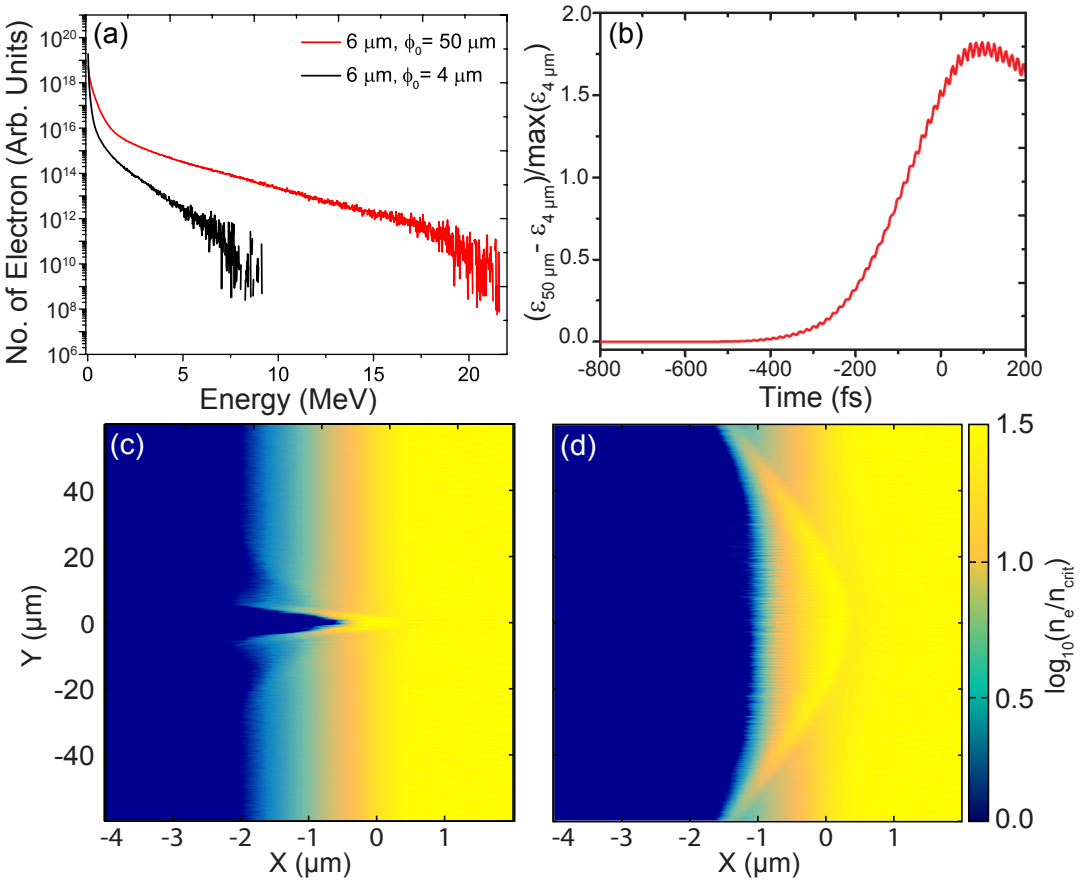

Figure 6.10: (a) Extracted electron spectra from simulations, 334 fs after the peak of the pulse arrived at the target, for the $\phi_0 = 50$ μm (red data) and $\phi_0 = 4$ μm (black data) focal spot cases. The fast electrons are sampled across the entire simulation box. (b) Plot of the normalised difference in total energy in the electron spectra (in (a)) for the $\phi_0 = 50$ μm cases to the $\phi_0 = 4$ μm case, as a function of time. Here, 0 fs represents the point where the peak of the laser pulse interacts with the target. (c) 2D electron density map, normalised to the critical density, for the $\phi_0 = 4$ μm spot case, and (d) same for the $\phi_0 = 50$ μm spot simulation.

this energy dependent increase will become apparent later). Conventionally accepted electron temperature scaling laws, depending solely on irradiance [79, 80] (as discussed in section 2.6.1), would predict identical electron temperatures for these simulations cases conducted at the same peak intensity. Thus, it is clear these scalings, although useful, overlook an important aspect of the absorption physics; namely the scaling of absorption with focal spot size. Furthermore, the empirical scaling of Davies [68] (Eq. 6.1) neglects this aspect, as the intensity was controlled via pulse energy changes.

To investigate this difference between the simulation cases, the total electron energy is calculated by integrating the electron spectrum at each simulation time step. This value is then normalised to the ratio of the two input pulse energies in order to correct for the large differences in input energy (due to the spot size differences). The

normalised energy difference in the total electron energy for the two cases (ϕ_0= 50 μm to 4 μm) as a function of time is displayed in Fig. 6.10(b), where 0 fs corresponds to the time at which the peak amplitude of the pulse interacts with the target. Initially the ratio of the total energy is the same, prior to the pulse arriving. As the interactions evolve, the ratio increases. It is close to zero for the first hundreds of femtoseconds, corresponding to the majority of the rising edge of the pulse (the pulse initially reaches the target within the first 100 fs of the simulation). After this, there is a rapid increase in the ratio, representing a significantly more efficient energy coupling to electrons when employing the larger (ϕ_0= 50 μm) focal spot. At its peak efficiency, a factor ∼1.75 times higher total energy is found for the large spot case compared to the smaller one, occurring approximately 100 fs after the arrival of the peak amplitude of the pulse (0 fs) corresponding to the pulse falling edge interaction. At later simulation times the difference begins to decrease as higher energy particles begin to leave the simulation boundaries.

This modelling, similar to the experimental findings, demonstrates there is a clear difference in the absorption between the two spot sizes, though it is not immediately clear why such a difference arises. In order establish if this is purely a surface interaction effect, such as changes in the surface absorption mechanisms, or if it is a volumetric effect within the target bulk, one can first compare the 2D electron density maps, displayed in Fig. 6.10(c) and (d), for each spot case. It is evident from these that there is a significant difference in the critical density surface (n_c) profile, the region where significant laser absorption to the plasma occurs. In the ϕ_0= 50 μm case (Fig. 6.10(d)) the n_c surface radius of curvature is large, that being effectively quasi-1D for the highest intensity regions of the spot intensity profile. Conversely, the ϕ_0= 4 μm case (Fig. 6.10(c)), displays a significantly smaller n_c surface radius of curvature. Considering the changes to the interaction surface curvature in terms of the $\mathbf{J} \times \mathbf{B}$ electron heating mechanism (see section 2.5.4) a smaller radius of curvature (i.e. more tightly curved), as formed in the smaller focal spot case, would result in reduced absorption as the efficiency of the $\mathbf{J} \times \mathbf{B}$ mechanism is significantly diminished for highly oblique angles of incidence. Similarly a more efficient production of fast electrons would be expected for the large focal spot case in the quasi-1D surface interaction when compared to a tighter focal spot surface geometry, for near identical pulses intensities.

To test if the absorption differences and the varying electron spectra between spot

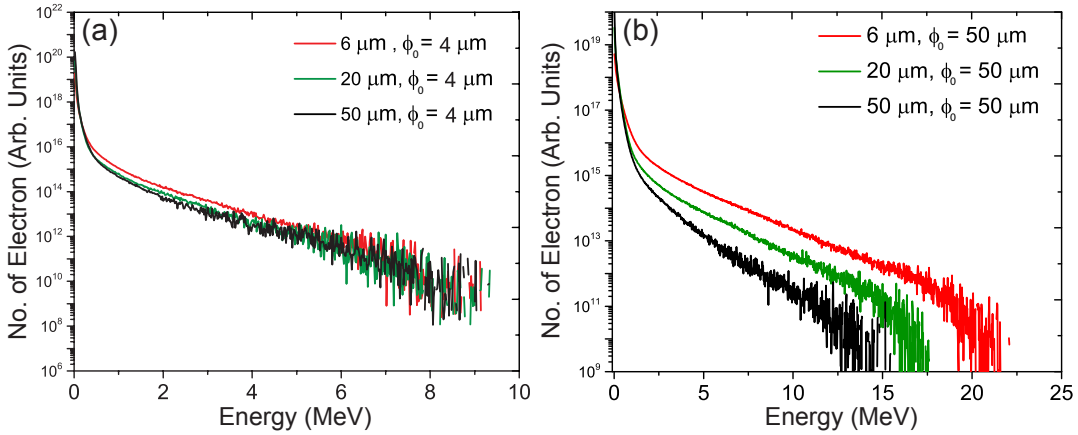

Figure 6.11: Extracted electron spectra from simulations, 334 fs after the peak of the pulse arrived at target, for varying target thicknesses, of 6 μm (red), 20 μm (green) and 50 μm (black), for (a) the ϕ_0= 4 μm and (b) the ϕ_0= 50 μm focal spot cases. The fast electrons are sampled across the entire simulation box.

cases is a volumetric effect within the target bulk, simulations are conducted investigating the effect of changing the target thickness for both focal spot sizes. The target thicknesses investigated are 6, 20 and 50 μm. For each case a representative electron spectrum is measured, as shown in Fig. 6.11, using the same conditions as for the results in Fig. 6.10(a). For the ϕ_0= 4 μm focal spot case (Fig. 6.11(a)) the electron spectrum and temperature appears to be essentially independent of the target thickness. However, for the larger spot case (Fig. 6.11(b)), there is a significant change in the electron spectra as the target thickness is changed. In this case, the thinnest target investigated (6 μm) shows the highest temperature and electron energies. These simulations show that as the focal spot size is increased or the target thickness decreased (for a constant intensity) a significant change is displayed in the measured electron spectra. This change (and the correlated change in the total absorption measured) therefore cannot be a solely due to a surface effect (e.g. changing of the dominance of the $\mathbf{J} \times \mathbf{B}$ mechanism) and must be in some way be related to the bulk interaction dynamics.

The results can be explained in a similar manner to an effect previously proposed in Mackinnon *et al.* [100]. In that work, in was shown via PIC simulations that the recirculating fast electron population within the target (i.e. those electrons which are accelerated from the front surface, reflect from the sheath field formed at the target rear and return to the front) enhances the electron density and temperature at the target rear and thereby enhances TNSA. Here, it is proposed that this recirculating electron

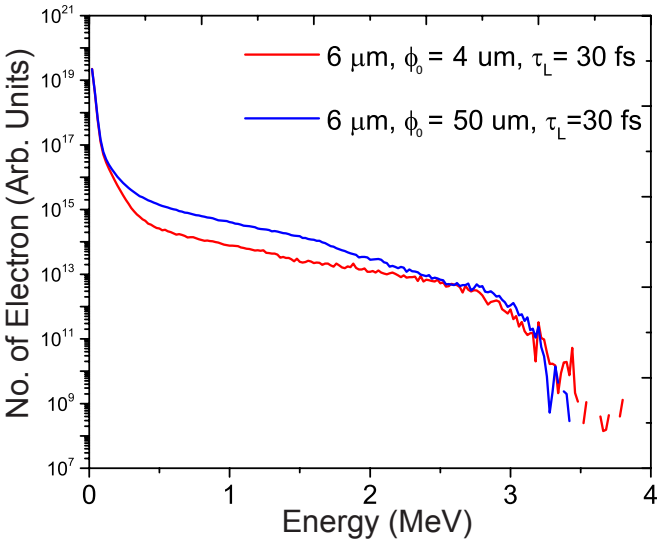

Figure 6.12: Extracted electron energy spectra from simulations, 334 fs after the peak of the pulse arrived at target, for a target thickness of 6 μm, for two focal spot sizes; ϕ_0= 4 μm (red) and ϕ_0= 50 μm (blue). In each case the interaction of a 30 fs pulse is simulated, as opposed to the 550 fs pulse used in the previous simulations. The fast electrons are sampled across the entire simulation box.

population may extract additional energy from the interacting laser pulse when they return to the front surface, resulting in a higher overall coupling efficiency. A stipulation for this therefore must be that upon returning to the front surface the laser must still be interacting. To directly test this concept the simulation results presented in Fig. 6.10(a), comparing the electron spectra at each focal spot size, is repeated for a much shorter, 30 fs, pulse duration; the results of which are shown in Fig. 6.12. This pulse duration is selected as it corresponds to the single pass time of an electron close to the average energy of the spectrum (≈5 MeV) within the target during the pulse duration and therefore gains no (or limited) additional energy during recirculation. Under this condition essentially little difference is measured in the electron spectra between the two focal spot sizes. This, coupled with the previous findings (Fig. 6.11) shows that the recirculating population of electrons within the target plays a important role in the laser-energy coupling dynamics in the interaction.

It is difficult to directly observe the temporal dynamics of this change in electron recirculation in the simulations after a large number of passes, given that there is a population of electrons constantly being injected while the pulse is present, in addition to the recirculating electron population. As there is a range of electron energies, after a certain distance or a number of passes through the target, the forward moving and recirculating populations become spatially indistinct. However, it is possible in the early

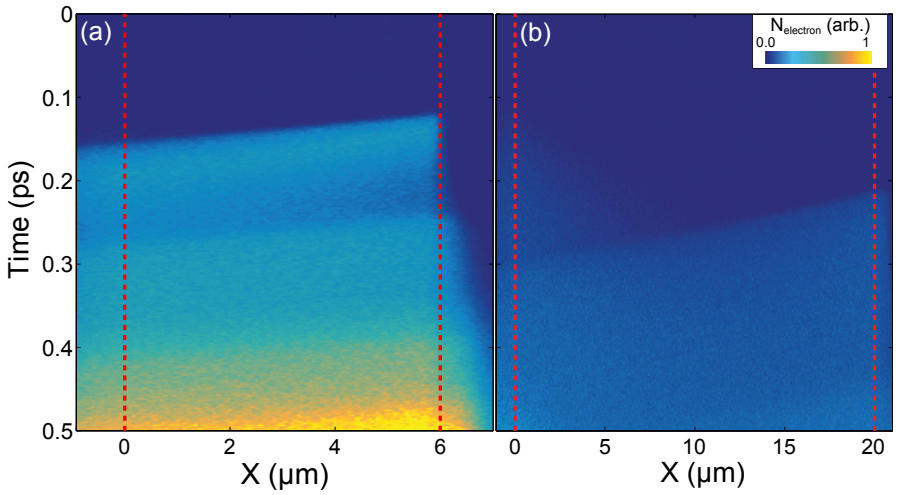

Figure 6.13: Time-space plot of the electron density of electrons with energy ≥150 keV, travelling in the negative direction (i.e. towards the target front) for a ϕ_0= 50 μm focal spot and target thickness (a) 6 μm and (b) 20 μm. Dashed red lines indicate the initial front and rear surface of the target.

stages of the interaction to observe recirculating electrons and the additional energy they gain upon returning to the front surface. Figure 6.13 shows this as a time-space map of the density of electrons with energy greater than 150 keV (to avoid sampling of the background electron population) moving towards the target front. This shows a significant increase in the number of fast electrons as the interaction evolves in time, in the thinner target case (Fig. 6.13(a)). While the energy gain and its dependence on the number of recirculations (given a sufficiently large focal spot size, pulse duration and electron energy) is clear from these results, the precise mechanism of energy exchange between the pulse and recirculating electrons is more difficult to determine. The process appears similar to that proposed in Krygier *et al.* [225], in which electrons leave the target front surface propagating towards the laser pulse. They are then turned around by a loop magnetic field, and in doing so, may extract additional energy from the pulse via direct laser acceleration [226]; a process which typically takes place in a long density scale length front surface plasma. Given the short density scale lengths present here, it is the recirculating population within the target which is turned around by the vacuum boundary sheath fields and, in a similar way, the electrons are then able to extract additional energy from the laser pulse.

6.5.2 Geometric model of recirculation-enhanced absorption

An important consequence that the above concept highlights is that laser intensity alone is not sufficient to predict changes in the absorption dynamics and the fast electron

spectrum. As the intensity may be varied either by changing the pulse energy, the pulse duration or the focal spot size, laser-energy coupling dynamics can be radically different depending on which of these parameters is varied. Thus there is a multi-dimensional parameter space in which the recirculation-enhanced absorption can occur. In order for the recirculating electrons to extract additional energy from the laser pulse, two conditions (one temporal and one spatial) must be met, these being; (i) the recirculation time must be shorter than the laser pulse duration, and (ii) the fast electron divergence angle must be small enough such that a sufficient number of electrons remain within the focal spot region upon their return to the front surface. The recirculation time and the degree to which electrons stay within the focal spot area is additional dependent upon the target thickness. It is, therefore, not immediately clear intuitively when enhanced absorption via the proposed recirculation method will be relevant, for given interaction conditions, and what region of the electron energy spectrum will be most affected.

In order to further understand this multi-dimensional interaction parameter space in a tractable manner, an analytical model based on a ballistic (i.e. no influence from self-generated fields or scattering within the target) approach to electron recirculation is developed. In this model an electron will gain a constant fraction of its initial energy upon re-interaction with the target front surface. Only electrons above 1 MeV are modelled, and thus collisional effects are ignored, as the distance travelled by the electron during the pulse duration is small compared to its stopping range. As stated earlier, the first condition for enhanced absorption through the proposed scheme is that the recirculation time must be shorter than the laser pulse duration. This can be related to the number of passes, n_τ, an electron will make during the pulse duration, τ_L, given by;

$$n_\tau = \frac{\nu_e \tau_L \cos(\theta_{div})}{2L} \tag{6.4}$$

where ν_e is the relativistically corrected electron velocity, L is the target thickness and θ_{div} is the electron's angle of propagation with respect to the central axis. For a propagation given angle it is also possible to show that the number of passes an electron will make before it leaves the laser focal spot region, n_{spot}, is;

$$n_{spot} = \frac{\phi_0}{2L \tan(\theta_{div})} \tag{6.5}$$

where, as before, ϕ_0 is the focal spot diameter (i.e. the FWHM size). If the energy

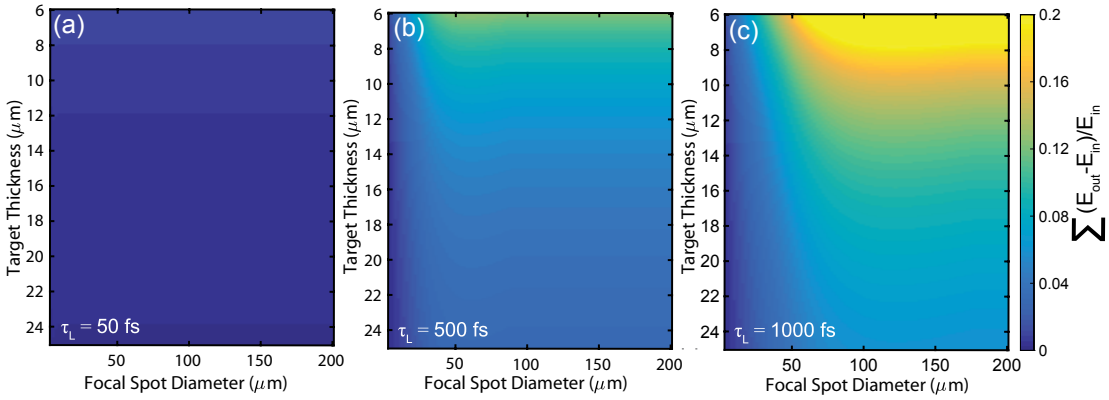

Figure 6.14: Target thickness and focal spot parameter space plots, showing electron energy gain described by the recirculation model (Eq. 6.6), for an irradiating pulse length of (a) 50 fs, (b) 500 fs and (c) 1000 fs. The colourmap represents the difference in total energy between the input and output spectra, normalised to the total energy of the input spectrum.

gain, E_{gain}, an electron of certain energy, E, may acquire from the laser is taken as a constant fraction of the electron energy, α, then it is possible to show the overall energy gained via recirculation will be the minimum of n_τ or n_{spot}. That is to say, either the electron will gain energy until it transversely leaves the irradiation region, as a result of its trajectory, or continue until the pulse ends. This can be expressed mathematically as;

$$E_{gain} = \frac{1}{2}(n_{spot} + n_\tau - |n_{spot} - n_\tau|)\alpha E \tag{6.6}$$

There is of course not a single electron energy or divergence angle, but in reality a distribution of values for both. The electron population is assumed to be described by an energy spectrum of the form $N(E) = N_0 e^{(-E/kT_e)}$, where T_e is the electron temperature and N_0 is the initial electron number at t=0. In terms of the distribution of electron divergences, this was shown to be energy dependent in Moore *et al.* [63], described by $\theta_{div}(E) = tan^{-1}(\bar{\theta}\sqrt{2/(\gamma - 1)})$, where $\bar{\theta}$ is the average divergence angle.

Using this model, the total energy gained by the electron population described by the input electron spectrum due to recirculation as a function of both focal spot size and target thickness can be investigated. Figure 6.14 shows the results of this modelling for a target thickness ranging from 6–25 μm and a focal spot size ranging from 4–200 μm, for three pulse durations; 50, 500 and 1000 fs. In each case the total energy gain is normalised to the total energy of the input spectrum. From this, it can be seen that for pulse durations of the order of the electron transit time (i.e. tens of femtoseconds), as in Fig. 6.14(a), there in no additional energy gain. This occurs as the recirculating population does not re-interact with the laser pulse a significant number of times, as

irradiation has ended, or almost, by the time they return to the front. However, for longer pulse durations, as in Fig. 6.14(b) and (c), there is significant energy gain for targets of thickness <20 μm when the focal spot size is on the order of >50 μm. The total energy gain is principally as a result of an enhancement in the higher energy tail of the electron spectrum (as also observed in simulations [Fig. 6.11(b)]). This is explained by the fact that the highest energy electrons have the lowest divergence angle values in the distribution, and as such the shortest recirculation time, thus spending more time interacting with the laser pulse. Lower energy electrons, with higher divergence angles, will move out of the focal spot region in a fewer number of passes through the target, and also return to the front surface a fewer number of times.

It is important to note that the exact conditions (i.e. target thickness and pulse length) for which significant gain occurs is highly dependent on the chosen electron energy spectrum and divergence-energy function, and additionally the choice of value of the gain coefficient α. Furthermore, the temporal evolution of the forward going fast electron population, as a result of the temporal evolution of the absorption dynamics at the front surface, is not considered. It is instead assumed that a high energy population already exists, which is then allowed to recirculate. Additionally, the escaping electron population (although often only on the order of a few percent) is not included in the model. These complexities, especially in regard to the self-consistent dynamics of the laser-injection and recirculating electron population, make this a highly non-trivial system to model analytically. As such, the presented model should not be seen as a calculation of the overall change in laser absorption, but illustrative of the parameter space in which the proposed concept of recirculation-enhanced absorption is relevant for given interaction conditions.

6.6 Conclusion

To conclude, this chapter has demonstrated the significance of laser focal spot size on the coupling of laser energy to overdense relativistic plasmas, i.e. absorption, during an intense laser-solid interaction. In particular the scaling of absorption with laser intensity has been investigated, with intensity variation achieved through separately varying the focal spot size and pulse energy.

Firstly this was investigated experimentally through the employment of novel and complementary diagnostic techniques developed specifically for these measurements. These include an integrating sphere and an angularly resolving electron detector, enabling well calibrated measurements of the total absorption of the intense laser pulse into dense plasma, and a quantification of the escaping electron population. In this investigation the intensity was varied separately through changing the energy contained in the pulse (for a fixed focal spot size) and by changing the focal spot size (for fixed pulse energy). For the former case, purely changing the pulse energy, excellent agreement is found between the absorption results and previously published absorption data reported in Ping *et al.* [75]. However, when intensity was varied through changing the focal spot size, for a fixed laser energy, a significantly higher fractional absorption was measured at the lower end of the intensity range, with a slower intensity scaling compared to that of the energy variation data. This result is also consistent with previous results on proton acceleration under defocussed geometries [195, 198], which show that the maximum proton energy and the number of protons accelerated scale differently for laser focal spot size variation compared to pulse energy variation.

Additionally, measurements of escaping fast electrons also demonstrate the need to consider the effect of focal spot size on laser absorption. It was seen that when a relatively large focal spot was utilised, which displayed high absorption using the optical diagnostics, there were minimal escaping electrons detected, making it difficult to compare with trends measured in the absorption results. However, this suggests that the extra fraction of laser energy absorbed at these lower intensities goes into electrons which are below the energy detection threshold (2.3 MeV) or to those trapped in the target by the strong fields generated inside and on the surfaces. This highlights the importance of using numerous diagnostics to elucidate the interaction physics. For example, future studies could additionally measure the generated proton and x-ray spectra to enable further understanding of the partitioning of the absorbed laser energy.

To further explore the underpinning physics, 2D PIC simulations were employed to test sample points from the two intensity change scans. At first, through study of the critical density surface profile, it was believed that differences in its curvature, between spot sizes, may, in part, have altered the absorption dynamics between cases. The large degree of critical surface curvature formed by the relatively smaller focal spot, with tighter focusing geometry, would result in a decrease in the efficiency of $\mathbf{J} \times \mathbf{B}$ heating

of electrons; a significant advantage in terms of coupling efficiency for large focal spots for otherwise identical laser intensities. However, through simulation of varying target thickneses, it was found that the surface effect described above does not fully account for differences in the simulation results. It is proposed that changes in absorption dynamics are in fact driven by a volumetric effect; this being additional heating of the recirculating electron population within the target when employing a defocused laser pulse. This effect only occurs in the case where the focal spot and pulse duration are sufficiency large, and the fast electron beam divergence is sufficiency small to enable the recirculating electron population to significantly re-interact with the laser irradiation region for a longer total time. As such, recirculation-enhanced absorption is turned off in the small focal spot case, or additionally for short (tens of femtosecond) pulse durations. This insight enabled the development of a simple geometric model of the recirculation dynamics which enables examination of the approximated parameter space (in terms of focal spot size, target thickness and pulse duration) where recirculation-enhanced absorption becomes relevant.

Overall, this investigation highlights conditions for optimisation of laser-energy coupling in laser-solid interactions, and thus has implications for a broad range of related applications, such as laser-driven ion acceleration and other radiation sources. The more immediate and significant impact, however, is likely to occur in terms of the design of experiments. For identical plasma parameters, the manner in which the laser intensity is altered (by pulse duration, energy or focal spot size) results in a significantly different intensity dependent scaling of absorption, due to the influence of the recirculating population of electrons within the target. The complex, interdependent parameter space upon which the absorption dynamics are dependent should be a key consideration for future experimental and simulation programmes.

Chapter 7

Conclusions & future work

The overarching objective of the work presented in this thesis was to experimentally investigate the influence of laser pulse focal spot size in ultra-intense laser-solid interactions. This has been achieved, first through the development of a plasma optic to achieve tight focusing of Petawatt-level laser pulses, investigation of the subsequent influence this tight focusing plays on proton beam properties generated via the TNSA mechanism, and finally, determination of the role focal spot size plays on laser-energy coupling to dense plasma. Over several experimental campaigns, involving innovations in optical and diagnostic techniques, and coupled numerical simulations, new understanding of laser-solid interaction physics and the role played by laser focal spot size has been achieved. This final chapter summarises the key findings of each investigation and discusses the main conclusions. Potential directions for future research into each of these areas are also discussed.

7.1 Development of ellipsoidal plasma mirrors for focusing of high power laser pulses

Chapter 4 reported on the design, testing and experimental demonstration of an ellipsoidal plasma mirror to enhance laser intensity via decreasing the focal spot size. This is motived by the desire to access new avenues in laser-plasma research and enhance well known concepts, such as laser-driven ion acceleration.

The focusing plasma mirror (FPM) design was optimised in terms of maximising the reflectivity in plasma operation. Reflectivity values on full power shots were found to be

lower than predicted, which is believed to have occurred due to a lower PM 'switch-on' intensity experimentally than the value utilised in the design. Furthermore, previous investigations [183] highlighted that spatial-intensity fluctuations in the laser near-field intensity distribution may lead to non-ideal ionisation dynamics adversely affecting optic reflectivity. This effect on FPM performance should be investigated in detail in future work, utilising experimental and modelling approaches. Additionally, through the use of temporally separated dual laser pulses, FPM reflectivity enhancement may be achieved, as investigated in Scott *et al.* [145] for planar plasma mirrors. That study reported PM reflectivity of 96% when the optic was pre-ionised by a controlled pre-pulse.

Through ray-trace modelling and low-intensity laser characterisation of the manufactured optics, the desired performance in terms of focal spot demagnification was demonstrated. Direct measurements of the focal spot formed by the FPM, demonstrated a factor of $\times 2.5$ reduction in focal spot size, resulting in an estimated factor of $\times 3.6$ intensity enhancement when considering the spot quality (i.e. percentage encircled energy) and the plasma reflectivity. As direct measurement of the focal spot formed by the FPM in full power irradiation is impractical, optic operation was indirectly diagnosed through employment in an investigation of laser-driven proton acceleration. An increase in the maximum energy of protons from thin foil targets, from 27 MeV to 53 MeV, which is almost a factor of two higher than with F/3.1 focusing, was measured. This is consistent with accepted TNSA laser intensity scaling. As a further development of this work, the addition of an anti-reflective (AR) coating could be investigated. This will increase the optic's temporal intensity contrast enhancement and enable experimentation with thin (tens-of-nanometer thick) targets. Through this investigation of interactions in a regime where relativistic induced transparency effects play a significant role will be made accessible, currently a sub-field receiving much research attention [94, 223].

The FPM demonstration highlights the validity of the design developed for this optic. This could be employed to develop FPMs for laser systems other than Vulcan-PW, including future laser systems under construction, i.e. the ELI facilities, enabling further increase in the feasible peak intensity in a cost effective manner. Furthermore, FPMs could be developed for the magnification of a focal spot, through an optic which induces an increase in focusing F/# in a compact manner. Typically, large F/# (such

as F/20) are logistically problematic in most target chambers due to the long focal length involved.

A key factor in the successful development of the FPM was selection of a viable manufacturing process. Two methods were trialled; injection moulding and diamond machining. The latter was chosen as the most viable, in the short term, due to its capability of producing the FPM design to a higher degree of accuracy and precision, and thus achieving greater focusing performance. A major development, which would make this non-reusable optic more feasible for usage involving large shot numbers, would be improvement of the injection moulding route. This may be revisited in future work, as it has the potential to result in the manufacture of a large quantity of optics, at reasonably low cost. However, accurate reproduction of the FPM design and reproducibility between optics will require significant improvement for this to be considered a feasible option.

The study has shown that a major aspect in the successful employment of the FPM, in terms of achieving intensity enhancement, is the optic's sensitivity to misalignment in the position of the input focal spot. Only when this was minimised was successful FPM operation achieved, resulting in the enhancement of maximum proton energies. It was shown that misalignment can occur not only as a result of the optic's placement relative to the input focus, but in fact also from an non-ideal wavefront profile of the input laser beam, caused by thermal gradients throughout the laser chain. Characterisation of the pulse wavefront aberrations should be a fundamental measurement when conducting a laser-solid experiment, much in the same way as pulse energy and duration, as this enables the true intensity to be calculated.

7.2 Influence of focal spot size approaching the laser wavelength on proton acceleration in the TNSA regime

Building upon the development of the F/1 FPM, the influence of employing such tight pulse focusing (with spot size near λ_L) on the properties of laser-driven proton beams in the TNSA regime was investigated in chapter 5.

Through comparison of the proton beam properties measured for this focusing scenario to larger focal spot irradiation, it was demonstrated that significant differences in the TNSA beam properties are observed. The most salient of these are; a slower

maximum proton energy laser intensity scaling; a more slowly decreasing proton spectrum (with a $\times 2.5$ enhancement in laser-to-proton energy conversion efficiency); and a significantly slower decrease in beam divergence with increasing proton energy under tight focusing compared to measurements using a larger focal spot. These were explained in terms of changes to the temporal evolution of the fast electron distribution at the target rear. The observation of a significantly higher number of protons emitted from the target edges, under tight focus irradiation, indicates the presence of enhanced lateral spreading of electrons toward the target edges. The source of this spreading is attributed to changes in the front surface interaction dynamics responsible, in part, for defining the absorption dynamics and subsequent electron injection into the target.

These findings highlight the importance of focal spot size for laser-driven proton acceleration in the TNSA regime, and in particular that tight focus usage is adverse in terms of maximising proton energies, due to dilution of the accelerating fields via increased lateral spreading. However, it is beneficial in regards to laser-to-proton energy conversion efficiency and beam collimation, due to the sheath spatial scale. As several laser facilities are actively developing FPMs for laser-solid interaction studies to enhance ion acceleration, then the findings of this chapter (and those of chapter 4) must be considered. The use of the tight focusing FPM could be employed in a future characterisation study of other aspects of laser-solid interactions, such as energetic photon emission, which may scale more favourably with the enhanced intensity generated by the extremely small focal spot.

In future work, the use of tight focusing with ultra-thin (nanometre-scale) foil targets should be investigated, enabled by the previously mentioned alteration to the FPM (AR coating addition). This will enable the characterisation of laser-driven ion acceleration in a regime where multiple ion acceleration schemes occur over the duration of the interaction [94]. This may enable the limiting factor of maximum proton energy in the TNSA results presented here to be overcome.

7.3 Influence of focal spot size on energy absorption in intense laser-solid interactions

Chapter 6 reports on an investigation of laser-energy absorption into dense plasma, utilising a suite of novel diagnostics developed to directly measure the total reflected

laser pulse energy. A key aspect of this study involved distinguishing between the influence of laser energy and focal spot size on the intensity scaling of laser absorption. Good agreement was found with previously published absorption scaling with intensity by variation of pulse energy. However, when the intensity was controlled via focal spot size, enhanced values were observed with a larger focal spot when compared with smaller focal spot geometries of equivalent intensity. Furthermore, a significantly slower absorption scaling with intensity was measured compared to the case where intensity was controlled via the pulse energy.

This result is attributed to additional energy extracted from the laser by the population of electrons recirculating within the target due to multiple interactions with the laser. This process depends upon the pulse duration, target thickness, focal spot size and the energy spectrum and divergence of the fast electrons. Measurements for the case where the focal spot size was altered were only conducted for one target thickness (6 μm) and therefore only the effect of one of the above dependencies was tested experimentally. This could be addressed in future studies by varying the target thickness to higher values, thus enabling the dependencies of recirculation enhanced absorption to be directly observed, to test the findings of the numerical simulations presented. Furthermore, this would also reinforce that the measured changes to absorption scaling are driven by the volumetric recirculation effect, and not, significantly, by the front surface interaction dynamics.

This investigation highlights, similarly to chapter 5, the importance of focal spot size on interaction dynamics, showing it is far beyond a parameter only used to define pulse intensity. Interestingly both investigations show a parameter space in which absorption is enhanced relative to interactions employing focal spots of a few microns in size ($\sim$4 μm). That is to say via the use of a large (hundreds of microns focal spot), or, as was suggested in chapter 5 (and the work in Klimo *et al.* [199] and Valenta *et al.* [200]), that enhanced absorption is achieved with a near-wavelength sized focal spot. Clearly, the focal spots employed in each study are orders of magnitude different in size, and display varying absorption enhancement mechanisms leading to the experimental findings. This further highlights the importance of studying the effects of altering focal spot size, due to the highly complex absorption dynamics displayed throughout the range of focal spot sizes investigated.

Finally, to further the usage of the developed integrating sphere, a third diagnostic

channel could be added. Due to the high degree of neutral density filtering required to avoid saturation and damage to the optical fibres fitted to the sphere, only light approximately ±60 nm around the laser fundamental wavelength was characterised. This is adequate in terms of absorption measurements, although it does not allow for characterisation of light out with this range, such as the generation of higher order harmonics. As such, a third spectrometer attached to the sphere, selectively filtered to block this range, would enable this characterisation. This will further our understanding of absorbed laser energy partitioning to secondary particles and radiation emission. Moreover this energy partitioning concept could be enhanced through the measurement of the generated proton and x-ray spectra, enabling further insight into the proposed absorption concepts.

7.4 Concluding remarks

The investigations presented within this thesis add to our understanding of the underlying physics of ultra-intense laser-solid interactions. They have also inspired new research directions, on certain key fundamental aspects of the role laser focal spot size plays in these interactions. The field of intense laser-solid interaction studies has matured over the past decade, motivated by the prospect of envisioned applications prompting numerous investigations exploring the dependencies and controllability of these interactions. A deeper understanding of the influence of key laser parameters, such as focal spot size, is important to the development of laser-driven particle and radiation sources, and applications such as hadron therapy and the fast ignition approach to ICF. In addition, several multi-petawatt laser facilities under development (e.g. Extreme Light Infrastructure, ELI) plan to increase peak laser intensities to the order of 10^{23} W/cm^2 via a combination of shorter laser pulses and tighter focusing. Understanding the role of laser focal spot size in laser-solid interaction physics is thus crucial for predications and modelling of new laser-plasma phenomena accessible at these ultra-high intensities.

Bibliography

[1] T. H. Maiman. Stimulated optical radiation in ruby. *Nature*, 187(4736):493–494, 1960.

[2] F. J. McClung, R. W. Hellwarth, *et al.* Giant optical pulsations from ruby. *Journal of Applied Physics*, 33(3):828–829, 1962.

[3] L. E. Hargrove, R. L. Fork, *et al.* Locking of He-Ne laser modes induced by synchronous intracavity modulation. *Applied Physics Letters*, 5(1):4–5, 1964.

[4] D. Strickland and G. Mourou. Compression of amplified chirped optical pulses. *Optics Communications*, 55(6):447–449, 1985.

[5] J. Zou, C. L. Blanc, *et al.* Design and current progress of the apollon 10 PW project. *High Power Laser Science and Engineering*, 3((e2)):4p, 2015.

[6] B. Rus, P. Bakule, *et al.* Eli-beamlines: Progress in development of next generation short-pulse laser systems. *Proceedings SPIE, Research Using Extreme Light: Entering New Frontiers with Petawatt-Class Lasers III*, (102410J), 2017.

[7] T. Tajima and J. M. Dawson. Laser electron accelerator. *Physical Review Letters*, 43(4):267–270, 1979.

[8] K. Nakajima, T. Kawakubo, *et al.* A proof-of-principle experiment of laser wakefield acceleration. *Physica Scripta*, 1994(T52):61, 1994.

[9] S. P. D. Mangles, C. D. Murphy, *et al.* Monoenergetic beams of relativistic electrons from intense laser-plasma interactions. *Nature*, 431(7008):535–538, 2004.

[10] C. G. R. Geddes, C. Toth, *et al.* High-quality electron beams from a laser wakefield accelerator using plasma-channel guiding. *Nature*, 431(7008):538–541, 2004.

[11] J. Faure, Y. Glinec, *et al.* A laser-plasma accelerator producing monoenergetic electron beams. *Nature*, 431(7008):541–544, 2004.

[12] S. J. Gitomer, R. D. Jones, *et al.* Fast ions and hot electrons in the laser-plasma interaction. *Physics of Fluids*, 29(8):2679–2688, 1986.

[13] R. A. Snavely, M. H. Key, *et al.* Intense high-energy proton beams from petawatt-laser irradiation of solids. *Physical Review Letters*, 85(14):2945–2948, 2000.

[14] S. C. Wilks, A. B. Langdon, *et al.* Energetic proton generation in ultra-intense laser-solid interactions. *Physics of Plasmas*, 8(2):542–549, 2001.

[15] A. J. Mackinnon, M. Borghesi, *et al.* Effect of plasma scale length on multi-MeV proton production by intense laser pulses. *Physical Review Letters*, 86(9):1769–1772, 2001.

[16] M. Hegelich, S. Karsch, *et al.* MeV ion jets from short-pulse-laser interaction with thin foils. *Physical Review Letters*, 89(8):085002, 2002.

[17] M. Roth, A. Blazevic, *et al.* Energetic ions generated by laser pulses: A detailed study on target properties. *Physical Review Accelerators and Beams*, 5(6):061301, 2002.

[18] J. C. Fernandez, D. C. Gautier, *et al.* Laser-plasmas in the relativistic-transparency regime: Science and applications. *Physics of Plasmas*, 24(5):056702, 2017.

[19] A. Macchi, M. Borghesi, *et al.* Ion acceleration by superintense laser-plasma interaction. *Reviews of Modern Physics*, 85(2):751–793, 2013.

[20] H. Daido, M. Nishiuchi, *et al.* Review of laser-driven ion sources and their applications. *Reports on Progress in Physics*, 75(5):056401, 2012.

[21] S. M. Hooker. Developments in laser-driven plasma accelerators. *Nature Photonics*, 7(10):775–782, 2013.

[22] S. Bulanov, T. Esirkepov, *et al.* Oncological hadrontherapy with laser ion accelerators. *Physics Letters A*, 299(2):240–247, 2002.

[23] K. W. D. Ledingham, P. McKenna, *et al.* High power laser production of short-lived isotopes for positron emission tomography. *Journal of Physics D: Applied Physics*, 37(16):2341, 2004.

[24] M. Roth, T. E. Cowan, *et al.* Fast ignition by intense laser-accelerated proton beams. *Physical Review Letters*, 86(3):436–439, 2001.

[25] C. M. Brenner, S. R. Mirfayzi, *et al.* Laser-driven x-ray and neutron source development for industrial applications of plasma accelerators. *Plasma Physics and Controlled Fusion*, 58(1):014039, 2016.

[26] S. Mirfayzi, A. Alejo, *et al.* Detector for imaging and dosimetry of laser-driven epithermal neutrons by alpha conversion. *Journal of Instrumentation*, 11(10):C10008, 2016.

[27] P. Antici, M. Migliorati, *et al.* A compact post-acceleration scheme for laser-generated protons. *Physics of Plasmas*, 18(7):073103, 2011.

[28] P. K. Patel, A. J. Mackinnon, *et al.* Isochoric heating of solid-density matter with an ultrafast proton beam. *Physical Review Letters*, 91(12):125004, 2003.

[29] G. Dyer, T. Ditmire, *et al.* Isochoric heating into the warm dense matter regime by laser-solid produced k-alpha x-rays. In *Frontiers in Optics*, page MT21. *Optical Society of America*, 2003.

[30] M. Borghesi, J. Fuchs, *et al.* Fast ion generation by high-intensity laser irradiation of solid targets and applications. *Fusion Science And Technology*, 49(3):412–439, 2006.

[31] V. Malka, J. Faure, *et al.* Principles and applications of compact laser-plasma accelerators. *Nature Physics*, 4(6):447–453, 2008.

[32] R. R. Wilson. Radiological use of fast protons. *Radiology*, 47(5):487–491, 1946.

[33] C. A. Tobias, J. H. Lawrence, *et al.* Pituitary irradiation with high-energy proton beams a preliminary report. *Cancer Research*, 18(2):121–134, 1958.

[34] M. Goitein and M. Jermann. The relative costs of proton and x-ray radiation therapy. *Clinical Oncology*, 15(1):S37–S50, 2003.

[35] D. Doria, K. F. Kakolee, *et al.* Biological effectiveness on live cells of laser driven protons at dose rates exceeding 10^9 Gy/s. *AIP Advances*, 2(1):011209, 2012.

[36] T. Ruth. Accelerating production of medical isotopes. *Nature*, 457(7229):536–537, 2009.

[37] K. Ledingham. Laser induced nuclear physics and applications. *Nuclear Physics A*, 752(2):633–644, 2005.

[38] P. Gould. Medical-isotope supply hit by production problems. *Physics World*, 21(10):12, 2008.

[39] S. Fritzler, V. Malka, *et al.* Proton beams generated with high-intensity lasers: Applications to medical isotope production. *Applied Physics Letters*, 83(15):3039–3041, 2003.

[40] R. Kidder. Application of lasers to the production of high-temperature and high-pressure plasma. *Nuclear Fusion*, 8(1):3, 1968.

[41] J. Nuckolls, L. Wood, *et al.* Laser compression of matter to super-high densities: Thermonuclear (CTR) applications. *Nature*, 239(5368):139–142, 1972.

[42] J. D. Kilkenny, S. G. Glendinning, *et al.* A review of the ablative stabilization of the rayleigh-taylor instability in regimes relevant to inertial confinement fusion. *Physics of Plasmas*, 1(5):1379–1389, 1994.

[43] J. Sanz. Self-consistent analytical model of the rayleigh-taylor instability in inertial confinement fusion. *Physical Review Letters*, 73(20):2700–2703, 1994.

[44] S. Atzeni, A. Schiavi, *et al.* Fluid and kinetic simulation of inertial confinement fusion plasmas. *Computer Physics Communications*, 169(1-3):153–159, 7 2005.

[45] M. Tabak, J. Hammer, *et al.* Ignition and high gain with ultrapowerful lasers*. *Physics of Plasmas*, 1(5):1626–1634, 1994.

[46] Y. Sentoku, W. Kruer, *et al.* Laser hole boring and hot electron generation in the fast ignition scheme. *Fusion Science and Technology*, 49(3):278–296, 2006.

[47] H. Sakagami, T. Johzaki, *et al.* Fast ignition integrated interconnecting code project for cone-guided targets. *Laser and Particle Beams*, 24(1):191–198, 2006.

[48] T. Nakamura, H. Sakagami, *et al.* Optimization of cone target geometry for fast ignition. *Physics of Plasmas*, 14(10):103105, 2007.

[49] R. Kodama, H. Shiraga, *et al.* Nuclear fusion: Fast heating scalable to laser fusion ignition. *Nature*, 418(6901):933–934, 2002.

[50] J. C. Fernandez, J. Honrubia, *et al.* Progress and prospects of ion-driven fast ignition. *Nuclear Fusion*, 49(6):065004, 2009.

[51] B. Hegelich, D. Jung, *et al.* Experimental demonstration of particle energy, conversion efficiency and spectral shape required for ion-based fast ignition. *Nuclear Fusion*, 51(8):083011, 2011.

[52] W. L. Kruer. The Physics Of Laser Plasma Interactions. *Westview Press*, 2003.

[53] P. Gibbon. Short Pulse Laser Interactions with Matter: An Introduction. *Imperial College Press*, 2005.

[54] F. Tombe. Maxwell's original equations. *The General Science Journal*, 05 2016.

[55] G. Voronov and N. B. Delone. Ionization of the xenon atom by the electric field of ruby laser emission. *JETP Letters*, 1(2):66–68, 1965.

[56] P. Agostini, G. Barjot, *et al.* Multiphoton ionization of hydrogen and rare gases. *IEEE Journal of Quantum Electronics*, 4(10):667–669, 1968.

[57] Y. Gontier and M. Trahin. Energetic electron generation by multiphoton absorption. *Journal of Physics B: Atomic and Molecular Physics*, 13(22):4383, 1980.

[58] L. Keldysh. Ionization in the field of a strong electromagnetic wave. *Soviet Physics JETP*, 20(5):1307–1314, 1965.

[59] A. Perelomov, V. Popov, *et al.* Ionization of atoms in an alternating electric field. *Soviet Physics JETP*, 23(5):924–934, 1966.

[60] A. Perelomov, V. Popov, *et al.* Ionization of atoms in an alternating electric field: *ii*. *Soviet Physics JETP*, 24(1):207–217, 1967.

[61] R. J. Gray, D. C. Carroll, *et al.* Laser pulse propagation and enhanced energy coupling to fast electrons in dense plasma gradients. *New Journal of Physics*, 16(11):113075, 2014.

[62] P. McKenna, D. Carroll, *et al.* Effects of front surface plasma expansion on proton acceleration in ultraintense laser irradiation of foil targets. *Laser and Particle Beams*, 26(4):591–596, 2008.

[63] C. I. Moore, J. P. Knauer, *et al.* Observation of the transition from thomson to compton scattering in multiphoton interactions with low-energy electrons. *Physical Review Letters*, 74(13):2439–2442, 1995.

[64] J. D. Lawson. Laser and accelerators. *IEE Transactions on Nuclear Science*, 26(3):4217–4219, 1979.

[65] P. M. Woodward. A method of calculating the field over a plane aperture required to produce a given polar diagram. *Journal of the Institution of Electrical Engineers - Part IIIA: Radiolocation*, 93(10):1554–1558, 1946.

[66] L. Schlessinger and J. Wright. Inverse-bremsstrahlung absorption rate in an intense laser field. *Physical Review A*, 20(5):1934–1945, 1979.

[67] D. D. Meyerhofer, H. Chen, *et al.* Resonance absorption in high-intensity contrast, picosecond laser-plasma interactions. *Physics of Fluids B: Plasma Physics*, 5(7):2584–2588, 1993.

[68] J. R. Davies. Laser absorption by overdense plasmas in the relativistic regime. *Plasma Physics and Controlled Fusion*, 51(1):014006, 2009.

[69] D. W. Forslund, J. M. Kindel, *et al.* Theory of hot-electron spectra at high laser intensity. *Physical Review Letters*, 39(5):284–288, 1977.

[70] N. G. Denisov. On a singularity of the field of an electromagnetic wave propagated in an inhomogeneous plasma. *Soviet Physics JETP-USSR*, 4(4):544–553, 1957.

[71] J. P. Freidberg, R. W. Mitchell, *et al.* Resonant absorption of laser light by plasma targets. *Physical Review Letters*, 28(13):795–799, 1972.

[72] F. Brunel. Not-so-resonant, resonant absorption. *Physical Review Letters*, 59(52):52–55, 1987.

[73] P. Gibbon and A. R. Bell. Collisionless absorption in sharp-edged plasmas. *Physical Review Letters*, 68(10):1535–1538, 1992.

[74] W. L. Kruer and K. Estabrook. J×B heating by very intense laser light. *The Physics of Fluids*, 28(1):430–432, 1985.

[75] Y. Ping, R. Shepherd, *et al.* Absorption of short laser pulses on solid targets in the ultrarelativistic regime. *Physical Review Letters*, 100(8):085004, 2008.

[76] X. L. Ge, X. X. Lin, *et al.* Directed fast electron beams in ultraintense picosecond laser irradiated solid targets. *Applied Physics Letters*, 107(9):091111, 2015.

[77] B. Bezzerides, S. J. Gitomer, *et al.* Randomness, Maxwellian distributions, and resonance absorption. *Physical Review Letters*, 44(10):651–654, 1980.

[78] F. Jüttner. Das maxwellsche gesetz der geschwindigkeitsverteilung in der relativtheorie. *Annalen der Physik*, 339(5):856–882, 1911.

[79] S. C. Wilks, W. L. Kruer, *et al.* Absorption of ultra-intense laser pulses. *Physical Review Letters*, 69(9):1383–1386, 1992.

[80] F. N. Beg, A. R. Bell, *et al.* A study of picosecond laser-solid interactions up to 10^{19} Wcm^{-2}. *Physics of Plasmas*, 4(2):447–457, 1997.

[81] C. D. Chen, P. K. Patel, *et al.* Bremsstrahlung and kα fluorescence measurements for inferring conversion efficiencies into fast ignition relevant hot electrons. *Physics of Plasmas*, 16(8):082705, 2009.

[82] A. Link, R. R. Freeman, *et al.* Effects of target charging and ion emission on the energy spectrum of emitted electrons. *Physics of Plasmas*, 18(5):053107, 2011.

[83] H. Alfvén. On the motion of cosmic rays in interstellar space. *Physical Review*, 55(5):425–429, 1939.

[84] J. R. Davies. Alfvén limit in fast ignition. *Physical Review E*, 69(6 Pt 2):065402, 2004.

[85] A. R. Bell, J. R. Davies, *et al.* Fast-electron transport in high-intensity short-pulse laser-solid experiments. *Plasma Physics and Controlled Fusion*, 39(5):653, 1997.

[86] D. A. MacLellan, D. C. Carroll, *et al.* Fast electron transport patterns in intense laser-irradiated solids diagnosed by modeling measured multi-mev proton beams. *Laser and Particle Beams*, 31(3):475–480, 2013.

[87] S. Kar, D. Adams, *et al.* Magnetic collimation of petawatt driven fast electron beam for prospective fast ignition studies. *Journal of Physics: Conference Series*, 244(2):022041, 2010.

[88] P. McKenna, A. P. L. Robinson, *et al.* Effect of lattice structure on energetic electron transport in solids irradiated by ultraintense laser pulses. *Physical Review Letters*, 106(18):185004, 2011.

[89] J. R. Davies, A. R. Bell, *et al.* Magnetic focusing and trapping of high-intensity laser-generated fast electrons at the rear of solid targets. *Physical Review E*, 59(5 Pt B):6032–6036, 1999.

[90] M. Coury, D. C. Carroll, *et al.* Injection and transport properties of fast electrons in ultraintense laser-solid interactions. *Physics of Plasmas*, 20(4):043104, 2013.

[91] J. S. Green, V. M. Ovchinnikov, *et al.* Effect of laser intensity on fast-electron-beam divergence in solid-density plasmas. *Physical Review Letters*, 100(1):015003, 2008.

[92] A. Higginson, R. J. Gray, *et al.* Near-100 MeV protons via a laser-driven transparency-enhanced hybrid acceleration scheme. *Nature Communications*, 9(724), 2018.

[93] S. P. Hatchett, C. G. Brown, *et al.* Electron, photon, and ion beams from the relativistic interaction of petawatt laser pulses with solid targets. *Physics of Plasmas*, 7(5):2076–2082, 2000.

[94] H. Padda, M. King, *et al.* Intra-pulse transition between ion acceleration mechanisms in intense laser-foil interactions. *Physics of Plasmas*, 23(6):063116, 2016.

[95] E. Clark, K. Krushelnick, *et al.* Measurements of energetic proton transport through magnetized plasma from intense laser interactions with solids. *Physical Review Letters*, 84(4):670–673, 2000.

[96] O. Tresca, D. C. Carroll, *et al.* Controlling the properties of ultraintense laser-proton sources using transverse refluxing of hot electrons in shaped mass-limited targets. *Plasma Physics and Controlled Fusion*, 53(10):105008, 2011.

[97] P. McKenna, D. C. Carroll, *et al.* Lateral electron transport in high-intensity laser-irradiated foils diagnosed by ion emission. *Physical Review Letters*, 98(14):145001, 2007.

[98] J. J. Santos, F. Amiranoff, *et al.* Fast electron transport in ultraintense laser pulse interaction with solid targets by rear-side self-radiation diagnostics. *Physical Review Letters*, 89(2):025001, 2002.

[99] Y. Sentoku, T. E. Cowan, *et al.* High energy proton acceleration in interaction of short laser pulse with dense plasma target. *Physics of Plasmas*, 10(5):2009–2015, 2003.

[100] A. J. Mackinnon, Y. Sentoku, *et al.* Enhancement of proton acceleration by hot-electron recirculation in thin foils irradiated by ultraintense laser pulses. *Physical Review Letters*, 88(21):215006, 2002.

[101] M. Passoni, L. Bertagna, *et al.* Target normal sheath acceleration: theory, comparison with experiments and future perspectives. *New Journal of Physics*, 12(4):045012, 2010.

[102] P. Mora. Plasma expansion into a vacuum. *Physical Review Letters*, 90(18):185002, 2003.

[103] P. Mora. Thin-foil expansion into a vacuum. *Physical Review E*, 72(5):056401, 2005.

[104] J. Schreiber, F. Bell, *et al.* Analytical model for ion acceleration by high-intensity laser pulses. *Physical Review Letters*, 97(4):045005, 2006.

[105] J. E. Crow, P. L. Auer, *et al.* The expansion of a plasma into a vacuum. *Journal of Plasma Physics*, 14(1):65–76, 1975.

[106] J. Denavit. Collisionless plasma expansion into a vacuum. *Physics of Fluids*, 22(7):1384–1392, 1979.

[107] J. Fuchs, P. Antici, *et al.* Laser-driven proton scaling laws and new paths towards energy increase. *Nature Physics*, 2(1):48–54, 2006.

[108] C. M. Brenner, A. P. L. Robinson, *et al.* High energy conversion efficiency in laser-proton acceleration by controlling laser-energy deposition onto thin foil targets. *Applied Physics Letters*, 104(8):081123, 2014.

[109] A. Maksimchuk, S. Gu, *et al.* Forward ion acceleration in thin films driven by a high-intensity laser. *Physical Review Letters*, 84(18):4108–4111, 2000.

[110] M. Allen, P. K. Patel, *et al.* Direct experimental evidence of back-surface ion acceleration from laser-irradiated gold foils. *Physical Review Letters*, 93(26):265004, 2004.

[111] J. Fuchs, Y. Sentoku, *et al.* Comparative spectra and efficiencies of ions laser-accelerated forward from the front and rear surfaces of thin solid foils. *Physics of Plasmas*, 14(5):053105, 2007.

[112] S. M. Pfotenhauer, A. Sachtleben, *et al.* Spectral shaping of laser generated proton beams. *New Journal of Physics*, 10(3):033034, 2008.

[113] L. Robson, P. T. Simpson, *et al.* Scaling of proton acceleration driven by petawatt-laser-plasma interactions. *Nature Physics*, 3(1):58–62, 2007.

[114] L. Romagnani, J. Fuchs, *et al.* Dynamics of electric fields driving the laser acceleration of multi-mev protons. *Physical Review Letters*, 95(19):195001, 2005.

[115] D. C. Carroll, P. McKenna, *et al.* Active manipulation of the spatial energy distribution of laser-accelerated proton beams. *Physical Review E*, 76(6):065401, 2007.

[116] M. Schollmeier, K. Harres, *et al.* Laser beam-profile impression and target thickness impact on laser-accelerated protons. *Physics of Plasmas*, 15(5):053101, 2008.

[117] M. Roth, E. Brambrink, *et al.* Laser accelerated ions and electron transport in ultra-intense laser matter interaction. *Laser and Particle Beams*, 23(1):95–100, 2005.

[118] T. E. Cowan, J. Fuchs, *et al.* Ultralow emittance, multi-mev proton beams from a laser virtual-cathode plasma accelerator. *Physical Review Letters*, 92(20):204801, 2004.

[119] M. Borghesi, A. J. Mackinnon, *et al.* Multi-mev proton source investigations in ultraintense laser-foil interactions. *Physical Review Letters*, 92(5):055003, 2004.

[120] A. Einstein. On the electrodynamics of moving bodies. *Annalen der Physik*, 17(50):891, 1905.

[121] G. Marx. Interstellar vehicle propelled by terrestrial laser beam. *Nature*, 211(5044):22–23, 1966.

[122] A. Macchi, S. Veghini, *et al.* "Light sail" acceleration reexamined. *Physical Review Letters*, 103(8):085003, 2009.

[123] T. Esirkepov, M. Yamagiwa, *et al.* Laser ion-acceleration scaling laws seen in multiparametric particle-in-cell simulations. *Physical Review Letters*, 96(10):105001, 2006.

[124] T. Esirkepov, M. Borghesi, *et al.* Highly efficient relativistic-ion generation in the laser-piston regime. *Physical Review Letters*, 92(17):175003, 2004.

[125] A. P. L. Robinson, M. Zepf, *et al.* Radiation pressure acceleration of thin foils with circularly polarized laser pulses. *New Journal of Physics*, 10(1):013021, 2008.

[126] A. Macchi, S. Veghini, *et al.* Radiation pressure acceleration of ultrathin foils. *New Journal of Physics*, 12(4):045013, 2010.

[127] J. Denavit. Absorption of high-intensity subpicosecond lasers on solid density targets. *Physical Review Letters*, 69(21):3052–3055, 1992.

[128] I. V. Pogorelsky, N. P. Dover, *et al.* Ion acceleration by laser hole-boring into plasmas. *AIP Conference Proceedings*, 1507(1):814–819, 2012.

[129] A. P. L. Robinson, P. Gibbon, *et al.* Relativistically correct hole-boring and ion acceleration by circularly polarized laser pulses. *Plasma Physics and Controlled Fusion*, 51(2):024004, 2009.

[130] A. P. L. Robinson, D.-H. Kwon, *et al.* Hole-boring radiation pressure acceleration with two ion species. *Plasma Physics and Controlled Fusion*, 51(9):095006, 2009.

[131] F. Dollar, C. Zulick, *et al.* Finite spot effects on radiation pressure acceleration from intense high-contrast laser interactions with thin targets. *Physical Review Letters*, 108(17):175005, 2012.

[132] O. Klimo, J. Psikal, *et al.* Monoenergetic ion beams from ultrathin foils irradiated by ultrahigh-contrast circularly polarized laser pulses. *Physical Review Accelerators and Beams*, 11(3):031301, 2008.

[133] T. P. Yu, A. Pukhov, *et al.* Stable laser-driven proton beam acceleration from a two-ion-species ultrathin foil. *Physical Review Letters*, 105(6):065002, 2010.

[134] S. Kar, K. F. Kakolee, *et al.* Ion acceleration in multispecies targets driven by intense laser radiation pressure. *Physical Review Letters*, 109(18):185006, 2012.

[135] M. D. Perry, D. Pennington, *et al.* Petawatt laser pulses. *Optics Letters*, 24(3):160–162, 1999.

[136] A. Dubietis, R. Butkus, *et al.* Trends in chirped pulse optical parametric amplification. *IEEE Journal of Selected Topics in Quantum Electronics*, 12(2):163–172, 2006.

[137] C. Danson, P. Brummitt, *et al.* Vulcan petawatt- an ultra-high-intensity interaction facility. *Nuclear Fusion*, 44(12):S239, 2004.

[138] F. Wagner, C. P. João, *et al.* Temporal contrast control at the phelix petawatt laser facility by means of tunable sub-picosecond optical parametric amplification. *Applied Physics B*, 116(2):429–435, 2014.

[139] S. Hooker and C. Webb. Laser Physics. *Oxford University Press*, 2010.

[140] C. Hooker, Y. Tang, *et al.* Improving coherent contrast of petawatt laser pulses. *Optics Express*, 19(3):2193–2203, 2011.

[141] C. Ziener, P. S. Foster, *et al.* Specular reflectivity of plasma mirrors as a function of intensity, pulse duration, and angle of incidence. *Journal of Applied Physics*, 93(1):768–770, 2003.

[142] G. Doumy, F. Quéré, *et al.* Complete characterization of a plasma mirror for the production of high-contrast ultraintense laser pulses. *Physical Review E*, 69(2):026402, 2004.

[143] P. Monot, G. Doumy, *et al.* High-order harmonic generation by nonlinear reflection of an intense high-contrast laser pulse on a plasma. *Optics Letters*, 29(8):893–895, 2004.

[144] B. Dromey, S. Kar, *et al.* The plasma mirror- a subpicosecond optical switch for ultrahigh power lasers. *Review of Scientific Instruments*, 75(3):645–649, 2004.

[145] G. G. Scott, V. Bagnoud, *et al.* Optimization of plasma mirror reflectivity and optical quality using double laser pulses. *New Journal of Physics*, 17(3):033027, 2015.

[146] D. Neely, P. Foster, *et al.* Enhanced proton beams from ultrathin targets driven by high contrast laser pulses. *Applied Physics Letters*, 89(2):021502, 2006.

[147] H. C. Kapteyn, A. Szoke, *et al.* Prepulse energy suppression for high-energy ultrashort pulses using self-induced plasma shuttering. *Optics Letters*, 16(7):490–492, 1991.

[148] T. Wittmann, J. P. Geindre, *et al.* Towards ultrahigh-contrast ultraintense laser pulses- complete characterization of a double plasma-mirror pulse cleaner. *Review of Scientific Instruments*, 77(8):083109, 2006.

[149] Y. Nomura, L. Veisz, *et al.* Time-resolved reflectivity measurements on a plasma mirror with few-cycle laser pulses. *New Journal of Physics*, 9(1):9, 2007.

[150] A. Dubietis, G. JonuAauskas, *et al.* Powerful femtosecond pulse generation by chirped and stretched pulse parametric amplification in BOO crystal. *Optics Communications*, 88(4-6):437–440, 1992.

[151] G. Cheriaux, B. Walker, *et al.* Aberration-free stretcher design for ultrashort-pulse amplification. *Optics Letters*, 21(6):414–416, 1996.

[152] W. Shaikh, I. Musgrave, *et al.* A high contrast dual OPCPA pre-amplifier system using both picosecond and nanosecond pump pulses for the vulcan petawatt facility. In *Lasers, Sources and Related Photonic Devices. Optical Society of America*, 2010.

[153] G. Cerullo, S. D. Silvestri, *et al.* Ultrafast optical parametric amplifiers. *Review of Scientific Instruments*, 74(1):1–18, 2003.

[154] J. M. Yang, P. McKenna, *et al.* Nuclear reactions in copper induced by protons from a petawatt laser-foil interaction. *Applied Physics Letters*, 84(5):675–677, 2004.

[155] R. Clarke, P. Simpson, *et al.* Nuclear activation as a high dynamic range diagnostic of laser-plasma interactions. *Nuclear Instruments and Methods in Physics Research Section A: Accelerators, Spectrometers, Detectors and Associated Equipment*, 585(3):117–120, 2008.

[156] D. C. Carroll, P. Brummitt, *et al.* A modified thomson parabola spectrometer for high resolution multi-mev ion measurements- application to laser-driven ion acceleration. *Nuclear Instruments and Methods in Physics Research Section A: Accelerators, Spectrometers, Detectors and Associated Equipment*, 620(1):23 –27, 2010.

[157] M. Roth. The diagnostics of ultra-short pulse laser-produced plasma. *Journal of Instrumentation*, 6(09):R09001, 2011.

[158] M. Borghesi, D. H. Campbell, *et al.* Electric field detection in laser-plasma interaction experiments via the proton imaging technique. *Physics of Plasmas*, 9(5):2214–2220, 2002.

[159] http://www.srim.org.

[160] P. McKenna, K. W. D. Ledingham, *et al.* Characterization of proton and heavier ion acceleration in ultrahigh-intensity laser interactions with heated target foils. *Physical Review E*, 70(3):036405, 2004.

[161] M. Sonoda, M. Takano, *et al.* Computed radiography utilizing scanning laser stimulated luminescence. *Radiology*, 148(3):833–838, 1983.

[162] N. Izumi, R. Snavely, *et al.* Application of imaging plates to x-ray imaging and spectroscopy in laser plasma experiments (invited). *Review of Scientific Instruments*, 77(10):10E325, 2006.

[163] A. L. Meadowcroft, C. D. Bentley, *et al.* Evaluation of the sensitivity and fading characteristics of an image plate system for x-ray diagnostics. *Review of Scientific Instruments*, 79(11):113102, 2008.

[164] I. J. Paterson, R. J. Clarke, *et al.* Image plate response for conditions relevant to laser-plasma interaction experiments. *Measurement Science and Technology*, 19(9):095301, 2008.

[165] S. G. Gales and C. D. Bentley. Image plates as x-ray detectors in plasma physics experiments. *Review of Scientific Instruments*, 75(10):4001–4003, 2004.

[166] B. R. Maddox, H. S. Park, *et al.* High-energy x-ray backlighter spectrum measurements using calibrated image plates. *Review of Scientific Instruments*, 82(2):023111, 2011.

[167] H. Chen, N. L. Back, *et al.* Absolute calibration of image plates for electrons at energy between 100 keV and 4 MeV. *Review of Scientific Instruments*, 79(3):033301, 2008.

[168] S. Holler, J.-C. Auger, *et al.* Observations and calculations of light scattering from clusters of spheres. *Applied Optics*, 39(36):6873–6887, 2000.

[169] L. Hanssen. Integrating-sphere system and method for absolute measurement of transmittance, reflectance, and absorptance of specular samples. *Applied Optics*, 40(19):3196–204, 2001.

[170] E. T. Gumbrell, R. A. Smith, *et al.* Picosecond optical probing of ultrafast energy transport in short pulse laser solid target interaction experiments. *Physics of Plasmas*, 5(10):3714–3721, 1998.

[171] U. Teubner, I. Uschmann, *et al.* Absorption and hot electron production by high intensity femtosecond uv-laser pulses in solid targets. *Physical Review E*, 54(4):4167–4177, 1996.

[172] M. Borghesi, A. J. Mackinnon, *et al.* Absorption of subpicosecond UV laser pulses during interaction with solid targets. *Physical Review E*, 60(6):7374–7381, 1999.

[173] R. Godwin, R. Sachsenmaier, *et al.* Angle-dependent reflectance of laser-produced plasmas. *Physical Review Letters*, 39(19):1198–1201, 1977.

[174] A. J. Rijke, S. Nijdam, *et al.* A calibrated integrating sphere setup to determine the infrared spectral radiant flux of high-intensity discharge lamps. *Journal of Physics D: Applied Physics*, 44(22):224007, 2011.

[175] J. C. Wyant and K. Creath. Basic Wavefront Aberration Theory For Optical Metrology. *Applied Optics and Optical Engineering*, 1992.

[176] C. Birdsall and A. Langdon. Plasma Physics via Computer Simulation. *Institute of Physics*, 2004.

[177] T. Arber. Epoch: Extendable pic open collaboration. http:// ccp-forge.cse.rl.ac.uk/gf/project/epoch/. , 2014.

[178] C. P. Ridgers, C. S. Brady, *et al.* Dense electron-positron plasmas and bursts of gamma-rays from laser-generated quantum electrodynamic plasmas. *Physics of Plasmas*, 20(5):056701, 2013.

[179] R. Capdessus and P. McKenna. Influence of radiation reaction force on ultraintense laser-driven ion acceleration. *Physical Review E*, 91(5):053105, 2015.

[180] A. Kon, M. Nakatsutsumi, *et al.* Geometrical optimization of an ellipsoidal plasma mirror toward tight focusing of ultra-intense laser pulse. *Journal of Physics: Conference Series*, 244(3):032008, 2010.

[181] M. Nakatsutsumi, A. Kon, *et al.* Fast focusing of short-pulse lasers by innovative plasma optics toward extreme intensity. *Optics Letters*, 35(13):2314–2316, 2010.

[182] R. Wilson, M. King, *et al.* Ellipsoidal plasma mirror focusing of high power laser pulses to ultra-high intensities. *Physics of Plasmas*, 23(3):033106, 2016.

[183] M. Nakatsutsumi, A. Kon, *et al.* High-energy proton acceleration using an innovative plasma-based fast (F/0.6) focusing optic. *Central Laser Facility Annual Report*, 2011.

[184] S. Weber, S. Bechet, *et al.* P3: An installation for high-energy density plasma physics and ultra-high intensity laser-matter interaction at ELI-beamlines. *Matter and Radiation at Extremes*, 2(4):149–176, 2017.

[185] I. Thiele, S. Skupin, *et al.* Boundary conditions for arbitrarily shaped and tightly focused laser pulses in electromagnetic codes. *Journal of Computational Physics*, 321:1110–119, 2016.

[186] T. M. Jeong, S. Weber, *et al.* Spatio-temporal modification of femtosecond focal spot under tight focusing condition. *Optics Express*, 23(9):11641–11656, 2015.

[187] O. N. Stavroudis and A. J. Ames. Confocal prolate spheroids in an off-axis system. *Journal of the Optical Society of America A, Optics and Image Science*, 9(11):2083–2088, 1992.

[188] C. Bourgenot, D. J. Robertson, *et al.* Tool offset optimisation for the machining of free-form optics with a non-zero gradient at the centre, 2015.

[189] C. Thaury, F. Quere, *et al.* Plasma mirrors for ultrahigh-intensity optics. *Nature Physics*, 3(6):424–429, 2007.

[190] F. Nürnberg, M. Schollmeier, *et al.* Radiochromic film imaging spectroscopy of laser-accelerated proton beams. *Review of Scientific Instruments*, 80(3):033301, 2009.

[191] A. J. Mackinnon, P. K. Patel, *et al.* Proton radiography of a laser-driven implosion. *Physical Review Letters*, 97(4):045001, 2006.

[192] D. A. MacLellan, D. C. Carroll, *et al.* Tunable mega-ampere electron current propagation in solids by dynamic control of lattice melt. *Physical Review Letters*, 113(18):185001, 2014.

[193] S. Kawata, T. Izumiyama, *et al.* Laser ion acceleration toward future ion beam cancer therapy- numerical simulation study. *Laser Therapy*, 22(2):103–114, 2013.

[194] C. Perego, D. Batani, *et al.* Target normal sheath acceleration analytical modeling, comparative study and developments. *Review of Scientific Instruments*, 83(2):02B502, 2012.

[195] C. Brenner, J. Green, *et al.* Dependence of laser accelerated protons on laser energy following the interaction of defocused, intense laser pulses with ultra-thin targets. *Laser and Particle Beams*, 29(3):345–351, 2011.

[196] C. M. Brenner, P. McKenna, *et al.* Modelling the effect of laser focal spot size on sheath- accelerated protons in intense laser-foil interactions. *Plasma Physics and Controlled Fusion*, 56(8):084003, 2014.

[197] M. Coury, D. C. Carroll, *et al.* Influence of laser irradiated spot size on energetic electron injection and proton acceleration in foil targets. *Applied Physics Letters*, 100(7):074105, 2012.

[198] J. S. Green, D. C. Carroll, *et al.* Enhanced proton flux in the MeV range by defocused laser irradiation. *New Journal of Physics*, 12(8):085012, 2010.

[199] O. Klimo, P. Valenta, *et al.* Laser absorption and ion acceleration under tight-focusing conditions. *44th EPS Conference on Plasma Physics*, (P5.225), 2017.

[200] P. Valenta. Tight-focusing of short intense laser pulses in particle-in-cell simulations of laser-plasma interaction. Master's thesis, *Czech Technical University in Prague Faculty of Nuclear Sciences and Physical Engineering Department of Physical Electronics*, 2017.

[201] Y. Fang, X. Ge, *et al.* Different effects of laser contrast on proton emission from normal large foils and transverse-size-reduced targets. *Plasma Physics and Controlled Fusion*, 58(7):075010, 2016.

[202] X. H. Yuan, D. C. Carroll, *et al.* The influence of preformed plasma on the surface-guided lateral transport of energetic electrons in ultraintense short laser-foil interactions. *Plasma Physics and Controlled Fusion*, 56(5):055001, 2014.

[203] K. Quinn, P. A. Wilson, *et al.* Laser-driven ultrafast field propagation on solid surfaces. *Physical Review Letters*, 102(19):194801, 2009.

[204] K. Zeil, J. Metzkes, *et al.* Robust energy enhancement of ultrashort pulse laser accelerated protons from reduced mass targets. *Plasma Physics and Controlled Fusion*, 56(8):084004, 2014.

[205] P. A. Norreys, M. Santala, *et al.* Observation of a highly directional γ-ray beam from ultrashort, ultraintense laser pulse interactions with solids. *Physics of Plasmas*, 6(5):2150–2156, 1999.

[206] S. Cipiccia, M. R. Islam, *et al.* Gamma-rays from harmonically resonant betatron oscillations in a plasma wake. *Nature Physics*, 7(11):867–871, 2011.

[207] M. Borghesi, A. J. MacKinnon, *et al.* Relativistic channeling of a picosecond laser pulse in a near-critical preformed plasma. *Physical Review Letters*, 78(5):879–882, 1997.

[208] J. H. Bin, W. J. Ma, *et al.* Ion acceleration using relativistic pulse shaping in near-critical-density plasmas. *Physical Review Letters*, 115(6):064801, 2015.

[209] V. L. Ginzburg. The Propagation of Electromagnetic Waves in Plasmas. *Pergamon*, 1964.

[210] K. Eidmann, R. Rix, *et al.* Absorption of intense high-contrast sub-picosecond laser pulses in solid targets. *Europhysics Letters*, 55(3):334, 2001.

[211] H. Nishimura, H. Azechi, *et al.* Experimental study of wavelength dependences of laser-plasma coupling, transport, and ablation processes. *Physical Review A*, 23(4):2011–2019, 1981.

[212] D. F. Price, R. M. More, *et al.* Absorption of ultrashort laser pulses by solid targets heated rapidly to temperatures 1–1000 eV. *Physical Review Letters*, 75(2):252–255, 1995.

[213] M. H. Key, M. D. Cable, *et al.* Hot electron production and heating by hot electrons in fast ignitor research. *Physics of Plasmas*, 5(5):1966–1972, 1998.

[214] W. Theobald, K. Akli, *et al.* Hot surface ionic line emission and cold k-inner shell emission from petawatt-laser-irradiated cu foil targets. *Physics of Plasmas*, 13(4):043102, 2006.

[215] J. Myatt, W. Theobald, *et al.* High-intensity laser interactions with mass-limited solid targets and implications for fast-ignition experiments on OMEGA EP. *Physics of Plasmas*, 14(5):056301, 2007.

[216] M. C. Levy, S. C. Wilks, *et al.* Petawatt laser absorption bounded. *Nature Communications*, 5(10):4149, 2014.

[217] B. C. Stuart, M. D. Feit, *et al.* Laser-induced damage in dielectrics with nanosecond to subpicosecond pulses. *Physical Review Letters*, 74(12):2248–2251, 1995.

[218] R. J. Gray, X. H. Yuan, *et al.* Surface transport of energetic electrons in intense picosecond laser-foil interactions. *Applied Physics Letters*, 99(17):171502, 2011.

[219] D. R. Rusby, L. A. Wilson, *et al.* Measurement of the angle, temperature and flux of fast electrons emitted from intense laser-solid interactions. *Journal of Plasma Physics*, 81(5):475810505, 2015.

[220] http://physics.nist.gov/physrefdata/star/text/estar.html.

[221] R. J. Gray, D. A. MacLellan, *et al.* Azimuthal asymmetry in collective electron dynamics in relativistically transparent laser-foil interactions. *New journal of physics*, 16(9):093027, 2014.

[222] B. Gonzalez-Izquierdo, R. J. Gray, *et al.* Optically controlled dense current structures driven by relativistic plasma aperture-induced diffraction. *Nature Physics*, 12(5):505–512, 2016.

[223] H. W. Powell, M. King, *et al.* Proton acceleration enhanced by a plasma jet in expanding foils undergoing relativistic transparency. *New Journal of Physics*, 17(10):103033, 2015.

[224] M. N. Quinn, X. H. Yuan, *et al.* Refluxing of fast electrons in solid targets irradiated by intense, picosecond laser pulses. *Plasma Physics and Controlled Fusion*, 53(2):025007, 2011.

[225] A. G. Krygier, D. W. Schumacher, *et al.* On the origin of super-hot electrons from intense laser interactions with solid targets having moderate scale length preformed plasmas. *Physics of Plasmas*, 21(2):023112, 2014.

[226] A. Pukhov, Z.-M. Sheng, *et al.* Particle acceleration in relativistic laser channels. *Physics of Plasmas*, 6(7):2847–2854, 1999.